Lagrangian Transport Structures in Three-dimensional Incompressible Time-periodic Flow

Submitted in partial fulfillment of the requirements

of the degree of

Doctor of Philosophy

of the

Indian Institute of Technology Bombay, India

and

Monash University, Australia
by

Bharath Ravu

Supervisors:

Prof. Devang V Khakhar (IIT Bombay)

Prof. Murray Rudman (Monash University)
Dr. Guy Metcalfe (Swinburne University of Technology)

The course of study for this award was developed jointly by

Monash University, Australia and the Indian Institute of Technology Bombay, India

and was given academic recognition by each of them.

The programme was administrated by The IITB-Monash Research Academy

(2019)

Declaration

I declare that this written submission represents my ideas in my own words and where other's ideas or words have been included, I have adequately cited and referenced the original sources. I also declare that I have adhered to all principles of academic honesty and integrity and have not misrepresented or fabricated or falsified any idea/data/fact/source in my submission. I understand that any violation of the above will be cause for disciplinary action by the Institute and can also evoke penal action from the sources which have thus not been properly cited or from whom proper permission has not been taken when needed.

Notice 1

Under the Copyright Act 1968, this thesis must be used only under the normal conditions of scholarly fair dealing. In particular no results or conclusions should be extracted from it, nor should it be copied or closely paraphrased in whole or in part without the written consent of the author. Proper written acknowledgement should be made for any assistance obtained from this thesis.

Notice 2

I certify that I have made all reasonable efforts to secure copyright permissions for third-party content included in this thesis and have not knowingly added copyright content to my work without the owner's permission.

Student Name: Bharath Ravu
IITB ID: 134024001
Monash ID: 25557033

Abstract

Understanding and controlling Lagrangian trajectories is a prerequisite in the design of efficient mixing devices for highly viscous fluids and microfluidics. Such devices often have spatial symmetry and/or time periodicity. Flow symmetries manifest as invariants of the flow, and destroying these invariants is a necessary, but not sufficient, condition for obtaining good mixing.

In this thesis, a closed, 3D incompressible, steady base flow is considered that has two invariants in the Stokes regime. First one, and then the second, invariant is destroyed and the Lagrangian structures in the resulting flows examined. The first invariant is destroyed by periodically reorienting the base flow, giving a one-invariant flow that occurs on a set of nested topological spheres. The one-invariant flow is further perturbed by inertia, giving a zero-invariant flow.

To compute Lagrangian structures accurately, a new divergence-free interpolation method is developed and presented. The method guarantees that any grid-based velocity data that samples a continuous divergence-free velocity field can be approximated by a representation that is analytically divergence-free and matches the velocity on the grid almost exactly. In 3D incompressible flows with one invariant, it is shown that isolated periodic points cannot exist; hence periodic lines and their manifolds constitute all of the Lagrangian structure. A hierarchy of periodic lines emerges in such flows whose connection and behaviour is controlled by resonance points (at a $1{:}n$ resonance point on a period-1 line, the net deformation is zero after n periods). These periodic lines, in turn, control transport in the flow. Here it is shown that global Lagrangian transport structures of one invariant flows can be completely understood and calculated numerically by identifying resonance points.

Upon inertial perturbation, 1:1 resonance points which always emerge as pairs on a period-1 line of the one-invariant flow give rise to a new mechanism of 3D chaotic transport that features non-heteroclinic connections of tubular transition regions. Tubular transition regions are generally observed in Hamiltonian systems of higher dimensions, and for the first time, are observed here in a 3D incompressible flow.

Acknowledgements

I thank IITB-Monash Research Academy for their financial support over the course of my PhD.

I thank my supervisors: Prof. Murray Rudman, Dr Guy Metcalfe and Prof. Devang Khakhar, for their continuous support at every stage, making my PhD journey comfortable. I also thank Dr Daniel Lester for his feedback on our research papers.

I thank the staff of IITB-Moansh Research Academy. You are wonderful and you made my journey enjoyable.

I thank my friends and my family for their love and support over the years.

Contents

Abstract **v**

Acknowledgements **vii**

List of Figures **xiii**

List of Tables **xxiii**

1 Introduction **1**

1.1 Background 1

1.2 Lagrangian transport 2

1.2.1 Chaotic advection 2

1.3 2D unsteady flows 3

1.4 3D flows 5

1.4.1 One invariant flow (or action-angle-angle flow) 6

1.4.2 3D transport mechanisms 7

1.5 Objectives 8

1.5.1 Approach 8

1.5.2 Necessity of a new divergence-free interpolation 9

1.6 Outline of the thesis 10

2 Periodically Reoriented Hemisphere Flow **13**

2.1 Base flow 13

2.1.1 Base flow in Stokes regime 14

2.1.2 Base flow in inertial regime 16

2.2 Periodically Reoriented Hemisphere Flow (PRHF) 18

2.3 PRHF - Stokes regime 19

2.3.1 Symmetry of the PRHF 20

2.3.2 Location of period-1 points 21

2.3.3 Three non-trivial period-1 points 23

2.3.4 Non-existence of isolated periodic points in one-action maps . . . 25
2.3.5 Enumeration of the invariant (or action) 26
2.4 Linearization of PRHF map 26
2.4.1 Multipliers in the Stokes regime 28
2.4.2 Multipliers in the inertial regime 29
2.5 Invariants of deformation tensor 30
2.5.1 Stokes regime 31

3 Computational Methods **33**

3.1 Obtaining the base flow velocity field of lid-driven hemisphere flow . . . 33
3.2 A new divergence-free interpolation method 35
3.2.1 Outline of the Finn and Chacon method 36
3.2.2 Overview of the new method 37
3.2.3 Derivation of the vector potential components in Cartesian coordinates 41
3.2.4 Method for general curvilinear coordinates 48
3.2.5 Test case 48
3.3 Creating analytically divergence-free base flow velocity field of lid-driven hemisphere flow 54
3.3.1 Base flow in the Stokes regime 54
3.3.2 Base flow in the inertial regime 55
3.4 Calculating the period-1 line of PRHF in the Stokes regime 56
3.4.1 Calculation of period-1 points using Broyden's method 57
3.5 Calculation of deformation tensor (or Jacobian) of the PRHF map 58
3.6 Calculation of higher order periodic lines of PRHF in the Stokes regime . 59
3.6.1 Finding n initial period-n points 60
3.6.2 Calculation of a period-n line using a known initial periodic point on that line 60
3.7 Calculation of isolated period-1 points of PRHF in the inertial regime . . 61

4 Numerical Analysis of PRHF in Stokes Regime **63**

4.1 Parameterization of periodic lines 63
4.2 The Lagrangian skeleton 64
4.2.1 Example: Reorientation angle $\Theta = \pi/4$ 65
4.2.2 Effect of reorientation angle on period-1 lines 71
4.3 Resonances in one invariant flows 73
4.3.1 Identification of resonance points on a period-1 line 74

4.3.2 1:1 Resonance (Fold bifurcation) 76
4.3.3 1:2 Resonance 77
4.3.4 1:3 Resonance 81
4.3.5 1:4 Resonance 86
4.3.6 2:6 resonance 89
4.4 Global Lagrangian structures from local resonance bifurcations 91
4.4.1 Example: $\Theta = \pi/8$ and $\beta = 4$ 91
4.4.2 Example: $\Theta = \pi/4$ and $\beta = 4$ 93
4.5 Summary 98

5 Numerical Analysis of PRHF in Inertial Regime **101**
5.1 Period-1 (or Fixed point) structures 102
5.1.1 Nature of isolated period-1 points 102
5.1.2 Numerical computation of manifolds 103
5.1.3 Some features of the isolated period-1 points 106
5.1.4 General conventions regarding figures 106
5.2 A preview of main results for finite *Re* 107
5.3 Two period-1 piercings on shells 110
5.3.1 Very low β value 110
5.3.2 Low β values 111
5.3.3 A chain of heteroclinic connections 115
5.4 One wiggle 120
5.4.1 $\Theta = \pi/5$ and $\beta = 10$ 120
5.4.2 $\Theta = \pi/4$ and $\beta = 9$ 122
5.5 Two wiggles 131
5.5.1 $\Theta = \pi/8$ and $\beta = 8$ 131
5.5.2 $\Theta = \pi/4$ and $\beta = 16$ 131
5.6 Summary 138

6 Conclusions **141**
6.1 Future work 145

A Interpolation Conditions **147**
A.1 Modified ABC flow 147

References **149**

List of Publications **157**

List of Figures

1.1 Types of periodic points in 2D flows. 4

1.2 Schematic of a flow driven by a titled rotating disk (reproduced from Fountain *et al.* (1998)). 6

2.1 Schematic of the lid driven hemisphere flow. 14

2.2 Schematic of the lid driven hemisphere flow. Continuous lines are representative streamlines of base flow. Dotted line is the stagnation line. . . . 15

2.3 Flow cross-section of streamlines in the x–y plane. The dashed line is the hemisphere and lid boundary. The lid moves left to right in the $+x$ direction. 15

2.4 A stream line of base flow (continuous black line) on the centre plane and its reflection (magenta) about y axis is shown for $Re = 1$ 17

2.5 Poincaré section at $x = 0$ plane of Re=1 base flow. 17

2.6 Schematic showing reorientation of the base flow. 19

2.7 Symmetry plane for $\Theta = \pi/4$. 21

2.8 Projection of a stream line of the base flow: (a) x–y projection and (b) x–z projection. 22

2.9 Enumeration of the action in the Stokes flow. $y_{SP} = 0.2588$ is the y coordinate of stagnation point. 24

2.10 Hemisphere lid: I_Θ is the symmetry plane and the lid velocity $U_W = 1$ . . 24

3.1 The mesh corresponding to hemisphere in the axial-radial plane. 34

3.2 Lid Velocity along x axis. 35

3.3 Spline basis functions $b_1, b_2, ...b_{n_x+3}$. The region of support for each spline is four times the grid spacing, and four splines contribute to the value of the function at any grid point. 41

3.4 Lagrangian trajectories computed from the analytic velocity field (solid line), using the new interpolation method (diamond), and using FC method (circle). (top) Oblique view. (bottom) Top view. The solid square indicates the initial condition of all three orbits, while hollow square, big diamond and big circle trajectory's end for respectively the analytic, the new method and the FC orbits. 52
3.5 Circle centred at a period-1 point on symmetry plane S_Θ. 56

4.1 For $\Theta = \pi/4$ and indicated values of β, (left) period-1 lines viewed perpendicular to symmetry plane in normal space coordinates, and (right) the same lines parameterized by action and arc length along the line. Arc length is in units of radius. Blue (red) are elliptic (hyperbolic) segments. . 65
4.2 Period-1 line on symmetry plane for $\beta = 16$ and $\Theta = \pi/4$. 67
4.3 Action and arc length along the period-1 line for $\beta = 16$ and $\Theta = \pi/4$. The lower figure is a close-up of the region inside the rectangle in the upper figure in which five different shells are defined corresponding to different numbers and types of piercings by the period-1 line. 68
4.4 Poincaré map of shell a_2 with two elliptic points (shell number 0.2); Left is top-front view, right is bottom view. 69
4.5 Poincaré map of shell a_{3T} with two elliptic points, and one parabolic point (shell number 0.42); Left is top-front view, right is bottom view. 69
4.6 Poincaré map of shell a_6 with four elliptic points and two hyperbolic points (shell number 0.44); Left is top-front view, right is bottom view. . . 70
4.7 Poincaré map of shell a_{5T} with three elliptic points, one hyperbolic point and one parabolic point (shell number 0.4555); Left is top-front view, right is bottom view. 70
4.8 Poincaré map of shell a_4 with three elliptic points and one hyperbolic point (shell number 0.47); Left is top-front view, right is bottom view. . . 71
4.9 Action and arc length along period-1 lines for $\beta = 8$, and $\Theta = 2\pi/8, 2\pi/11$ and $2\pi/16$ 72
4.10 Appearance of a first wiggle as function of Θ and the corresponding β value at appearance. The corresponding β value lies within the error bar. . 72
4.11 Period-1 line and Poincaré maps of flow on several shells. Oblique view. . 73
4.12 Possible eigenvalues (λ_1 and λ_2) shown with the unit circle on complex plane for period-1 points; $\lambda_3 = 1$, which is not shown here. 75
4.13 Action and Trace values of period-1 points along the segment of the period-1 line inside rectangular box in figure 4.2 77

4.14 A close up of the segment of the period-1 line inside the rectangular box in Figure 4.13 (a). Also plotted are local Poincaré sections on three neighbouring shells. The upper and lower sections correspond to shells containing degenerate points and the middle section is on a shell half way between. Note that the shell-normal coordinate has been expanded for clarity. 78

4.15 (a) Period-1 line for $\beta = 2$ and $\Theta = \pi/4$ on symmetry plane. (b) Action and trace along the period-1 line 79

4.16 Period-1 and Period-2 lines for $\beta = 2$ and $\Theta = \pi/4$ 80

4.17 Action vs Arclength of period-1 and period-2 lines for $\beta = 2$ and $\Theta = \pi/4$ 80

4.18 Local Poincaré sections of shells near 1:2 resonance point for $\Theta = \pi/4$ and $\beta = 2$. Note that the shell-horizontal and shell-normal coordinate has been expanded for clarity. 81

4.19 (a) Period-1 line for $\beta = 1$ and $\Theta = \pi/8$ on symmetry plane. (b) Action and trace along the period-1 line 82

4.20 Period-1 and period-3 lines for $\beta = 1$ and $\Theta = \pi/8$ 83

4.21 (a) Action is plotted along period-1 line and three period-3 lines for $\Theta = pi/8$ and $\beta = 1$ (b) Top right segment of figure (a) 84

4.22 Local Poincaré sections of shells near the 1:3 resonance point for $\Theta = \pi/8$ and $\beta = 1$. Note that the shell-horizontal and shell-normal coordinate has been expanded for clarity. 85

4.23 P1 and P4 lines for $\beta = 1$ and $\Theta = \pi/8$ 86

4.24 (a) Action is plotted along period-1 and period-4 lines for $\Theta = pi/8$ and $\beta = 1$ (b) Top right segment of figure (a) 87

4.25 Local Poincaré sections of shells near 1:4 resonance point for $\Theta = \pi/8$ and $\beta = 1$. Note that the shell-horizontal and shell-normal coordinate has been expanded for clarity. 88

4.26 A period-1 line (P1), a period-2 line (P2) and three period-6 lines ($P6_1, P6_2$ and $P6_3$) coordinating via 1:2 resonance point and 2:6 resonance points for $\Theta = \pi/4$ and $\beta = 2$. 90

4.27 (a) The Period-1 line for $\beta = 4$ and $\Theta = \pi/8$ on the symmetry plane. (b) Action and trace along the period-1 line 92

4.28 $\Theta = \pi/8$ and $\beta = 4$, Period-1 line P_1 and period-2 line $P2_1$ are on symmetry plane, and period-2 line $P2_2$ is symmetric about symmetry plane; Elliptic line segments are coloured blue, hyperbolic line segments are coloured red and degenerate points are coloured green. Five 1 : 2 resonance points on P_1 are also shown with numbers 1 – 4. 93

4.29 Action against arc length of periodic lines (P1, $P2_1$ and $P2_2$) shown in figure 4.28 are plotted. Three horizontal lines correspond to action values (0.5285, 0.5588, 0.5919). 94

4.30 Periodic lines shown in figure 4.28 imparting its character on to shell 0.5285; Stroboscopic map on Shell seen from (a) Bottom (b) Top-side (c) Stroboscopic map on shell is projected on to a plane; Period-1 line piercing point on the shell is represented by solid circle and period-2 lines piercing point on the shell is represented by solid square; blue colour for elliptic and red colour for hyperbolic stability 95

4.31 Periodic lines shown in figure 4.28 imparting its character on to shell 0.5588; Stroboscopic map on Shell seen from (a) Bottom (b) Top-side (c) Stroboscopic map on shell is projected on to a plane; Period-1 line piercing point on the shell is represented by solid circle and period-2 lines piercing point on the shell is represented by solid square; blue colour for elliptic and red colour for hyperbolic stability 96

4.32 Periodic lines shown in figure 4.28 imparting its character on to shell 0.5919; Stroboscopic map on Shell seen from (a) Bottom (b) Top-side (c) Stroboscopic map on shell is projected on to a plane; Period-1 line piercing point on the shell is represented by solid circle and period-2 lines piercing point on the shell is represented by solid square; blue colour for elliptic and red colour for hyperbolic stability 97

4.33 $\Theta = \pi/4$ and $\beta = 4$, Period-1 line P_1 and period-2 line $P2_1$ are on symmetry plane, and period-2 line $P2_2$ is symmetric about symmetry plane; Elliptic line segments are coloured blue, hyperbolic line segments are coloured red and degenerate points are coloured green. Four 1:2 resonance points on P_1 are also shown with numbers 1 – 3. 98

5.1 A typical 2D unstable manifold of a hyperbolic period-1 point 104

5.2 In the limit $Re \rightarrow 0$, isolated period-1 points approach points on the Stokes period-1 line. 105

5.3 Schematic of the main results for the inertial PRHF 109

5.4 Stokes flow period-1 structures in the increasing order of complexity . . . 110

5.5 For $\Theta = \pi/8$ and $\beta = 0.1$: (a) For $\Theta = \pi/8$ and $\beta = 0.1$: a thin slice of the hemisphere centred at the symmetry plane containing isolated period-1 points which are shown as solid circles for $Re = 1$, 1D manifolds of isolated period-1 points (black continuous line), and the Stokes period-1 line (wide transparent blue line); (b) the same period-1 line and the isolated period-1 points paramaterized by action and arc length along the line. Arc length is in units of radius. 112

5.6 A fluid particle orbit (mint colour) for 4.85×10^4 periods with parameters $\Theta = \pi/8$, $\beta = 0.1$; Isolated period-1 points (in solid circles) and their 1D manifolds(black continuous lines with arrows showing the direction of the manifolds) are also seen. 113

5.7 A thin slice of the hemisphere with the width about 10^{-2} centered at the symmetry plane viewed perpendicular to the symmetry plane; Three particle orbits for $\beta = 0.1$ and $\Theta = pi/8$ are shown in black, magenta, and mint colours for $Re = 0$ in (a), $Re = 0.01$ in (b) and $Re = 1$ in (c). In (a), solid blue colour line represents Stokes period-1 line. In (b) and (c), solid circles represent isolated period-1 points of hyperbolic focus nature and black continuous line represents 1d manifolds. 114

5.8 Logarithm of no of periods required for a particle orbit to form one torus for $\beta = 0.1$ and $\Theta = \pi/8$ versus logarithm of Reynolds numbers; 5 solid circles on lines correspond to 5 different Reynolds number values. i.e. Re $=\{ 0.01, 0.05, 0.1, 0.5, 1\}$ 115

5.9 For $\Theta = \pi/8$ and indicated values of β: (left) a thin slice of the hemisphere centred at the symmetry plane containing the Stokes period-1 line which is shown as a continuous line and isolated period-1 points which are shown as solid circles for $Re = 1$ is viewed perpendicular to the symmetry plane; (right) the same period-1 line and the isolated period-1 points paramaterized by action and arc length along the line. 116

5.10 For $\Theta = \pi/8$ and indicated values of β: (left) a thin slice of the hemisphere with width about 10^{-2} centred at the symmetry plane containing particles orbits which are shown as dots with separate colours for different orbits for $Re = 1$ and the isolated period-1 points which are shown as solid circles; (right) Trace 1 vs Trace2 of the period-1 points of both stokes flow and Re=1 flow; small dots represent stokes period-1 points; bigger dots represent $Re = 1$ flow period-1 points. 117

5.11 For $\Theta = \pi/4$ and $\beta = 8$: (a) Stokes Period-1 line and the isolated period-1 points of $R = 1$ flow; (b) Trace 1 vs Trace2 of the period-1 points of both the Stokes flow and Re=1 flow (small dots represent stokes period-1 points and bigger dots represent $Re = 1$ flow); (c) The Stokes period-1 line and the isolated period-1 points of $Re = 1$ flow are parameterized by action and arc length. 118

5.12 For $\Theta = \pi/4$ and $\beta = 8$ (a thin slice of the hemisphere centered at the symmetry plane viewed perpendicular the symmetry plane): Isolated period-1 points are shown as solid circles; Thick transparent line represents the Stokes period-1 line; Continuous black line represents 1D manifolds of the isolated period-1 points; Small dots represent 2D manifolds of the isolated period-1 points (2D unstable manifold of point 5 in magenta, 2D stable manifold of point 4 in green, 2D unstable manifold of point 3 in chocolate and 2D stable manifold of point 2 in violet) 119

5.13 For $\Theta = \pi/5$ and $\beta = 10$: (a) Stokes Period-1 line and the isolated period-1 points of $R = 1$ flow; (b) Trace 1 vs Trace2 of the period-1 points of both the Stokes flow and Re=1 flow (small dots represent stokes period-1 points and bigger dots represent $Re = 1$ flow); (c) The Stokes period-1 line and the isolated period-1 points of $Re = 1$ flow are parameterized by action and arc length. 121

5.14 For $\Theta = \pi/5$ and $\beta = 10$ (a thin slice of the hemisphere centered at the symmetry plane viewed perpendicular the symmetry plane): Isolated period-1 points are shown as solid circles; Thick transparent line represents the Stokes period-1 line; Continuous black line represents 1D manifolds of the isolated period-1 points; Small dots represent 2D manifolds of the isolated period-1 points (2D unstable manifold of point 7 in green, 2D unstable manifold of point 5 in magenta, 2D stable manifold of point 4 in sky blue, 2D unstable manifold of point 3 in chocolate and 2D stable manifold of point 2 in violet) 123

5.15 A 3D view of the manifolds and their interactions of the period-1 points 6 and 7 for $\Theta = \pi/5$ and $\beta = 10$ 124

5.15 A 3D view of the interaction of the manifolds of the period-1 points 4,5 and 6 for $\Theta = \pi/5$ and $\beta = 10$ 125

5.15 A 3D view of the interaction of the manifolds of the period-1 points 3 and 4 for $\Theta = \pi/5$ and $\beta = 10$ 126

5.16 A 3D view of the isolated period-1 points and their manifolds for $\Theta = \pi/5$ and $\beta = 10$: (top) 1D stable manifold in yellow and 2D unstable manifold in green for point 7, 1D unstable manifold in orange and 1d stable manifold in cyan for point 6, and 1d stable manifold in white and 2D unstable manifold in magenta for point 5; (bottom) 1D stable manifold in white and 2D unstable manifold in magenta for point 5, 1D unstable manifold in salmon colour and 2D stable manifold in sky blue for point 4, and 1D stable manifold in green-yellow and 2D unstable manifold in chocolate colour for point 3. 127

5.17 For $\Theta = \pi/4$ and $\beta = 9$: (a) Stokes period-1 line and the isolated period-1 points of $R = 1$ flow; (b) Trace 1 vs Trace2 of the period-1 points of both the Stokes flow and Re=1 flow (small dots represent stokes period-1 points and bigger dots represent $Re = 1$ flow); (c) The Stokes period-1 line and the isolated period-1 points of $Re = 1$ flow are parameterized by action and arc length. 128

5.18 For $\Theta = \pi/4$ and $\beta = 9$ (a thin slice of the hemisphere centered at the symmetry plane viewed perpendicular the symmetry plane): Isolated period-1 points are shown as solid circles; Thick transparent line represents the Stokes period-1 line; Continuous black line represents 1D manifolds of the isolated period-1 points; Small dots represent 2D manifolds of the isolated period-1 points (2D unstable manifold of point 7 in green, 2D unstable manifold of point 5 in magenta, 2D stable manifold of point 4 in sky blue, 2D unstable manifold of point 3 in chocolate colour and 2D stable manifold of point 2 in violet) 129

5.19 A 3D view of the isolated period-1 points and their manifolds for $\Theta = \pi/4$ and $\beta = 9$: (top) 1D stable manifold in yellow and 2D unstable manifold in green for point 7, 1D unstable manifold in orange and 1d stable manifold in cyan for point 6, and 1d stable manifold in white and 2D unstable manifold in magenta for point 5; (bottom) 1D stable manifold in white and 2D unstable manifold in magenta for point 5, 1D unstable manifold in salmon colour and 2D stable manifold in sky blue for point 4, and 1D stable manifold in green-yellow colour and 2D unstable manifold in chocolate colour for point 3. 130

5.20 For $\Theta = \pi/8$ and $\beta = 8$: (a) Stokes Period-1 line and the isolated period-1 points of $R = 1$ flow; (b) Trace 1 vs Trace2 of the period-1 points of both the Stokes flow and Re=1 flow (small dots represent stokes period-1 points and bigger dots represent $Re = 1$ flow); (c) The Stokes period-1 line and the isolated period-1 points of $Re = 1$ flow are parameterized by action and arc length. 132

5.21 For $\Theta = \pi/8$ and $\beta = 8$ (a thin slice of the hemisphere centered at the symmetry plane viewed perpendicular the symmetry plane): Isolated period-1 points are shown as solid circles; Thick transparent line represents the Stokes period-1 line; Continuous black line represents 1D manifolds of the isolated period-1 points; Small dots represent 2D manifolds of the isolated period-1 points (2D unstable manifold of point 7 in green, 2D unstable manifold of point 5 in magenta, 2D unstable manifold of point 3 in chocolate colour and 2D stable manifold of point 2 in violet) 133

5.22 A 3D view of the manifolds of the hyperbolic-node period-1 point 4 for $\Theta = \pi/8$ and $\beta = 8$: 1D unstable manifold in salmon colour and 2D stable manifold in sky blue colour. 133

5.23 A 3D view of the isolated period-1 points and their manifolds for $\Theta = \pi/8$ and $\beta = 8$: (top) 1D stable manifold in yellow and 2D unstable manifold in green for point 7, 1D unstable manifold in orange and 1d stable manifold in cyan for point 6, and 1d stable manifold in white and 2D unstable manifold in magenta for point 5; (bottom) 1D stable manifold in white and 2D unstable manifold in magenta for point 5, 1D unstable manifold in salmon colour and 2D stable manifold in sky blue for point 4, and 1D stable manifold in green yellow and 2D unstable manifold in chocolate colour for point 3. 134

5.24 For $\Theta = \pi/4$ and $\beta = 16$: (a) Stokes Period-1 line and the isolated period-1 points of $R = 1$ flow; (b) Trace 1 vs Trace2 of the period-1 points of both the Stokes flow and Re=1 flow (small dots represent stokes period-1 points and bigger dots represent $Re = 1$ flow); (c) The Stokes period-1 line and the isolated period-1 points of $Re = 1$ flow are parameterized by action and arc length. 135

5.25 For $\Theta = \pi/4$ and $\beta = 16$ (a thin slice of the hemisphere centered at the symmetry plane viewed perpendicular the symmetry plane): Isolated period-1 points are shown as solid circles; Thick transparent line represents the Stokes period-1 line; Continuous black line represents 1D manifolds of the isolated period-1 points; Small dots represent 2D manifolds of the isolated period-1 points (2D unstable manifold of point 4 in green, 2D unstable manifold of point 6 in magenta and 2D unstable manifold of point 8 in chocolate colour). 136

5.26 A 3D view of the isolated period-1 points and their manifolds for $\Theta = \pi/4$ and $\beta = 16$: (top) 1D stable manifold in yellow and 2D unstable manifold in green for point 4, 1D unstable manifold in orange and 1d stable manifold in cyan for point 5, and 1d stable manifold in white and 2D unstable manifold in magenta for point 6; (bottom) 1D stable manifold in white and 2D unstable manifold in magenta for point 6, 1D unstable manifold in salmon colour and 2D stable manifold in sky blue colour for point 7, and 1D stable manifold in green-yellow and 2D unstable manifold in chocolate colour for point 8. 137

List of Tables

1.1 Range of flows. 3
1.2 Different kinds of flows generated from Lid-driven hemisphere system . . 9

2.1 Eigenvalues of the degenerate points on a period-1 line 29
2.2 Nature of a period-1 point from eigenvalues of the deformation tensor computed there. 30

3.1 Errors in the interpolated velocity field on the boundary of a $42 \times 42 \times 42$ grid. 49
3.2 Errors in the interpolated velocity field on a $42 \times 42 \times 42$ grid. 50
3.3 Errors in the interpolated velocity field on the boundary of a $165 \times 165 \times 165$ grid. 50
3.4 Errors in the interpolated velocity field on a $165 \times 165 \times 165$ grid. 51
3.5 Interpolation conditions for the base flow in the Stokes regime. 55
3.6 Interpolation conditions for the base flow in the inertial regime. 56

4.1 Resonances, and their corresponding eigenvalues and trace values on periodic lines; $\lambda_3 = 1$ for each periodic point 76

A1 Interpolation conditions for f - modified ABC flow. 147
A2 Interpolation conditions for A_y - modified ABC flow. 147
A3 Interpolation conditions for A_z - modified ABC flow. 148

Chapter 1

Introduction

1.1 Background

Mixing is an important aspect of many industrial applications such as food processing, steel production, polymer blending, paint processing, petrochemical processing, microfluidics, etc. (Thakur *et al.*, 2003; Erwin, 2011), and in naturally occurring flows such as dispersion of pollutants in the atmosphere and ocean (Wiggins, 2005; Samelson, 2013), and mixing of magma flows in the mantle of the earth (Coltice *et al.*, 2017). In many applications, one wants to achieve uniform mixing quickly. One way to achieve this is through turbulence where chaotic velocity field necessarily produces chaotic transport of fluid particles (Dimotakis, 2005).

However, for highly viscous fluids, generating turbulence may require excessive energy input or result in high temperatures from viscous dissipation. Likewise, at small length scales, turbulence is difficult to achieve. Hence, mixing by turbulence is not suitable for highly viscous fluids (Todd, 2004) and microfluidics (Squires and Quake, 2005; Nguyen and Wu, 2004; Suh and Kang, 2010; Priye *et al.*, 2013; Ward and Fan, 2015), and mixing in many applications must be undertaken in a laminar regime. Mixing happens via advection of fluid particles and diffusion: advection is caused by stirring of the fluid and diffusion is caused by the thermal motion of the fluid molecules. In laminar flows, diffusion is slow compared to the advection of fluid particles. So advection determines the quality of mixing. Good mixing is achieved by advection first, then followed by diffusion in laminar flows once gradient have become high due to stretching and folding.

1.2 Lagrangian transport

Mixing requires neighbouring fluid particle trajectories to deviate from each other rapidly. The Lagrangian view of a flow field is most convenient for investigating mixing aspects of the flow (Cartwright *et al.*, 1999; Wiggins and Ottino, 2004). The advection of a fluid particle in a fluid domain is obtained by integrating a set of non-linear differential equations which are

$$\frac{d\boldsymbol{x}}{dt} = \boldsymbol{V}(\boldsymbol{x}, t), \tag{1.1}$$

where $\boldsymbol{V}$ is the fluid velocity, $\boldsymbol{x}$ is the fluid particle position and t is time. In this thesis, vectors and tensors are always shown as bold letters. In general, equation (1.1) is a special case of a dynamical system. It is a remarkable fact that the phase space (a collection of all possible states) of (1.1) coincides with the physical space of the fluid, and a fluid particle trajectory is equivalent to a phase space trajectory of a dynamical system (Katok and Hasselblatt, 1995; Ott, 2002). Dynamical systems theory describes the time evolution of a system in the phase space and is suited to study the behaviour of fluid particles in a fluid flow (Ottino, 1989; Wiggins, 2003). Hence, the concepts of dynamical systems theory are employed to analyse mixing.

1.2.1 Chaotic advection

Understanding Lagrangian trajectories and controlling them is the key to efficient mixing by laminar flows (Aref, 2002; Haller, 2015; Aref *et al.*, 2017). The no-intersection theorem states that two distinct trajectories never intersect in a finite time. The no-intersection theorem, together with the number of degrees of freedom of a system constrains the type of trajectories possible in that system. The quality of mixing depends on how much chaos the laminar flow admits, where chaos is defined as "aperiodic long-term behaviour in a deterministic system that exhibits sensitive dependence on initial conditions" (Strogatz, 2001). One key feature of chaos is that nearby trajectories diverge exponentially. We want as much chaos as we can get to have good mixing. Chaotic behaviour of a laminar flow system is not due to external noise (or random forces). When a fully deterministic velocity field produces stochastic type Lagrangian trajectories, this situation is called chaotic advection (Aref, 1984). What are the necessary conditions on a system to exhibit chaotic behaviour? The time evolution equations of the system must be non-linear, and the system should have a minimum three degrees of freedom (i.e. the number of variables needed to specify the system completely).

Poincaré-Bendixson theorem describes the long term behaviour of a trajectory in 2D bounded flows. One important result of the Poincaré-Bendixson theorem is that chaotic trajectories cannot occur in bounded steady two-dimensional (2D) flows (Hilborn, 2000). Lagrangian chaotic trajectories can occur in 2D unsteady flows and three-dimensional (3D) steady or unsteady flows. A chaotic system does not have a closed form solution for its governing differential equation (Hilborn, 2000) and is sometimes called a non-integrable system. Integrable systems, whose time evolution equations have closed-form solutions, cannot have chaos. Thus, chaos must be studied through numerical computations or experiments.

Chaotic transport can occur in 2D or 3D unsteady flows, where streamlines of the flow vary (i.e. streamlines of the flow cross at successive times). Chaotic transport can also occur in 3D steady flow, where streamlines of the flow remain unchanging. This kind of chaotic transport is called streamline chaos. The possible combinations of dimensionality and time-dependence are shown in table 1.1 with a description of the key mixing characteristics. In this thesis, only incompressible flow (i.e. $\boldsymbol{\nabla} \cdot \boldsymbol{V} = 0$) is considered, and unsteady flow is restricted to mean periodic in time. The constraints imposed by volume-preservation, by symmetries of the system and by the geometry of a system determine what kind of Lagrangian trajectories are possible for that system. While the primary focus of this thesis is Lagrangian structures in 3D periodic flows, in the following sections, key aspects of 2D unsteady and 3D flows will be discussed as they inform the main body of this thesis.

Table 1.1: Range of flows.

	2D	**3D**
Unsteady	Chaos	Chief subject of this thesis
Steady	No chaos	Streamline chaos

1.3 2D unsteady flows

In 2D, an equivalence exists between advection of a fluid particle in an incompressible flow and the time evolution of a Hamiltonian system in phase space (Ottino, 1990; Morrison, 1998; Salmon, 1988). In incompressible fluids, the fluid volume is conserved, and in a Hamiltonian system, the phase space volume is conserved (Liouville's theorem, Jordan (2004)). Velocity in a 2D steady incompressible flow can be obtained from a scalar stream function $\psi(x, y)$ via

$$v_x = \frac{\partial \psi}{\partial y}, \quad v_y = -\frac{\partial \psi}{\partial x} \tag{1.2}$$

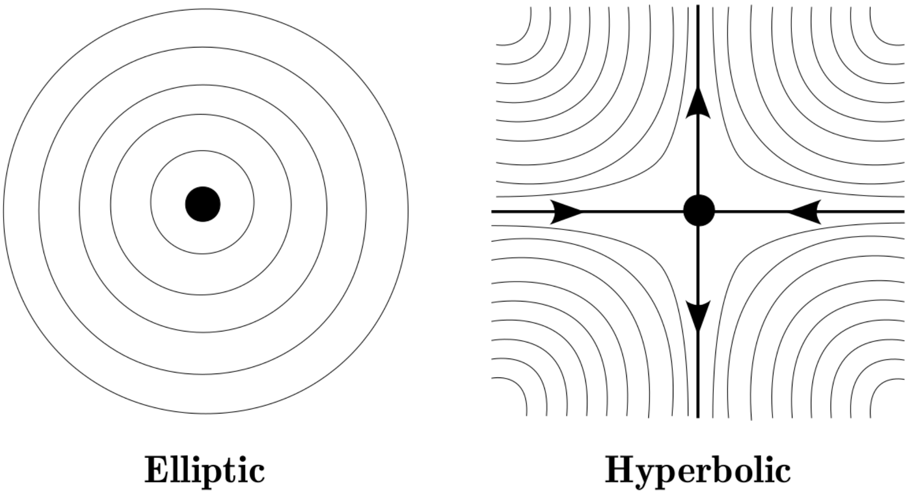

Figure 1.1: Types of periodic points in 2D flows.

The stream function ψ plays the same role as a Hamiltonian function in a system with one degree of freedom (Aref, 1983). Aref was the first to study chaotic advection through a process of stretching and folding in the 2D blinking vertex flow in the laminar regime (Aref, 1984). Because there is an equivalence between time-dependent 1D Hamiltonian systems and 2D incompressible unsteady flows, time-dependent 1D Hamiltonian systems theory, which is well established, has been widely applied to understand transport mechanisms in 2D incompressible unsteady flows (Aref, 1984; Ottino, 1989; Chaiken *et al.*, 1987; Boyland *et al.*, 2000; Lester *et al.*, 2009, 2010). In 2D unsteady flows, most work on chaotic advection has been done with time-periodic flows.

In 2D time-periodic flows, periodic points play a significant role in understanding fluid transport (Ottino, 1989). An n^{th} order periodic point returns to its original position after n periods of the flow. Three different kinds of periodic points exist in 2D flows: elliptic, hyperbolic and parabolic. Fluid transport in the neighbourhood of an elliptic and a hyperbolic periodic points are shown in figure 1.1. In figure 1.1, although, fluid particle trajectories are shown as continuous lines, actually they move discretely on these lines because fluid particle positions are recorded after each period in time-periodic flows. Fluid particles in the neighbourhood of an elliptic periodic point (also called a stable fixed point) orbit around the periodic point forming islands which are barriers to fluid transport across the orbit. Fluid particle trajectories in the neighbourhood of a hyperbolic periodic point (also called an unstable fixed point) expand in one direction and contract in another direction supporting mixing. At a parabolic periodic point, the net deformation is zero. Because the lower order periodic points exert more influence on the Lagrangian structures than the higher order periodic points, computing period-1 points and establishing their type is essential to determining the nature of fluid transport in their neighbourhood.

In 2D time-periodic flows, fluid particles in the neighbourhood of an elliptic periodic point move on closed orbits which can be thought of as tori in three-dimensional space that is obtained by the rotation of 2D spatial space (x_1, x_2) about an axis such that it comes back to its original position after one full period. On perturbation, these tori, breakdown into chaotic trajectories via a well-established mechanism (the KAM theorem, Arnold (1978)). In Hamiltonian theory, the KAM theorem has an important consequence in the perturbation of an integrable Hamiltonian system. A torus is a topological product of two circles, and it has two different time-periods (or frequencies) each for separate circle. For small perturbations (almost integrable), the tori with rational ratios of the frequencies (or winding number) break first, and the tori with irrational ratios survive. As the perturbation increases, the last survivor is the one with ratios of frequencies equal to the most irrational number (Hilborn, 2000; Ottino, 1989).

1.4 3D flows

Most of the studies on "chaotic advection" have been in 2D unsteady flows, and very few studies exist in 3D flows. Because the phase space of a Hamiltonian system is always even dimensional space, Hamiltonian theory cannot be directly applied to 3D incompressible flows (Aref *et al.*, 2017; Cheng and Sun, 1989) and little is known about the mechanisms of transport in three dimensions (Wiggins, 2010). The reasons for this are the explosion of topological complexity that comes with three dimensions and local breakdown of the existing theory (Hamiltonian theory) that describes mixing.

In practice, mixing devices often have spatial symmetry and/or time periodicity. These symmetries in the 3D incompressible flow manifest as invariants or conserved quantities of the flow. Each invariant corresponds to a symmetry (Mezić and Wiggins, 1994; Haller and Mezić, 1998). In time periodic 3D flows, a map which returns the position of a fluid particle after one period can be defined. Such maps in 3D incompressible flows are called Liouvillian maps (Cartwright *et al.*, 1994). In what follows, this concept will become concrete for 3D flows. If an n dimensional system has k invariants of motion, then trajectories of the system live on $n - k$ dimensional space. For flows with invariants, the common nomenclature for position coordinates of fluid particles is action-angle coordinates. A fluid particle trajectory can be expressed in an action-angle coordinate system. Action variables take the values of constants of the motion, and angle variables represent the varying part of the motion. Three-dimensional flows both steady and unsteady can be categorised based on the number of constants of motion (or invariants). Cartwright *et al.* (1996) classified integrable Liouvillian maps into four types: (a) zero actions; three angles

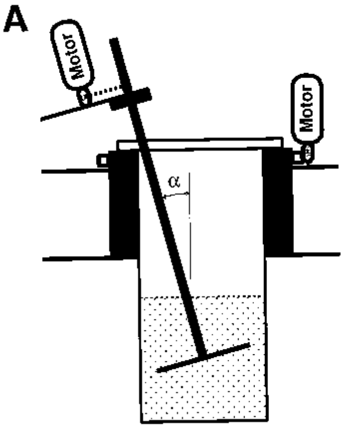

Figure 1.2: Schematic of a flow driven by a titled rotating disk (reproduced from Fountain *et al.* (1998)).

$(\theta_1, \theta_2, \theta_3)$, (b) one action; two angles (I, θ_1, θ_2), (c) two actions; one angle (I_1, I_2, θ), and (d) three actions; zero angles (I_1, I_2, I_3). In two actions maps (action-action-angle maps), fluid particles are constrained to move on closed invariant curves, and in one-action maps (action-angle-angle maps), fluid particles are constrained to move on closed invariant surfaces.

Whenever a flow consists of closed streamlines, on perturbation, the flow turns into tori, an example of such flow is presented in the following. A flow driven by a tilted rotating disk inside a cylindrical container (shown in figure 1.2) is studied experimentally as well as numerically in Fountain *et al.* (1998, 2000). In this flow, when the tilt angle of the rotating disk (α in the figure 1.2) is zero, streamlines are closed circles. When the rotating disk is tilted, tori are formed. Increasing the tilt angle at a constant rotational speed of the disk increases the chaotic region, and increasing the rotational speed of the disk for a fixed tilt angle also increases chaos in the system. This thesis will have a particular emphasis on action-angle-angle flows, and a review of such flows follows.

1.4.1 One invariant flow (or action-angle-angle flow)

In one invariant 3D flows, fluid particles are constrained to move on 2D invariant surfaces. Invariant surfaces of one-action maps can be one of two types: nested tori or nested spheroids (Aref *et al.*, 2017; Moharana *et al.*, 2013; Alexandroff, 1961). Because the fluid particle motion is restricted to 2D surfaces while preserving area, Hamiltonian motion is expected on each invariant surface except in the neighbourhood of stagnation points, where the true 3D character of the flow manifests (Bajer, 1994). As discussed in section 1.3, periodic points play a key organising role in 2D unsteady flows. In one invariant 3D flows, the equivalent concept is a periodic line, which will be discussed later in section 2.3.4. A period-n line is a set of continuous period-n points which return to their original locations after n-periods. There can be more than one period-n line. The coexistence of space-filling invariant surfaces and a periodic line means the periodic line pierces the invariant surfaces - the point of piercing on an invariant surface acts as a 2D periodic point of that invariant surface. In one-action maps (or time-periodic flows with one invariant), periodic points of the periodic line can be elliptic, hyperbolic or parabolic (or degenerate) in the same way as for 2D flows.

Degenerate points occur when there is zero net deformation at a point on a periodic line. Degenerate points have an order associated with them. At an n^{th} order degenerate point, the local deformation is zero after n periods. The role of elliptic and hyperbolic points of a periodic line in one-action maps are well understood (Aref *et al.*, 2017), but the role of degenerate points of a periodic line in the construction of Lagrangian structures is not. Period-doubling and period-tripling bifurcations which are associated with second order and third-order degenerate points correspondingly have been observed (Dullin *et al.*, 1999; Mullowney *et al.*, 2005; Smith *et al.*, 2016). However, a general framework of degenerate points (all orders of degenerate points) and their connection to Lagrangian structures in one-invariant flows are not well established. Establishing such a general framework of degenerate points is one important result of this thesis.

1.4.2 3D transport mechanisms

Although 3D transport is poorly understood, a number of transport mechanisms which improves mixing have been identified. When nested toroidal surfaces of action-action-angle flows are perturbed, 3D chaotic transport can occur via "resonance induced dispersion" (RID) (Cartwright *et al.*, 1995, 1996; Vainchtein *et al.*, 2007, 2008; Vainchtein and Abudu, 2012; Meiss, 2012). In RID, under small perturbations, there exist resonance regions within tori that have local defects where tracers randomly jump between the 1D streamlines of the unperturbed flow. In other regions of space away from resonance, action variables change slowly compared to the angle variable and hence particle trajectories slowly drift from unperturbed streamlines. Since fluid particles continuously visit these resonance regions and are being pushed to different streamlines at these regions, 3D chaos is generated. Smith *et al.* (2017) observed 3D chaotic transport occurring via "localised shear-induced dispersion" (LSID) mechanism, which is similar to RID. In LSID, fluid particles are pushed between streamlines near a localized shear. When nested spheroidal surfaces are perturbed, 3D chaotic transport can occur via "resonance induced merger" (RIM) mechanism (Speetjens *et al.*, 2006a,b; Pouransari *et al.*, 2010). In RIM, some of the spheroidal shells merge forming an adiabatic structure that has an inner and outer adiabatic shell connected by localised tubes. Transverse transport is much faster through the merging tubes than on the adiabatic shells. The important feature of these mechanisms is that they have small regions of space where fast 3D transport happens upon perturbation. While these are the only three transport mechanisms that have been described in the literature so far, there are unanswered questions about them. For example, is "resonance induced merger" mechanism generic for systems with nested spheroids or are there other transport mechanisms for the nested spheroids case? It is likely that there may be other transport mechanisms.

1.5 Objectives

The main objectives of this thesis are:

1. To identify the Lagrangian features that organises global transport in 3D flows with one invariant and to find a way to numerically calculate all the Lagrangian structures in such flows. How the global Lagrangian transport structures are formed in such a flow is not completely known (Wiggins, 2010).

2. To uncover how Lagrangian transport structures evolve as the flow transitions from one invariant flow (topologically spheres) to a zero invariant flow upon inertial perturbation and also to find out 3D transport mechanisms.

3. To develop a new divergence-free interpolation method. Because, to study (1) and (2), a divergence-free interpolation method is required to accurately compute 3D Lagrangian structures. The importance of a divergence-free interpolation method is explained in section 1.5.2.

1.5.1 Approach

To achieve the objectives mentioned above, an incompressible 3D flow with one invariant is selected that can be perturbed from one invariant flow to zero invariant flow by some perturbation. A lid-driven cavity flow system in the Stokes regime suits this purpose. Most of the studies on lid-driven cavity flows are two-dimensional cavities; there are fewer studies of three-dimensional cavities (Shankar and Deshpande, 2000). The particular cavity used here is a hemisphere, and we are aware of no previous study of lid-driven flow in a hemisphere. Moreover, studying this system is viable through experiment and simulation, although this study is limited to simulation.

The invariants of the cavity driven flow with and without inertial effects are considered next. Reynolds number (*Re*) is the ratio of inertial forces to viscous forces. In the Stokes limit ($Re = 0$), when the lid moves uniformly in one direction, the velocity is steady and has left-right and fore-aft symmetries. This flow is an action-action-angle flow (i.e. a flow with two invariants), and hence the fluid particles are constrained to move on closed 1D curves (a picture is shown in figure 2.2). There is no chaos in this flow. To remove one of the invariants of the flow, the velocity is made unsteady by periodically reorienting the direction of the lid motion, thus producing a one-invariant flow. This one invariant flow can be further perturbed by inertia ($Re > 0$) to generate a zero invariant flow. Different kinds of flows that are considered in this thesis generated from lid-driven hemisphere cavity system are shown in table 1.2. This will be elaborated in chapter 2.

Table 1.2: Different kinds of flows generated from Lid-driven hemisphere system

Lid motion	Velocity	*Re*	No. of invariants
Uniform	Steady	$Re = 0$	2
Periodic reorientation	Unsteady	$Re = 0$	1
Periodic reorientation	Unsteady	$Re > 0$	0

1.5.2 Necessity of a new divergence-free interpolation

Extensive numerical computations of Lagrangian structures is essential to understand fluid transport. Computing Lagrangian trajectories require knowledge of the velocity field everywhere in the domain. The hemisphere lid-driven cavity does not have an analytical expression for the velocity that can be integrated to get particle trajectories, but a discrete velocity field can be obtained using computational methods. To integrate trajectories with a discrete velocity field, an interpolation scheme is required to obtain a continuous velocity field from the discrete field. For velocity fields determined from computational methods or experimental measurements, standard velocity interpolation schemes never explicitly preserve the solenoidal nature of the underlying incompressible flow, leading to localised and uncontrolled artificial perturbations in the flow. These perturbations are not an issue for a fully chaotic region of the flow because the shadowing lemma (Hammel *et al.*, 1987; Grebogi *et al.*, 1990; Ottino *et al.*, 1995) describes how long and how closely the particle tracking follows some true orbit of the chaotic flow. However, the picture changes markedly near the boundaries between chaotic and regular regions (e.g. around cantori), and when the flow has symmetries that should be obeyed. When the main point is to introduce *small, controlled* perturbations to study the effects of symmetry-breaking on the development of Lagrangian coherent structures, spurious divergences can render the computational orbits completely inaccurate because, in the computation, material surfaces no longer function as barriers to transport. Similarly, identifying critical points such as elliptic and hyperbolic points (and lines) becomes difficult if not impossible. Typical velocity interpolation schemes interpolate velocity components independently. In incompressible flows, interpolating velocity components via any scheme separately does not preserve volume conservation, which is a consequence of a divergence-free velocity. Early (and ongoing) work on explicitly divergence-free interpolation was motivated by applications in which data is sparse and scattered and used radial basis function to produce global interpolation schemes (Handscomb, 1993; Narcowich and Ward, 1994; Lowitzsch, 2005). Finn and Chacón (2005) were the first to produce an interpolation scheme to obtain a continuous divergence-free velocity field from gridded data. At the beginning of this thesis work, Finn and Chacón's method was used. However, it was found that the interpolated values of velocity components on the 3D grid points did not necessarily recover the same values of the discrete velocity components which were used for the interpolation and that sometimes the interpolated velocity could vary significantly from the grid velocities on which they are based. This presented a difficulty in accurately computing Lagrangian structures. This difficulty motivated the development of a new explicitly and exactly divergence-free interpolation method, based on B-splines, to calculate a C^2 continuous analytic vector potential from discrete 3D velocity data on a regular grid. A continuous analytically divergence-free velocity field can then be obtained from the curl of the potential. The new method ensures that the analytic velocity field matches the grid values almost everywhere, with errors that are two to four orders of magnitude lower than those of existing interpolation methods. This method is employed to track fluid particles in all the simulations of this thesis.

1.6 Outline of the thesis

The workhorse of this thesis, lid-driven hemisphere flow, is introduced in chapter 2. All the different kinds of flows that are produced from the hemisphere flow, and their symmetries and invariants are described in this chapter. Some of the features of one invariant flows are also presented there. A new divergence-free interpolation method and all the other numerical techniques that are used in this thesis are discussed in chapter 3. The organisation of Lagrangian structures in one invariant flows and a method to numerically calculate them in one invariant flows are discussed in chapter 4. In that chapter, a general framework of a type of resonance bifurcations which occur on periodic lines is presented and how these resonance bifurcations organise all of the Lagrangian structures in one invariant flows are explained. A method to numerically calculate all the Lagrangian structures in one invariant flows using these resonance bifurcations is also presented. The transformation of Lagrangian structures as one invariant flow changes to zero invariant flow by inertial perturbation is discussed in chapter 5. Some of the main results of this chapter are the transformation of nested spheroids to nested tori upon perturbation, formation of a chain of heteroclinic connections in the perturbed flow, and a new transport mechanism through which 3D chaotic advection happens. The conclusions of this thesis and future work are presented in chapter 6.

Chapter 2

Periodically Reoriented Hemisphere Flow

The system being considered for the study of three-dimensional chaos is a lid-driven cavity flow in a hemisphere, as shown in figure 2.1. The spherical domain $r \in [0, 1]$, $\theta \in [0, \pi]$ and $\phi \in [0, \pi]$ is preferred over $r \in [0, 1]$, $\theta \in [\pi/2, \pi]$ and $\phi \in [0, 2\pi]$ where θ is the polar angle and ϕ is the azimuthal angle, because the later has discontinuity where ϕ plane and $\phi + \pi$ plane joins inside hemisphere. The selected domain also removes the coordinate singularity from the interior of the domain that arises when $\sin\theta = 0$. The fluid inside the hemisphere is viscous and incompressible. In this work, two categories of flow are made based on Reynolds number of the fluid; zero-Reynolds number flow which is discussed in chapter 4; and non-zero Reynolds number flow which is discussed in chapter 5.

2.1 Base flow

A steady flow is generated with uniform lid motion $U_W = 1$ in the x direction ($\phi = 0$). This flow is called here the base flow field $\boldsymbol{u}(\boldsymbol{x})$ and it is only a function of space. The base flow is the fundamental building block from which all other flows will be constructed. A dynamical system is defined in equation (2.1) from the base flow field.

$$\frac{d\boldsymbol{x}}{dt} = \boldsymbol{u}(\boldsymbol{x}), \quad \boldsymbol{x}(0) = \boldsymbol{x}_0, \tag{2.1}$$

where $\boldsymbol{x}(0)$ is the fluid particle position at time $t = 0$.
The solution of equation (2.1) is

$$\boldsymbol{x}(t) = \boldsymbol{\Phi}_t(\boldsymbol{x}_0), \tag{2.2}$$

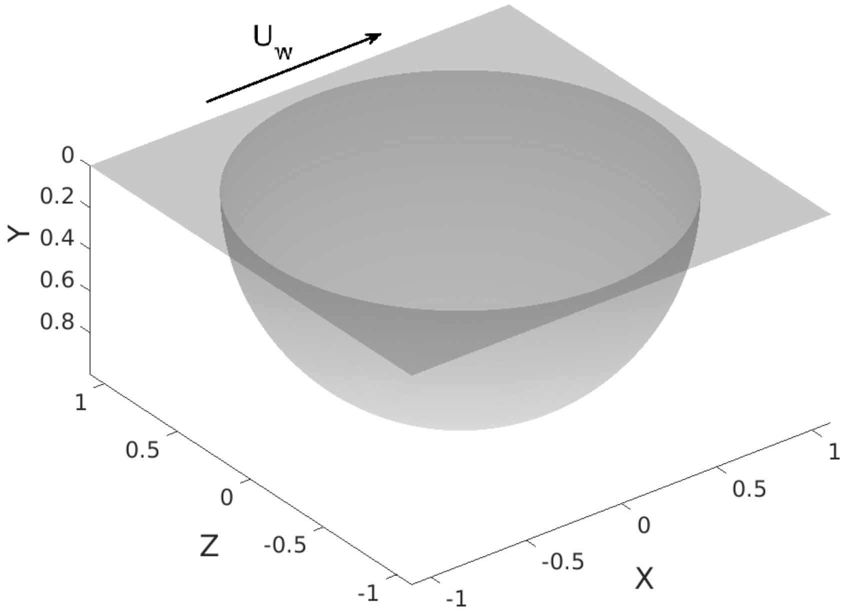

Figure 2.1: Schematic of the lid driven hemisphere flow.

where the map $\mathbf{\Phi}_t$ is called the evolution operator.

2.1.1 Base flow in Stokes regime

The base flow is considered in the limit where Reynolds number goes to zero. To understand this flow, streamlines are obtained by tracking a few fluid particles. In the Stokes limit, all streamlines are closed, and they are topological circles. Streamlines on the central plane ($z = 0$) are shown in figure 2.3. The base flow has a stagnation line that is attached to the hemisphere boundary (the dashed line in figure 2.2). The stagnation line endpoints are: $(0, 0.1624, 0.9867)$ and $(0, 0.1624, -0.9867)$ in Cartesian coordinates.

Symmetries of the base flow field of zero Reynolds number flow:

Symmetries in a volume-preserving flow correspond to invariants (or conserved quantities) of the flow (Haller and Mezić, 1998). Invariants in a flow restrict the motion of particles. In three-dimensional flows, a flow with two invariants has particle trajectories which are one-dimensional, and one invariant flow has particle trajectories which are two-dimensional. True three-dimensional particle transport happens only in flows with no invariants.

Symmetries in the base flow field manifest as symmetries in Lagrangian trajectories (Franjione *et al.*, 1989; Ottino *et al.*, 1992; Speetjens *et al.*, 2004)). The base flow field has two symmetries - a fore-aft symmetry (in the x direction) and a left-right symmetry (in the z direction). In order to express the symmetries of the base flow field in

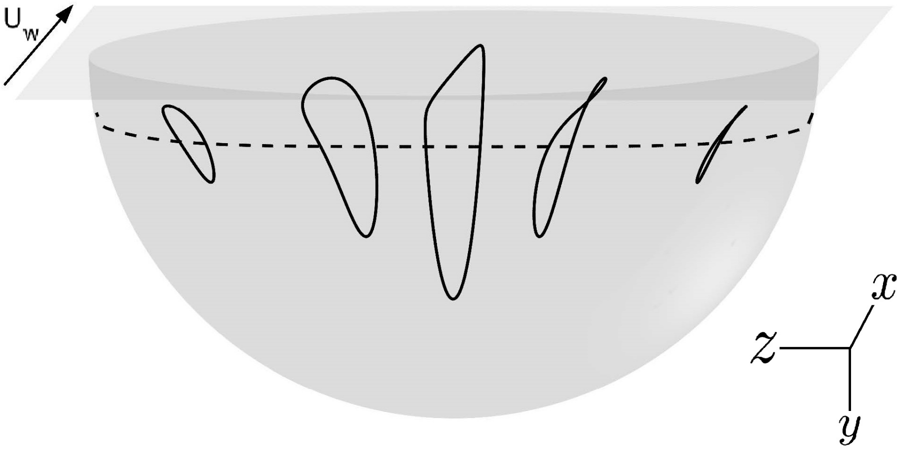

Figure 2.2: Schematic of the lid driven hemisphere flow. Continuous lines are representative streamlines of base flow. Dotted line is the stagnation line.

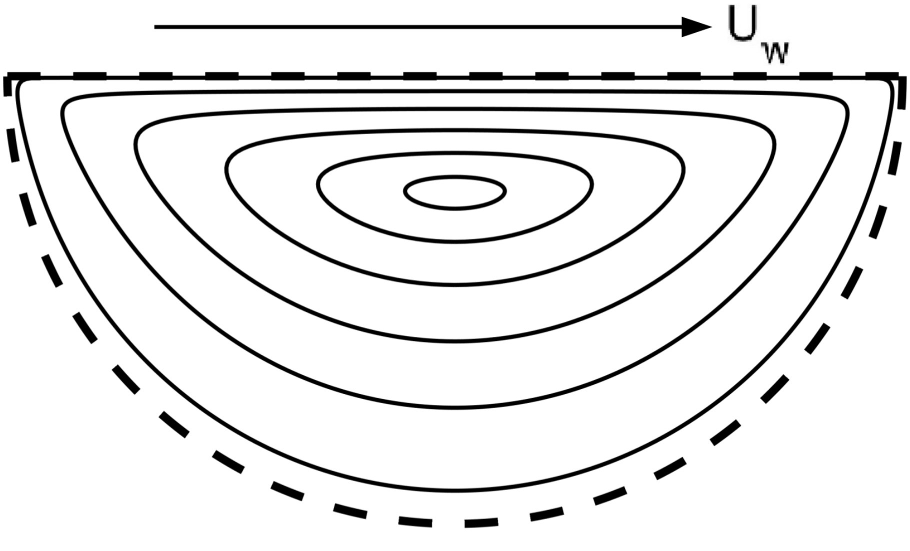

Figure 2.3: Flow cross-section of streamlines in the x–y plane. The dashed line is the hemisphere and lid boundary. The lid moves left to right in the $+x$ direction.

a mathematical form, two maps S_x and S_z are introduced that reflect a particle position about $x = 0$ and $z = 0$ correspondingly:

$$S_x : (x, y, z) \to (-x, y, z), \tag{2.3}$$

$$S_z : (x, y, z) \to (x, y, -z). \tag{2.4}$$

Fore-aft symmetry of the base flow (*i.e.* in the x–direction) results in a time-reversal symmetry,

$$\mathbf{\Phi}_t = S_x \mathbf{\Phi}_t^{-1} S_x. \tag{2.5}$$

Left-right symmetry of the base flow (*i.e.* in the z–direction) results in a reflection symmetry,

$$\mathbf{\Phi}_t = S_z \mathbf{\Phi}_t S_z. \tag{2.6}$$

The base flow field has two invariants which come from the two symmetries of the flow. Fluid particle trajectories are topological circles and the flow does not admit chaos anywhere.

2.1.2 Base flow in inertial regime

The base flow field of non-zero Reynolds number flow has only one symmetry (left-right) as given by equation (2.6). The fore-aft symmetry in equation (2.5) is lost by introducing inertia to the system as will be shown in chapter 5.

To show the fore-aft symmetry breaking with inertia, a streamline for $Re = 1$ flow on the centre plane and its reflection about y axis is shown in figure 2.4. In this figure, the black line is the streamline, and the magenta line is the reflection of the streamline. The difference between them is clearly visible in the zoomed-in parts of the figures. In the Stokes base flow, a streamline and its reflection about the y axis overlap completely.

To understand this flow, three fluid particles which are spatially apart from each other are tracked on both sides of the $z = 0$ plane. Plotting full trajectories of these particles looks cumbersome, hence only the intersections of these trajectories on the $x = 0$ plane are shown in figure 2.5 which is the Poincaré section. Different colours in the Poincaré section represent different particles, and the Poincaré section is symmetric from the $z = 0$ plane due to the left-right symmetry. In this figure, a schematic of a sample particle trajectory is shown in sky-blue colour line, and the intersections of this trajectory on the $x = 0$ plane are shown as orange spheres. From the Poincaré section of this figure, it is evident that streamlines move on nested tori. A sample torus is shown in yellow in this figure. There exist two sets of nested tori, one on each side of the $z = 0$ plane. The

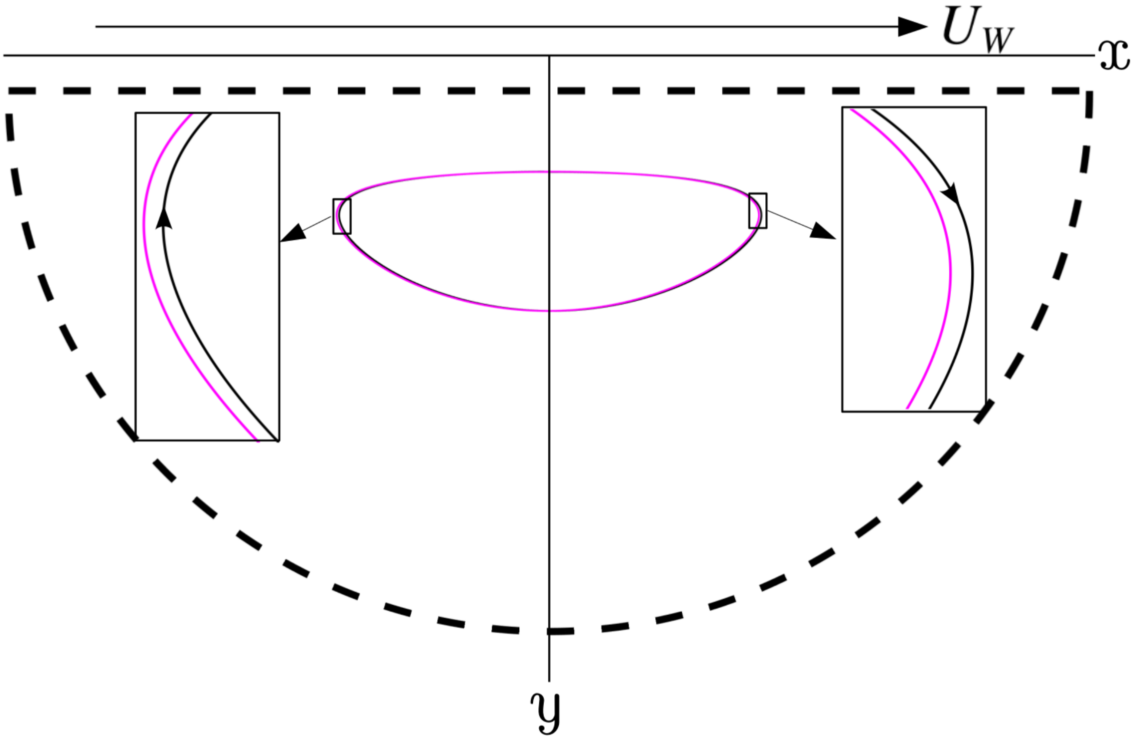

Figure 2.4: A stream line of base flow (continuous black line) on the centre plane and its reflection (magenta) about y axis is shown for $Re = 1$

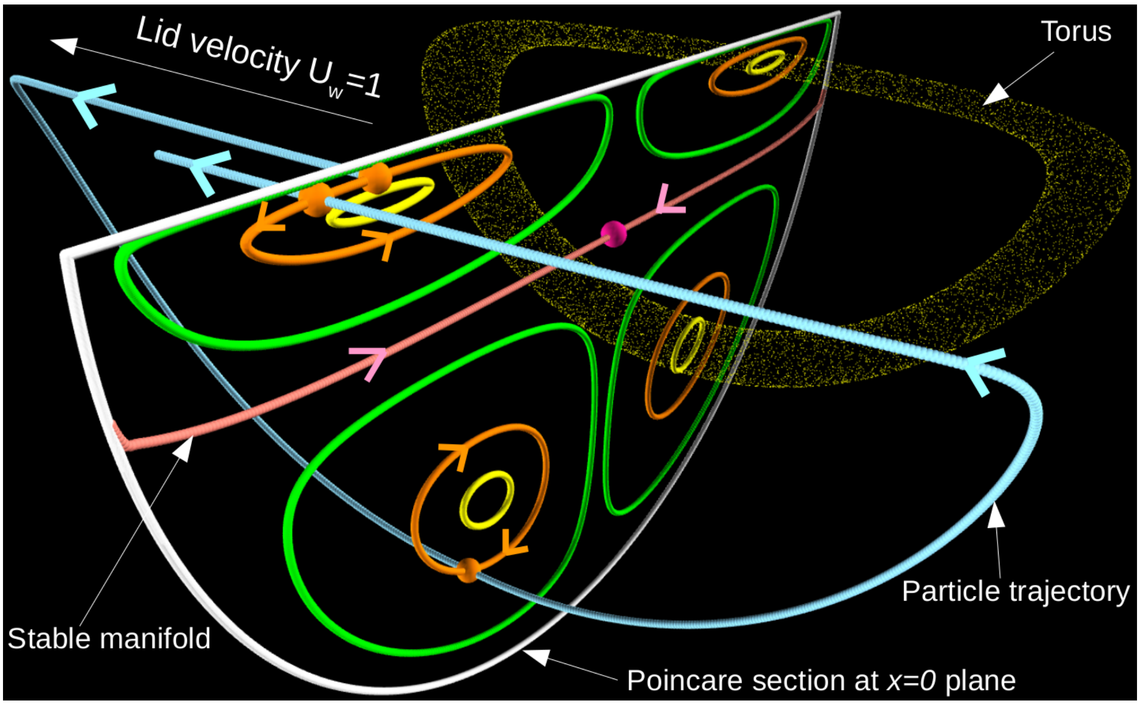
Lid velocity U_w=1
Torus
Stable manifold
Particle trajectory
Poincare section at x=0 plane

Figure 2.5: Poincaré section at $x = 0$ plane of Re=1 base flow.

pink sphere in this figure is the stagnation point whose position in Cartesian coordinates is $(0.0035, 0.2589, 0)$, and the salmon coloured lines represent stable manifolds of the stagnation point. These stable manifolds become the centres of the nested tori.

2.2 Periodically Reoriented Hemisphere Flow (PRHF)

The base flow has two symmetries in the Stokes regime and one symmetry in the inertial regime. One way to break one of the symmetries in the Stokes regime and the only symmetry in the inertial regime is to make the base flow unsteady. The way in which it is done here is to rotate the direction of the lid motion by an angle Θ as shown in figure 2.6. In this flow model, the direction in which the lid moves keeps changing after sliding in that direction for a fixed amount of time. Note that the lid does not rotate, only the direction in which the lid moves. This flow is called Periodically Reoriented Hemisphere Flow (PRHF). Two parameters will characterize the system in this flow;

- **Reorientation angle Θ:** the angle by which the lid changes its direction.
- **Lid displacement β:** the distance the lid slides in one direction before changing its direction.

β is non-dimensional and is normalized with the radius of the hemisphere. Because the lid velocity $U_W = 1, \beta$ also represents time. For this re-oriented flow, the velocity field is written as

$$\boldsymbol{v}(\boldsymbol{x}, t) = R_{(m\Theta)}\boldsymbol{u}(\boldsymbol{x}), \quad m = \lfloor \frac{t}{\beta} \rfloor, \tag{2.7}$$

where $\lfloor . \rfloor$ is the floor function and $R_{m\Theta}$ rotates the base velocity field by an angle $m\Theta$ in an anti-clockwise direction.

Continuous particle trajectories can be obtained by integrating the velocity $\boldsymbol{v}(\boldsymbol{x}, t)$. In this thesis, to reduce the complexity of higher dimensions, we always work with discrete trajectories instead of continuous trajectories. A discrete trajectory contains fluid particle positions that are equally spaced in time for period β. They are also called temporal Poincaré sections or stroboscopic maps.

Tracking fluid particles in PRHF requires the velocity $\boldsymbol{v}(\boldsymbol{x}, t)$ to be evaluated from the base flow field using equation (2.7). However, it is numerically convenient to use an equivalent flow without changing the direction of lid motion, but by rotating the entire hemisphere by an angle Θ in a clockwise direction after the lid moves in the x-direction for β time. This approach is preferred to compute Lagrangian structures because the same

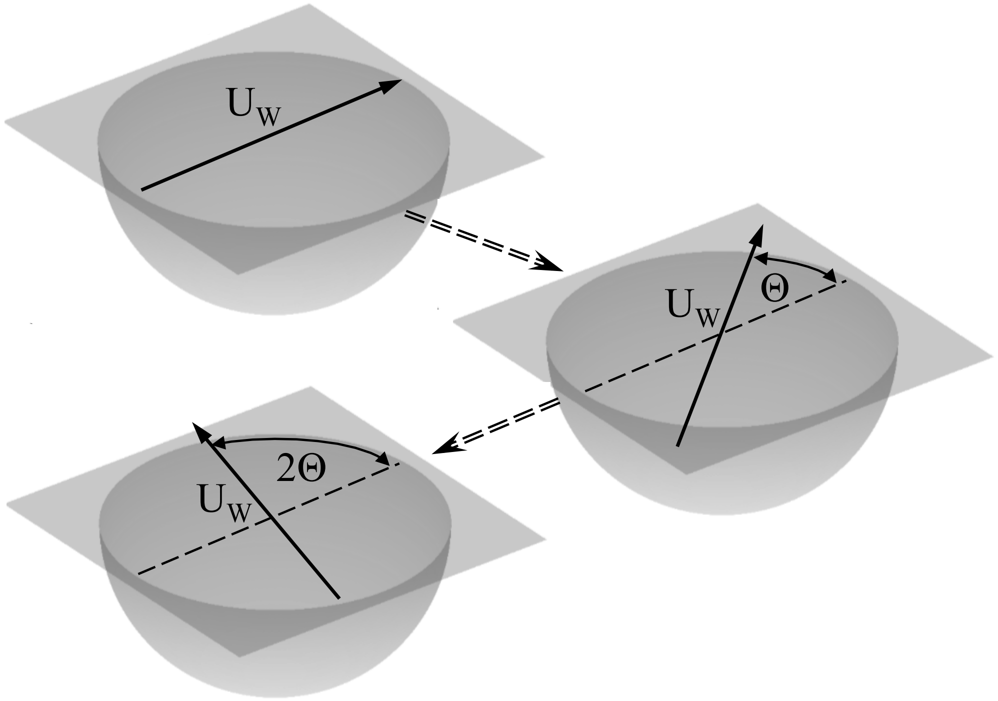

Figure 2.6: Schematic showing reorientation of the base flow.

base velocity field can be used. In this way a time-periodic map can be written as

$$\boldsymbol{\Psi}_{(\beta,\Theta)} = R_{-\Theta}\boldsymbol{\Phi}_{\beta}. \tag{2.8}$$

Here $\boldsymbol{\Phi}_{\beta}$ is the base flow map for lid displacement β and $R_{-\Theta}$ is the rotation of the hemisphere in the clockwise direction by an angle Θ. All computations are done using the map $\boldsymbol{\Psi}_{(\beta,\Theta)}$ as the basic building block of the time-periodic flow in this work. We often drop the subscript (β,Θ) from equation (2.8) and simply write the time-periodic map as $\boldsymbol{\Psi}$, however (β,Θ) will always be implied. A temporal Poincaré section can be obtained via

$$\boldsymbol{x}_{k+1} = \boldsymbol{\Psi}(\boldsymbol{x}_k), \quad \boldsymbol{x}_k = \boldsymbol{x}(k\beta), \tag{2.9}$$

where $\boldsymbol{x}_k$ is a particle position after k periods (i.e. time=$k\beta$).

2.3 PRHF - Stokes regime

In the Stokes regime, the base flow has two symmetries, and one of the symmetries of the base flow is broken in PRHF. PRHF in the Stokes regime has a time-reversal-reflection symmetry, which will be proved in section 2.3.1. The symmetry manifests as an invariant of the system, and the system is called as an action-angle-angle flow system. Fluid particle trajectories are constrained to move on closed invariant surfaces. To imagine an invariant surface, consider a closed invariant curve of the base flow on the central plane ($z = 0$ plane), if this is rotated about the y axis, it sweeps a surface, which is an invariant surface of the PRHF. In PRHF, fluid particle advection takes place on nested spheroids. The map $\boldsymbol{\Psi}$ is a one-action map in the Stokes regime.

2.3.1 Symmetry of the PRHF

In this section, the existence of time-reversal-reflection symmetry for PRHF in the Stokes regime is proved.

Substituting equation (2.5) (with $t = \beta$) into equation (2.8):

$$\begin{aligned}\boldsymbol{\Psi} &= R_{-\Theta}\boldsymbol{\Phi}_{\beta}\\ &= R_{-\Theta}S_x{\boldsymbol{\Phi}_{\beta}}^{-1}S_x\\ &= R_{-\Theta}S_x{\boldsymbol{\Phi}_{\beta}}^{-1}R_{-\Theta}^{-1}R_{-\Theta}S_x\\ &= R_{-\Theta}S_x(R_{-\Theta}\boldsymbol{\Phi}_{\beta})^{-1}R_{-\Theta}S_x\\ &= R_{-\Theta}S_x\boldsymbol{\Psi}^{-1}R_{-\Theta}S_x\end{aligned}$$

Defining

$$R_{-\Theta}S_x = S_{\Theta}, \tag{2.10}$$

then allows $\boldsymbol{\Psi}$ to be written as

$$\boldsymbol{\Psi} = S_{\Theta}\boldsymbol{\Psi}^{-1}S_{\Theta}. \tag{2.11}$$

This is the time-reversal-reflection symmetry of the map $\boldsymbol{\Psi}$, where it can be shown that S_{Θ} is the map that reflects a particle about the plane $\theta = \pi/2 - \Theta/2$ (see figure 2.7). Defining the set of all the points on the plane $\theta = \pi/2 - \Theta/2$ as $\boldsymbol{I}_{\Theta}$, it immediately follows that

$$\boldsymbol{I}_{\Theta} = S_{\Theta}\boldsymbol{I}_{\Theta}. \tag{2.12}$$

A similar symmetry occurs inside the driven-lid cylinder, which has been extensively studied (Malyuga *et al.*, 2002; Speetjens *et al.*, 2004, 2006a,b; Pouransari *et al.*, 2010)

The importance of the symmetry in equation (2.11) is twofold. First, it is enough to look for Lagrangian coherent structures on one side of symmetry plane $\boldsymbol{I}_{\Theta}$, as they will be mirrored across this plane. Second, period-1 points (and by extension period-1 lines) must lie on the symmetry plane $\boldsymbol{I}_{\Theta}$. The latter can be proved by considering a period-1 point $\boldsymbol{x}_{P1}$. It is shown in section 2.3.2 that this point must lie on the symmetry plane S_{Θ}.

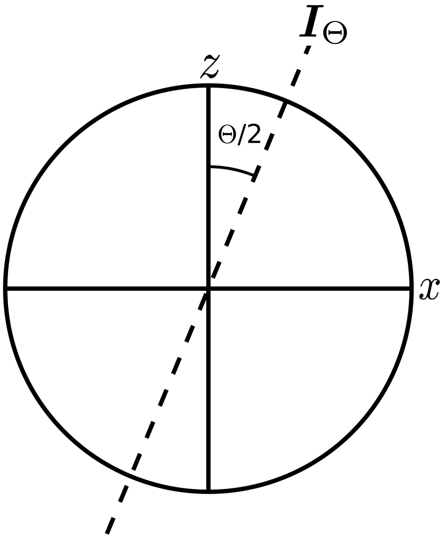

Figure 2.7: Symmetry plane for $\Theta = \pi/4$.

2.3.2 Location of period-1 points

From the definition of a period-1 point (or fixed point) of map $\boldsymbol{\Psi}$, we write

$$\begin{aligned} \boldsymbol{x}_{P1} &= \boldsymbol{\Psi}\boldsymbol{x}_{P1} \\ &= R_{-\Theta}\boldsymbol{\Phi}_\beta \boldsymbol{x}_{P1}. \end{aligned} \tag{2.13}$$

Applying R_Θ to both sides of equation (2.13), we find

$$R_\Theta \boldsymbol{x}_{P1} = \boldsymbol{\Phi}_\beta \boldsymbol{x}_{P1}. \tag{2.14}$$

We now consider separately how each coordinate of $\boldsymbol{x}_{P1}$ is modified by application of the map $\boldsymbol{\Phi}_\beta$. We first note that because the point $\boldsymbol{\Phi}_\beta \boldsymbol{x}_{P1}$ must be rotated to complete one full period of the reoriented flow map (see equation 2.13) then $\boldsymbol{\Phi}_\beta \boldsymbol{x}_{P1} \neq \boldsymbol{x}_{P1}$. Because rotation about the y-axis does not change the y–coordinate of a point, application of R_Θ to $\boldsymbol{x}_{P1}$ results in

$$(R_\Theta \boldsymbol{x}_{P1})_y = (\boldsymbol{x}_{P1})_y, \tag{2.15}$$

or from equation (2.14)

$$(\boldsymbol{\Phi}_\beta \boldsymbol{x}_{P1})_y = (\boldsymbol{x}_{P1})_y, \tag{2.16}$$

i.e. the y–coordinate of a period-1 point is not changed by application of the base flow (see figure 2.8a). Because streamlines of the base flow are symmetric about $x = 0$ and the y components of $\boldsymbol{x}_{P1}$ and $\boldsymbol{\Phi}_\beta \boldsymbol{x}_{P1}$ are the same, it can be seen from figure 2.8a and

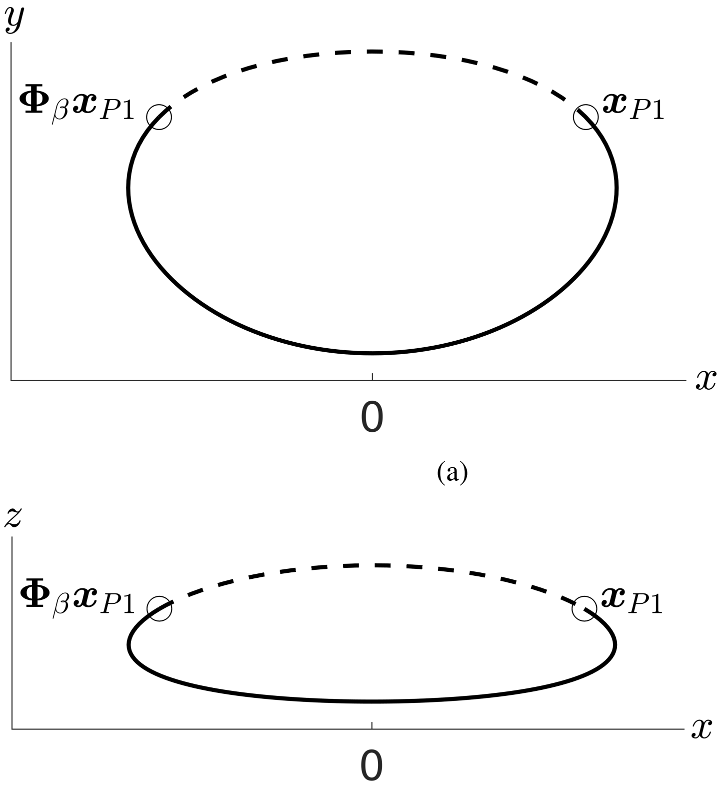
y
$\boldsymbol{\Phi}_\beta \boldsymbol{x}_{P1}$
$\boldsymbol{x}_{P1}$
x
0
z
$\boldsymbol{\Phi}_\beta \boldsymbol{x}_{P1}$
$\boldsymbol{x}_{P1}$
x
0

(a)

(b)

Figure 2.8: Projection of a stream line of the base flow: (a) x–y projection and (b) x–z projection.

figure 2.8b that the following must also be true:

$$\begin{aligned}(\boldsymbol{\Phi}_\beta \boldsymbol{x}_{P1})_z &= (\boldsymbol{x}_{P1})_z \\ (\boldsymbol{\Phi}_\beta \boldsymbol{x}_{P1})_x &= -(\boldsymbol{x}_{P1})_x\end{aligned} \tag{2.17}$$

Equation (2.16) and equation (2.17) can then be written without reference to coordinate directions as,

$$\boldsymbol{\Phi}_\beta \boldsymbol{x}_{P1} = S_x \boldsymbol{x}_{P1} \tag{2.18}$$

By substituting equation (2.18) in equation (2.14), we get

$$\begin{aligned}R_\Theta \boldsymbol{x}_{P1} &= S_x \boldsymbol{x}_{P1} \\ \boldsymbol{x}_{P1} &= R_{-\Theta} S_x \boldsymbol{x}_{P1}\end{aligned} \tag{2.19}$$

Using equation (2.10) to replace $R_{-\Theta} S_x$ by S_Θ, we find

$$\boldsymbol{x}_{P1} = S_\Theta \boldsymbol{x}_{P1} \tag{2.20}$$

Hence, $\boldsymbol{x}_{P1} \in I_\Theta$, *i.e.* $P1$ points must lie on the symmetry plane I_Θ.

2.3.3 Three non-trivial period-1 points

In this section, it is shown that three period-1 points must exist on the symmetry plane for all parameter values of Θ and β. In PRHF, because the rotation is about the y axis, the points on the y axis do not change during rotation. During the lid motion, two points on y axis do not move, the first point $(0, 1, 0)$ is at the bottom of the hemisphere, and the second point is the central stagnation point $(0, y_{SP}, 0)$, where $y_{SP} = 0.2588$ (see figure 2.9). The points $(0, 1, 0)$ and $(0, y_{SP}, 0)$ are two non-trivial period-1 points, because they do not change during the lid motion and during the rotation about y axis. The third period-1 point is on the hemisphere lid, and the details about this point are given below. It will be shown in chapter 3 that these three period-1 points belong to the same period-1 line.

Assume a fluid particle is at $\boldsymbol{x}_0$ on hemisphere lid (see figure 2.10). The requirement for the particle to be a period-1 point is that it will move to a point $\boldsymbol{x}_0'$ on hemisphere lid after β lid displacement such that $\boldsymbol{x}_0'$ is the reflection of the point $\boldsymbol{x}_0$ about z axis (see figure 2.10). i.e.

$$\boldsymbol{x}_0' = \boldsymbol{\Phi}_\beta \boldsymbol{x}_0 \tag{2.21}$$

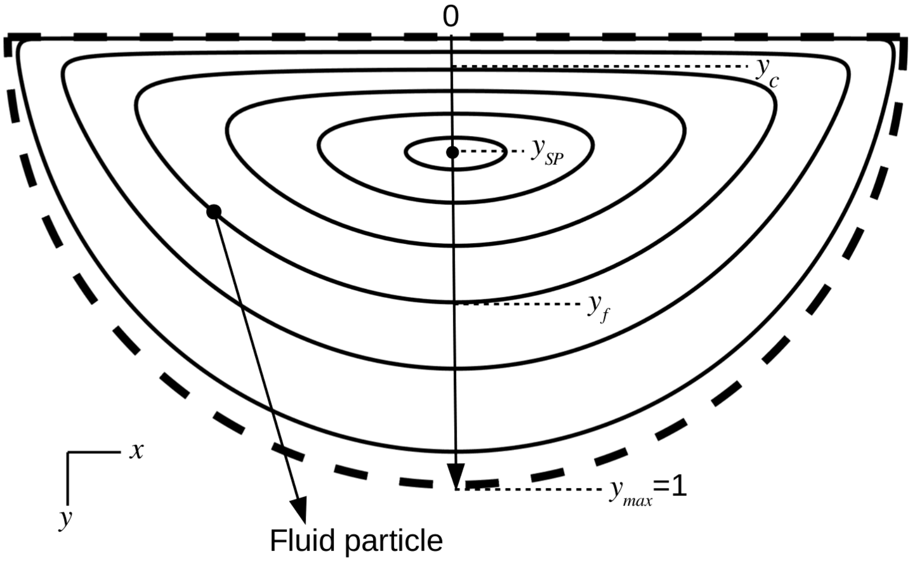
0
y_c
y_{SP}
y_f
x
y
y_{max}=1
Fluid particle

Figure 2.9: Enumeration of the action in the Stokes flow. $y_{SP} = 0.2588$ is the y coordinate of stagnation point.

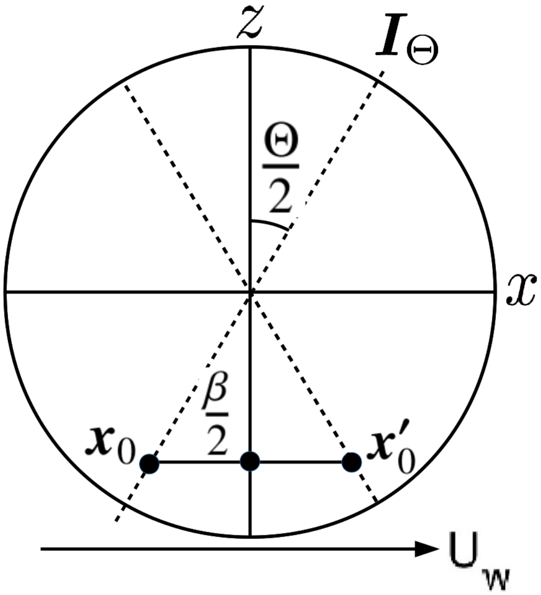
z
$\boldsymbol{I}_\Theta$
$\frac{\Theta}{2}$
x
$\frac{\beta}{2}$
$\boldsymbol{x}_0$
$\boldsymbol{x}'_0$
U_w

Figure 2.10: Hemisphere lid: I_Θ is the symmetry plane and the lid velocity $U_W = 1$

and

$$\boldsymbol{x}_0 = R_{-\Theta}\boldsymbol{x}'_0. \tag{2.22}$$

Hence, $\boldsymbol{x}_0 = \boldsymbol{\Psi}\boldsymbol{x}_0$. Since the lid velocity is unity, the distance between the points $\boldsymbol{x}_0$ and $\boldsymbol{x}'_0$ is β. From the figure 2.10, we can see that the position coordinates of the period-1 point $\boldsymbol{x}_0$ on hemisphere lid is $(-\beta/2, 0, -\frac{\beta/2}{\tan(\Theta/2)})$. The distance from the centre $(0, 0, 0)$ to the period-1 point $\boldsymbol{x}_0$ is $\frac{\beta/2}{\sin(\Theta/2)}$. For $\Theta = \pi/3$ and $\beta = 1$, the period-1 point will be on the rim.

2.3.4 Non-existence of isolated periodic points in one-action maps

In principle, in a one-invariant flow a coordinate transformation can be used to map fluid particle positions (x, y, z) to $\boldsymbol{\xi}(\theta_1, \theta_2, I)$, where I represents the action variable and (θ_1, θ_2) represent angle variables.

$$\boldsymbol{\xi} = \begin{bmatrix} \theta_1 \\ \theta_2 \\ I \end{bmatrix} \tag{2.23}$$

When the system parameters Θ and β are fixed, a map can be defined as

$$\boldsymbol{\xi} \mapsto \boldsymbol{f}(\boldsymbol{\xi}), \tag{2.24}$$

where $\boldsymbol{f}$ is continuous in (θ_1, θ_2, I). $\boldsymbol{\xi}_0$, $\boldsymbol{\xi}_1$, $\boldsymbol{\xi}_2$, ..., $\boldsymbol{\xi}_k$ is a fluid particle orbit for k periods, where

$$\boldsymbol{\xi}_n = \boldsymbol{f}(\boldsymbol{\xi}_{n-1}), \quad n = 1, 2, 3, \ldots, k. \tag{2.25}$$

Period-n fixed point equation, by definition, is

$$\boldsymbol{f}^n(\boldsymbol{\xi}) - \boldsymbol{\xi} = 0. \tag{2.26}$$

Since $\boldsymbol{f}$ and $\boldsymbol{\xi}$ are three-dimensional vectors, equation (2.26) can be split component wise into three equations as

$$f_1^n(\theta_1, \theta_2, I) - \theta_1 = 0, \tag{2.27a}$$

$$f_2^n(\theta_1, \theta_2, I) - \theta_2 = 0, \tag{2.27b}$$

$$f_3^n(\theta_1, \theta_2, I) - I = 0 \Rightarrow I - I = 0. \tag{2.27c}$$

Because the action variable of a fluid particle does not change in the Stokes flow, equation (2.27)c is not an independent equation (i.e this equation is satisfied at every point in the domain). Equation (2.27)a and equation (2.27)b represent two-dimensional surfaces that are either closed or attached to the boundary, and the intersection of these two surfaces will be the solution of equation (2.27) which is the same as equation (2.26). If the two surfaces intersect (i.e if the solution exists for some order of period n), the intersection must be a line and it cannot be a point. So equation (2.26) cannot have point solutions. Hence, isolated period-1 points cannot exist in the PRHF in the Stokes limit. Periodic lines with the ends attached to the boundary or closed periodic lines are possible.

2.3.5 Enumeration of the invariant (or action)

In this action-angle-angle system (or simply one action system), all the fluid particles are constrained to move on invariant surfaces that are topological spheres. The term "shell" is introduced here to describe them. In principle, we could transform conformally the hemisphere into a sphere. This would make spheroids into actual spherical shells centred on the stagnation point y_{SP}. Instead of making this laborious transform, an effective action coordinate (I) is defined in the following. Each shell here is labelled with a number, zero for stagnation point and one for the outer most shell. This way, each shell has a unique number.

To compute shell number of a fluid particle, the particle is rotated about the y axis such that it lies on the central plane ($z = 0$ plane). Then the streamline of that particle is computed on the central plane using the base flow field in the Stokes regime. The streamline intersects the y axis twice: at y_c and once at y_f as shown in figure 2.9 (with $y_c < y_f$). Action value is computed via

$$I = \frac{y_f - y_{SP}}{y_{max} - y_{SP}}, \tag{2.28}$$

where $y_{SP} = 0.2588$ is the y coordinate of the stagnation point. Enumeration of invariants of fluid particles allows us to group fluid particles according to their shell. The usefulness of computing invariant values to understand Lagrangian structures on shells will be seen later in chapter 4.

2.4 Linearization of PRHF map

Period-1 points are fixed points of the PRHF map $\boldsymbol{\Psi}$. To understand the advection of fluid particles in the neighbourhood of period-1 points, we find linear approximation of the map $\boldsymbol{\Psi}$ at period-1 points using Taylor series expansion of $\boldsymbol{\Psi}$. At a period-1 point $\boldsymbol{x}_{P1}$, this expansion is

$$\boldsymbol{\Psi}(\boldsymbol{x}) = \boldsymbol{x}_{P1} + \left[\frac{\partial \boldsymbol{\Psi}(\boldsymbol{x}_{\boldsymbol{P1}})}{\partial \boldsymbol{x}}\right](\boldsymbol{x} - \boldsymbol{x}_{P1}) + O((\boldsymbol{x} - \boldsymbol{x}_{\boldsymbol{P1}})^2), \tag{2.29}$$

where $\frac{\partial \boldsymbol{\Psi}(\boldsymbol{x}_{P1})}{\partial \boldsymbol{x}} = \boldsymbol{F}$ is the Jacobian (or deformation tensor).

A new variable $\boldsymbol{\zeta}$ which is displacement from the period-1 point is introduced as

$$\boldsymbol{\zeta} = \boldsymbol{x} - \boldsymbol{x}_{\boldsymbol{P1}}, \tag{2.30}$$

which allows equation (2.29) to be written as

$$\boldsymbol{\Psi}(\boldsymbol{x}) - \boldsymbol{x}_{P1} = \boldsymbol{F}\boldsymbol{\zeta} + O(\boldsymbol{\zeta}^2). \tag{2.31}$$

The map for $\boldsymbol{\zeta}$ becomes

$$\boldsymbol{\zeta} \mapsto \boldsymbol{\Psi}(\boldsymbol{x}) - \boldsymbol{x}_{P1}, \tag{2.32}$$

or

$$\boldsymbol{\zeta} \mapsto \boldsymbol{F}\boldsymbol{\zeta} + O(\boldsymbol{\zeta}^2). \tag{2.33}$$

For small $\boldsymbol{\zeta}$ (after linearization), we find that the application of $\boldsymbol{\Psi}$ to a point $\boldsymbol{x}_0$ whose displacement from $\boldsymbol{x}_{P1}$ is $\boldsymbol{\zeta}_0$, will be displaced to $\boldsymbol{\zeta}_1$.

$$\boldsymbol{\zeta}_1 \simeq \boldsymbol{F}\boldsymbol{\zeta}_0, \quad \boldsymbol{\zeta}_k = \boldsymbol{\zeta}(t = k\beta), \tag{2.34}$$

where $\boldsymbol{\zeta}_k$ is the displacement of the particle after k periods.

The deformation tensor $\boldsymbol{F} = \frac{\partial \boldsymbol{\Psi}}{\partial x}$ has eigenvalues λ_1, λ_2, λ_3 and corresponding eigenvectors $\boldsymbol{e}_1, \boldsymbol{e}_2$ and $\boldsymbol{e}_3$. The eigenvalues λ_1, λ_2 and λ_3 are also called multipliers of the period-1 point $\boldsymbol{x}_{P1}$. $|\lambda_1\lambda_2\lambda_3| = 1$ for volume preserving maps. The eigenvalues of the deformation tensor evaluated at the period-1 point $\boldsymbol{x}_{P1}$ determine the nature of advection of fluid particles in the neighbourhood of the period-1 point. The eigenvalues can be three real or one real and two complex. Assume λ is a real eigenvalue and $\boldsymbol{e}$ is the corresponding eigenvector. The eigenvector direction is unstable if $\lambda > 1$, null direction (or no change) if $\lambda = 1$, stable if $0 < \lambda < 1$, stable if $-1 < \lambda < 0$ (points move discretely towards the period-1 point while jumping between two sides of the eigendirection), unstable if $\lambda < -1$ (points move discretely away from the period-1 point while jumping between two sides of the eigendirection). A period-1 point is called hyperbolic if the magnitude of any one of the three multipliers of the period-1 point is not equal to one. Stable and unstable manifolds are associated with a hyperbolic point. A stable manifold,

$$W^s(\boldsymbol{x}_{P1}) = \{\boldsymbol{x} : \boldsymbol{\Psi}^k(\boldsymbol{x}) \to \boldsymbol{x}_{P1}, k \to +\infty\}, \tag{2.35}$$

and an unstable manifold,

$$W^u(\boldsymbol{x}_{P1}) = \{\boldsymbol{x} : \boldsymbol{\Psi}^k(\boldsymbol{x}) \to \boldsymbol{x}_{P1}, k \to -\infty\}. \tag{2.36}$$

Manifolds can be one-dimensional or two-dimensional based on the magnitude of the multipliers of a period-1 point. 1D manifolds (stable or unstable) are invariant curves and 2D manifolds (stable or unstable) are invariant surfaces.

2.4.1 Multipliers in the Stokes regime

The PRHF in the Stokes regime does not have isolated periodic points, it only has periodic lines (see section 2.3.4). It can be seen from the following description that a period-1 point of a period-1 line has one of the eigenvalues equal to one. First, assume that one of the eigenvalues of a period-1 point $\boldsymbol{x}_{P1}$ is equal to one (say $\lambda_3 = 1$). Consider a point $\boldsymbol{x}_{P1} + \epsilon\boldsymbol{e}_3$, which is in the eigenvector $\boldsymbol{e}_3$ direction of eigenvalue λ_3, ϵ is a small value. Substituting $\boldsymbol{x}_{P1} + \epsilon\boldsymbol{e}_3$ in equation (2.29), we obtain

$$\begin{aligned}\boldsymbol{\Psi}(\boldsymbol{x}_{P1} + \epsilon\boldsymbol{e}_3) &= \boldsymbol{x}_{P1} + \boldsymbol{F}|_{\boldsymbol{x}=\boldsymbol{x}_{P1}}\epsilon\boldsymbol{e}_3 \\ &= \boldsymbol{x}_{P1} + \epsilon\boldsymbol{e}_3.\end{aligned} \tag{2.37}$$

It follows from equation (2.37) that the point $\boldsymbol{x}_{P1} + \epsilon\boldsymbol{e}_3$ is also a period-1 point and thus that the eigenvector direction $\boldsymbol{e}_3$ is the null direction, which is tangent to the period-1 line. Every period-1 point on the period-1 line always has an eigenvector in the null direction for which the eigenvalue is one. To simplify later analysis, we will always define this to be $\lambda_3 = 1$. Because λ_3 is fixed and is one, the stability of a period-1 point depends on the eigenvalues λ_1 and λ_2. Three types of stabilities are possible for a period-1 point of PRHF in the Stokes regime, elliptic, hyperbolic and degenerate points.

- **Elliptic point:** Eigenvalues λ_1 and λ_2 are complex.
- **Hyperbolic point:** Eigenvalues λ_1 and λ_2 are real, and $|\lambda_1| \neq 1$ and $|\lambda_2| \neq 1$, and $\lambda_1 = 1/\lambda_2$.
- **Degenerate point:** A period-1 point is called an n^{th} order degenerate point if the net deformation at that point after n periods is zero. If $\boldsymbol{x}_{P1}$ is an n^{th} order degenerate point and $\boldsymbol{F}$ is the deformation tensor computed there. $\boldsymbol{F}^n$ becomes,

$$\left[\frac{\partial \boldsymbol{\Psi}(\boldsymbol{x}_{P1})}{\partial \boldsymbol{x}}\right]^n = \begin{bmatrix} 1 & 0 & 0 \\ 0 & 1 & 0 \\ 0 & 0 & 1 \end{bmatrix}, \tag{2.38}$$

or

$$\boldsymbol{\zeta} \simeq \boldsymbol{F}^n \boldsymbol{\zeta}, \tag{2.39}$$

where $\boldsymbol{\zeta}$ is the displacement from the period-1 point. At an n^{th} order degenerate point, eigenvalues of the deformation tensor satisfy,

$$\lambda_1^n = 1, \quad \lambda_2^n = 1, \quad \lambda_3^n = 1. \tag{2.40}$$

The eigenvalues at an n^{th} order degenerate point will be $\lambda_{1,2} = e^{\pm i(2\pi/n)}$ and $\lambda_3 = 1$. Degenerate points of order three or above are elliptic period-1 points as they have complex eigenvalues, which can be seen in table 2.1.

Table 2.1: Eigenvalues of the degenerate points on a period-1 line

Order of degeneracy	λ_1	λ_2	λ_3
First	1	1	1
Second	-1	-1	1
Third	-0.5+$\sqrt{\frac{3}{4}}i$	-0.5-$\sqrt{\frac{3}{4}}i$	1
Fourth	$-i$	i	1
$\vdots$	$\vdots$	$\vdots$	$\vdots$
n^{th}	$e^{i(2\pi/n)}$	$e^{-i(2\pi/n)}$	1

2.4.2 Multipliers in the inertial regime

By adding inertia to the PRHF, the time reversal-reflection symmetry is lost, and fluid particles motion is not restricted to 2D invariant surfaces. In the PRHF with finite *Re* case, isolated period-1 points are found instead of periodic lines (This will be discussed in great detail later in chapter 5). The classification of isolated period-1 points of the PRHF in the inertial regime is presented in table 2.2.

The eigenvalue analysis described in sections 2.4.1 and 2.4.2 to determine the nature of period-1 point stability applies to the higher order periodic points also. The eigenvalues of the deformation tensor are obtained using the map $\boldsymbol{\Psi}^n$ for an n^{th} order periodic point.

Table 2.2: Nature of a period-1 point from eigenvalues of the deformation tensor computed there.

λ_1	λ_2	λ_3	Nature of stability
real and $\lvert\lambda_1\rvert \neq 1$	real and $\lvert\lambda_2\rvert \neq 1$	real and $\lvert\lambda_3\rvert \neq 1$	Hyperbolic node
real and $\lvert\lambda_1\rvert < 1$	complex and $\lvert\lambda_2\rvert > 1$	complex and $\lvert\lambda_3\rvert > 1$	Hyperbolic focus (spiralling out)
real and $\lvert\lambda_1\rvert > 1$	complex and $\lvert\lambda_2\rvert < 1$	complex and $\lvert\lambda_3\rvert < 1$	Hyperbolic focus (spiralling in)

2.5 Invariants of deformation tensor

As well as of using eigenvalues of deformation tensor $\boldsymbol{F}$ to determine stability, invariants of $\boldsymbol{F}$ can also be used. The invariants of the deformation are introduced first and discussed their significance later. The characteristic equation for eigenvalues λ of a deformation tensor $\boldsymbol{F}$ is given by

$$p(\lambda) = \lambda^3 - (\mathrm{Tr}\,\boldsymbol{F})\lambda^2 + \frac{1}{2}((\mathrm{Tr}\,\boldsymbol{F})^2 - \mathrm{Tr}\,\boldsymbol{F}^2)\lambda - det(\boldsymbol{F}), \tag{2.41}$$

where 1) $\mathrm{Tr}\,\boldsymbol{F}$ is the trace of the deformation tensor denoted by τ (also termed first trace),

$$\tau = \mathrm{Tr}\,\boldsymbol{F} = \lambda_1 + \lambda_2 + \lambda_3 \tag{2.42}$$

2) $det(\boldsymbol{F})$ is determinant of $\boldsymbol{F}$,

$$det(\boldsymbol{F}) = \lambda_1\lambda_2\lambda_3 \tag{2.43}$$

3) the term $\frac{1}{2}((\mathrm{Tr}\,\boldsymbol{F})^2 - \mathrm{Tr}\,\boldsymbol{F}^2)$ in equation (2.41) is called the second trace and denoted by σ .

$$\sigma = \frac{1}{2}((\mathrm{Tr}\,\boldsymbol{F})^2 - \mathrm{Tr}\,\boldsymbol{F}^2) = \lambda_1\lambda_2 + \lambda_2\lambda_3 + \lambda_3\lambda_1 \tag{2.44}$$

$\mathrm{Tr}\,\boldsymbol{F}$, $det(\boldsymbol{F})$ and σ are invariants of the deformation tensor $\boldsymbol{F}$. Because $det(\boldsymbol{F}) = 1$ for volume preserving maps, the characteristic equation of the Deformation Tensor $\boldsymbol{F}$ can be written as,

$$p(\lambda) = \lambda^3 - \tau\lambda^2 + \sigma\lambda - 1. \tag{2.45}$$

It is shown in section 2.5.1 that the stability of a period-1 point in the Stokes regime can be determined by the trace value of the deformation tensor at the point.

2.5.1 Stokes regime

Because $\lambda_3 = 1$ (by definition) and $det(\boldsymbol{F}) = 1$, we can write,

$$\lambda_2 = 1/\lambda_1. \tag{2.46}$$

Substituting equation (2.46) in equation (2.44), we get

$$\begin{aligned} \sigma &= \lambda_1\lambda_2 + \lambda_2\lambda_3 + \lambda_3\lambda_1 \\ &= \lambda_1 + 1/\lambda_1 + 1 \\ &= \tau. \end{aligned} \tag{2.47}$$

Since $\tau = \sigma$ and $det(\boldsymbol{F}) = 1$, the stability of a period-1 point depends only on one invariant, which is τ of the deformation tensor.

The characteristic equation (2.45) can be written as,

$$\begin{aligned} p(\lambda) &= \lambda^3 - \tau(\lambda^2 - \lambda) - 1 \\ &= (\lambda - 1)(\lambda^2 + (1 - \tau)\lambda + 1). \end{aligned} \tag{2.48}$$

The solutions of this equation are 1 and $\frac{1}{2}((\tau - 1) \pm \sqrt{\tau^2 - 2\tau - 3}))$. We can characterize the nature of a period-1 point of a period-1 line line by calculating the trace of the deformation tensor evaluated at that point. If $\tau \in (-1, 3)$, the term $\tau^2 - 2\tau - 3$ is negative, the period-1 point is elliptic. If $\tau > 3$, then the period-1 point is hyperbolic, if $\tau < -1$, then the period-1 point is hyperbolic. The trace value of an n^{th} order degenerate point is obtained by,

$$\tau = 1 + 2\cos(2\pi/n). \tag{2.49}$$

It will be shown later in chapter 4 that degenerate points on periodic lines are easily identified using their trace values.

Chapter 3

Computational Methods

To investigate transport in the PRHF, a number of numerical methods have been utilised: 1) base flow calculation, 2) a new divergence-free interpolation method, 3) calculation of analytically divergence-free base flow velocity flow, 4) calculation of period-1 line of the PRHF in the Stokes limit, 5) calculation of deformation tensor, 6) calculation of higher-order periodic lines of the PRHF in the Stokes limit, and 7) calculation of isolated period-1 points of the PRHF in the inertial regime. This chapter details these numerical techniques.

3.1 Obtaining the base flow velocity field of lid-driven hemisphere flow

The governing equation for flow of an incompressible Newtonian fluid as considered in this thesis, is the incompressible Navier-Stokes equation, given by

$$\frac{\partial \boldsymbol{v}}{\partial t} + \boldsymbol{v} \cdot \nabla \boldsymbol{v} = -\frac{\nabla p}{\rho} + \nu \nabla^2 \boldsymbol{v}, \tag{3.1}$$

where ρ is density, ν is kinematic viscosity, p is pressure and $\boldsymbol{v}$ is velocity of the fluid. The boundary conditions for the base flow are: $v_x = 1, v_y = 0, v_z = 0$, at $y = 0$, and $\boldsymbol{v} = 0$ at $|\boldsymbol{x}| = 1$ (see figure 2.1).

An analytical solution for equation (3.1) is not available for the hemisphere geometry so equation (3.1) is solved numerically using the *Semtex* code developed by Blackburn and Sherwin (2004). *Semtex* is a 2D spectral element method, here in (r, z) and uses Fourier expansion functions for the spatially periodic direction θ to solve for the steady or unsteady velocity field. The hemisphere is treated in terms of cylindrical coordinates to obtain velocity using *Semtex*. Because the hemisphere velocity is periodic in azimuthal

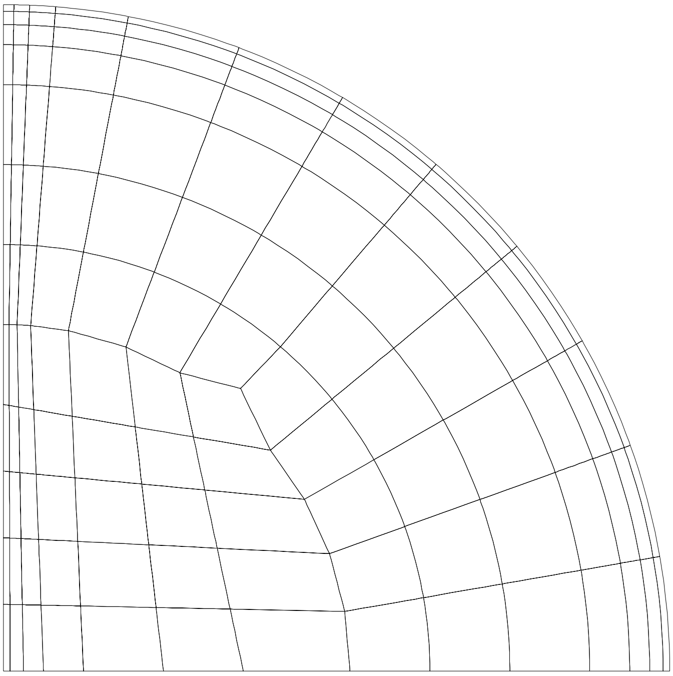

Figure 3.1: The mesh corresponding to hemisphere in the axial-radial plane.

direction θ, the Fourier expansion is done in that direction. A two-dimensional mesh as shown in figure 3.1 in axial-radial plane is used for hemisphere geometry in the *Semtex* velocity calculations.

Semtex provides $\boldsymbol{v}$ on the mesh in figure 3.1, but for later methods $\boldsymbol{v}$ is required on a uniform grid. $\boldsymbol{v}$ on the mesh is then interpolated spectrally onto a uniform grid in spherical polar coordinates (r, θ, ϕ). The interpolated velocity field on the unifrom grid is in cylindrical polar coordinates and is converted to spherical polar velocity components (v_r, v_θ, v_ϕ) for use in particle tracking.

To obtain base flow in the Stokes limit, the kinematic viscosity is set to $\nu = 10^{15}$ in the *Semtex* velocity calculations so equivalent to Stokes flow. To obtain base flow in the finite *Re* flow, $\nu = 1/Re$ is set in the *Semtex* velocity calculations because the kinematic viscosity is set as the inverse of the Reynold number in *Semtex*. There is a discontinuity in the velocity along the line where the sliding lid meets the equator of the hemisphere, which presents a significant numerical difficulty due to the spectral nature of *semtex*. The discontinuity is removed by using a continuous ramp in lid velocity from zero to 1, and constant lid velocity here is replaced using a continuous function $1 - e^{-2000(1-r^2)^3}$ (see Figure 3.2).

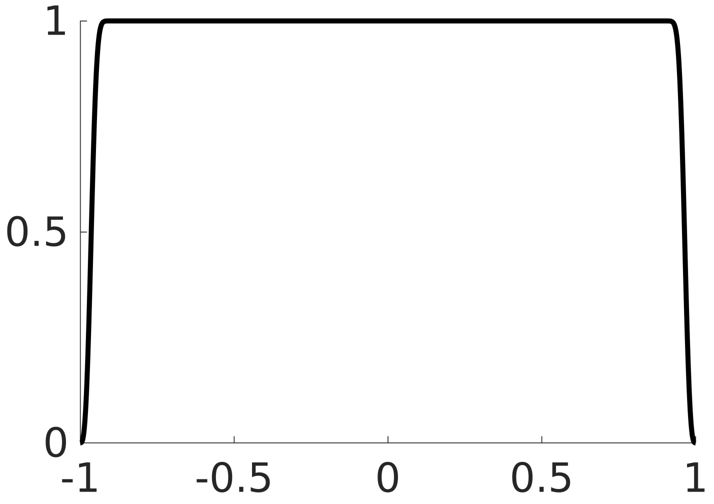

Figure 3.2: Lid Velocity along x axis.

To compute a particle trajectory, velocity data between grid points is needed, and hence, an interpolation scheme is needed. It is possible to get velocity at any arbitrary point by spectral interpolation of the *Semtex* solution, but it would be computationally very expensive and not practical for the extremely long integration times typical of the computations presented in subsequent chapters.

In an incompressible flow, if the volume is not conserved during particle advection, fluid particles do not remain on their corresponding invariant surfaces or lines, leading to inaccurate Lagrangian transport structures. Typical velocity interpolation schemes interpolate velocity components independently. In incompressible flows, interpolating velocity components via any scheme separately does not preserve volume conservation, which is a critical point of this project. Finn and Chacón (2005), hereafter referred to as FC, were the first to produce an interpolation scheme to obtain a continuous divergence-free velocity field from gridded data. At first in my thesis work, FC method was implemented to obtain a continuous divergence-free velocity field, but it is found that the interpolated velocity varied significantly from the grid velocities on which they were based. A new divergence-free interpolation is developed that ensures the interpolated velocity field matches the grid values almost everywhere, with errors that are two to four orders of magnitude lower than the FC method. This was published as Ravu *et al.* (2016) and is presented in the next section.

3.2 A new divergence-free interpolation method

The starting point is velocity data (v_x, v_y, v_z) specified on a grid of points (x, y, z) distributed throughout the domain of interest. It is assumed below that the grid is uniformly spaced (although it does not have to be) and that the grid data accurately samples an underlying continuous, incompressible velocity field. The data may come from numerical computation or experimental measurement.

We consider the three-dimensional grid $[x_0, ...x_{n_x}]$, $[y_0, ...y_{n_y}]$ and $[z_0, ...z_{n_z}]$ with spacing (h_x, h_y, h_z) between nodes, where the grid point (p, q, r) is given by

$$x_p = x_0 + ph_x, \quad y_q = y_0 + qh_y, \quad z_r = z_0 + rh_z,$$

and $p = 0, ..., n_x$, $q = 0, ..., n_y$ and $r = 0, ..., n_z$.

Before presenting the method and because this scheme will be benchmarked with that of FC, it is instructive to outline the interpolation method of FC.

3.2.1 Outline of the Finn and Chacon method

FC calculate a spline function for a vector potential $\boldsymbol{A} = (A_x, A_y, A_z)$ from discrete velocity data and then differentiate $\boldsymbol{A}$ analytically to obtain a divergence-free velocity. They choose a vector potential gauge in which $A_x = 0$ (although other gauges are possible), and the divergence-free velocity components are given by

$$v_x = \frac{\partial A_z}{\partial y} - \frac{\partial A_y}{\partial z} \tag{3.2a}$$

$$v_y = -\frac{\partial A_z}{\partial x} \tag{3.2b}$$

$$v_z = \frac{\partial A_y}{\partial x}. \tag{3.2c}$$

FC calculate the vector potential components on the grid by discrete numerical quadrature of the integrals

$$A_y(x, y, z) = \int_{x_0}^{x} v_z(x', y, z)dx' \tag{3.3a}$$

$$A_z(x, y, z) = \int_{y_0}^{y} v_x(x_0, y', z)dy' - \int_{x_0}^{x} v_y(x', y, z)dx', \tag{3.3b}$$

calculating the line integrals with the trapezoidal rule. After calculating the discrete vector potential, FC fit a tricubic spline to get a C^2 continuous vector potential.

Equation (3.3) uses the information of v_y and v_z on the 3D grid points and v_x only at the $x = x_0$ plane grid points to calculate the vector potential. When using the FC approach, it is found that values of v_x, v_y and v_z on the 3D grid points do not necessarily recover the same values of the discrete velocity components which were used to calculate the vector potential. The error in the velocity components has two parts which are independent. One part comes from the approximations used in the line integrals of equation (3.3). The other part comes from fitting splines to discrete vector potential components A_y and A_z rather than to the velocities directly (i.e. to $\frac{\partial A_y}{\partial x}$ and $\frac{\partial A_z}{\partial x}$). This can introduce errors when $\frac{\partial A_y}{\partial x}$ and $\frac{\partial A_z}{\partial x}$ are evaluated from the splines fitted to $\boldsymbol{A}$. Because of these two potential error sources, it is found that the derived velocities at the grid points can sometimes vary significantly from the grid velocities on which they are based.

The method presented here, while similar in spirit to that of FC, constructs the spline functions for the vector potential directly from the grid-based velocity data. In the FC method, spline functions for the vector potential are fitted to the approximate discrete vector potential which is computed from the grid-based velocity data, whereas in the new method, derivatives of the spline function for A are fitted directly to the velocity data.

3.2.2 Overview of the new method

A vector potential in terms of spline functions is defined and decomposed the problem of specifying the coefficients of the 3D splines into three one-dimensional coefficient problems that can each be independently and rapidly inverted to specify the coefficients. A divergence-free velocity field $\boldsymbol{V} = (v_x, v_y, v_z)$ can always be written as the curl of a vector potential $\boldsymbol{A} = (A_x, A_y, A_z)$:

$$v_x = \frac{\partial A_z}{\partial y} - \frac{\partial A_y}{\partial z} \tag{3.4a}$$

$$v_y = \frac{\partial A_x}{\partial z} - \frac{\partial A_z}{\partial x} \tag{3.4b}$$

$$v_z = \frac{\partial A_y}{\partial x} - \frac{\partial A_x}{\partial y}. \tag{3.4c}$$

As in FC, the gauge freedom is utilised to simplify the mathematics and the algorithm by setting one of the components of $\boldsymbol{A}$ to zero. In what follows $A_z = 0$ is set; although, setting A_x or A_y to zero provides an equivalent scheme and may be preferable depending on the nature of the problem. Gauge choices will be discussed further in the example problems. Having set $A_z = 0$, $\boldsymbol{V} = \boldsymbol{\nabla} \times \boldsymbol{A}$ becomes

$$v_x = -\frac{\partial A_y}{\partial z} \tag{3.5a}$$

$$v_y = \frac{\partial A_x}{\partial z} \tag{3.5b}$$

$$v_z = \frac{\partial A_y}{\partial x} - \frac{\partial A_x}{\partial y} \tag{3.5c}$$

In equation (3.5) the gridded velocity data implicitly contains information about derivatives of $\boldsymbol{A}$ at the grid points. A_y can be calculated from discrete velocity component v_x using equation (3.5a), and A_x can be calculated from discrete velocity component v_y using equation (3.5b). However, in general if v_z is calculated by substituting A_x and A_y into equation (3.5c), the calculated v_z does not match the data value of v_z. This is because many different functions for v_z can be chosen that satisfy $\boldsymbol{\nabla} \cdot \boldsymbol{V} = 0$.

3.2.2.1 Calculating v_z

Due to the incompressibility constraint, fluid velocity components are not independent: v_z can be calculated from v_x and v_y as

$$v_z(x, y, z) = \int_{z_0}^{z} \left(-\frac{\partial v_x}{\partial x}(x, y, z') - \frac{\partial v_y}{\partial y}(x, y, z') \right) dz' + C(x, y), \tag{3.6}$$

where $C(x, y)$ is an integration function. Its specification uniquely fixes v_z. In particular we choose,

$$C(x, y) = v_z(x, y, z_0), \tag{3.7}$$

where z_0 is any plane on which v_z is given, most often a boundary condition, but it could also be a symmetry plane. When v_x and v_y from equation (3.5) are substituted into equation (3.6), it becomes

$$v_z(x, y, z) = \frac{\partial A_y}{\partial x} - \frac{\partial A_x}{\partial y} + C(x, y) \tag{3.8}$$

We absorb $C(x, y)$ into A_y by redefining the vector potential to $\boldsymbol{A} = (A_x, A_y^*, 0)$, where $A_y^* = A_y + f(x, y)$ and $C(x, y) = \partial f / \partial x$. Because both v_x and v_y depend only on partial derivatives with respect to z, this has no effect on v_x and v_y. However, v_z becomes

$$v_z = \frac{\partial A_y}{\partial x} + \frac{\partial f}{\partial x} - \frac{\partial A_x}{\partial y}. \tag{3.9}$$

Without loss of generality, we can set A_x and A_y to zero at the z_0 plane: $A_x(x, y, z_0) = 0$, $A_y(x, y, z_0) = 0$, the choice of which clearly does not affect the curl of the vector potential, i.e. the velocity is uneffected. Then at z_0, from equation (3.9),

$$v_z(x, y, z_0) = \frac{\partial f}{\partial x}(x, y), \tag{3.10}$$

from which $f(x, y)$ can be determined from the data given for v_z at z_0.

So far, the method above ensures that the curl of the vector potential reproduces exactly the same v_x, v_y as the data on the 3D grid points and the same v_z on the 2D grid at $z = z_0$. However, this still permits deviations in the derived v_z component on other grid points. This is because

$$v_z = \int \frac{\partial v_z}{\partial z} dz = \int \left(-\frac{\partial v_x}{\partial x} - \frac{\partial v_y}{\partial y} \right) dz$$

and the derivatives of the spline fit to v_x and v_y do not necessarily match the actual derivatives of the velocity field. If the given discrete velocity field is not sampled from a divergence-free velocity field, then large deviations are expected in the derived v_z velocity component. There are four different ways to match the v_z component exactly as the data on the grid points of boundary planes.

Case 1: Match v_z only on the grid points at $z = z_0$.
In this case, $f(x, y)$ is calculated using equation (3.10) such that $\partial f/\partial x = v_z$ on the $z = z_0$ plane grid points, A_y is obtained using equation (3.5a) such that $\partial A_y/\partial z = -v_x$ on the grid points and A_x is obtained using equation (3.5b) such that $\partial A_x/\partial z = v_y$ on the grid points. We can calculate f, A_x and A_y in any order.

Case 2: Match v_z on the grid points at $z = z_0$, $y = y_0$ and $y = y_{n_y}$.
In this case ,we first calculate A_y^* $(= A_y + f)$ in the same way as in case 1. This allows us to rewrite equation (3.9) as

$$\frac{\partial A_x}{\partial y} = \frac{\partial A_y}{\partial x} + \frac{\partial f}{\partial x} - v_z. \tag{3.11}$$

Finally, we obtain A_x using equations (3.5b) and (3.11) such that $\partial A_x/\partial z = v_y$ on all grid points and $\frac{\partial A_y}{\partial x} + \frac{\partial f}{\partial x} - \frac{\partial A_x}{\partial y}$ equals v_z on grid points at $z = z_0$, $y = y_0$ and $y = y_{n_y}$. In section 3.2.3, a method to calculate the vector potential coefficients for this case is derived and found that it works well for all the test cases in section 3.2.5.

Case 3: Match v_z on grid points at $z = z_0$, $z = z_{n_z}$, $y = y_0$ and $y = y_{n_y}$.
In this case, we first calculate A_y^* $(= A_y + f)$ in the same way as in case 1 and next obtain A_x such that $\partial A_x/\partial z = v_y$ on all the grid points and $\frac{\partial A_y}{\partial x} + \frac{\partial f}{\partial x} - \frac{\partial A_x}{\partial y}$ equals v_z on the grid points at $z = z_0$,$z = z_{n_z}$, $y = y_0$ and $y = y_{n_y}$. This approach increases the complexity in calculating the spline coefficients for A_x.

Case 4: Matching v_z on all boundary plane grid points.
It is possible to match the v_z component exactly on all six boundary grid planes; however, the computation is cumbersome, and I have not (yet) investigated a test case where it was necessary to do this. In this case, we first calculate f in the same way as in case 1 and

next calculate A_y and A_x together simultaneously such that $\partial A_y/\partial z = -v_x$ and $\partial A_x/\partial z = v_y$ on the grid points and $\frac{\partial A_y}{\partial x} + \frac{\partial f}{\partial x} - \frac{\partial A_x}{\partial y}$ equals v_z on the grid points of all boundary planes.

3.2.2.2 *Spline definition*

We need to calculate spline functions for A_x, A_y and f. We use standard B-splines, as discussed by Habermann and Kindermann (2007), that are C^2 continuous and have compact support. Once the spline coefficients of the vector potential $\boldsymbol{A}$ are determined, which is the main focus of this algorithm, the velocity field is determined simply through taking analytical derivatives of $\boldsymbol{A}$.

Each spline approximation is written as a tensor product of 1D B-splines:

$$A_x(x, y, z) = \sum_{i=1}^{n_x+3} \sum_{j=1}^{n_y+3} \sum_{k=1}^{n_z+3} c_{ijk} b_i(x) b_j(y) b_k(z), \tag{3.12a}$$

$$A_y(x, y, z) = \sum_{i=1}^{n_x+3} \sum_{j=1}^{n_y+3} \sum_{k=1}^{n_z+3} d_{ijk} b_i(x) b_j(y) b_k(z), \tag{3.12b}$$

and

$$f(x, y) = \sum_{i=1}^{n_x+3} \sum_{j=1}^{n_y+3} e_{ij} b_i(x) b_j(y). \tag{3.12c}$$

In equations (3.12) the coefficients c_{ijk}, d_{ijk} and e_{ij} are what need to be determined from the data. Note that the grid spacing (h_x, h_y, h_z) is implicit in the definition of the functions b_i,

$$b_i(x) = \phi\left(\frac{x - x_0}{h_x} - (i-2)\right), i = 1, ..., n_x + 3. \tag{3.13}$$

where $\phi(t)$ is the normalised spline function given by

$$\phi(t) = \begin{cases} (2 - |t|)^3, & 1 \leq |t| \leq 2 \\ 4 - 6|t|^2 + 3|t|^3, & |t| \leq 1 \\ 0, & \text{elsewhere.} \end{cases} \tag{3.14}$$

The functions b_i are shown in figure 3.3. The region of support for each spline is four times the grid spacing in that direction: four splines contribute to the value of the function at any grid point.

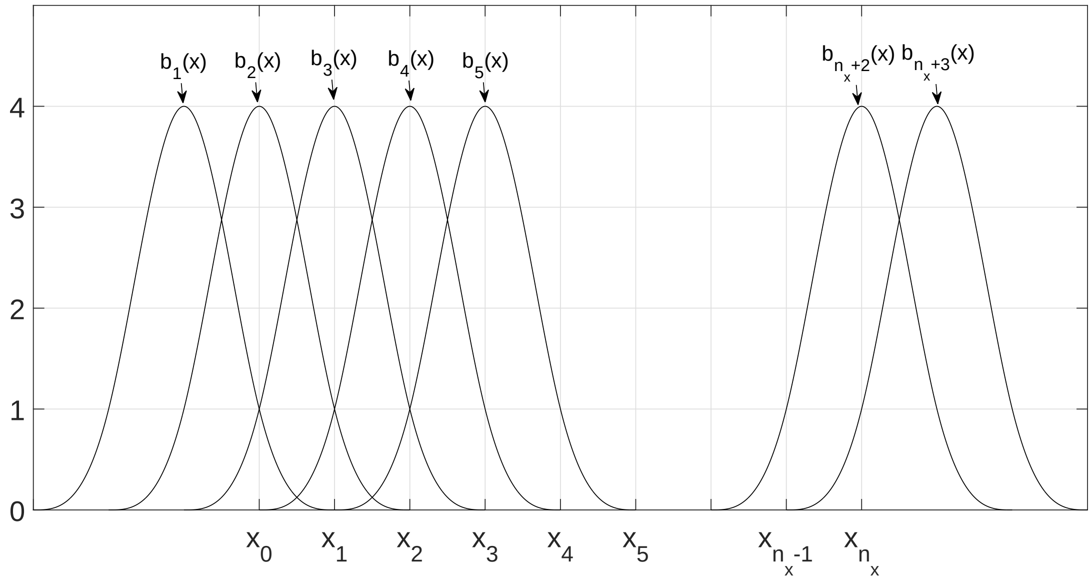

Figure 3.3: Spline basis functions $b_1, b_2, ...b_{n_x+3}$. The region of support for each spline is four times the grid spacing, and four splines contribute to the value of the function at any grid point.

3.2.3 Derivation of the vector potential components in Cartesian coordinates

Before constructing all two- and three-dimensional splines based on a one-dimensional spline fit, I first explain how the spline fit works by considering B-splines in one-dimension.

3.2.3.1 Properties of the one-dimensional cubic spline

We consider the uniform grid $[x_0, ...x_{n_x}]$ with grid spacing h_x and write the spline function $s(x)$ as a linear combination of the basis functions,

$$s(x) = \sum_{i=1}^{n_x+3} c_i b_i(x). \tag{3.15}$$

As each basis function spans only four grid spacings, equation (3.15) generalizes to

$$s(x) = \sum_{i=l}^{m} c_i b_i(x), \quad l = \left\lfloor \frac{x - x_0}{h_x} + 1 \right\rfloor, \quad m = min(l + 3, n_x + 3), \tag{3.16}$$

where $\lfloor . \rfloor$ is the floor function.

In the algorithm to follow, in some cases we will need to fit a spline to data, in others we will need to fit the derivatives of the spline to data. On the grid point x_p, only three splines are non-zero and we write, from equation (3.15),

$$\begin{aligned} s(x_p) &= c_{p+1}b_{p+1}(x_p) + c_{p+2}b_{p+2}(x_p) + c_{p+3}b_{p+3}(x_p), \\ &= c_{p+1} + 4c_{p+2} + c_{p+3}, \quad p = 0, ..., n_x. \end{aligned} \tag{3.17}$$

The first derivative of the spline function is then

$$\begin{aligned} s'(x_p) &= c_{p+1}b'_{p+1}(x_p) + c_{p+2}b'_{p+2}(x_p) + c_{p+3}b'_{p+3}(x_p) \\ &= \frac{1}{h_x}(-3c_{p+1} + 3c_{p+3}), \quad p = 0, ..., n_x, \end{aligned} \tag{3.18}$$

and the second derivative is

$$\begin{aligned} s''(x_p) &= c_{p+1}b''_{p+1}(x_p) + c_{p+2}b''_{p+2}(x_p) + c_{p+3}b''_{p+3}(x_p) \\ &= \frac{6}{h_x^2}(c_{p+1} - 2c_{p+2} + c_{p+3}), \quad p = 0, ..., n_x. \end{aligned} \tag{3.19}$$

To find the coefficients in equation (3.15), we require $n_x + 3$ independent conditions. There are two different cases to consider. In one case, we know the value of the function on the grid points. In the other case, we know the value of the first derivatives. We first explain how to calculate the spline coefficients c_i from function values on the grid points. Then we explain how to calculate the spline coefficients c_i from first derivative values on the grid points.

3.2.3.2 Computing spline coefficients from function values on the grid

Denote the function values on the grid $y_0, y_1, \cdots, y_n$. From equation (3.17) at x=x_p

$$s(x_p) = c_{p+1} + 4c_{p+2} + c_{p+3} = y_p, \quad p = 0, 1, ...n_x. \tag{3.20}$$

The function values on the grid provide $n_x + 1$ conditions, and we require two more conditions to compute the $n_x + 3$ coefficients. There are three choices for these last two conditions.

Case 1: We know the second derivatives of the function at both ends, so that from equation (3.19)

$$\frac{\partial^2 s}{\partial x^2}(x_0) = \frac{6}{h_x^2}(c_1 - 2c_2 + c_3) = \alpha_0, \tag{3.21a}$$

$$\frac{\partial^2 s}{\partial x^2}(x_{n_x}) = \frac{6}{h_x^2}(c_{n_x+1} - 2c_{n_x+2} + c_{n_x+3}) = \alpha_{n_x}. \tag{3.21b}$$

Case 2: We know the first derivatives of the function at both ends, so that from equation (3.18),

$$\frac{\partial s}{\partial x}(x_0) = \frac{1}{h_x}(-3c_1 + 3c_3) = \beta_0, \tag{3.22a}$$

$$\frac{\partial s}{\partial x}(x_{n_x}) = \frac{1}{h_x}(-3c_{n_x+1} + 3c_{n_x+3}) = \beta_{n_x}. \tag{3.22b}$$

Case 3: The function is periodic, so that

$$\frac{\partial s}{\partial x}(x_0) = \frac{\partial s}{\partial x}(x_{n_x}) \quad \Rightarrow \quad -c_1 + c_3 = -c_{n_x+1} + c_{n_x+3}, \tag{3.23a}$$

$$\frac{\partial^2 s}{\partial x^2}(x_0) = \frac{\partial^2 s}{\partial x^2}(x_{n_x}) \quad \Rightarrow \quad c_1 - 2c_2 + c_3 = c_{n_x+1} - 2c_{n_x+2} + c_{n_x+3}. \tag{3.23b}$$

To solve for the coefficients in equation (3.15) we have $n_x + 1$ of the required $n_x + 3$ interpolation conditions from equation (3.20). The final two conditions come from choice of the appropriate pair of equations (3.21) to 3.23.

3.2.3.3 Computing spline coefficients from function derivatives on the grid

Denote the function derivative values on the grid $y'_0, y'_1, \cdots, y'_n$. From equation (3.18) at $x{=}x_p$

$$s'(x_p) = \frac{1}{h_x}(-3c_{p+1} + 3c_{p+3}) = y'_p, \quad p = 0, 1, ...n_x. \tag{3.24}$$

The function derivatives on the grid provide $n_x + 1$ conditions, and without loss of generality we can set

$$s(x_0) = 0, \tag{3.25}$$

leaving the requirement of one additional condition to solve for the $n_x + 3$ coefficients. There are again three choices for this last condition.

Case 1: We know the second derivatives of the function at x_0, so that from equation (3.19)

$$\frac{\partial^2 s}{\partial x^2}(x_0) = \frac{6}{h_x^2}(c_1 - 2c_2 + c_3) = \alpha_0. \tag{3.26}$$

Case 2: We know the second derivative of the function at x_{n_x}, so that from equation (3.19)

$$\frac{\partial^2 s}{\partial x^2}(x_{n_x}) = \frac{6}{h_x^2}(c_{n_x+1} - 2c_{n_x+2} + c_{n_x+3}) = \alpha_{n_x}. \tag{3.27}$$

Case 3: The function is periodic, so that

$$\frac{\partial^2 s}{\partial x^2}(x_0) = \frac{\partial^2 s}{\partial x^2}(x_{n_x}) \quad \Rightarrow \quad c_1 - 2c_2 + c_3 = c_{n_x+1} - 2c_{n_x+2} + c_{n_x+3}. \tag{3.28}$$

To solve for the coefficients in equation (3.15) we have $n_x + 1$ of the required $n_x + 3$ interpolation conditions from equation (3.24). One interpolation condition always comes from equation (3.25). The final condition comes from choice of the appropriate equation (3.26) to 3.28.

3.2.3.4 *Computing the $f(x, y)$ spline coefficients*

We calculate a spline function for $f(x, y)$, defined via equation (3.10), such that $\partial f/\partial x = v_z$ on the grid points in the z_0 plane. The calculation of f has two steps. In step one, for each y on the grid, we fit a 1-D spline in the x-direction. In step two, we construct a 2-D spline fit in x and y for the 1-D splines calculated in step one.

We write equation (3.12c) as

$$\begin{aligned} f(x, y) &= \sum_{i=1}^{n_x+3} b_i(x)\left(\sum_{j=1}^{n_y+3} b_j(y)e_{ij}\right) \\ &= \sum_{i=1}^{n_x+3} b_i(x)\tilde{f}_i(y) \end{aligned} \tag{3.29}$$

and define two 1D spline functions $f_q^*(x)$ and $\tilde{f}_i(y)$ from equation (3.29) as

$$f_q^*(x) = f(x, y_q) = \sum_{i=1}^{n_x+3} b_i(x)e_{iq}^*, \quad q \in [0, n_y] \tag{3.30}$$

and

$$\tilde{f}_i(y) = \sum_{j=1}^{n_y+3} b_j(y)e_{ij}, \quad i \in [1, n_x + 3]. \tag{3.31}$$

For each value of $y(y_q)$, we compute coefficients e^*_{iq} in equation (3.30) as described in 3.2.3.3 with interpolation conditions

$$\frac{\partial f^*_q}{\partial x}(x_p) = v_z(x_p, y_q, z_0), \quad p \in [0, n_x], \tag{3.32}$$

which comes from equations (3.10) and (3.30). For each value of i, we compute coefficients e_{ij} in equation (3.31) as described in section 3.2.3.2 with interpolation conditions

$$\tilde{f}_i(y_q) = e^*_{iq}, \quad q \in [0, n_y], \tag{3.33}$$

which comes from equations (3.30) and (3.31). To compute the coefficients e_{ij} in equation (3.31) requires information about $\partial \tilde{f}_i / \partial y$ as a function of y that is calculated from $\partial v_z / \partial y$ as

$$\frac{\partial f}{\partial y}(x, y) = \sum_{i=1}^{n_x+3} b_i(x) \frac{\partial \tilde{f}_i}{\partial y}(y). \tag{3.34}$$

For each value of $y(y_q)$

$$\frac{\partial f}{\partial y}(x, y_q) = \sum_{i=1}^{n_x+3} b_i(x) e'^*_{iq}, \tag{3.35}$$

and we compute the coefficients e'^*_{iq} in equation (3.35) as described in section 3.2.3.3 for each q with the interpolation conditions

$$\frac{\partial^2 f}{\partial y \partial x}(x_p, y_q) = \frac{\partial v_z}{\partial y}(x_p, y_q, z_0), p \in [0, n_x], \tag{3.36}$$

which comes from equations (3.10) and (3.30). Finally

$$\frac{\partial \tilde{f}_i}{\partial y}(y_q) = e'^*_{iq}, \quad i \in [1, n_x + 3]. \tag{3.37}$$

3.2.3.5 *Computing spline coefficients for A_y*

We calculate a spline function for A_y such that $\partial A_y / \partial z = -v_x$ on the grid points. The calculation of A_y has three steps. In step one, for each pair of (x, y) grid coordinates we fit a 1-D spline in the z-direction. In step two, for each x on the grid, we construct a 2-D spline fit in z and y for the 1-D splines calculated in step one. In step three, we construct a 3-D spline fit in x,y and z for the 2-D splines calculated in step two.

We rewrite equation (3.12b) as

$$A_y(x, y, z) = \sum_{k=1}^{n_z+3} b_k(z) \left(\sum_{j=1}^{n_y+3} b_j(y) \left(\sum_{i=1}^{n_x+3} b_i(x) d_{ijk} \right) \right) \tag{3.38}$$

and define three 1D spline functions $A^*_{y,p,q}(z)$, $\tilde{A}_{y,p,k}(y)$ and $\tilde{\tilde{A}}_{y,j,k}(x)$ from equation (3.38) as

$$A^*_{y,p,q}(z) = A_y(x_p, y_q, z) = \sum_{k=1}^{n_z+3} b_k(z) d^*_{pqk}, \quad p \in [0, n_x], \quad q \in [0, n_y] \tag{3.39}$$

$$\tilde{A}_{y,p,k}(y) = \sum_{j=1}^{n_y+3} b_j(y) d^{**}_{pjk}, \quad p \in [0, n_x], \quad k \in [1, n_z + 3] \tag{3.40}$$

$$\tilde{\tilde{A}}_{y,j,k}(x) = \sum_{i=1}^{n_x+3} b_i(x) d_{ijk}, \quad j \in [1, n_y + 3], \quad k \in [1, n_z + 3] \tag{3.41}$$

We compute coefficients d^*_{pqk} in equation (3.39) as described in section 3.2.3.3 for each p and q with interpolation conditions

$$\frac{\partial A^*_{y,p,q}}{\partial z}(z_r) = -v_x(x_p, y_q, z_r), \quad r \in [0, n_z] \tag{3.42}$$

which comes from equations (3.39) and (3.5a). Next we compute coefficients d^{**}_{pjk} in equation (3.40) as described in section 3.2.3.2 for each p and k with the interpolation conditions

$$\tilde{A}_{y,p,k}(y_q) = d^*_{pqk}, \quad q \in [0, n_y], \tag{3.43}$$

which comes from equations (3.39) and (3.40). Finally we compute coefficients d_{ijk} in equation (3.41) as described in section 3.2.3.2 for each j and k with the interpolation conditions

$$\tilde{\tilde{A}}_{y,j,k}(x_p) = d^{**}_{pjk}, \quad p \in [0, n_x], \tag{3.44}$$

which comes from equations (3.40) and (3.41).

The computation of the A_x spline coefficients is done in the same way as for the A_y coefficients. The following way of calculating A_x ensures that v_z matches on the y_0 and y_{n_y} plane grid points.

3.2.3.6 Computing spline coefficients for A_x

We calculate a spline function for A_x such that $\partial A_x/\partial z = v_y$ on the grid points and $\frac{\partial A_y}{\partial x} + \frac{\partial f}{\partial x} - \frac{\partial A_x}{\partial y} = v_z$ on the grid points of the two boundary planes y_0 and y_{n_y}.

We rewrite equation (3.12a) as

$$A_x(x, y, z) = \sum_{k=1}^{n_z+3} b_k(z) \left(\sum_{j=1}^{n_y+3} b_j(y) \left(\sum_{i=1}^{n_x+3} b_i(x) c_{ijk} \right) \right) \tag{3.45}$$

and define three 1D spline functions $A^*_{x,p,q}(z)$, $\tilde{A}_{x,p,k}(y)$ and $\tilde{\tilde{A}}_{x,j,k}(x)$ from equation (3.45) as

$$A^*_{x,p,q}(z) = A_x(x_p, y_q, z) = \sum_{k=1}^{n_z+3} b_k(z)c^*_{pqk}, \quad p \in [0, n_x], \quad q \in [0, n_y] \tag{3.46}$$

$$\tilde{A}_{x,p,k}(y) = \sum_{j=1}^{n_y+3} b_j(y)c^{**}_{pjk}, \quad p \in [0, n_x], \quad k \in [1, n_z + 3] \tag{3.47}$$

$$\tilde{\tilde{A}}_{x,j,k}(x) = \sum_{i=1}^{n_x+3} b_i(x)c_{ijk}, \quad j \in [1, n_y + 3], \quad k \in [1, n_z + 3]. \tag{3.48}$$

We compute the coefficients c^*_{pqk} in equation (3.46) as described in section 3.2.3.3 for each p and q with interpolation conditions

$$\frac{\partial A^*_{x,p,q}}{\partial z}(z_r) = v_y(x, x_p, y_q, z_r) \quad r \in [0, n_z], \tag{3.49}$$

which come from equations (3.46) and (3.5b). Next we compute coefficients c^{**}_{pjk} in equation (3.47) as described in section 3.2.3.2 for each p and k with interpolation conditions

$$\tilde{A}_{x,p,k}(y_q) = c^*_{pqk}, \quad q \in [0, n_y] \tag{3.50}$$

together with $\frac{\partial \tilde{A}_{x,p,k}(y)}{\partial y}$ at y_0 and y_{n_y}, calculated by solving the following spline problem at y_0 and y_{n_y}:

$$\frac{\partial A_x}{\partial y}(x_p, y_q, z) = \sum_{k=1}^{n_z+3} b_k(z)\frac{\partial \tilde{A}_{x,p,k}(y_q)}{\partial y}, \tag{3.51}$$

where $\frac{\partial A_x}{\partial y}(x_p, y_q, z_r)$ is calculated via equation (3.11). Matching $\frac{\partial A_x}{\partial y}(x_p, y_q, z_r)$, which is computed via equation (3.11), ensures that the velocity component v_z matches the grid data on the y_0 and y_{n_y} planes.

Finally we compute the coefficients c_{ijk} in equation (3.48) as described in section 3.2.3.2 for each j and k with interpolation conditions

$$\tilde{\tilde{A}}_{x,j,k}(x_p) = c^{**}_{pjk}, \quad p \in [0, n_x], \tag{3.52}$$

which come from equations (3.47) and (3.48)

The method described above computes spline functions for A_x, A_y and f, such that the curl of the vector potential $(A_x, A^*_y, 0)$ is not just divergence-free but also exactly matches v_x and v_y on the 3d grid points and exactly matches v_z on the z_0, y_0 and y_{n_y} boundary plane grid points.

3.2.4 Method for general curvilinear coordinates

The interpolation method described above in Cartesian coordinates readily generalises to curvilinear coordinates and in this section the results of the generalisation in terms of contravariant vector components are outlined.

In arbitrary curvilinear coordinates ξ^i, the velocity can be written using contravariant velocity components v^1,v^2 and v^3 as

$$\boldsymbol{V} = v^1\vec{\nabla}\xi^2 \times \vec{\nabla}\xi^3 + v^2\vec{\nabla}\xi^3 \times \vec{\nabla}\xi^1 + v^3\vec{\nabla}\xi^1 \times \vec{\nabla}\xi^2. \tag{3.53}$$

In equation (3.53) the partial time derivatives of the coordinates ξ^i are given by

$$\frac{\partial \xi^i}{\partial t} = \boldsymbol{V} \cdot \vec{\nabla}\xi^i = \frac{v^i}{J}, \tag{3.54}$$

where J is the Jacobian given by $J^{-1} = (\vec{\nabla}\xi^1 \cdot \vec{\nabla}\xi^2 \times \vec{\nabla}\xi^3)$, and the divergence is

$$\vec{\nabla} \cdot \boldsymbol{V} = \frac{1}{J}\sum_i \frac{\partial v^i}{\partial \xi^i}. \tag{3.55}$$

For an incompressible fluid, $\sum_i \frac{\partial v^i}{\partial \xi^i} = 0$, and the general coordinate divergence in terms of contravariant components resembles the divergence in Cartesian coordinates, except there is an extra factor of J to carry along. When we apply this interpolation method to a flow in cylindrical or spherical coordinates, we first compute contravariant velocity components using equation (3.54), in order to treat the contravariant velocity components similarly to Cartesian velocity components. This allows us to calculate the vector potential in generalized coordinates in the same way as we do for Cartesian coordinates.

3.2.5 Test case

To demonstrate the efficacy of the interpolation method developed above, we consider a model test flow for which the velocity field is defined analytically. While we compare velocity fields to estimate the accuracy of the interpolation, more importantly, we also compute Lagrangian quantities, in order to compare the accuracy of Lagrangian coherent structures obtained using the new divergence-free interpolation method versus using other interpolation methods. In particular, we benchmark against the FC method because it is currently most commonly utilized in practice.

Table 3.1: Errors in the interpolated velocity field on the boundary of a 42 × 42 × 42 grid.

		FC Method	New method
v_x	L_1 norm	1.2e-03	5.63e-15
	L_2 norm	1.5e-03	7.76e-15
	L_∞ norm	4.7e-03	33.6e-15
v_y	L_1 norm	5.38e-04	0.85e-15
	L_2 norm	7.9e-04	1.30e-15
	L_∞ norm	20.0e-04	12.9e-15
v_z	L_1 norm	5.38e-04	0.84e-15
	L_2 norm	7.9e-04	1.24e-15
	L_∞ norm	20.0e-04	9.99e-15

We consider a divergence-free analytic velocity field that is a modification of the ABC flow defined by

$$v_x = \cos x[\,\sin z + \cos y] \tag{3.56a}$$

$$v_y = \sin y[\,\sin x + \cos z] \tag{3.56b}$$

$$v_z = -\sin x \cos z - \cos y \sin z \tag{3.56c}$$

We have chosen this form of velocity field to ensure that all velocity components are dependent on all three coordinate directions. We calculate discrete velocity data from equation (3.56) on a uniform 42 × 42 × 42 grid over the coordinate range ($-\frac{\pi}{4} \le x \le \frac{7\pi}{4}$), ($-\frac{\pi}{4} \le y \le \frac{7\pi}{4}$), and ($-\frac{\pi}{4} \le z \le \frac{7\pi}{4}$). The coordinate ranges are chosen such that the boundary velocity is non-zero and periodic in all three coordinate directions. The vector potential $\boldsymbol{A}$ (in a gauge with $A_x = 0$) is calculated from this grid data with the method from section 3.2.3 and with the method of FC. Constructing splines for both the new method and the FC method require additional interpolation closure conditions, which are listed in tables A1, A2 and A3 in Appendix A. Velocity fields are then calculated via $\boldsymbol{V} = \boldsymbol{\nabla} \times \boldsymbol{A}$ on the same grid and compared with the analytic velocity field for both methods both on grid points and between the grid points. In tables 3.1 and 3.2 are global metrics that show the deviations from the analytic solution respectively on the boundary grid points and the entire grid. While FC is fairly accurate, the new method is accurate on the grid nearly to machine precision.

With the same vector potentials computed from the 42 × 42 × 42 grid, velocity fields are calculated via $\boldsymbol{V} = \boldsymbol{\nabla} \times \boldsymbol{A}$ on a finer grid of points (165 × 165 × 165) and compared with the analytic velocity field for both methods. The aim is not to ensure that the original sampled vector field is recovered (which it must by construction), but to ensure that the

Table 3.2: Errors in the interpolated velocity field on a $42 \times 42 \times 42$ grid.

		FC Method	New method
v_x	L_1 norm	1.3e-03	6.44e-15
	L_2 norm	1.7e-03	8.45e-15
	L_∞ norm	5.3e-03	41.9e-15
v_y	L_1 norm	7.65e-04	0.74e-15
	L_2 norm	9.68e-04	1.22e-15
	L_∞ norm	20.0e-04	23.7e-15
v_z	L_1 norm	7.65e-04	0.81e-15
	L_2 norm	9.68e-04	1.24e-15
	L_∞ norm	20.0e-04	16.8e-15

Table 3.3: Errors in the interpolated velocity field on the boundary of a $165 \times 165 \times 165$ grid.

		FC Method	New method
v_x	L_1 norm	1.2e-03	2.81e-05
	L_2 norm	1.5e-03	4.92e-05
	L_∞ norm	4.8e-03	19.8e-05
v_y	L_1 norm	5.55e-04	4.58e-06
	L_2 norm	8.00e-04	8.21e-06
	L_∞ norm	21.0e-04	29.2e-06
v_z	L_1 norm	5.55e-04	4.62e-06
	L_2 norm	8.00e-04	8.21e-06
	L_∞ norm	21.0e-04	28.3e-06

errors that arise *in between* velocity data points are also small. In tables 3.3 and 3.4 are global metrics that show the deviations from the analytic solution on the boundary grid points and the entire grid correspondingly. Again, although FC is fairly accurate, the new method is two orders of magnitude more accurate.

More importantly, a Lagrangian trajectory is tracked from a single initial position $(-\pi/8, -\pi/8, -\pi/8)$ with a velocity field derived from the analytic solution, the new method and the FC method. In all three cases, Matlab's ode45 routine with relative tolerance 5×10^{-14} and absolute tolerance 10^{-15} is used to obtain particle trajectories, which are plotted in figure 3.4. We emphasize that the only difference in the way these results were obtained is the interpolation scheme—in every other respect (resolution, time-stepping, etc.) the computational methods are identical. Also, note that figure 3.4 shows only a fraction of the total trajectory computed. While it is clear from figure 3.4 that the new method

Table 3.4: Errors in the interpolated velocity field on a 165 × 165 × 165 grid.

		FC Method	New method
v_x	L_1 norm	1.3e-03	3.59e-05
	L_2 norm	1.7e-03	5.43e-05
	L_∞ norm	5.4e-03	19.8e-05
v_y	L_1 norm	7.89e-04	6.25e-06
	L_2 norm	9.80e-04	10.0e-06
	L_∞ norm	21.0e-04	31.1e-06
v_z	L_1 norm	7.89e-04	6.32e-06
	L_2 norm	9.80e-04	10.0e-06
	L_∞ norm	21.0e-04	28.4e-06

allows accurate tracking of Lagrangian trajectories for *much* longer, can we quantify how much more accurate is it?

One way to approach answering that question is via a conjecture about shadowing that Hammel *et al.* (1987) demonstrated numerically to be true for certain chaotic flows. Because a chaotic flow amplifies every small error, a numerical trajectory will shadow a true trajectory of the dynamical system to some accuracy only for some length of time that depends on a "noise" amplitude, i.e. a number that characterizes the size of all errors, no matter their source. The Hammel-Yorke-Grebogi conjecture is that for a noise amplitude δ the numerical trajectory deviates from the true trajectory by an amount $\Delta \leq \sqrt{\delta}$ up to an orbit length $L \sim \delta^{-1/2}$, i.e. that the length at which a true orbit and a numerical orbit in a chaotic flow separate goes as the inverse of the square root of the noise amplitude.

While it would be difficult to estimate the noise amplitude directly, the ratio of the noise amplitude of the new method to the noise amplitude of FC can be estimated as the square of the ratio of the arc length at which the FC orbit separates from the analytic orbit L_Δ^{FC} to the arc length L_Δ^{new} at which the new method trajectory separates from the analytic trajectory:

$$\frac{\delta^{new}}{\delta^{FC}} \sim \left(\frac{L_\Delta^{FC}}{L_\Delta^{new}}\right)^2 \approx 1.5 \times 10^{-4}. \tag{3.57}$$

Here the lengths L_Δ are determined by the value we choose for Δ that then specifies that deviation has occurred. The ratio of noise amplitudes are computed for approximately 10,000 particle initial positions distributed uniformly throughout the domain and chose $\Delta = 10^{-4}$. While, of course, an imperfect measure, the average noise amplitude for the new method is $O(10^{-4})$ times smaller than that for FC.

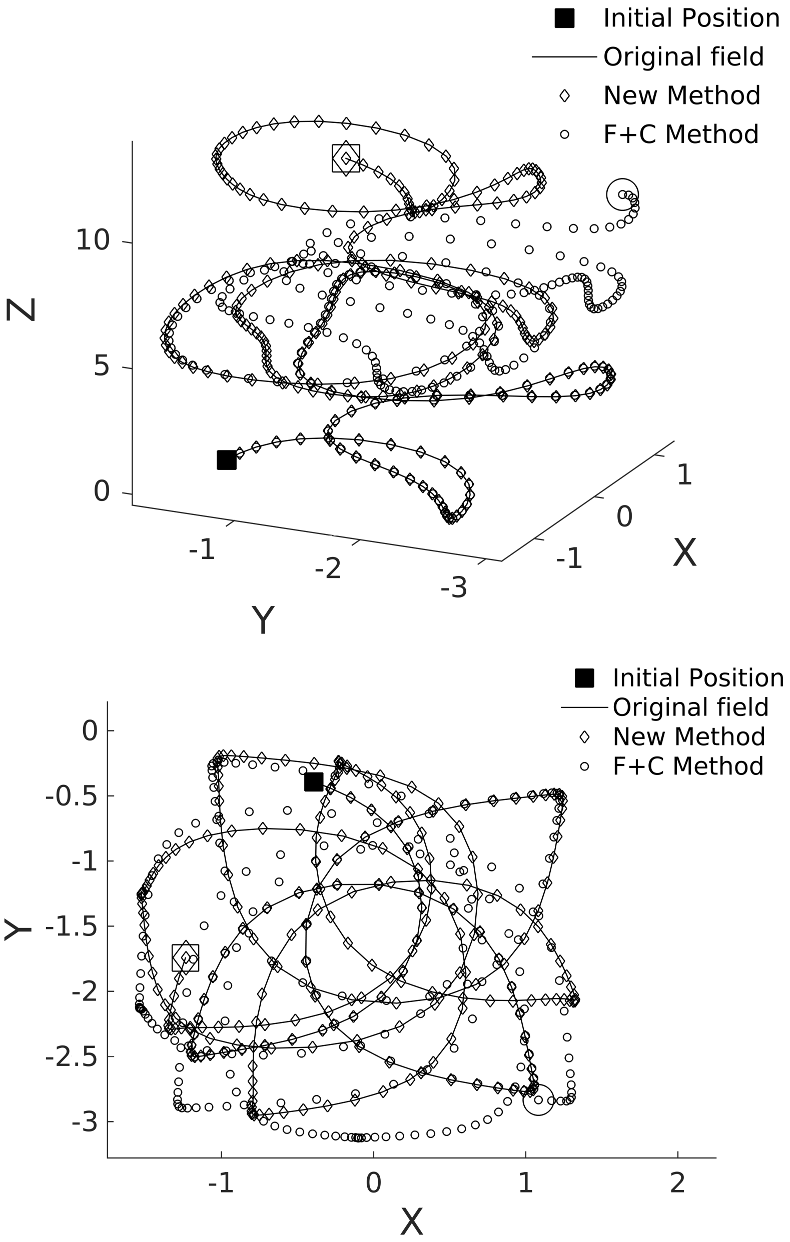

Figure 3.4: Lagrangian trajectories computed from the analytic velocity field (solid line), using the new interpolation method (diamond), and using FC method (circle). (top) Oblique view. (bottom) Top view. The solid square indicates the initial condition of all three orbits, while hollow square, big diamond and big circle trajectory's end for respectively the analytic, the new method and the FC orbits.

Another two test cases of this method, a steady 3D Taylor-Couette flow at a moderate Reynolds number (cylindrical coordinates) and the PRHF in the Stokes regime (spherical coordinates) can be found in Ravu *et al.* (2016).

3.3 Creating analytically divergence-free base flow velocity field of lid-driven hemisphere flow

In order to remove the singular coordinate from the interior of the domain that arises when $\sin\theta = 0$, we preferred the spherical domain $r \in [0,1]$, $\theta \in [0,\pi]$ and $\phi \in [0,\pi]$ over choosing $\theta \in [0,\pi/2]$ and $\phi \in [-\pi,\pi]$ where θ is the polar angle and ϕ is the azimuthal angle. The velocity field is calculated in cylindrical polar coordinates (v_r, v_θ and v_z) using the spectral-element/Fourier code *Semtex* (Blackburn and Sherwin, 2004). It is then interpolated spectrally onto a uniform grid with the grid points defining a uniform mesh in spherical polar coordinates(r,θ,ϕ) with $n_r = 100$, $n_\theta = 100$ and $n_\phi = 320$. The uniform grid is considered here because the method described in section 3.2 to calculate analytically divergence-free velocity field from discrete data requires the grid to be uniform. The interpolated cylindrical polar velocity field on this grid is then transformed to spherical polar velocity components (v_r, v_θ, v_ϕ). Contravariant velocity components (v^r,v^θ, v^ϕ) are computed via equation (3.54) as

$$v^r = r^2\sin(\theta)v_r \tag{3.58a}$$

$$v^\theta = r\sin(\theta)v_\theta \tag{3.58b}$$

$$v^\phi = rv_\phi \tag{3.58c}$$

with the Jacobian $J = r^2\sin(\theta)$.

3.3.1 Base flow in the Stokes regime

An advantageous gauge choice for this problem is $A_\phi = 0$. This choice ensures $v^\phi = 0$ everywhere on the $\phi = 0$ and $\phi = \pi$ planes on which hemisphere lid lies (see figure 2.1), which can be proved as follows. With $A_\phi = 0$, the velocity is

$$v^r = -\frac{\partial A_\theta}{\partial\phi}, \tag{3.59a}$$

$$v^\theta = \frac{\partial A_r}{\partial\phi}, \tag{3.59b}$$

$$v^\phi = \frac{\partial A_\theta}{\partial r} - \frac{\partial A_r}{\partial\theta} + \frac{\partial f}{\partial r}(r,\theta). \tag{3.59c}$$

We set $A_r(r,\theta,0) = 0$ and $A_\theta(r,\theta,0) = 0$ which makes $f(r,\theta) = 0$ in equation (3.59c) since $v^\phi(r,\theta,0) = 0$. From the fore-aft symmetry of the flow $v^\theta(r,\theta,\phi) = -v^\theta(r,\theta,\pi-\phi)$ which with equation (3.59b) implies that

$$A_r(r,\theta,\phi_{n_\phi}) = \int_{(r,\theta,0)}^{(r,\theta,\pi)} v^\theta d\phi = 0. \tag{3.60}$$

Similarly, from the fore-aft symmetry $v^r(r,\theta,\phi) = -v^r(r,\theta,\pi-\phi)$ which with equation (3.59a) implies that

$$A_\theta(r,\theta,\phi_{n_\phi}) = -\int_{(r,\theta,0)}^{(r,\theta,\pi)} v^r d\phi = 0. \tag{3.61}$$

At the end of this argument the gauge choice of $A_\phi = 0$ means that we can set $A_r(r,\theta,\phi_{n_\phi}) = 0$ and $A_\theta(r,\theta,\phi_{n_\phi}) = 0$ and simplify the computation. A_θ and A_r are computed as described in subsection 3.2.3.5 with the additional closure interpolation conditions listed in table 3.5.

Table 3.5: Interpolation conditions for the base flow in the Stokes regime.

Spline Direction	A_r	A_θ
ϕ	$A_r(r,\theta,\phi_0) = 0$ $A_r(r,\theta,\phi_{n_\phi}) = 0$	$A_\theta(r,\theta,\phi_0) = 0$ $A_\theta(r,\theta,\phi_{n_\phi}) = 0$
θ	$\frac{\partial^2 A_r}{\partial\theta\partial\phi}(r,\theta_0,\phi) = \frac{\partial^2 A_r}{\partial\theta\partial\phi}(r,\theta_{n_\theta},\phi)$ $\frac{\partial^2 A_r}{\partial\theta\partial\phi}(r,\theta,\phi_{n_\phi}) = \frac{\partial v_\theta}{\partial\theta}(r,\theta,\phi_{n_\phi})$	$\frac{\partial A_\theta}{\partial\theta}(r,\theta_0,\phi) = \frac{\partial A_\theta}{\partial\theta}(r,\theta_{n_\theta},\phi)$ $\frac{\partial A_\theta}{\partial\theta}(r,\theta_0,\phi) = 0$
r	$\frac{\partial^2 A_r}{\partial r\partial\phi}(r_0,\theta,\phi) = \frac{\partial v_\theta}{\partial r}(r_0,\theta,\phi)$ $\frac{\partial^2 A_r}{\partial r\partial\phi}(r_{n_r},\theta,\phi) = \frac{\partial v_\theta}{\partial r}(r_{n_r},\theta,\phi)$	$\frac{\partial A_\theta}{\partial r}(r_0,\theta,\phi) = 0$ $\frac{\partial A_\theta}{\partial r}(r_{n_r},\theta,\phi) = 0$

3.3.2 Base flow in the inertial regime

Because the fore-aft symmetry is absent in the inertial regime, equations (3.60) and (3.61) are not true and hence $A_r(r,\theta,\phi_{n_\phi}) \neq 0$ and $A_\theta(r,\theta,\phi_{n_\phi}) \neq 0$. We use the additional closure interpolation conditions listed in table 3.6 in the inertial regime.

Velocities are obtained, as usual, from the curl of a vector potential and particles advected using equation (3.54). MATLAB's ode45 is used to integrate fluid particle trajectories.

Table 3.6: Interpolation conditions for the base flow in the inertial regime.

Spline Direction	A_r	A_θ
ϕ	$A_r(r,\theta,\phi_0) = 0$ $\frac{\partial^2 A_r}{\partial\phi^2}(r,\theta,\phi_0) = \frac{\partial^2 A_r}{\partial\phi^2}(r,\theta,\phi_{n_\phi})$	$A_\theta(r,\theta,\phi_0) = 0$ $\frac{\partial^2 A_\theta}{\partial\phi^2}(r,\theta,\phi_0) = \frac{\partial^2 A_\theta}{\partial\phi^2}(r,\theta,\phi_{n_\phi})$
θ	$\frac{\partial^2 A_r}{\partial\theta\partial\phi}(r,\theta_0,\phi) = \frac{\partial^2 A_r}{\partial\theta\partial\phi}(r,\theta_{n_\theta},\phi)$ $\frac{\partial^2 A_r}{\partial\theta\partial\phi}(r,\theta,\phi_{n_\phi}) = \frac{\partial v_\theta}{\partial\theta}(r,\theta,\phi_{n_\phi})$	$\frac{\partial A_\theta}{\partial\theta}(r,\theta_0,\phi) = \frac{\partial A_\theta}{\partial\theta}(r,\theta_{n_\theta},\phi)$ $\frac{\partial A_\theta}{\partial\theta}(r,\theta_0,\phi) = 0$
r	$\frac{\partial^2 A_r}{\partial r\partial\phi}(r_0,\theta,\phi) = \frac{\partial v_\theta}{\partial r}(r_0,\theta,\phi)$ $\frac{\partial^2 A_r}{\partial r\partial\phi}(r_{n_r},\theta,\phi) = \frac{\partial v_\theta}{\partial r}(r_{n_r},\theta,\phi)$	$\frac{\partial A_\theta}{\partial r}(r_0,\theta,\phi) = 0$ $\frac{\partial A_\theta}{\partial r}(r_{n_r},\theta,\phi) = 0$

3.4 Calculating the period-1 line of PRHF in the Stokes regime

We know from section 2.3.2 that period-1 points exist in the PRHF only on the symmetry plane and also from section 2.3.4 that isolated periodic points (not part of periodic lines) can not exist in the Stokes regime of PRHF. This makes the search for period-1 lines easier.

As a starting point for determining the period-1 line, we first find the central fixed point, $(r,\theta,\phi) = (r_s,\pi/2,\pi/2)$ (see section 2.3.3). We know from the symmetry of the flow that this point will be on a line that goes from the origin $(0,\pi/2,\pi/2)$ to the base of the hemisphere $(1,\pi/2,\pi/2)$. On this line, v_ϕ changes sign and has a value of zero at the central fixed point. This fact and the bisection method is used to find r_s. Define a period-1 line (say P1) which goes through the central fixed point, and the period-1 line can be divided into two parts ($\mathrm{P1}_U$ and $\mathrm{P1}_L$), $\mathrm{P1}_U$ goes from the central fixed point to one

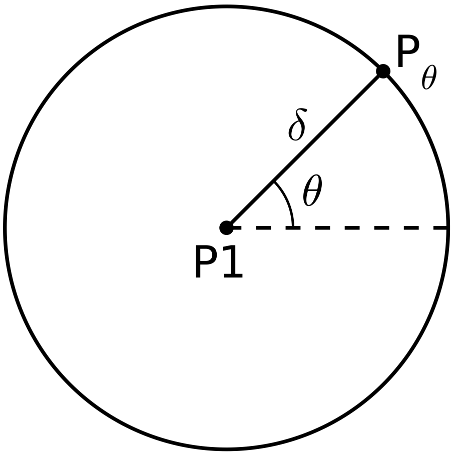

Figure 3.5: Circle centred at a period-1 point on symmetry plane S_Θ.

end, and $\mathrm{P1}_L$ goes from the central fixed point to the other boundary. We then compute the two parts of P1, ($\mathrm{P1}_U$, $\mathrm{P1}_L$) separately using the following methodology.

Choose a small increment, δ, and create a circle of radius δ centred around a known period-1 point on the symmetry plane (initially the central fixed point). The increment δ will be the distance between two consecutive period-1 points along P1. P1 intersects this circle at two points, and we choose an inital guess, P_θ (shown in figure 3.5). Because $\{\Phi_{\beta/2}(\boldsymbol{x}_{P1})\}_x = 0$ for a period-1 point $\boldsymbol{x}_{P1}$ (see figure 2.8a and figure 2.8b), the x–component (*i.e.* $\{\Phi_{\beta/2}(P_\theta)\}_x$) will change sign around the circle and will be zero where P1 intersects the circle. Again, we use the bisection method to find the value of θ at which P1 intersects the circle. We use this value of P_θ as the starting point for the next point on P1, and so on.

For all parameter values of Θ and β, we found that the $\mathrm{P1}_U$ part of period-1 line connects the central fixed point to the fixed point on the lid, and the $\mathrm{P1}_L$ part of period-1 line connects the central fixed point to the fixed point at the bottom of the hemisphere.

To compute period-1 lines other than the period-1 line which connect the three fixed points, we created a grid on the symmetry plane and used the grid points as an initial guess for Broyden's method (discussed in section 3.4.1) to search for any other period-1 points. We did not find any. We conclude that only one period-1 line exists.

3.4.1 Calculation of period-1 points using Broyden's method

To find period-1 points, a displacement function $\boldsymbol{G}(\boldsymbol{x})$ which returns the displacement vector of a particle after one time-period is defined as

$$\boldsymbol{G}(\boldsymbol{x}) = \boldsymbol{\Psi}(\boldsymbol{x}) - \boldsymbol{x}, \tag{3.62}$$

where $\boldsymbol{\Psi}$ is the time-periodic map of the PRHF (see section 2.2). Period-1 points of the PRHF are fixed points of the map $\boldsymbol{\Psi}$. At a period-1 point, $||\boldsymbol{G}(\boldsymbol{x})|| = 0$, because $\boldsymbol{\Psi}(\boldsymbol{x}) = \boldsymbol{x}$ at that point. The roots of the equation (3.62) are period-1 points of the PRHF and if they exist, can be found using Broyden's method. Broyden's method is a variant of Newton's method. To compute a period-1 point, an initial guess $\boldsymbol{x}_0$ is chosen and the next approximation to the period-1 point is obtained via equation (3.63).

$$\boldsymbol{x}_n = \boldsymbol{x}_{n-1} + \Delta\boldsymbol{x}_n, \tag{3.63}$$

where

$$\Delta\boldsymbol{x}_n = -\boldsymbol{J}_{\boldsymbol{n}}^{-1}(\boldsymbol{x}_{n-1})\boldsymbol{G}(\boldsymbol{x}_{n-1}), \tag{3.64}$$

where

$$\boldsymbol{J}_n = \boldsymbol{J}_{n-1} + \frac{\Delta \boldsymbol{G}_n - \boldsymbol{J}_{n-1}\Delta \boldsymbol{x}_n}{||\Delta \boldsymbol{x}_n||^2}\Delta \boldsymbol{x}_n^T. \tag{3.65}$$

This process is recursively done until $||\boldsymbol{G}(\boldsymbol{x}_n)||$ or $||\Delta \boldsymbol{x}_n||$ converges to the value 10^{-9}. If the convergence does not happen by 80 iterations, the process is terminated for that initial condition, and the code restarts with the next initial guess. During iterations, if an approximation point goes out of the fluid domain, the length of vector $\Delta \boldsymbol{x}_n$ is decreased until the point (i.e. $\boldsymbol{x}_n$ in equation (3.63)) stays inside the domain.

In Broyden's method, Jacobian ($\boldsymbol{J} = \frac{\partial \boldsymbol{G}}{\partial \boldsymbol{x}}$) is updated via equation (3.65) unlike in Newton's method where Jacobian is computed at every iteration. This improves the speed of the computation.

For Stokes flow, no extra period-1 points are found. For higher order periodic points of the Stokes flow and period-1 points of the inertial PRHF, the same method is used. At a period-n point, $\boldsymbol{\Psi}^n\boldsymbol{x} = \boldsymbol{x}$. To compute an n^{th} order periodic point, $\boldsymbol{G}(\boldsymbol{x})$ is replaced with $\boldsymbol{G}^n(\boldsymbol{x})$ in equations (3.64) and (3.65), although the calculations are carried out in the same way ($\boldsymbol{G}^n(\boldsymbol{x})$ is defined in equation (3.66)).

$$\boldsymbol{G}^n(\boldsymbol{x}) = \boldsymbol{\Psi}^n(\boldsymbol{x}) - \boldsymbol{x}. \tag{3.66}$$

3.5 Calculation of deformation tensor (or Jacobian) of the PRHF map

The nature of the stability of periodic points (or periodic lines) can be understood from the eigenvalues of the deformation tensor computed at them (see section 2.4). The deformation tensor of the map $\boldsymbol{\Psi} = (\Psi_1, \Psi_2, \Psi_3)$ at a point $\boldsymbol{x}^* = (x_1^*, x_2^*, x_3^*)$ is

$$\begin{aligned} \boldsymbol{F} &= \left.\frac{\partial \boldsymbol{\Psi}}{\partial \boldsymbol{x}}\right|_{\boldsymbol{x}=\boldsymbol{x}^*} \\ &= \begin{bmatrix} \frac{\partial \Psi_1}{\partial x_1} & \frac{\partial \Psi_1}{\partial x_2} & \frac{\partial \Psi_1}{\partial x_3} \\ \frac{\partial \Psi_2}{\partial x_1} & \frac{\partial \Psi_2}{\partial x_2} & \frac{\partial \Psi_2}{\partial x_3} \\ \frac{\partial \Psi_3}{\partial x_1} & \frac{\partial \Psi_3}{\partial x_2} & \frac{\partial \Psi_3}{\partial x_3} \end{bmatrix}_{\boldsymbol{x}=\boldsymbol{x}^*}. \end{aligned} \tag{3.67}$$

Because an analytical function of the map $\boldsymbol{\Psi}$ does not exist, the differentials in equation (3.67) are evaluated numerically by considering six points (two in the x direction, two in the y direction and two in the z direction) which are at a distance ϵ from the centre point. Finite differences are used to estimate the derivatives. The formula to compute approximations of the differentials in equation (3.67) is

$$\begin{bmatrix} \frac{\Psi_1(x_1^*+\epsilon,x_2^*,x_3^*)-\Psi_1(x_1^*-\epsilon,x_2^*,x_3^*)}{2\epsilon} & \frac{\Psi_1(x_1^*,x_2^*+\epsilon,x_3^*)-\Psi_1(x_1^*,x_2^*-\epsilon,x_3^*)}{2\epsilon} & \frac{\Psi_1(x_1^*,x_2^*,x_3^*+\epsilon)-\Psi_1(x_1^*,x_2^*,x_3^*-\epsilon)}{2\epsilon} \\ \frac{\Psi_2(x_1^*+\epsilon,x_2^*,x_3^*)-\Psi_2(x_1^*-\epsilon,x_2^*,x_3^*)}{2\epsilon} & \frac{\Psi_2(x_1^*,x_2^*+\epsilon,x_3^*)-\Psi_2(x_1^*,x_2^*-\epsilon,x_3^*)}{2\epsilon} & \frac{\Psi_2(x_1^*,x_2^*,x_3^*+\epsilon)-\Psi_2(x_1^*,x_2^*,x_3^*-\epsilon)}{2\epsilon} \\ \frac{\Psi_3(x_1^*+\epsilon,x_2^*,x_3^*)-\Psi_3(x_1^*-\epsilon,x_2^*,x_3^*)}{2\epsilon} & \frac{\Psi_3(x_1^*,x_2^*+\epsilon,x_3^*)-\Psi_3(x_1^*,x_2^*-\epsilon,x_3^*)}{2\epsilon} & \frac{\Psi_3(x_1^*,x_2^*,x_3^*+\epsilon)-\Psi_3(x_1^*,x_2^*,x_3^*-\epsilon)}{2\epsilon} \end{bmatrix}. \tag{3.68}$$

A value of $\epsilon = 10^{-6}$ was used in subsequent calculations. The stability of a period-1 point is obtained from the eigenvalues of the deformation tensor which is calculated using equation (3.68) by replacing $\boldsymbol{x}^*$ with the period-1 point. The eigenvalues of the deformation tensor are calculated using the Matlab function "eig".

Similarly, the stability of an n^{th} order periodic point can be obtained from the eigenvalues of the deformation tensor of the map $\boldsymbol{\Psi}^n$ at that point. The deformation tensor $\frac{\partial \boldsymbol{\Psi}^n}{\partial \boldsymbol{x}}\Big|_{\boldsymbol{x}=\boldsymbol{x}^*}$ of the map $\boldsymbol{\Psi}^n$ is calculated numerically using

$$\begin{bmatrix} \frac{\Psi_1^n(x_1^*+\epsilon,x_2^*,x_3^*)-\Psi_1^n(x_1^*-\epsilon,x_2^*,x_3^*)}{2\epsilon} & \frac{\Psi_1^n(x_1^*,x_2^*+\epsilon,x_3^*)-\Psi_1^n(x_1^*,x_2^*-\epsilon,x_3^*)}{2\epsilon} & \frac{\Psi_1^n(x_1^*,x_2^*,x_3^*+\epsilon)-\Psi_1^n(x_1^*,x_2^*,x_3^*-\epsilon)}{2\epsilon} \\ \frac{\Psi_2^n(x_1^*+\epsilon,x_2^*,x_3^*)-\Psi_2^n(x_1^*-\epsilon,x_2^*,x_3^*)}{2\epsilon} & \frac{\Psi_2^n(x_1^*,x_2^*+\epsilon,x_3^*)-\Psi_2^n(x_1^*,x_2^*-\epsilon,x_3^*)}{2\epsilon} & \frac{\Psi_2^n(x_1^*,x_2^*,x_3^*+\epsilon)-\Psi_2^n(x_1^*,x_2^*,x_3^*-\epsilon)}{2\epsilon} \\ \frac{\Psi_3^n(x_1^*+\epsilon,x_2^*,x_3^*)-\Psi_3^n(x_1^*-\epsilon,x_2^*,x_3^*)}{2\epsilon} & \frac{\Psi_3^n(x_1^*,x_2^*+\epsilon,x_3^*)-\Psi_3^n(x_1^*,x_2^*-\epsilon,x_3^*)}{2\epsilon} & \frac{\Psi_3^n(x_1^*,x_2^*,x_3^*+\epsilon)-\Psi_3^n(x_1^*,x_2^*,x_3^*-\epsilon)}{2\epsilon} \end{bmatrix}. \tag{3.69}$$

3.6 Calculation of higher order periodic lines of PRHF in the Stokes regime

To compute a period-n line with the method presented in this section requires an initial period-n point, which can be any point on that line. So, a period-n line is computed here in two steps: 1) calculate any one period-n point on the period-n line, 2) calculate the full period-n line using the initial period-n point. In chapter 4, the central role that degenerate points play in higher order periodicities will be discussed. Without going into detail here, these will provide a starting guess for higher order points. For example, n period-n lines intersect at an n^{th} order degenerate point on a period-1 line. This n^{th} order degenerate point cannot be used as an initial period-n point for all the n period-n lines to calculate them because this point belongs to all the lines. To calculate these n period-n lines, a separate initial period-n point for every period-n line is needed (i.e. total n initial period-n points). The n^{th} order degenerate point is used to calculate n initial period-n points which are needed for the calculation of n period-n lines. The initial n period-n points are calculated first as described in section 3.6.1, then the corresponding n period-n lines are calculated as described in section 3.6.2.

3.6.1 Finding n initial period-n points

- Compute an n^{th} order degenerate point on the period-1 line as described in section 4.3.1.
- Create a spherical grid of points which are almost equidistant from each other in a small sphere of radius 0.1 centred around the degenerate point. Because n period-n lines intersect at this degenerate point, this sphere contains segments of all the n period-n lines.
- Calculate the magnitude of the displacement function $\boldsymbol{G}^n(\boldsymbol{x})$ at each grid point from equation (3.66).
- Arrange the grid points as an array in ascending order of $||\boldsymbol{G}^n(\boldsymbol{x})||$, since smaller values of $||\boldsymbol{G}^n(\boldsymbol{x})||$ are closer to period-n lines, such points are good initial guesses for Broyden's method which is used to find n initial period-n points.
- The grid points which were sorted according to the magnitude of $\boldsymbol{G}^n(\boldsymbol{x})$ are then used one by one as initial guess for Broyden's method and initial period-n points are calculated.
- Continue finding period-n points from the grid points until at least one separate initial period-n point for every period-n line is found.
- From the computed period-n points, select one period-n point for each period-n line and use them as initial points to calculate n period-n lines as decribed in the next section 3.6.2.

3.6.2 Calculation of a period-n line using a known initial periodic point on that line

Assume Pn is a period-n line to be computed, and $\boldsymbol{x}_k$ is a known initial period-n point on that line. Pn is divided at the point $\boldsymbol{x}_k$ into two parts: Pn_L and Pn_R. These two parts are calculated separately in the same way as described below.

1. Compute the deformation tensor $\frac{\partial \boldsymbol{\Psi}^n}{\partial \boldsymbol{x}}\Big|_{\boldsymbol{x}=\boldsymbol{x}_k}$ at $\boldsymbol{x}_k$. Because the point $\boldsymbol{x}_k$ belongs to the period-n line, one of its eigenvalues of the deformation tensor (i.e. $\frac{\partial \boldsymbol{\Psi}^n}{\partial \boldsymbol{x}}\Big|_{\boldsymbol{x}=\boldsymbol{x}_k}$) will be one (say $\lambda_3 = 1$), and the eigenvector $\boldsymbol{e}_3$ corresponding to this eigenvalue is tangent to the period-n line (see section 2.4.1).
2. Compute eigenvector $\boldsymbol{e}_3$.

3. Choose $\boldsymbol{x}'_{k+1} = \boldsymbol{x}_k \pm \epsilon \boldsymbol{e}_3$ where sign is chosen to ensure $\boldsymbol{x}'_{k+1}$ is continuation of segment $\boldsymbol{x}_{k-1} \rightarrow \boldsymbol{x}_k$. $\epsilon = 5 \times 10^{-3}$ is used.

   Note: In the first iteration, to calculate $\boldsymbol{x}'_{k+1}$, minus sign is used in the calculation of Pn_L and plus sign is used in the calculation of Pn_R. The signs can be interchanged in the first iteration, but the important thing is different signs must be used in the calculation of Pn_L and Pn_R. This makes the search for periodic points of Pn_L and Pn_R line segments happen in opposite directions from the initial periodic point.

4. Create a sphere centred at $\boldsymbol{x}'_{k+1}$ with radius $\epsilon/5$ and search for the root of equation (3.66) inside the sphere using Broyden's method to find $\boldsymbol{x}_{k+1}$ which is the next period-n point on the line after $\boldsymbol{x}_k$. If the root is not found within the desired convergence value (10^{-9}), increase the radius of the sphere and do the same process again to find $\boldsymbol{x}_{k+1}$, and this process is continued until the root is found within the desired convergence value. This process will always find the root.

5. Continue steps (1) to (4) recursively to calculate period-n points along the line until the line touches the boundary or the line reaches the initial point if the periodic line is closed, because a periodic line can be closed or periodic line ends are attached to the hemisphere boundary (see section 2.3.4).

3.7 Calculation of isolated period-1 points of PRHF in the inertial regime

Time-reversal-reflection symmetry is broken in the PRHF in the inertial regime. Period-1 points can exist anywhere in the hemisphere domain unlike for Stokes flow where they exist only on the symmetry plane. To find period-1 points, a hemispherical grid of points in the entire hemisphere domain is created such that the distance between neighbouring grid points is roughly equal for all grid points. $|\boldsymbol{G}(\boldsymbol{x})|$ values (see equation 3.62) at all the grid points are evaluated, and the grid points are arranged in ascending order of their $|\boldsymbol{G}(\boldsymbol{x})|$ values. These grid points are then used as initial guess points for the Broyden's method (see section 3.4.1) to find period-1 points. Any repeated values of period-1 points from the Broyden's method are discarded. It is found that all the period-1 points are spatially located very close to the Stokes period-1 line when $Re \in (0, 1)$ and also the period-1 points are isolated, i.e. are not part of period-1 lines.

Since all the period-1 points are found spatially close to the Stokes period-1 line, the points of the Stokes period-1 line are considered as initial guess for the Broyden's method in later calculations of period-1 points in the inertial regime.

Chapter 4

Numerical Analysis of PRHF in Stokes Regime

Mixing devices often have spatial symmetry which manifests into an invariant of the flow. A flow with an invariant in three-dimensions is called an action-angle-angle flow (or one action flow). Without a proper understanding of global Lagrangian transport structures of the one action flows, efficient mixing is difficult to achieve. Numerical computation of Lagrangian structures is essential to understand fluid transport. How global Lagrangian structures organise in one action flows is not entirely known (Wiggins, 2010). In this chapter, it is shown how global Lagrangian structures are organized in one action flows and how to calculate them numerically using PRHF. The PRHF in the Stokes regime is a one action flow. In one action flows, fluid particles are constrained to move on two-dimensional surfaces which are sometimes called invariant surfaces (or level surfaces). In PRHF, the 2D invariant surfaces are closed, and they are topological spheres. The invariant surfaces are called just shells in this thesis. In one invariant flows, because isolated periodic points cannot occur (see section 2.3.4), periodic lines (all orders of periodic lines) and their manifolds constitute all of the Lagrangian structures.

4.1 Parameterization of periodic lines

To know the fluid transport on a shell, it is necessary to know all the periodic points (or periodic lines piercings) and their stability on the shell. Even after having calculated a periodic line numerically, it is difficult to infer from the plot how many times the periodic line pierces a particular shell. To know the number of periodic line piercings and their stability on any shell, the arc length along the periodic line from one of the ends of the periodic line is first defined. For example, on a period-1 line, arc length is calculated as the distance of a period-1 point along the period-1 line from the bottom point ($r = 1, \theta = \pi/2, \phi = \pi/2$). The shell number is a proxy for the action variable and is enumerated arbitrarily in such way that it has a value of one on the hemisphere and lid boundaries, and zero at the central fixed point (see section 2.3.5). One way to describe the periodic line is to enumerate the action variable along it as a function of arc length. If the line is also colour coded with the stability of each point (i.e. elliptic or hyperbolic) at the piercing site, this will help to understand the global transport of particles in this flow. The action-arc length plots are used in later sections to discuss the number of periodic line piercings on shells.

4.2 The Lagrangian skeleton

Generally, lower order periodic lines are more important than higher-order periodic lines. Period-1 line is the most important of all because it becomes the Lagrangian skeleton of the PRHF system. The PRHF system has two parameters, lid displacement β, and lid reorientation angle Θ. The advection of a fluid particle is obtained by the periodic map $\mathbf{\Psi}_{(\Theta,\beta)}$ (see equation 2.8). A period-1 line is a line of fixed points of the map $\mathbf{\Psi}$. It is shown in section 2.3.2 that PRHF can have period-1 lines only on the symmetry plane in Stokes regime. Three non-trivial period-1 points exists for all parameter values (see section 2.3.3): a period-1 point on the lid; a central stagnation point ($r = 0.258868$, $\theta = \pi/2$, $\phi = \pi/2$) and another stagnation point at the base of the hemisphere ($r = 1$, $\theta = \pi/2$ and $\phi = \pi/2$). When a numerical search for period-1 lines is employed, only one period-1 line is found on the symmetry plane for all the parameter values. It is concluded that for the Stokes PRHF there is only a single period-1 line that runs from the bottom stagnation point through the central stagnation point and attached at the lid on the symmetry plane. Period-1 lines are computed numerically using the method described in section 3.4 for various parameter values. Eigenvalues of deformation tensor of period-1 points are calculated numerically as described in section 3.5. The stability of a period-1 point is determined based on the eigenvalues of the deformation tensor evaluated at that point. From section 2.3.5, one of the eigenvalues of a period-1 point must be one. The other two eigenvalues determine the nature of that particular period-1 point (see section 2.4.1). In all the figures of the thesis, elliptic periodic points and elliptic periodic line segments are coloured blue, hyperbolic periodic points and hyperbolic periodic line segments are coloured red, and degenerate points are coloured green for easy identification. Wherever a period-1 line pierces a shell, it imparts its character (hyperbolic, elliptic, or degenerate) to the Hamiltonian motion on the shell in the neighbourhood of the piercing (Gómez and

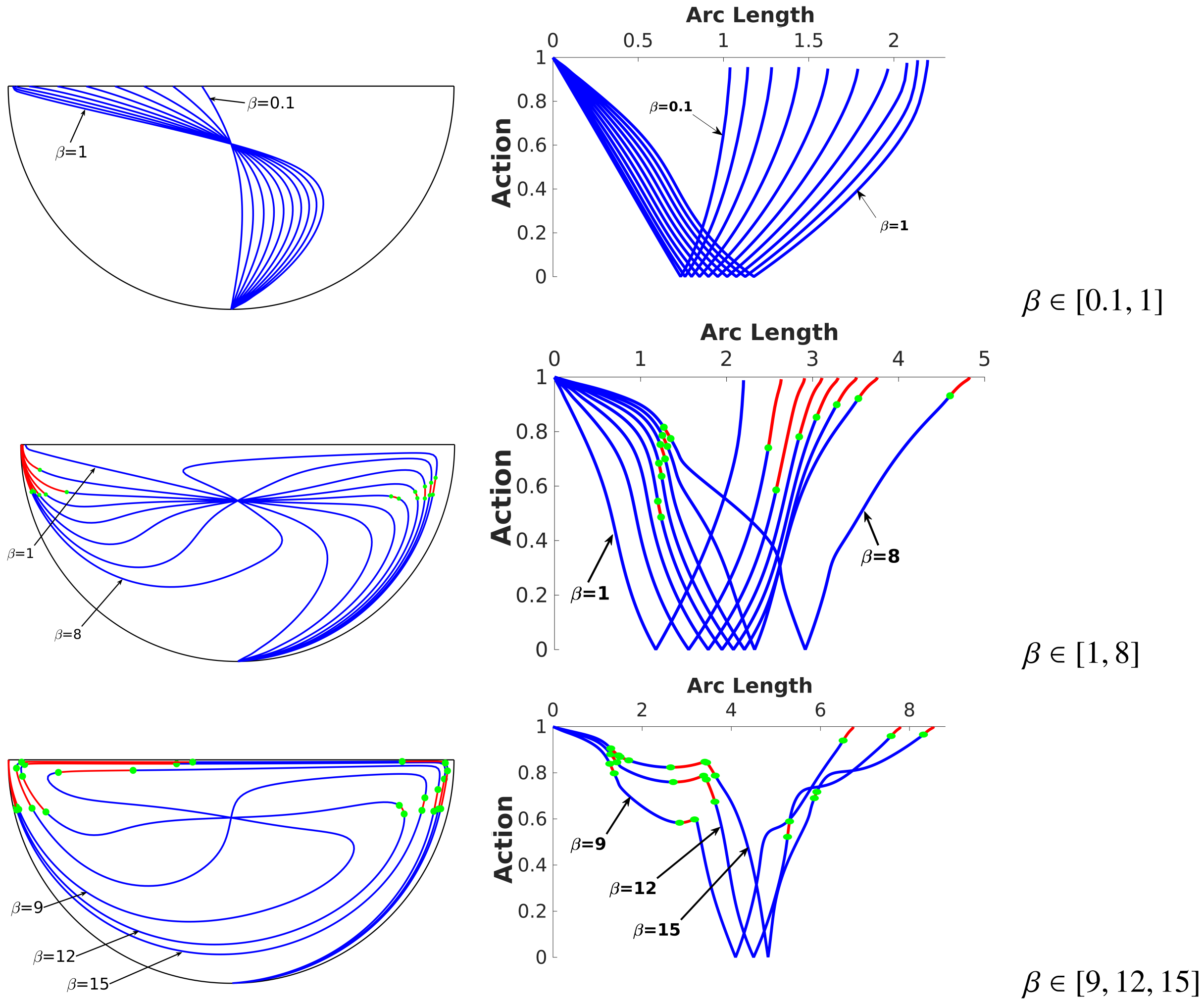

Figure 4.1: For $\Theta = \pi/4$ and indicated values of β, (left) period-1 lines viewed perpendicular to symmetry plane in normal space coordinates, and (right) the same lines parameterized by action and arc length along the line. Arc length is in units of radius. Blue (red) are elliptic (hyperbolic) segments.

Meiss, 2002). In the neighbourhood of an elliptic piercing point, particles move around the piercing on closed curves. In the neighbourhood of a hyperbolic piercing point, particles contract in one direction and expand in another direction. In the neighbourhood of a degenerate point, the net deformation is zero.

4.2.1 Example: Reorientation angle $\Theta = \pi/4$

To look at how the period-1 line changes with the parameters, $\Theta = \pi/4$ is considered in the analysis below, although the investigation has shown that different Θ values give qualitatively similar results. In the limit, $\beta \to 0$, all fluid particles rotate about the y axis like a rigid body rotation, and their orbits stay on invariant circles. The centres of these invariant circles form a stagnation line which runs through the y axis. The stagnation line can also be considered as a period-1 line. Period-1 lines on the symmetry plane for values of β from 0.1 to 1 (top), 1 to 8 (middle), and 9,12 and 15 (bottom) are shown in figure 4.1 (Left side) . The equivalent period-1 lines parameterised by action (shell number) and arc length are seen in the right-hand column of Figure 4.1. Period-1 lines are coloured according to their local characters in figure 4.1.

From figure 4.1, it is seen that the tangent to a period-1 line at the central stagnation point rotates anti-clockwise with increasing β. As β increases from 0, the end of the period-1 line which is attached to the lid moves toward the hemisphere boundary and stops at the rim when β reaches a particular value β_c (see section 2.3.3). The period-1 line ending at the rim then stays there for all β values greater than β_c. The other end of the period-1 line is fixed at the bottom of the hemisphere. Because both the ends of period-1 lines are fixed for a given β and the tangent to the period-1 line at the central stagnation point rotates anti-clockwise with increasing β, the length of period-1 line must increase with increasing β, as seen in the extent of the x axis in figure 4.1(right). As the rotation occurs at the central stagnation point, the period-1 line is pushed towards the boundary. Because the ends of the period-1 line are attached to the boundaries and the line passes through the central stagnation point, every shell will be pierced at least twice. For $\beta = 0$ to 8, the shell number changes monotonically with arc length from the outermost shell at the base (value 1) to the central fixed point (value 0) and then from the central fixed point to the outermost shell at the top (value 1 again). Thus each shell is pierced twice for $\beta \lessapprox 8$. For $\beta \gtrapprox 8$, the shell number no longer changes monotonically with arc length along the period-1 line. Between $\beta = 8$ and 9 a "wiggle" appears on the period-1 line segment in which some shells are now pierced four times, i.e. action vs arc length is no longer monotonic from the centre to the boundary. For each wiggle two local extrema arise, one minimum, one maximum and all shells between these two extrema have two additional piercings. As β increases still further, the period-1 line becomes increasingly convoluted, rolling up around the central fixed point. As a consequence, additional wiggles are created that may cause shells to have more than two additional piercings on some shells.

An example with $\beta = 16$ is now provided that shows, how period-1 points on shells connect via manifolds and how the manifolds govern the fluid transport by considering a few shells, and how some of the topologies of invariant surfaces can be simply and quickly understood from the plot of shell number versus arc length. A period-1 line on the symmetry plane is shown in figure 4.2 for $\beta = 16$, and the corresponding action-arc length plot of the period-1 line is shown in figure 4.3. The shells a_2, a_{3T}, a_4, a_{5T} and a_6 shown in figure 4.3 provide representative examples of the different transport structures that come from the period-1 piercings on these shells. The shells have been chosen to have a different number of piercings and different piercing characters. In the subscript of

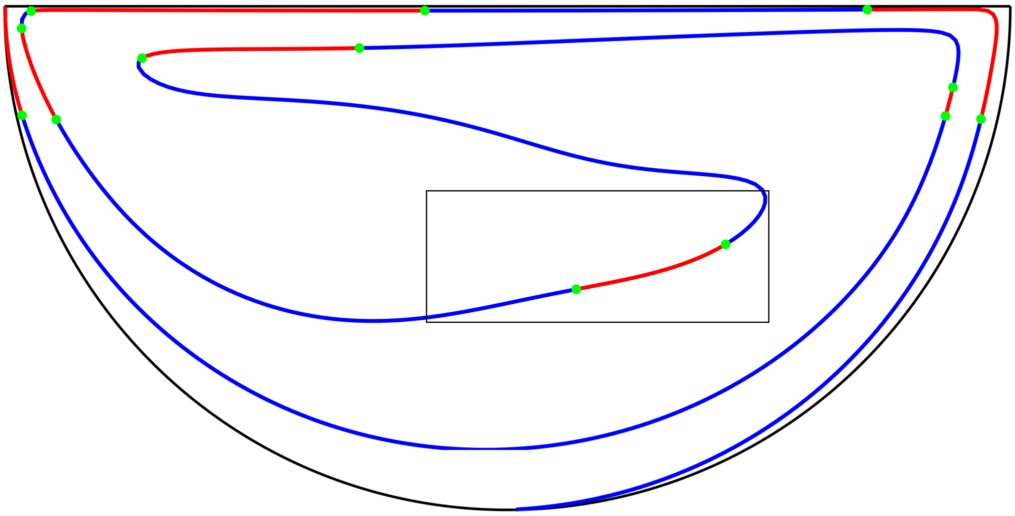

Figure 4.2: Period-1 line on symmetry plane for $\beta = 16$ and $\Theta = \pi/4$.

the shell labelling, the number represents the number of period-1 points and "T" means a tangency of the curve to a shell in this plot. The Poincaré section on each of these shells is shown in detail in Figures 4.4 to 4.8. In all these figures, yellow spheres represent the central stagnation point; green spheres represent degenerate points of either first order or second order (see section 2.4.1).

All shells with shell number values less than a_{3T} have a similar topology with two elliptic piercings as shown in Figure 4.4. On the Poincaré map of shell a_2 shown in figure 4.4, two sets of topological concentric circles is noticed, and fluid particles orbits are restricted to stay on these circles. The Poincaré map of shell a_{3T} is shown in figure 4.5, and it has two elliptic piercings and one first-order degenerate point (or parabolic point). In this figure, no deformation is noticed in the neighbourhood of the degenerate point (green sphere), particles orbits staying on topological concentric circles are noticed in the neighbourhood of elliptic points. In fluid particles orbits away from the period-1 point piercings shown in this figure, some stay on closed loops, and some form higher-order islands. The Poincaré map of shell a_6 is shown in figure 4.6, and it has two homoclinic connections with four elliptic piercings and two hyperbolic piercings. Each homoclinic connection has two elliptic and one hyperbolic piercing points, and fluid particles orbits inside the homoclinic connection stay on topological concentric circles. In fluid particles orbits outside the homoclinic connections shown in this figure, some stay on closed loops, and some form higher-order islands. The Poincaré map of shell a_{5T} is shown in figure 4.7, and it has three elliptic, one hyperbolic and one degenerate piercing points. In this figure, a homoclinic connection of the hyperbolic point is seen. The Poincaré map of shell a_4 is shown in figure 4.8, and it has three elliptic and one hyperbolic piercing points. In this figure, a homoclinic connection of the hyperbolic point is seen.

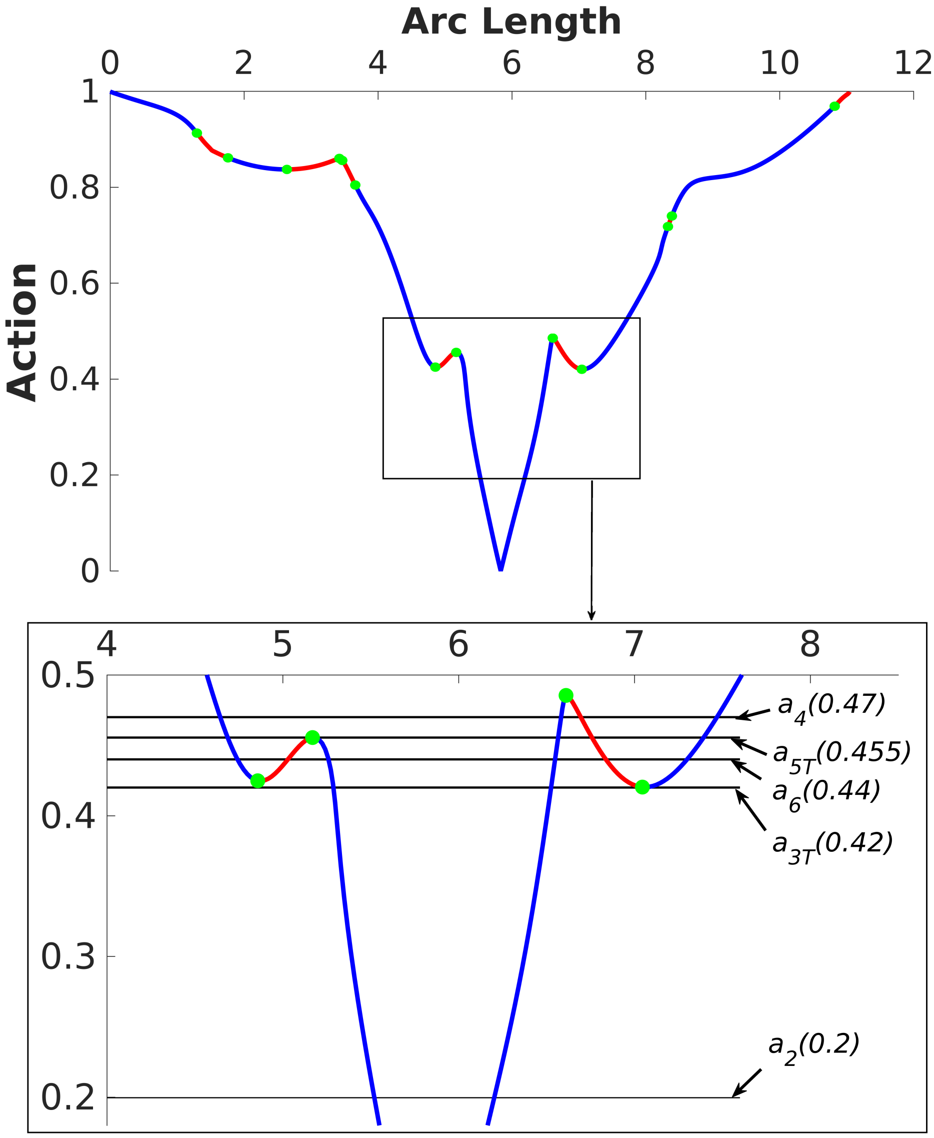

Figure 4.3: Action and arc length along the period-1 line for $\beta = 16$ and $\Theta = \pi/4$. The lower figure is a close-up of the region inside the rectangle in the upper figure in which five different shells are defined corresponding to different numbers and types of piercings by the period-1 line.

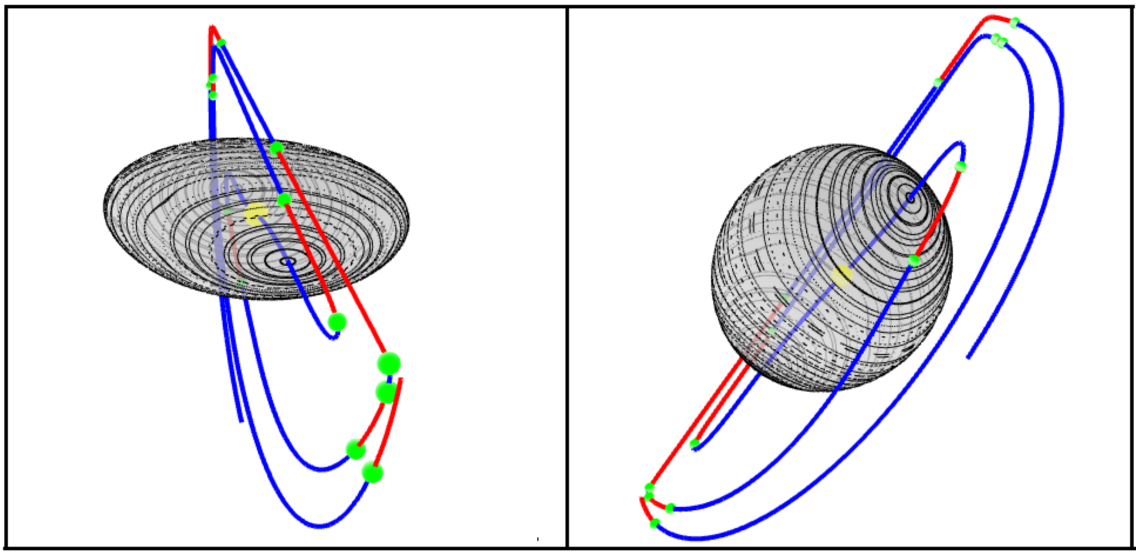

Figure 4.4: Poincaré map of shell a_2 with two elliptic points (shell number 0.2); Left is top-front view, right is bottom view.

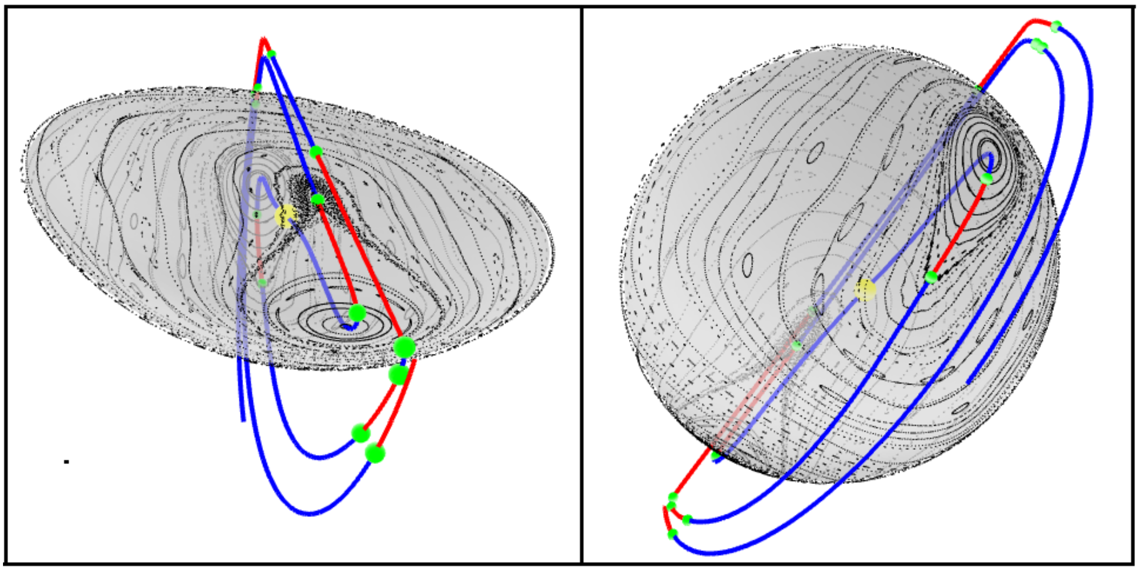

Figure 4.5: Poincaré map of shell a_{3T} with two elliptic points, and one parabolic point (shell number 0.42); Left is top-front view, right is bottom view.

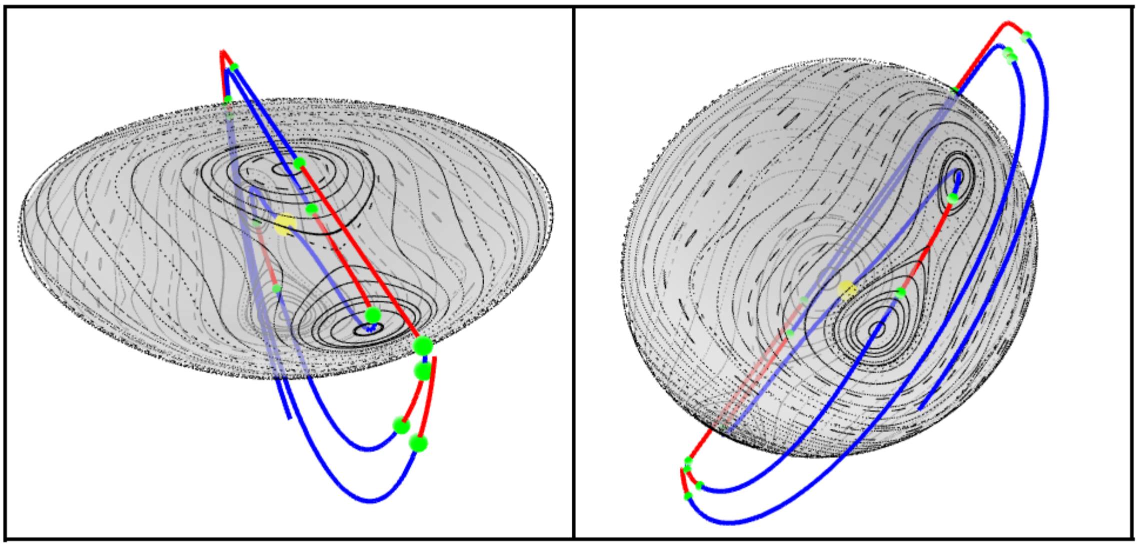

Figure 4.6: Poincaré map of shell a_6 with four elliptic points and two hyperbolic points (shell number 0.44); Left is top-front view, right is bottom view.

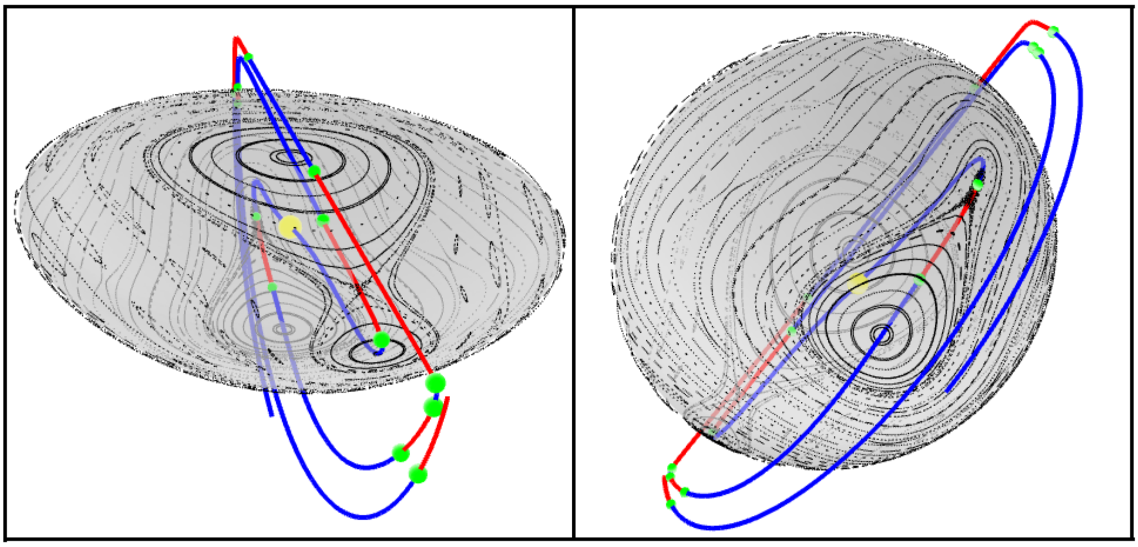

Figure 4.7: Poincaré map of shell a_{5T} with three elliptic points, one hyperbolic point and one parabolic point (shell number 0.4555); Left is top-front view, right is bottom view.

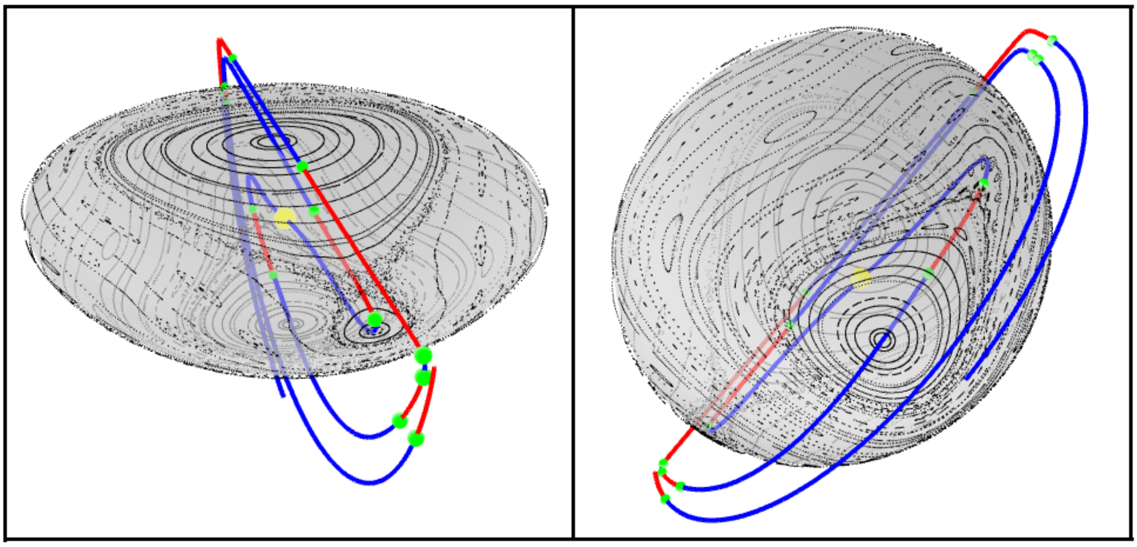

Figure 4.8: Poincaré map of shell a_4 with three elliptic points and one hyperbolic point (shell number 0.47); Left is top-front view, right is bottom view.

4.2.2 Effect of reorientation angle on period-1 lines

The reorientation angle can be written as $\Theta = 2\pi/n$, where n can be even, odd or irrational. Numerical computation of period-1 lines found no qualitative difference in Lagrangian structures whether n is even or odd or irrational. For $\beta = 8$ and $\Theta = \{2\pi/16, 2\pi/11, 2\pi/8\}$, action vs arc length of period-1 lines are shown in figure 4.9. It is noted from the figure 4.9 that, for a fixed β value, as Θ decreases, the length of the period-1 line increases. As the length of period-1 line increases, the number of period-1 piercings on some shells increases, which in turn increases the complexity of the Lagrangian structures on those shells. Hence, the complexity of the Lagrangian structures increases as Θ decreases while keeping β fixed or as β increases while keeping Θ fixed (see section 4.2.1. Because the length of the period-1 line increases either with decreasing Θ or with increasing β, β needs to be increased monotonically with reorientation angle to observe the appearance of first wiggle as shown in figure 4.10.

A period-1 line and three different shells with Poincaré section for a particular example is shown in figure 4.11. The organisation of fluid transport in the neighbourhood of period-1 piercings is determined by the stability of the period-1 piercing points. The entire transport structures on these shells look complicated in this figure. In the next section, how the degenerate points on periodic lines organise the complete Lagrangian structures in one-invariant volume-preserving flows is presented which will show how the seeming complexity of figure 4.11 arises from a hierarchical application of simple principals.

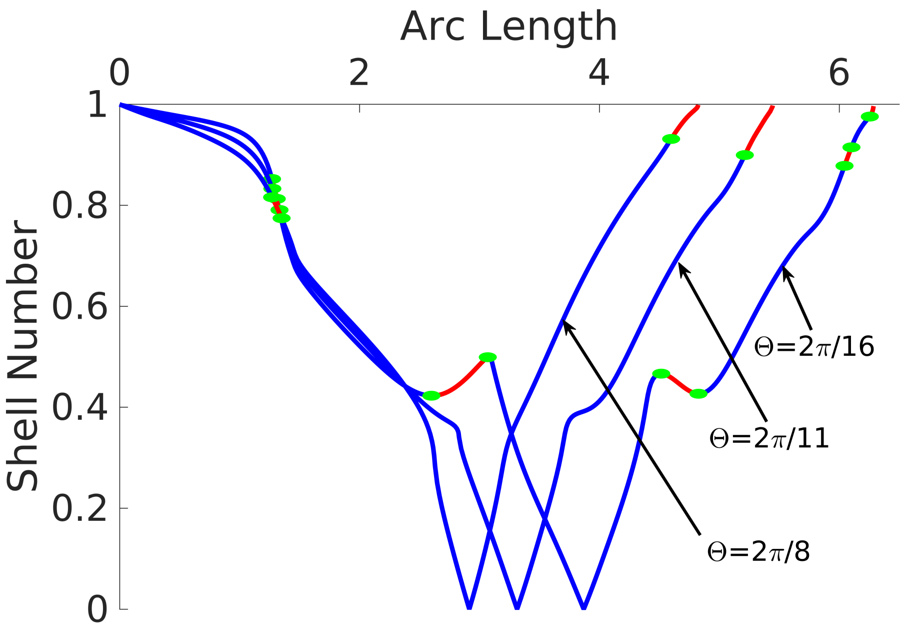

Figure 4.9: Action and arc length along period-1 lines for $\beta = 8$, and $\Theta = 2\pi/8, 2\pi/11$ and $2\pi/16$

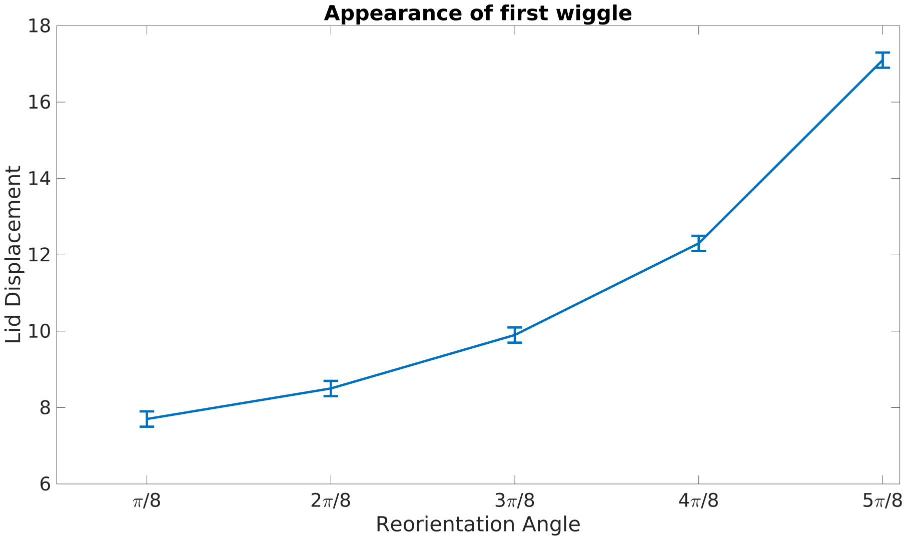

Figure 4.10: Appearance of a first wiggle as function of Θ and the corresponding β value at appearance. The corresponding β value lies within the error bar.

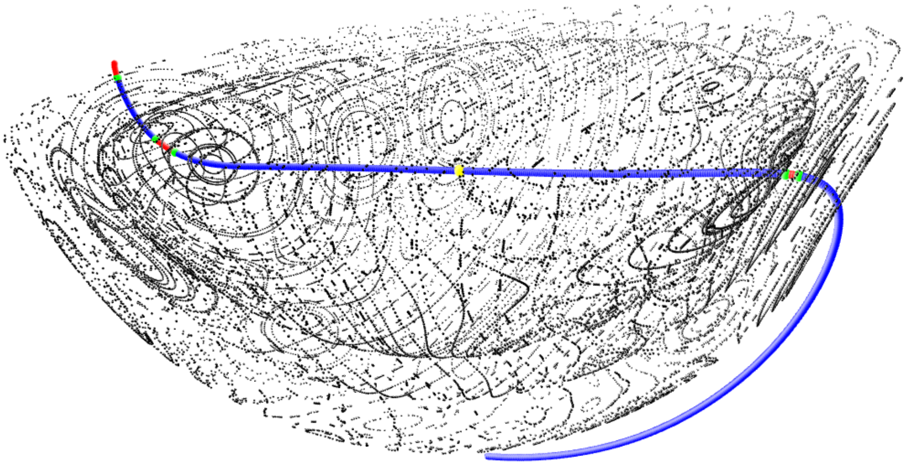

Figure 4.11: Period-1 line and Poincaré maps of flow on several shells. Oblique view.

4.3 Resonances in one invariant flows

In bifurcation theory, the topology of a dynamical system changes as the parameter of the system goes through a bifurcation point (or critical point) (Kuznetsov, 1998). A type of bifurcation points is found in the PRHF, that, in the shell normal direction at degenerate points, the local topology changes. This behaviour can be viewed in terms of classical planar bifurcation theory by establishing an analogy between the PRHF and a 2D system in classical planar bifurcation theory. Because the fluid particles move on nested spheroids, nested spheroids can be considered as the direct product of a two-dimensional phase space (angle variables θ_1, θ_2) and a parameter space (action variable I). Using this concept, a three-dimensional PRHF can be reduced to a two-dimensional system with a parameter. The phase space variables of the two-dimensional system are $\boldsymbol{\theta}(\theta_1, \theta_2)$, and the parameter of the system is I. Whenever I goes through a degenerate point, the local topology changes.

Degenerate points are called resonance points in classical planar bifurcation theory (Kuznetsov, 1998). The resonance bifurcations are local bifurcations because these bifurcations occur in the neighbourhood of periodic points (or fixed points). It is found that, at degenerate points, lower order periodic lines and higher order periodic lines intersect. For example, on a period-1 line, n period-n lines pass through a 1:n resonance point (or n^{th} order degenerate point) except for 1:1 and 1:2 resonance points. Period-1 line is tangent to an invariant surface at 1:1 resonance. A period-2 line passes through a 1:2 resonance point on a period-1 line. The reason only one period-2 line exists at a 1:2 resonance point instead of two period-2 lines is discussed in section 4.3.3. Similar to resonance points on period-1 lines, resonance points can also exist on higher-order periodic lines. An analogy can be made between resonance points on a period-1 line to resonance points on a higher order periodic line in the following way. A period-m line of map $\mathbf{\Psi}$ can be considered as a period-1 line of map $\mathbf{\Psi}^m$. This way, resonance points on the period-m line are treated as resonance points on a period -1 line but with the map $\mathbf{\Psi}^m$. In general, on a period-m line, m:p resonance points exist, where $p > m$ and $p = m \times n$, where n is a positive integer. n $(= p/m)$ period-p lines intersect at the m:p resonance point on the period-m line. Resonances such as 2:3 can not occur, because a point simultaneously cannot be a period-2 and period-3 point. Although 2D behaviour associated with periodic lines was noted in Malyuga *et al.* (2002) and Pouransari *et al.* (2010), the consequences of the degenerate points was not fully explored. Smith *et al.* (2016) discussed a detailed analysis of a 1:3 resonance in their flow but did not discuss general m:p resonances.

By identifying the resonance points on a lower order periodic line, all the higher-order periodic lines which intersect at the corresponding resonance points on the lower order periodic line can be calculated. Because higher-order periodic lines intersect at a resonance point on a lower order periodic line, the resonance point is identified first, and then the higher order periodic lines are calculated using the method discussed in section 3.6. The significance of the resonance points is that the three-dimensional one invariant flows can be completely understood hierarchically by finding the resonance points on the period-1 line first, and then computing the corresponding higher-order periodic lines, this process can be recursively pursued by finding higher order resonance points on the period-2 line and so on. In other words, we can keep finding extended structures starting with period-1 lines until enough Lagrangian transport structures are uncovered for any given purpose. Although the resonance points can be identified on a periodic line of any order and calculate corresponding higher periodic lines, the analysis of resonance bifurcation points is restricted mainly to period-1 lines in this thesis. To demonstrate resonance points on higher-order periodic lines, an example of a 2:6 resonance is presented in section 4.3.6.

4.3.1 Identification of resonance points on a period-1 line

To calculate higher-order periodic lines extending from a resonance point on a lower-order periodic line, it is necessary to identify the resonance point on the lower-order periodic line. The identification of resonance points on a period-1 line is described in this section. The method described here is applicable to resonance points on higher-order period lines also. Define the eigenvalues of the deformation tensor computed at a period-1 point as λ_1, λ_2 and λ_3. Because the action variable is a conserved quantity, λ_3 can be chosen to be one as shown in section 2.4.1. Because the flow on an invariant surface is area-preserving, the product $\lambda_1 \lambda_2 = 1$. The eigenvalues λ_1 and λ_2 can be real positive as

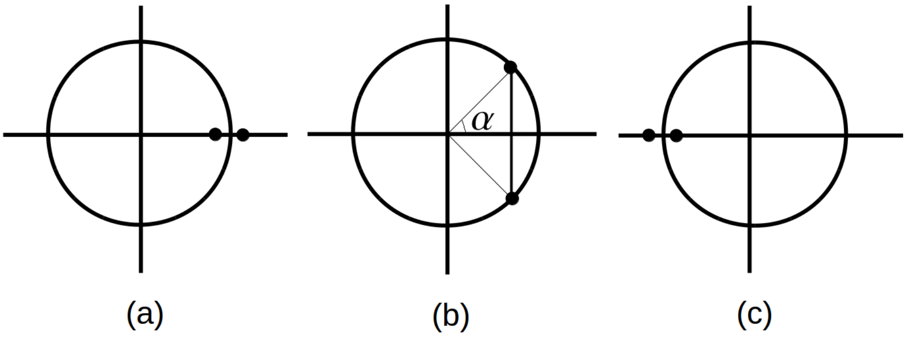

Figure 4.12: Possible eigenvalues (λ_1 and λ_2) shown with the unit circle on complex plane for period-1 points; $\lambda_3 = 1$, which is not shown here.

shown in figure 4.12(a), or real negative as shown in figure 4.12(c), or complex values ($e^{\pm i\alpha}$) as shown in figure 4.12(b). The local rotaion angle is α.

At an n^{th} order degenerate point on the perid-1 line (1:n resonance point), $F^n = I$, where F is the deformation tensor (or Jacobian). $F^n = I$ implies $\lambda_1^n = 1$, $\lambda_2^n = 1$ and $\lambda_3^n = 1$. The eigenvalues of deformation tensor at an n^{th} order degenerate point are $\lambda_3 = 1$ and $\lambda_{1,2} = e^{\pm i(2\pi/n)}$. The local rotation α at the n^{th} order degenerate point,

$$\alpha = \frac{2\pi}{n}. \tag{4.1}$$

The trace of the deformation tensor F at an n^{th} order degenerate point is obtained via

$$\mathrm{Tr}\, F = 1 + 2\cos(2\pi/n), \tag{4.2}$$

where n is the order of the degeneracy. Eigenvalues, the local rotation angle and the trace values of the deformation tensor of resonance bifurcation points on periodic lines are given in table 4.1. Eigenvalues λ_1 and λ_2 (so does trace values) change continuously along a period-1 line. The trace of the deformation tensor of a period-1 point on a period-1 line is obtained via equation (4.2), and is

$$\mathrm{Tr}\, F = 1 + \lambda_1 + \lambda_2. \tag{4.3}$$

Because the trace values of resonance points are known, we can identify them on a period-1 line by computing the trace values. After identifying resonance points, the corresponding higher-order periodic lines can then be obtained using the method discussed in section 3.6. Similarly, resonance points on higher-order periodic lines (period-2 and above) are also identified in the same way. For example, to identify resonance points on a period-2 line, trace values on the period-2 line points are calculated with the map

Table 4.1: Resonances, and their corresponding eigenvalues and trace values on periodic lines; $\lambda_3 = 1$ for each periodic point

λ_1	λ_2	α	Trace	Period-1 line ($\mathbf{\Psi}$)	Period-2 line ($\mathbf{\Psi}^2$)	$\dots$	Period-m line ($\mathbf{\Psi}^m$)
1	1	0	3	1:1	2:2	$\dots$	m:m
-1	-1	π	-1	1:2	2:4	$\dots$	m:$2m$
$-\frac{1}{2} + \frac{\sqrt{3}}{2}i$	$-\frac{1}{2} - \frac{\sqrt{3}}{2}i$	$2\pi/3$	0	1:3	2:6	$\dots$	m:$3m$
i	$-i$	$\pi/2$	1	1:4	2:8	$\dots$	m:$4m$
$\vdots$	$\vdots$	$\vdots$	$\vdots$	$\vdots$	$\vdots$	$\vdots$	$\vdots$
$e^{i(2\pi/n)}$	$e^{-i(2\pi/n)}$	$2\pi/n$	$1 + 2\cos(\frac{2\pi}{n})$	1:n	2:$2n$	$\dots$	m:$n \times m$

$\mathbf{\Psi}^2$ and identified them as given in table 4.1. Although an infinite number of resonances are possible corresponding to every root of unity because resonances higher than order 4 (i.e. $n \geq 5$) are expected to have subharmonic bifurcation solutions only when exceptional conditions hold (Gelfreich, 2002), the analysis here is restricted to the first four resonances (1:1, 1:2, 1:3 and 1:4) that will generally be encountered. In classical planar bifurcation theory the first four resonances are collectively named the strong resonances.

4.3.2 1:1 Resonance (Fold bifurcation)

At a 1:1 resonance point, the eigenvalues $\lambda_1, \lambda_2, \lambda_3$ are all one, and the local rotation angle is zero. The net deformation here after one period (or one time application of the map $\mathbf{\Psi}$) is zero. The resonance point is a first order degenerate point. The period-1 line changes its characteristics from elliptic to hyperbolic (or hyperbolic to elliptic) across this degenerate point. The eigenvalues λ_1 and λ_2 change from complex to real (or real to complex).

A period-1 line on the symmetry plane for $\Theta = \pi/4$ and $\beta = 16$ is shown in figure 4.2. To demonstrate the effect of 1:1 resonance points on fluid transport, a segment of the period-1 line shown inside the box on figure 4.2 is considered. The trace vs arc length in this box are shown in figure 4.13. The two points which have a trace=3 can be seen in this figure to occur at points that coincide with extrema in action. "Local extrema" on the action vs arc length occurs when the period-1 line is tangent to an invariant shell at the 1:1 resonance point (can also be considered to be where a period-1 line "folds" over). For a planar bifurcation the 1:1 corresponds to a fold singularity in the parameter space. Here, it's a literal fold of a curve in real space. In this period-1 line segment, the period-1 line goes from elliptic to hyperbolic through a 1:1 resonance point and hyperbolic to elliptic through another 1:1 resonance point. In the PRHF, it is observed that 1:1 resonance

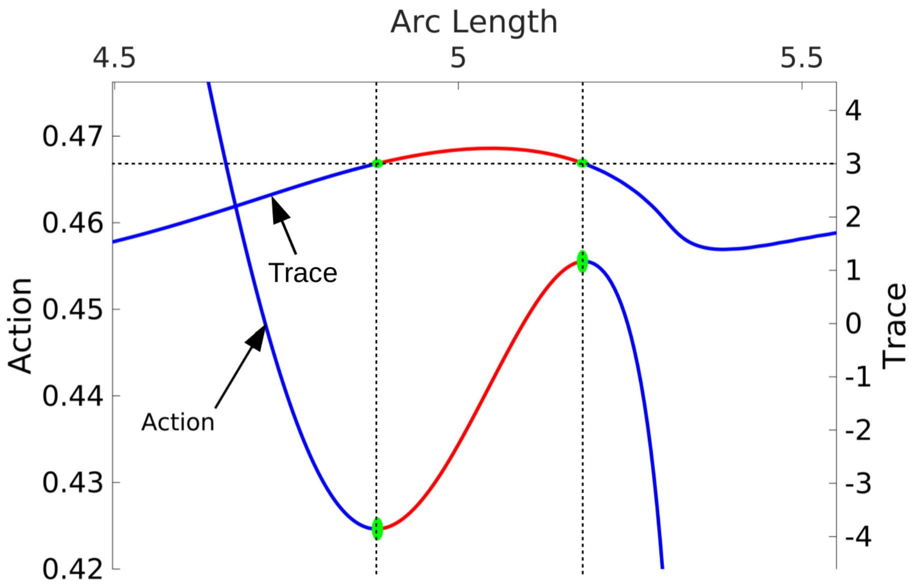

Figure 4.13: Action and Trace values of period-1 points along the segment of the period-1 line inside rectangular box in figure 4.2

points always occur in pairs, and the pair of 1:1 resonance points are always connected through a hyperbolic segment, forming a wiggle like structure as shown in the action vs arc length plot as seen in figure 4.13. The local Poincaré sections on the invariant surfaces corresponding to the 1:1 resonance points are shown in figure 4.14, in which the shell-normal coordinate is stretched for clarity. The upper and lower sections contain a degenerate point and an elliptic point, and the middle section contains a hyperbolic point and two elliptic points. The stable and unstable manifolds of hyperbolic point of the middle section have homoclinic orbits.

4.3.3 1:2 Resonance

At 1:2 resonance point a period-2 line intersects the period-1 line. At a 1:2 resonance point, the eigenvalues are $\lambda_1 = \lambda_2 = -1$ and $\lambda_3 = 1$, and the local rotation angle is π. The net deformation at a 1:2 resonance point is zero after two periods. The stability of period-1 points on the period-1 line changes at the 1:2 resonance point from elliptic to hyperbolic (or hyperbolic to elliptic), and the resonance occurs when the eigenvalues (λ_1, λ_2) change from complex to real negative (or real negative to complex).

The 1:2 resonance is described with an example of $\Theta = \pi/4$ and $\beta = 2$. The period-1 line on the symmetry plane for $\Theta = \pi/4$ and $\beta = 2$ is shown in figure 4.15(a). The action and trace values of the period-1 line are shown in figure 4.15(b). In this figure, the 1:2 degenerate point coloured green has a trace value of -1 (see table 4.1). The change of stability of the period-1 line at a 1:2 degenerate point is also seen in figure4.15(b). The

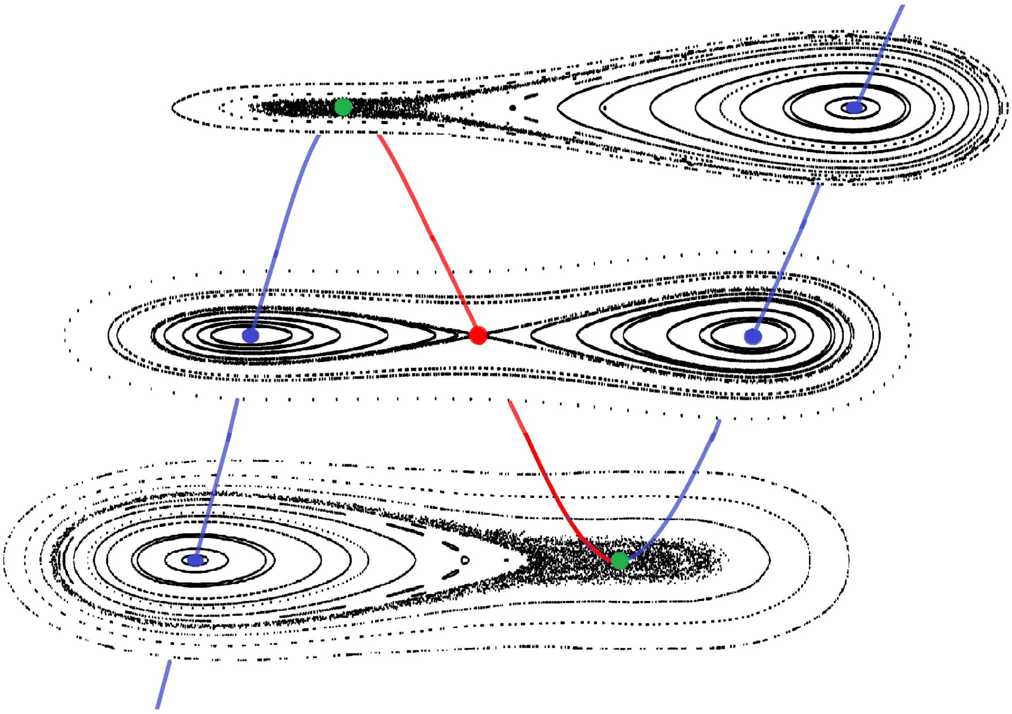

Figure 4.14: A close up of the segment of the period-1 line inside the rectangular box in Figure 4.13 (a). Also plotted are local Poincaré sections on three neighbouring shells. The upper and lower sections correspond to shells containing degenerate points and the middle section is on a shell half way between. Note that the shell-normal coordinate has been expanded for clarity.

period-2 line which goes through the 1:2 resonance point is computed numerically using the method discussed in section 3.6. The period-1 (P1) and period-2 (P2) lines are shown in figure 4.16. Action values on the period-1 line and period-2 line are plotted against their arc lengths in figure 4.17. The arc length of P1 and P2 lines are shifted so that at a 1:2 resonance point, the arc length is zero. From figure 4.17, we observe that the period-2 line is symmetric about the symmetry plane and the period-2 line ends are attached to the boundary of the hemisphere. The local Poincaré sections corresponding to a 1:2 resonance point of the period-1 line is shown in figure 4.18. The shell-normal coordinate is stretched in the figure 4.18. The lower section with an action value 0.7583 contains a 1:2 degenerate point and the upper section with an action value 0.7692 contains one period-1 hyperbolic point and two period-2 elliptic points. All the piercing sites on sections are shown with solid spheres, blue spheres for elliptic points, red spheres for hyperbolic points, and a green sphere for degenerate point. The stable and unstable manifolds of the hyperbolic point on a period-1 line have homoclinic orbits (see figure 4.18).

The reason a single period-2 line passes through a second order degenerate point instead of two period-2 lines is discussed in the following. In general, a chain of n period-n elliptic islands appear on an invariant surface in the neighbourhood of an n^{th} order

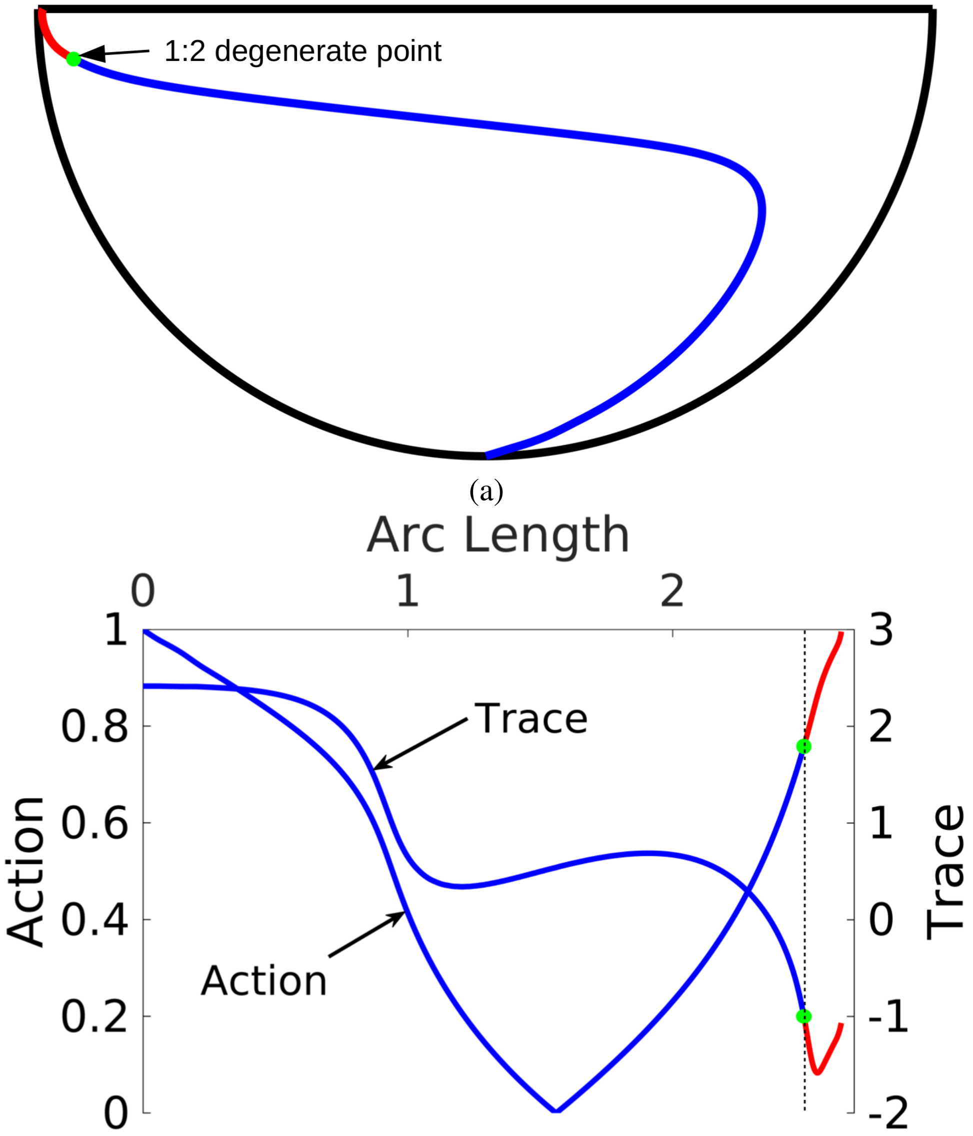

(a)

(b)

Figure 4.15: (a) Period-1 line for $\beta = 2$ and $\Theta = \pi/4$ on symmetry plane. (b) Action and trace along the period-1 line

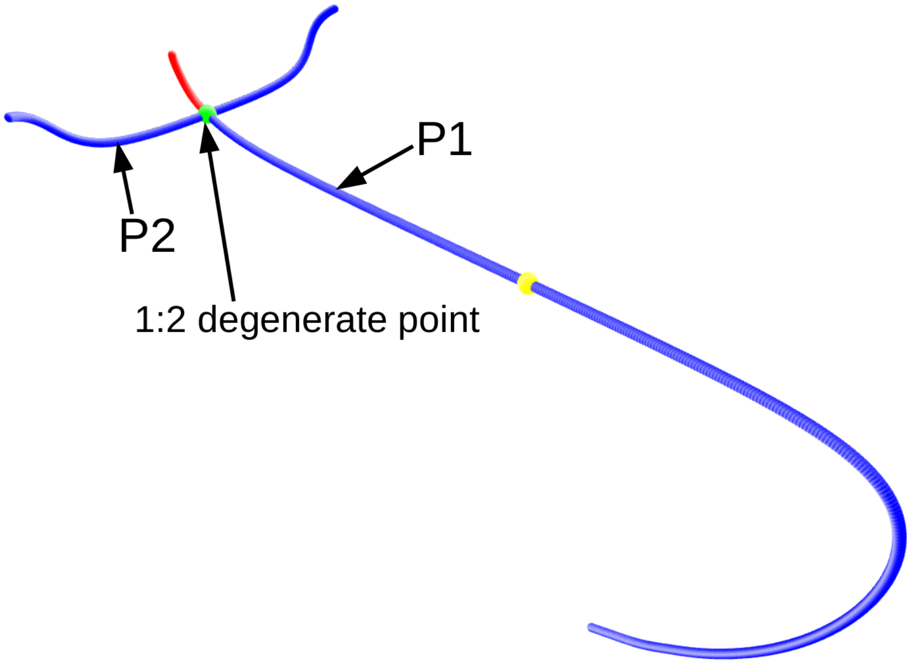
P1
P2
1:2 degenerate point

Figure 4.16: Period-1 and Period-2 lines for $\beta = 2$ and $\Theta = \pi/4$

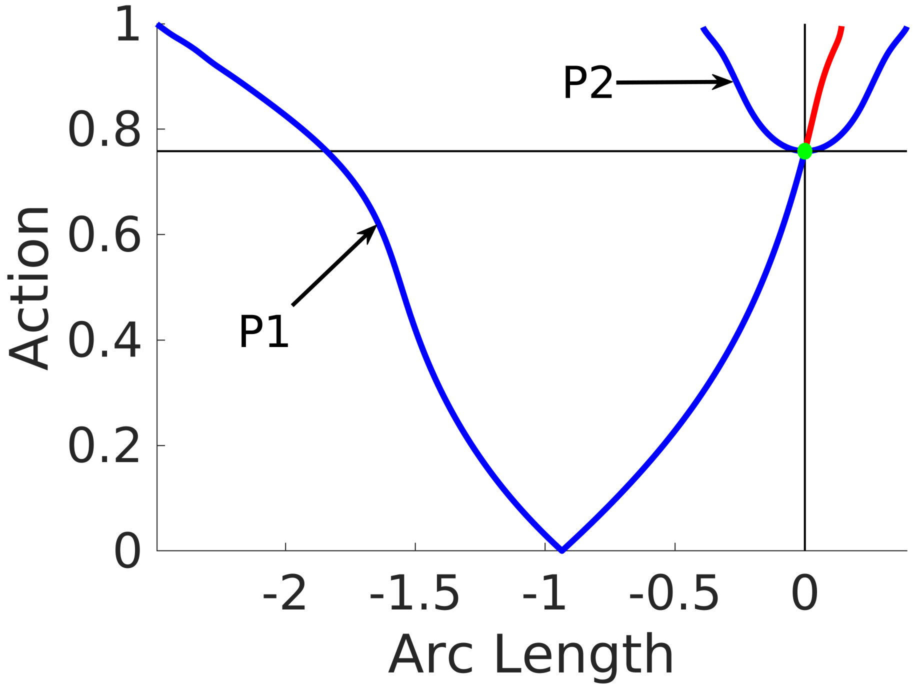

Figure 4.17: Action vs Arclength of period-1 and period-2 lines for $\beta = 2$ and $\Theta = \pi/4$

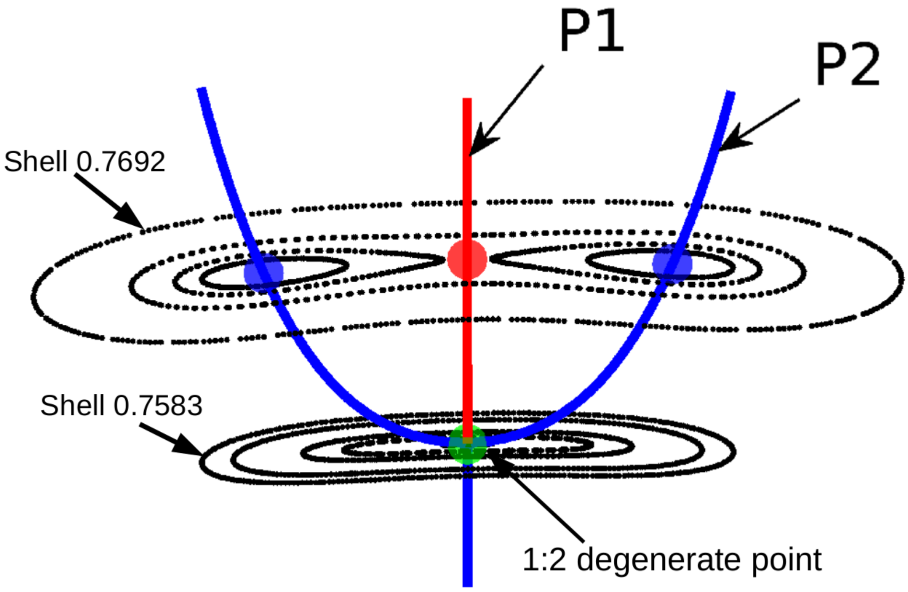

Figure 4.18: Local Poincaré sections of shells near 1:2 resonance point for $\Theta = \pi/4$ and $\beta = 2$. Note that the shell-horizontal and shell-normal coordinate has been expanded for clarity.

degenerate point and the centres of these islands are period-n elliptic points, as shown in the upper sections of figures 4.18, 4.22 and 4.25. For order of degeneracy ≥ 3 (i.e. $n \geq 3$): the degenerate points are elliptic period-1 points (due to complex eigenvalues as shown in table 4.1) and the period-1 line character does not change at these degenerate points. The chain of n elliptic islands are connected by the manifolds of n period-n hyperbolic points, forming heteroclinic connections. In contrast, at a second order degenerate point, the period-1 line changes its character from elliptic to hyperbolic, and the two elliptic islands are connected by manifolds of a hyperbolic period-1 point instead of two period-2 hyperbolic points as shown in the figure 4.18, forming a homoclinic connection. It is because of the existence of this hyperbolic period-1 point, two additional hyperbolic period-2 points are not possible to connect the islands. Hence there is only one period-2 line which passes through the 1:2 degenerate point.

4.3.4 1:3 Resonance

A 1:3 resonance point has eigenvalues $\lambda_{1,2} = e^{(\pm i2\pi/3)}, \lambda_3 = 1$, and the net deformation at the resonance point after 3 periods is zero. The local rotation angle is $2\pi/3$. Three period-3 lines extend from such a point. The properties of a 1:3 resonance point are described using an example with $\Theta = \pi/8$ and $\beta = 1$. The same parameters is used to discuss i:4 resonance later in section 4.3.5. A period-1 line on the symmetry plane is shown in figure 4.19(a). Action and trace values of the deformation tensor on the period-1

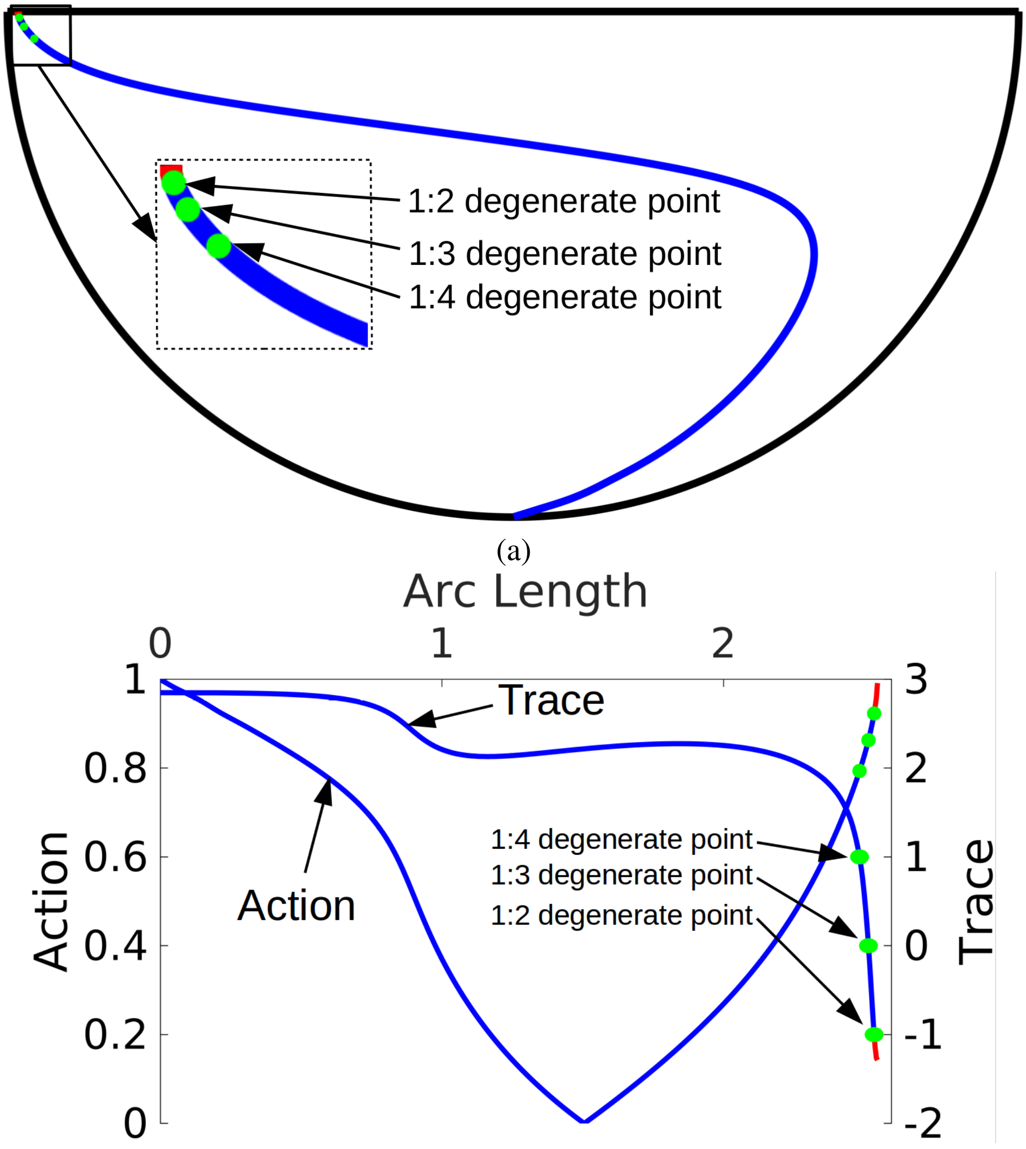

(a)

(b)

Figure 4.19: (a) Period-1 line for $\beta = 1$ and $\Theta = \pi/8$ on symmetry plane. (b) Action and trace along the period-1 line

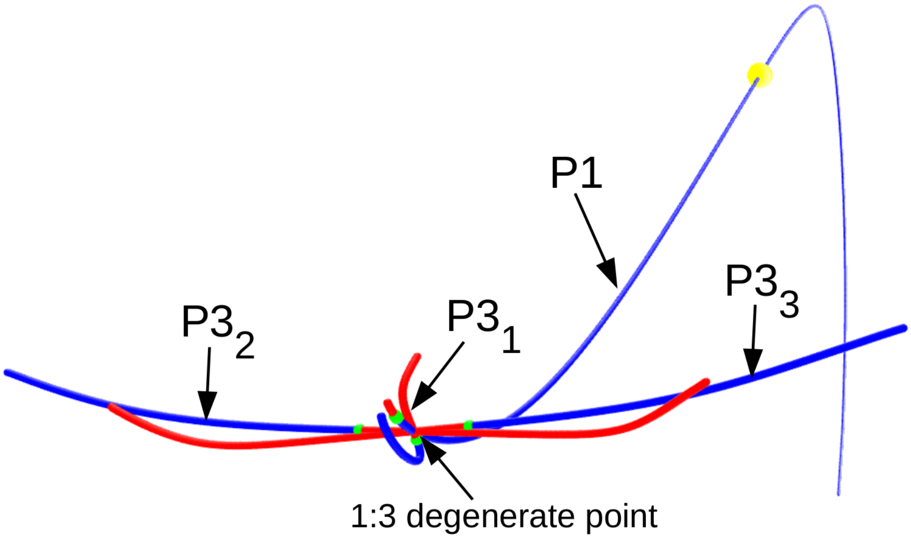

Figure 4.20: Period-1 and period-3 lines for $\beta = 1$ and $\Theta = \pi/8$

line is shown in figure 4.19(b). In figure 4.19(b), the trace line has a point with trace value 0, which corresponds to 1:3 resonance point (see table 4.1). The 1:3 degenerate point is also shown on the period-1 line in figure 4.19(a). Three period-3 lines ($P3_1$,$P3_2$ and $P3_3$) extend from the 1:3 resonance point and are computed numerically using the method discussed in section3.6. The period-1 line (P1) and three period-3 lines are shown in figure 4.20. P1 and $P3_1$ lines are on the symmetry plane. Action values on the period-1 line and period-3 lines are plotted against arc lengths in figure 4.21(a). Arc lengths of period-1 and period-3 lines are defined so that arc length is zero at the 1:3 resonance point. A close-up fof the rectangular box in in figure 4.21(a) is shown in figure 4.21(b). From figure 4.21(b) and figure 4.20, It is observed that, all period-3 line ends are attached to the hemisphere boundary. $P3_2$ and $P3_3$ are reflections of each other at the symmetry plane, and can be defined by equation (4.4).

$$P3_3 = S_\Theta P3_2, \tag{4.4}$$

where S_Θ is the map that reflects a particle about the symmetry plane.

. The local Poincaré sections corresponding to the 1:3 resonance point is shown in figure 4.22. The shell-normal coordinate is stretched for clarity in this figure. The lower section with an action value of 0.8607 contains three extrema (first order period-3 degenerate points) where the three period-3 lines are tangent to the shell and a period-1 elliptic point. The middle section with an action value of 0.8628 contains three period-3 elliptic points and the 1:3 resonance point through which the period-1 line and all period-3 lines pass (by definition). The upper section with an action value of 0.8649 contains three period-3 elliptic points, three period-3 hyperbolic points, and a period-1 elliptic point.

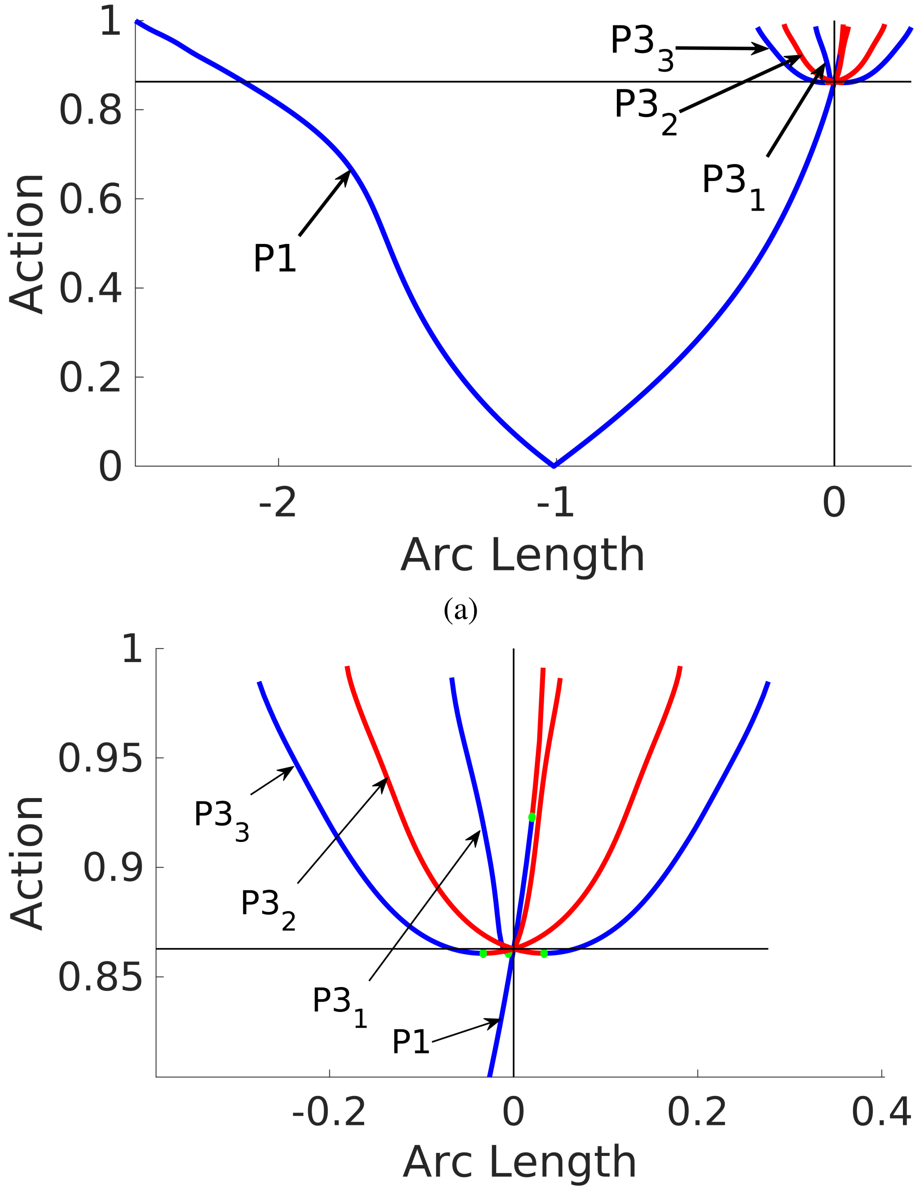

(a)

(b)

Figure 4.21: (a) Action is plotted along period-1 line and three period-3 lines for $\Theta = pi/8$ and $\beta = 1$ (b) Top right segment of figure (a)

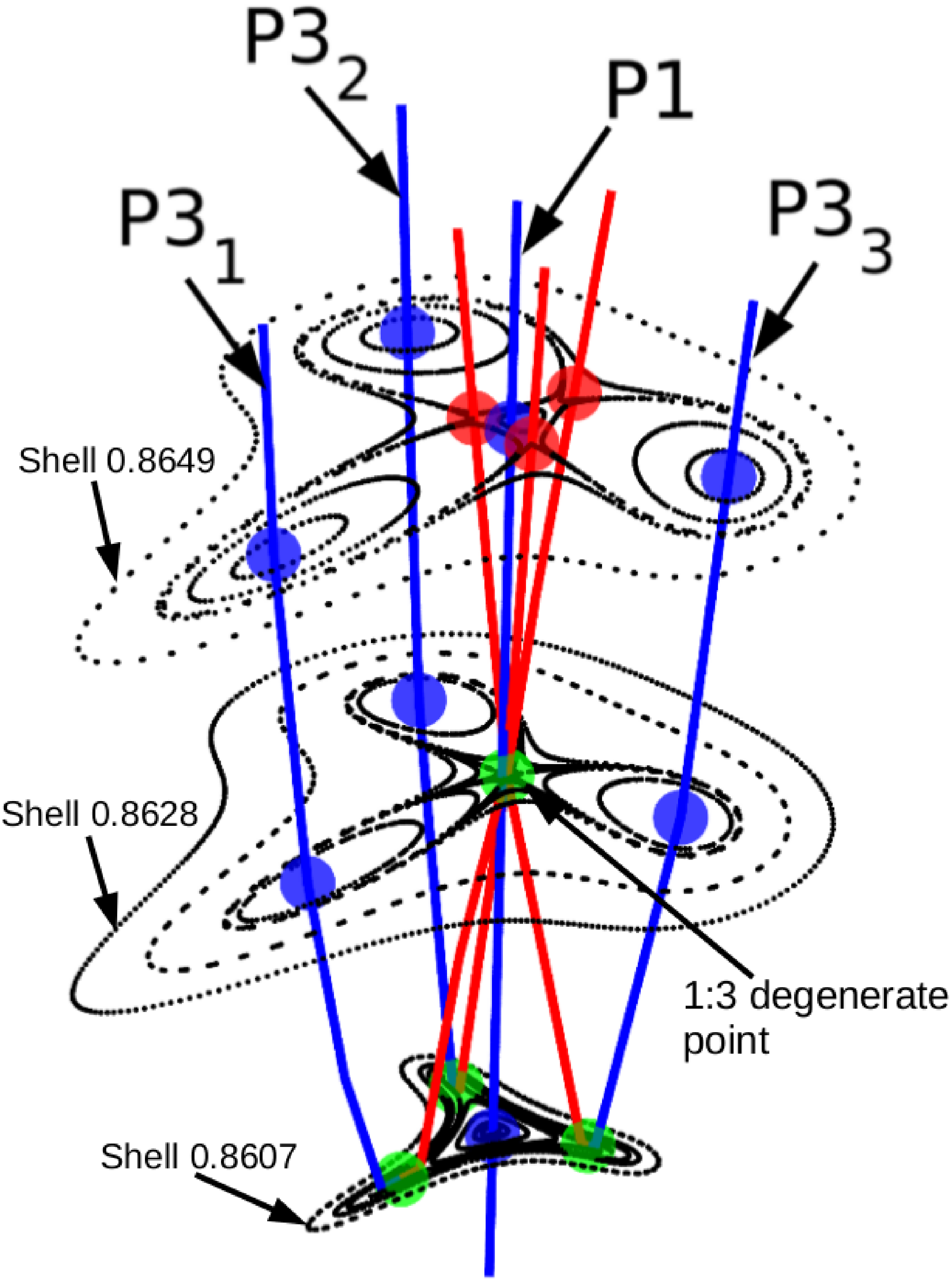
$P3_2$
P1
$P3_1$
$P3_3$
Shell 0.8649
Shell 0.8628
1:3 degenerate point
Shell 0.8607

Figure 4.22: Local Poincaré sections of shells near the 1:3 resonance point for $\Theta = \pi/8$ and $\beta = 1$. Note that the shell-horizontal and shell-normal coordinate has been expanded for clarity.

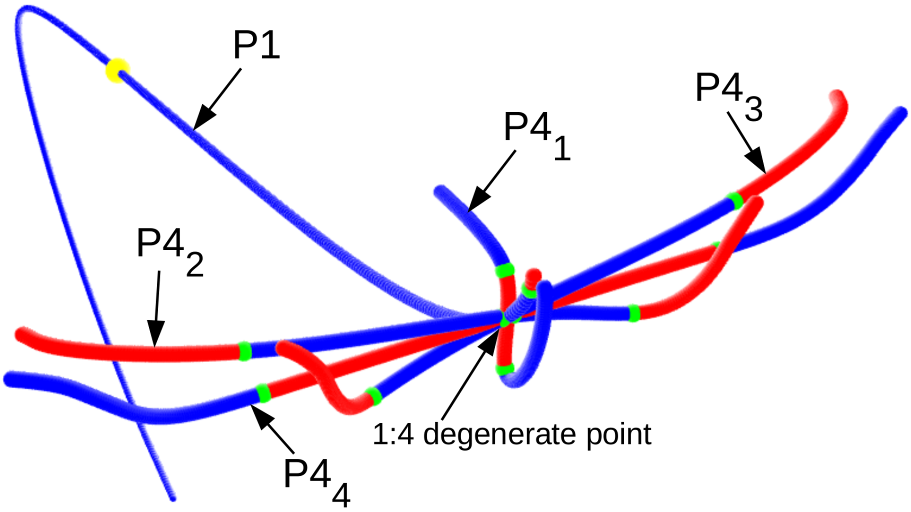

Figure 4.23: P1 and P4 lines for $\beta = 1$ and $\Theta = \pi/8$

All the piercings sites on Poincaré sections are shown with solid spheres, blue for elliptic point, red for hyperbolic point and green for degenerate point. The stable and unstable manifolds of the period-3 hyperbolic points on the upper section have heteroclinic connections. The heteroclinic connections create four islands, and these islands act as transport barriers.

4.3.5 1:4 Resonance

A 1:4 resonance point has eigenvalues $\lambda_{1,2} = e^{(\pm i2\pi/4)}, \lambda_3 = 1$ (or $\mathrm{Tr} = 1$). The net deformation at the resonance point is zero after four periods, and the local rotation angle is $\pi/2$. Four period-4 lines extend from this resonance point. In figure 4.19(b), the trace line has a point with trace value 1, which corresponds to the 1:4 resonance point. The 1:4 degenerate point is also shown on the period-1 line in figure 4.19(a). The four period-4 lines lines passing through the 1:4 resonance point are computed numerically using the method described in section 3.6. The period-1 line (P1) and four period-4 lines ($P4_1$-$P4_4$) are shown in 3D view in figure 4.23. The action values on the period-1 line and four period-4 lines are plotted against arc length in figure 4.24(a). Again, arc length is defined as distance from the 1:4 resonance point. A close-up of the rectangular box in figure 4.24(a) is shown in figure 4.24(b). From figure 4.23 and figure 4.24(b), it is observed that $P4_1$ lies on the symmetry plane, $P4_4$ is symmetric about the symmetry plane, and $P4_3$ and $P4_2$ are reflections of each other about the symmetry plane given in equation (4.5).

$$P3_4 = S_\Theta P4_2 \tag{4.5}$$

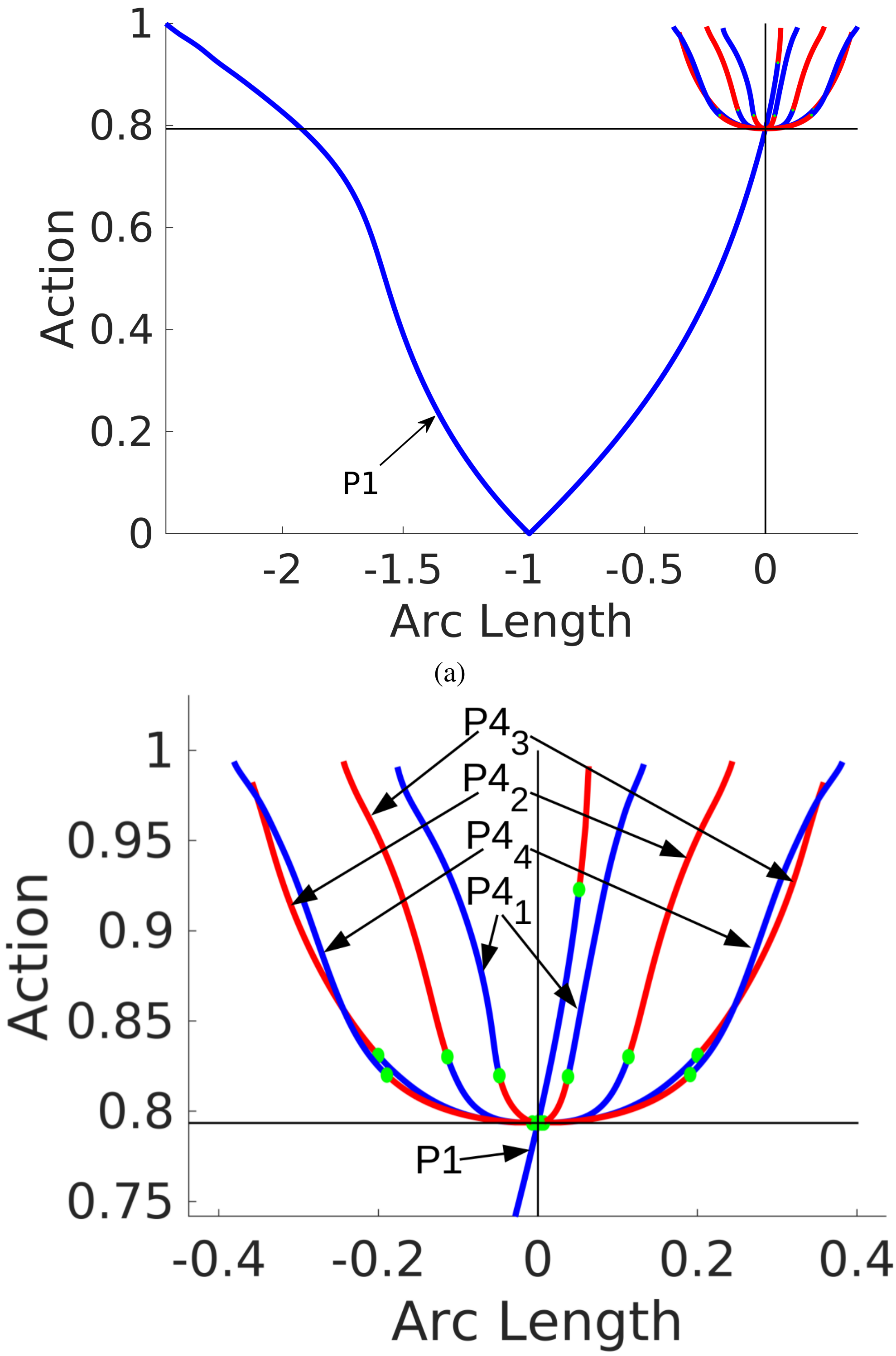

(a)

(b)

Figure 4.24: (a) Action is plotted along period-1 and period-4 lines for $\Theta = pi/8$ and $\beta = 1$ (b) Top right segment of figure (a)

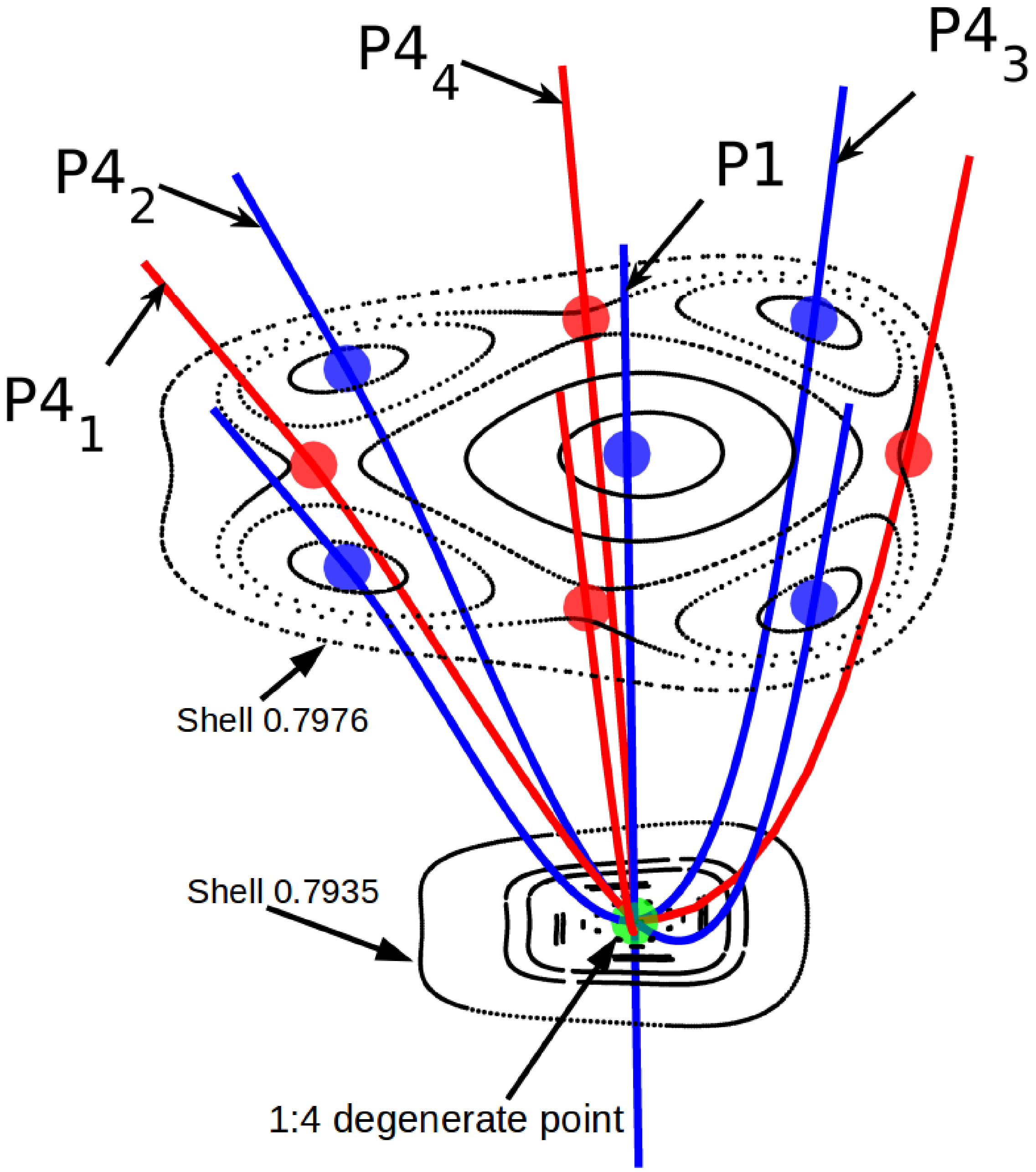
P4$_4$
P4$_3$
P4$_2$
P1
P4$_1$
Shell 0.7976
Shell 0.7935
1:4 degenerate point

Figure 4.25: Local Poincaré sections of shells near 1:4 resonance point for $\Theta = \pi/8$ and $\beta = 1$. Note that the shell-horizontal and shell-normal coordinate has been expanded for clarity.

where S_Θ is the map that reflects a particle about the symmetry plane. All four period-4 lines are attached to the hemisphere boundary.

The local Poincaré section corresponding to this 1:4 resonance point is shown in figure 4.25. Shell horizontal and normal coordinates are stretched for clarity in this figure. The lower section with an action value of 0.7935 contains a 1:4 degenerate point and the upper section with an action value of 0.7976 contains four period-4 elliptic points, four period-4 hyperbolic points and one period-1 elliptic point. All the piercings sites on a Poincaré section are shown with solid spheres. The stable and unstable manifolds of the period-4 hyperbolic points on upper section have heteroclinic connections. The heteroclinic connections create five islands, and these islands act as transport barriers.

Similarly, other resonances ($n > 5$) on the period-1 line can be identified with trace values, and the corresponding higher-order periodic line structures can be calculated.

4.3.6 2:6 resonance

One of the main findings of this thesis is that resonance points, coordinating lower-order periodic lines and higher-order periodic lines, act as nodes in the Lagrangian network of periodic lines in one invariant flows. These resonance points organise periodic lines, which then controls fluid transport. Resonances on period-1 lines are discussed so far. To demonstrate the organisation of periodic lines by resonances on higher-order periodic lines, a 2:6 resonance is described with the example of $\Theta = \pi/4$ and $\beta = 2$, which is the same example used in section 4.3.3 to describe 1:2 resonance. A 1:2 resonance point is identified on the period-1 line of $\Theta = \pi/4$ and $\beta = 2$, and the period-2 line which passes through the 1:2 resonance point is calculated. On this period-2 line, 2:6 resonance points are identified, and the corresponding period-6 lines which pass through them are calculated numerically using the method discussed in section 3.6. The 2:6 resonance points and its associated higher-order periodic lines are shown in figure 4.26. In this figure, a period-2 line (P2) intersects the period-1 line (P1) at the 1:2 resonance point and three period-6 lines ($P6_1, P6_2$ and $P6_3$) intersect the period-2 line at the 2:6 resonance point. In this figure, there is a symmetric structure on the other side of the period-2 line (due to the symmetry in the PRHF), only the 2:6 resonance point is shown, the period-6 lines are not shown here for clarity. Otherwise, the periodic lines look crowded in this figure. Complete Lagrangian structures in a one-invariant flow can be calculated systematically, by first identifying resonance points on period-1 lines and calculating their corresponding higher-order periodic lines, next identifying resonance points on period-2 lines and calculating their corresponding higher-order periodic lines. This process is continued

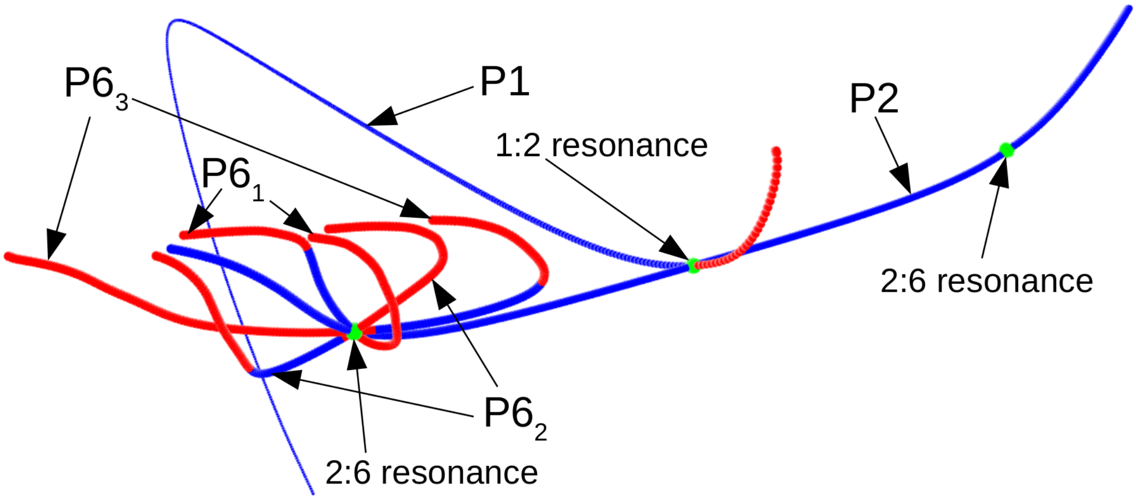
P6$_3$
P1
P2
1:2 resonance
P6$_1$
2:6 resonance
P6$_2$
2:6 resonance

Figure 4.26: A period-1 line (P1), a period-2 line (P2) and three period-6 lines ($P6_1$, $P6_2$ and $P6_3$) coordinating via 1:2 resonance point and 2:6 resonance points for $\Theta = \pi/4$ and $\beta = 2$.

recursively until all the Lagrangian structures are obtained or until enough Lagrangian structures are obtained for any given purpose.

4.4 Global Lagrangian structures from local resonance bifurcations

In all the examples of the resonances from 1:2 to 1:4 discussed till now, the higher order periodic lines extended from the corresponding resonance points to the hemisphere boundary. A higher-order periodic line from a resonance point can sometimes connect with another resonance point of the same order and forms a global Lagrangian structure. Such type of coordination between the resonance points is discussed here with 1:2 resonances.

4.4.1 Example: $\Theta = \pi/8$ and $\beta = 4$

A period-1 line on the symmetry plane for $\Theta = \pi/8$ and $\beta = 4$ is shown in figure 4.27 (a). The action and trace values of the deformation tensor along the period-1 line are shown in figure 4.27(b). In figure 4.27(b), the trace line has five points with trace -1, which correspond to 1:2 resonance points. These five 1:2 resonance points belong to five different shells. The four 1:2 resonance points are labelled 1-4, and are shown on the action line in figure 4.27(b). Period-2 lines corresponding to the four 1:2 resonance points are computed numerically using the method described in section 3.6 and are shown in figure 4.28. It is seen in this figure, that, period-2 lines extending from the resonace points 1 and 3 join together to form a single closed period-2 line ($P2_1$), and period-2 lines extending from the resonace points 2 and 4 join together to form another single closed period-2 line ($P2_2$).

The period-1 line and the two period-2 lines impart their character on to shells as a consequence of the stability of the lines at the piecings points. Action values on the period-1 line and the period-2 lines are plotted against arc length in figure 4.29. To examine the influence of the period-2 lines on shells, three shells (shell values 0.5285, 0.5588 and 0.5919) shown in figure 4.29 are chosen.

Shell 0.5285:

The Poincaré section of shell 0.5285 including the period-1 and period-2 lines, and piercings are shown in figure 4.30. Figure 4.30: (a) presents the view from the bottom of the hemisphere, (b) presents the view from the side-top of the hemisphere and (c) presents the flattened out view of the shell on a 2D sheet. All piercings sites on the Poincaré section are shown with solid spheres. Shell 0.5285 contains four period-2 elliptic points, four period-2 hyperbolic points and two period-1 elliptic points. The stable and unstable manifolds of the four period-2 hyperbolic points have heteroclinic connections.

Shell 0.5588:

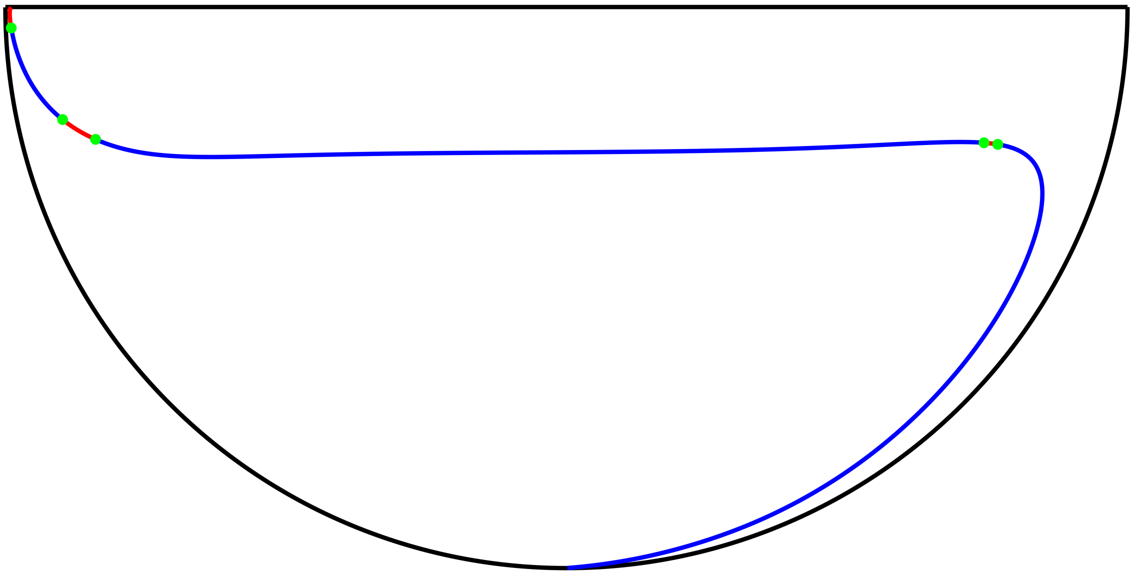

(a)

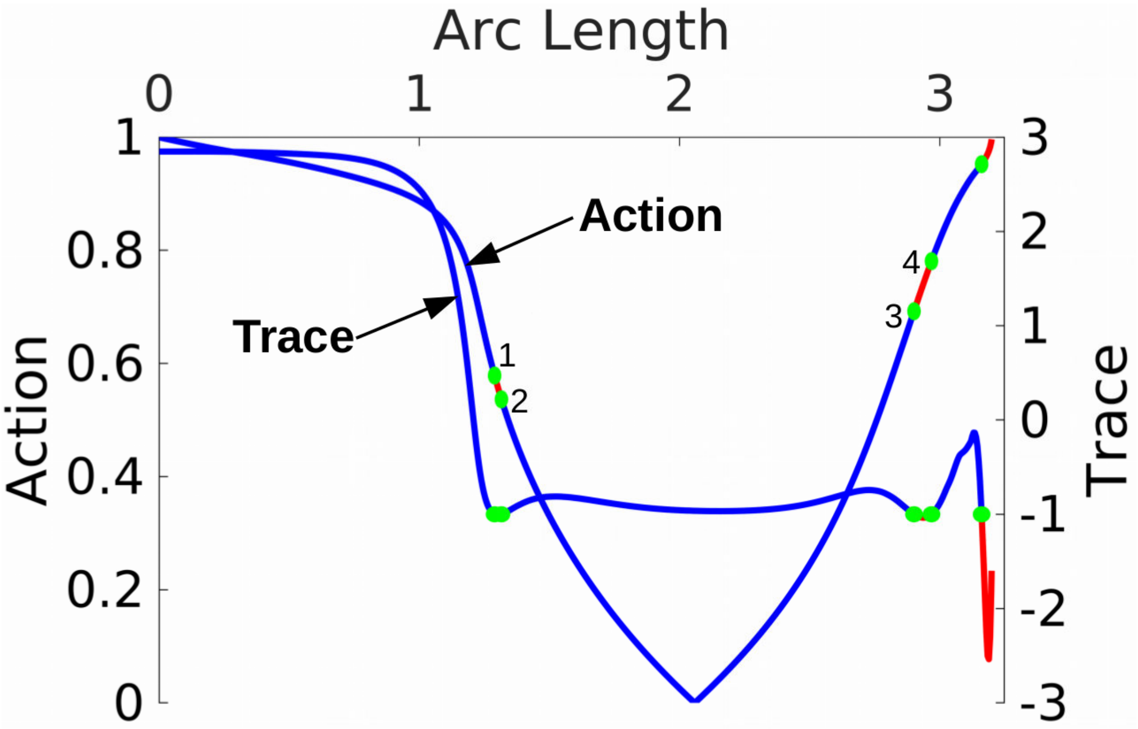

(b)

Figure 4.27: (a) The Period-1 line for $\beta = 4$ and $\Theta = \pi/8$ on the symmetry plane. (b) Action and trace along the period-1 line

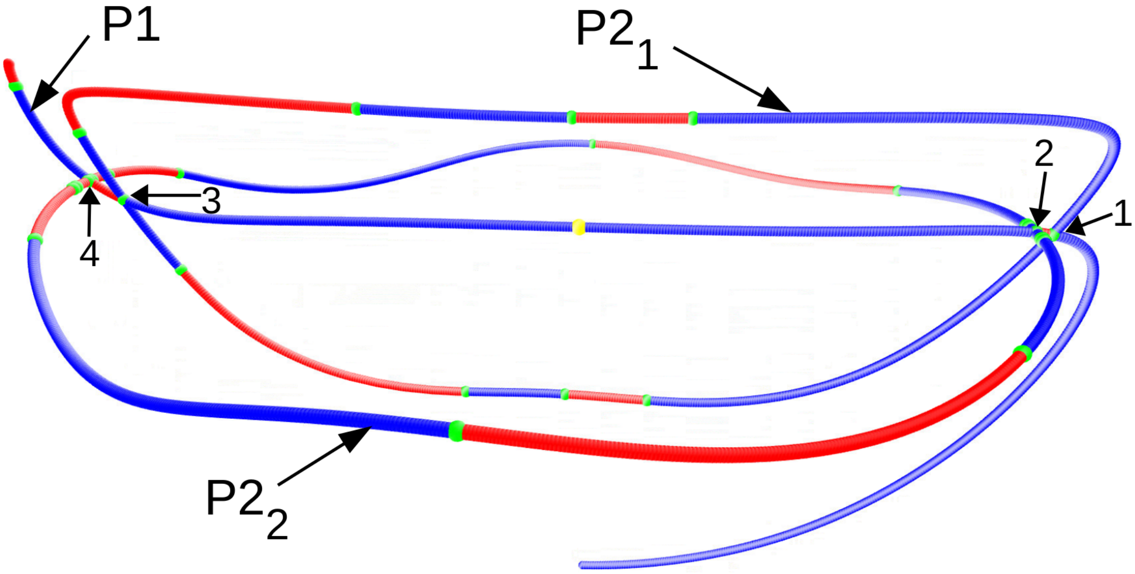

Figure 4.28: $\Theta = \pi/8$ and $\beta = 4$, Period-1 line P_1 and period-2 line $P2_1$ are on symmetry plane, and period-2 line $P2_2$ is symmetric about symmetry plane; Elliptic line segments are coloured blue, hyperbolic line segments are coloured red and degenerate points are coloured green. Five 1 : 2 resonance points on P_1 are also shown with numbers 1 – 4.

A similar Poincaré section for shell 0.5288 is shown in figure 4.31. The views are the same as the previous shell. This shell contains four period-2 elliptic points, two period-2 hyperbolic points, a period-1 elliptic point and a hyperbolic period-1 point. The stable and unstable manifolds of two period-2 hyperbolic points have heteroclinic connections. The stable and unstable manifolds of period-1 hyperbolic point have homoclinic connections.

Shell 0.5919:

A similar Poincaré section for shell 0.5919 is shown in figure 4.32. The views are the same as the previous shell. The shell contains two period-2 elliptic points, two period-2 hyperbolic points and two period-1 elliptic points. The stable and unstable manifolds of two period-2 hyperbolic points have heteroclinic connections.

4.4.2 Example: $\Theta = \pi/4$ and $\beta = 4$

Another example that has a different number of 1:2 resonance points on the period-1 line to the previous example is considered to examine the connections of period-2 lines emanating from the 1:2 resonance points. The period-1 line ($P1$) and two period-2 lines ($P2_1$, $P2_2$) for $\Theta = \pi/4$ and $\beta = 4$ are shown in figure 4.33. The 1:2 resonance points on the period-1 line are labelled 1-3 in this figure. It is seen in this figure, that, period-2 lines extending from the resonance points 1 and 3 join together to form a single closed period-2 line ($P2_1$), and a period-2 line extending from the resonance point 2 attaches to the hemisphere boundary.

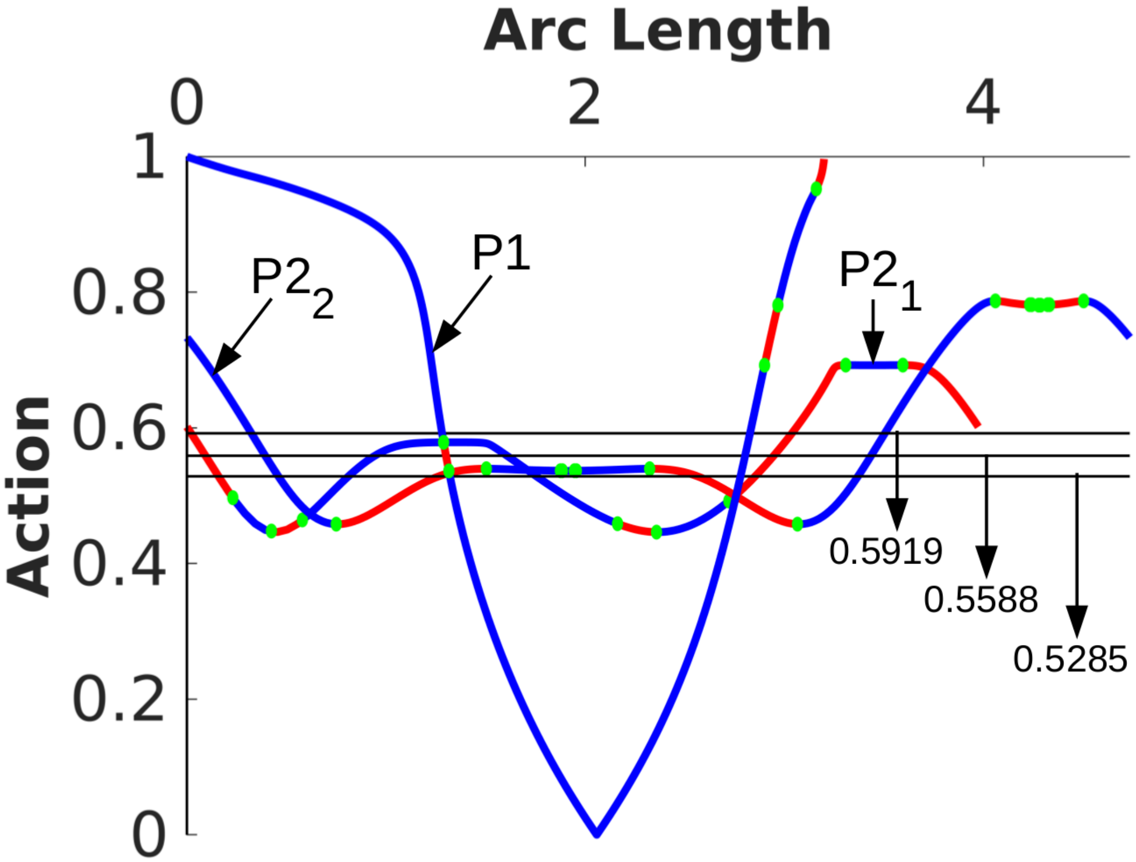

Figure 4.29: Action against arc length of periodic lines (P1, $P2_1$ and $P2_2$) shown in figure 4.28 are plotted. Three horizontal lines correspond to action values (0.5285, 0.5588, 0.5919).

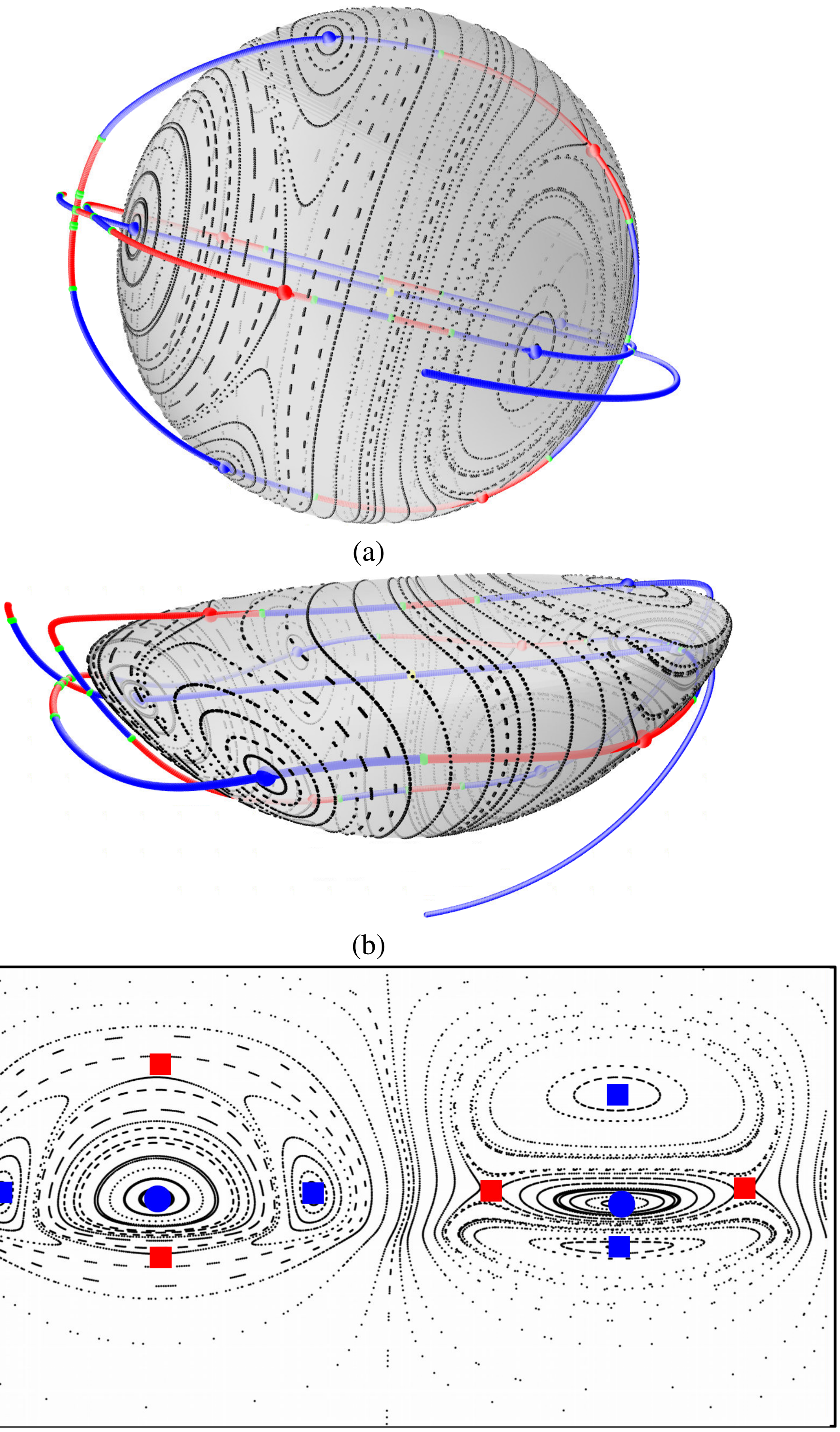

(a)

(b)

(c)

Figure 4.30: Periodic lines shown in figure 4.28 imparting its character on to shell 0.5285; Stroboscopic map on Shell seen from (a) Bottom (b) Top-side (c) Stroboscopic map on shell is projected on to a plane; Period-1 line piercing point on the shell is represented by solid circle and period-2 lines piercing point on the shell is represented by solid square; blue colour for elliptic and red colour for hyperbolic stability

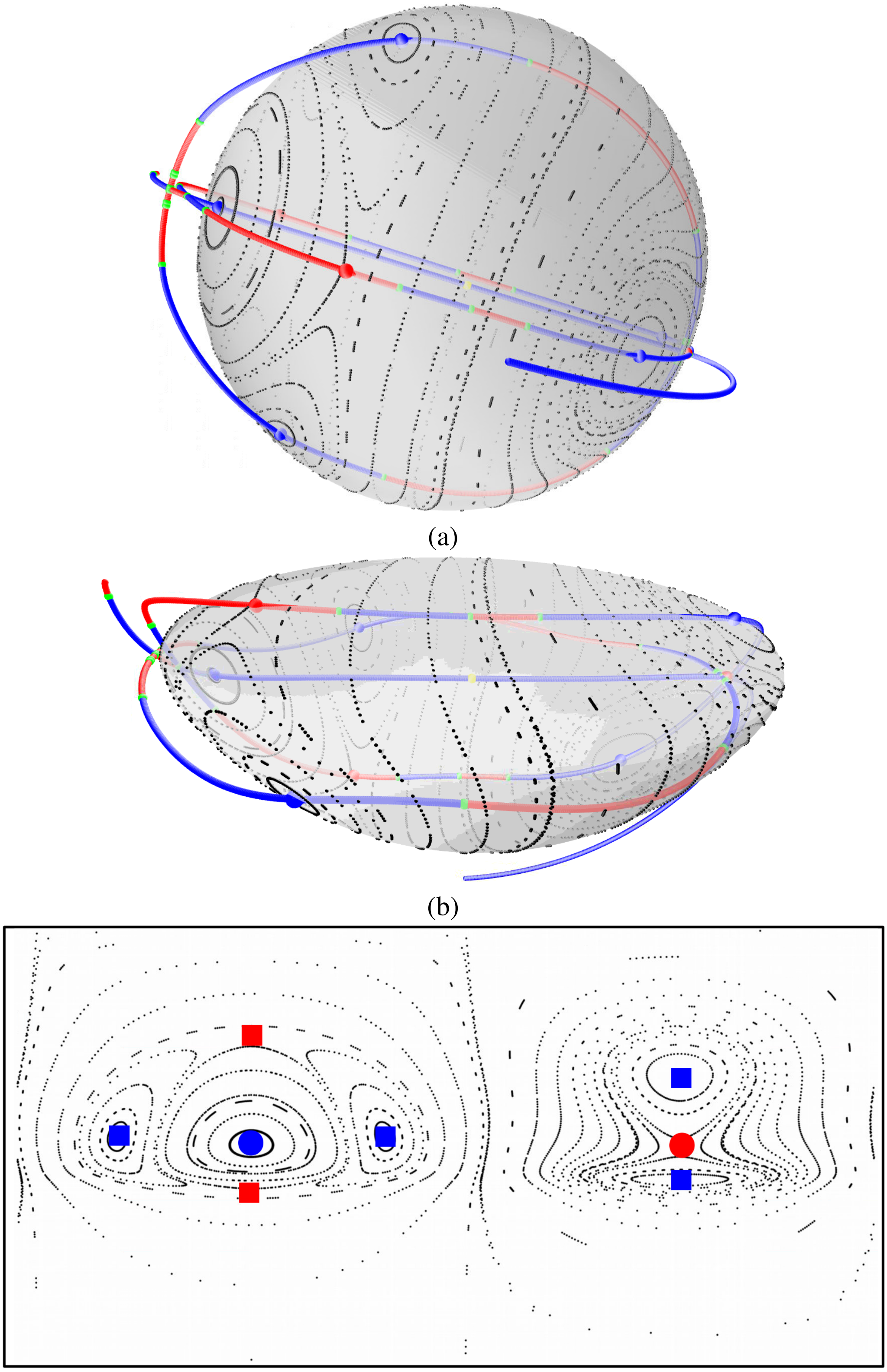

(a)

(b)

(c)

Figure 4.31: Periodic lines shown in figure 4.28 imparting its character on to shell 0.5588; Stroboscopic map on Shell seen from (a) Bottom (b) Top-side (c) Stroboscopic map on shell is projected on to a plane; Period-1 line piercing point on the shell is represented by solid circle and period-2 lines piercing point on the shell is represented by solid square; blue colour for elliptic and red colour for hyperbolic stability

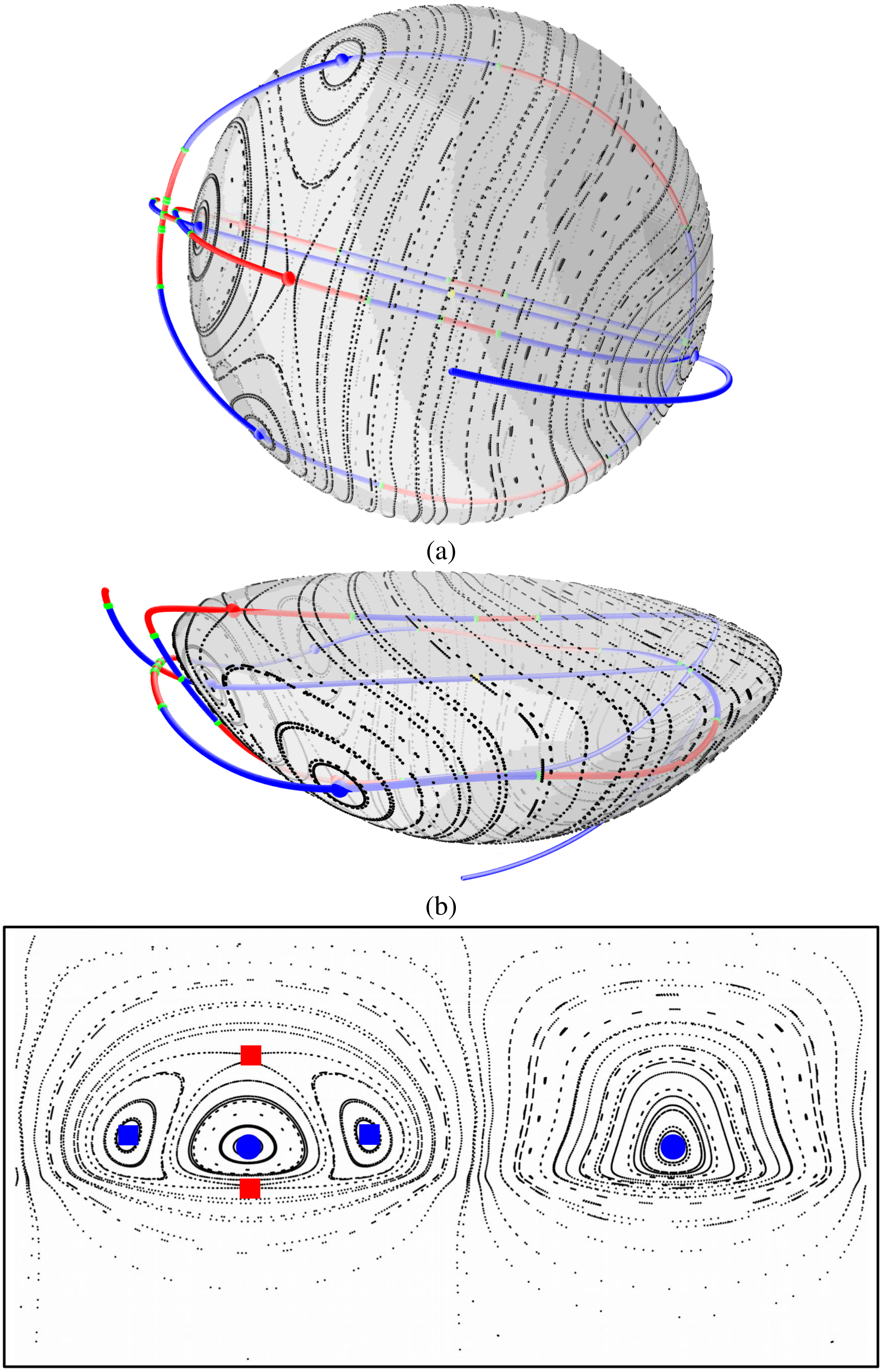
(a)

(b)

(c)

Figure 4.32: Periodic lines shown in figure 4.28 imparting its character on to shell 0.5919; Stroboscopic map on Shell seen from (a) Bottom (b) Top-side (c) Stroboscopic map on shell is projected on to a plane; Period-1 line piercing point on the shell is represented by solid circle and period-2 lines piercing point on the shell is represented by solid square; blue colour for elliptic and red colour for hyperbolic stability

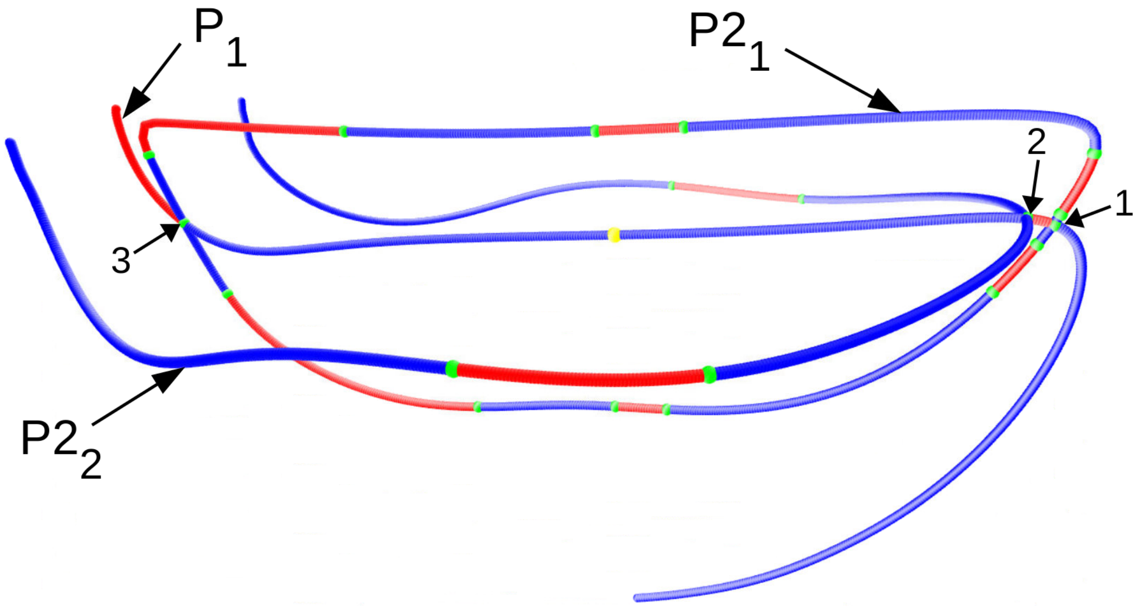

Figure 4.33: $\Theta = \pi/4$ and $\beta = 4$, Period-1 line P_1 and period-2 line $P2_1$ are on symmetry plane, and period-2 line $P2_2$ is symmetric about symmetry plane; Elliptic line segments are coloured blue, hyperbolic line segments are coloured red and degenerate points are coloured green. Four 1:2 resonance points on P_1 are also shown with numbers 1 – 3.

4.5 Summary

The PRHF in the Stokes regime has a time reversal-reflection symmetry, and it is enough to look for Lagrangian structures on one side of the symmetry plane because they mirror across this plane. The PRHF in the Stokes regime is a one action flow because of the time reversal-reflection symmetry it possesses. The flow topology consists of closed invariant surfaces which are topologically equivalent to nested spheres, with fluid particles being constrained to move on the invariant surfaces. The advection of fluid particles on an invariant surface is Hamiltonian everywhere except at stagnation points. The organisation of Lagrangian structures in one action flows is not well understood, and it is essential to efficient mixing. One action flows can not have isolated periodic points, they can only have periodic lines which are either closed or the ends of the periodic lines are attached to the boundary. Hence, periodic lines and their manifolds constitute all of the Lagrangian structures in one action flows. Numerical computation of Lagrangian structures is vital to understand fluid transport. The overarching key result of this chapter is that no matter how complex the Lagrangian structure of this class of flow appears, it can now be fully understood through the hierarchical calculation of canonical Lagrangian structures at resonant degenerate points on periodic lines. Ultimately this occurs because of the global constraint on deformation from volume preservation and the local constraint of no deformation tangent to periodic lines.

The action variable (or "Shell number") has proven to be a valuable concept in understanding Lagrangian structures in one action flows. Although an individual fluid particle has a fixed shell number (or action value), the way in which shell number changes along the periodic line allows significant understanding of topology to be gained. Plotting action as a function of distance (or arclength) along a periodic line allows us to determine the number of periodic line piercings and their stability on any shell by drawing a horizontal line at the shell values. The local Lagrangian topology on any shell can be quickly inferred from the action-arclength plots of the periodic lines. The method of enumerating action and plotting it against arclength along periodic lines can be applied to any topologically similar one action flow in which the action variable can be quantified some way.

Period-1 line being the most important of all the other order periodic lines forms the Lagrangian skeleton of the flow. In the Stokes PRHF, a single period-1 line which connects three non-trivial fixed points (a point at the bottom of the hemisphere, a central stagnation point which is at the centre of the topological spheres and a point on the lid) exists on the symmetry plane for all parameter values. By finding action values along the period-1 line, it is found that the period-1 line intersects each shell at least twice. In the limit $\beta \to 0$, the period-1 line is a stagnation line that coincides with the y axis. As β increases, the tangent to the period-1 line at the central stagnation point rotates anti-clockwise which increases the total length of the period-1 line (since both the ends of a period-1 line are fixed). For very low β values, the entire period-1 is elliptic and pierces each invariant surface only twice. As β increases from very low to low values, hyperbolic segments start appearing on the period-1 line, although it still pierces each invariant surface twice. Wherever a period-1 line pierces on a shell, the stability of the piercing period-1 point is imparted on to the shell in the neighbourhood of the piercing site. As β increases further, the period-1 line starts folding inside hemisphere that leads to the creation of two local extrema (one minimum, one maximum) in action vs arc length plot. The two local extreme together constitute a wiggle. Each local extrema in the action vs arc length plot correspond to a point at which the period-1 line becomes tangent to one of the shells. Each of these points also a first-order degenerate point and corresponds with a cusp on the 2D shell Poincaré section. A single wiggle accommodates two first order degenerate points, and the period-1 line segment between these degenerate points is of hyperbolic type. Both the sides of the period-1 line segments are of elliptic type. A wiggle of a period-1 line makes two additional period-1 piercings of invariant shells over a range of shell numbers.

The degenerate points on periodic lines are analogous to fixed point resonances in classical planar bifurcation theory. At an n^{th} order degenerate point (or 1:n resonance point), n period-n lines intersect the period-1 line except for $n = 1$ and 2. At a first order degenerate point, the period-1 line is tangent to one of the shells. At a second order degenerate point, a period-2 line intersects the periodic-1 line. In general, at a m:p resonance point on a period-m line, n ($= p/m$) period-p lines intersect. The resonance points on a periodic line are easily identified by the trace values on the periodic line. A higher-order periodic line intersecting with a lower order periodic line at a resonance point can be calculated numerically by identifying the resonance point. The significance of these resonances points is that one action flows can be completely understood by finding the resonance points on the period-1 lines first, and then computing the corresponding higher-order periodic lines, and then computing period-2 lines and the corresponding higher-order periodic lines, and so on. This process is pursued recursively until enough Lagrangian transport structures are uncovered for any given purpose. 1:1, 1:2, 1:3 and 1:4 resonances are called strong resonances.

A higher-order periodic line extending from a resonance point may attach to the boundary, or higher-order periodic lines extending from different resonance points can sometimes join together to form a closed periodic line. These resonance bifurcations are local bifurcations because they can be found in the neighbourhood of periodic points (or fixed points). The Lagrangian structures emanating from different resonance bifurcation points connect together and form truly global transport structures. With this way of building extended structures from lower order to higher order periodic lines, truly global Lagrangian transport structures can be uncovered for any one action flow. With the Re=0 in the PRHF, Lagrangian structures are now fully understood. In the next chapter, I will show how these structures break down to quasi-chaotic structures upon perturbation.

Chapter 5

Numerical Analysis of PRHF in Inertial Regime

A 3D incompressible flow with one invariant can have invariant surfaces that are either topologically spheres as seen in the previous chapter or topologically tori. To generate 3D chaotic transport, the flow invariants must be destroyed by perturbing the flow. What are the transport mechanisms that produce 3D chaos upon perturbation of one invariant flows? The answer is not completely known. So far, three transport mechanisms that generate 3D chaos have been observed: resonance induced dispersion (Cartwright *et al.*, 1996; Vainchtein *et al.*, 2007, 2008; Vainchtein and Abudu, 2012; Meiss, 2012), localised shear-induced dispersion (Smith *et al.*, 2017), resonance induced merger (Speetjens *et al.*, 2006a,b; Pouransari *et al.*, 2010). In particular, "resonance induced merger" is observed when nested spheroidal surfaces are perturbed. Is the "resonance induced merger" mechanism generic for systems with nested spheroids or are there other transport mechanisms for the case of nested spheroids? In this chapter, the question is answered, and a new mechanism featuring non-heteroclinic tubular transition regions is described. The progression of Lagrangian structures from one invariant flow to zero invariant flow after the inertial perturbation is also described in this chapter.

The PRHF in the Stokes regime is an incompressible invariant flow due to its time-reversal reflection symmetry, and fluid particle transport is constrained to two-dimensional invariant surfaces. To generate three-dimensional fluid transport, in this chapter, finite inertia of fluid flow is considered that breaks the fore-aft symmetry in the base flow that further breaks the time-reversal-reflection symmetry of the PRHF. The effect of for-aft symmetry breaking via inertia on particle trajectories in the base flow are discussed in section 2.1.2. The left-right symmetry of the base flow still exists in the inertial flow.

Breaking the time-reversal-reflection symmetry of the PRHF results in the loss of the invariant which exists in the Stokes limit. Hence the conserved coordinate in the Stokes flow is no longer conserved in the inertial flow, and fluid particles move in three-dimensions. Although the symmetry is lost with the inertia, the flow appears to have some remnants of the symmetry at least in the range $Re \in (0, 1)$ that will be seen in this chapter.

5.1 Period-1 (or Fixed point) structures

Since period-1 structures are the most important Lagrangian structures, the approach in understanding fluid transport in the inertial regime begins through the computation of period-1 points and their manifolds. In the Stokes flow, a single period-1 line exists on the symmetry plane for all system parameter values (β and Θ). In the inertial flow, a numerical search discussed in section 3.7 did not find any period-1 lines; instead, isolated period-1 points were found which are not part of any period-1 line. In this thesis, the use of the words "symmetry plane", "shell number (or action)" and "period-1 line" always refers to the Stokes regime. The use of the word "isolated period-1 point" always refers to the inertial regime. In the following subsections: the nature of the isolated period-1 points is discussed in section 5.1.1; some features of the isolated period-1 points in the inertial flow are discussed in section 5.1.3; the details of the numerical computation of the manifolds of the isolated period-1 points are discussed in section 5.1.2; some general conventions used in the figures of this chapter are discussed in section 5.1.4.

5.1.1 Nature of isolated period-1 points

Isolated period-1 points are numerically calculated using the method discussed in section 3.7. The nature of fluid transport in the neighbourhood of an isolated period-1 point is determined by the eigenvalues of the deformation tensor (or multipliers) evaluated at the isolated period-1 point. Multipliers are computed by computing the deformation tensor numerically as described in section 3.5. Period-1 points are categorized mainly into two types based on the values of the multipliers: a hyperbolic-node for three real values, and a hyperbolic focus for two complex and one real value (see section 2.4.2).

A hyperbolic focus point has a 1d manifold and a spiralling 2d manifold. The spiralling can be into or out of the periodic point based on the magnitude of the eigenvalues. A hyperbolic-node period-1 point has three 1D manifolds. As discussed in section 2.5, the stability of an isolated period-1 point can also be determined from the trace τ (termed trace1) and the second trace σ (termed trace2) values (defined in section 2.5) of the deformation tensor evaluated at that point. A period-1 point has either 1D stable and 2D unstable manifolds if $\sigma > \tau$ at the period-1 point or 1D unstable and 2D stable manifolds if $\sigma < \tau$ at the period-1 point (Dullin and Meiss, 2008). The trace1 vs trace2 plots of isolated period-1 points will be shown in later sections to identify the stability of isolated period-1 points quickly. The number of unstable directions is called the Morse index (Bott, 1982).

5.1.2 Numerical computation of manifolds

To compute a 1d manifold of a period-1 point numerically, 15 points which are between the distance of 10^{-6} to 10^{-5} from the period-1 point along the corresponding eigenvector direction on both sides of the period-1 point are considered. The 15 points separately on each side are then tracked forward in time if the corresponding eigenvalue is greater than one and tracked backwards in time if the corresponding eigenvalue is less than one until enough the 1D manifold structure is obtained. Because the manifolds of the period-1 points (or fixed points) belong to the map $\boldsymbol{\Psi}$, fluid particles which are on a 1D manifold do not move continuously as time progresses along the 1D manifold line; instead, they move discretely. To view a 1D manifold of a period-1 point, orbits of the 15 points can be plotted as dots in 3D space that looks like a dotted line. In the later sections of this chapter, the dotted 1D manifold lines are shown as continuous lines for a better view in manifold figures. To compute a 2d manifold of a hyperbolic-focus period-1 point numerically, a set of 100 points are uniformly placed on a sphere of radius 10^{-5} centred around the hyperbolic-focus period-1 point. The 100 points are tracked forward in time if the absolute value of the corresponding complex eigenvalue is greater than one, or tracked backwards in time if the absolute value of the corresponding complex eigenvalue is less than one until enough 2D manifold structure is obtained. In the later sections of this chapter, the 100 points and their positions after every period are plotted as dots which constitute a surface in 3D space to show the computed 2D manifolds. 1D and 2D manifolds of all the isolated period-1 points form the advection template that organises all trajectories.

Hyperbolic-node periodic point manifolds:

When manifolds of a hyperbolic-focus period-1 point are calculated numerically and plotted, surprisingly, only two 1D manifolds directions are seen instead of three 1D manifolds. The same thing is noticed with all other hyperbolic-focus period-1 points also that fluid particles in the neighbourhood of a hyperbolic-focus period-1 point are driven along only two eigenvector directions. The reason for this behaviour is explained below.

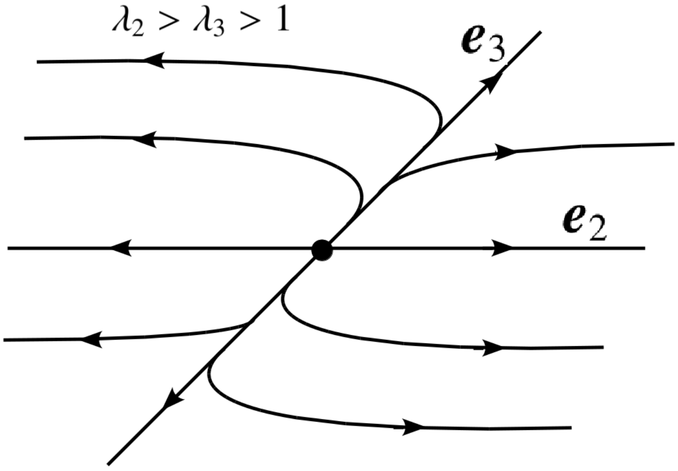

Figure 5.1: A typical 2D unstable manifold of a hyperbolic period-1 point

Assume λ_1, λ_2 and λ_3 are eigenvalues, and $\boldsymbol{e}_1$, $\boldsymbol{e}_2$ and $\boldsymbol{e}_3$ are corresponding eigenvectors of the deformation tensor evaluated at a period-1 point. Assume a case where $\lambda_1 < 1$ and $\lambda_2 > \lambda_3 > 1$. The period-1 point has a 1D stable manifold corresponding to the eigenvalue λ_1 in the $\boldsymbol{e}_1$ direction and a 2D unstable manifold corresponding to the eigenvalues λ_2 and λ_3 on a plane containing $\boldsymbol{e}_2$ and $\boldsymbol{e}_3$ vectors. Consider a point $\boldsymbol{\zeta}_0$ on the plane of the 2D unstable manifold in the neighbourhood of the period-1 point. The point $\boldsymbol{\zeta}_0$ can be expressed as a linear combination of eigenvectors $\boldsymbol{e}_2$ and $\boldsymbol{e}_3$ since it resides on the plane containing $\boldsymbol{e}_2$ and $\boldsymbol{e}_3$ vectors,

$$\boldsymbol{\zeta}_0 = c_2\boldsymbol{e}_2 + c_3\boldsymbol{e}_3. \tag{5.1}$$

The displacement of the point $\boldsymbol{\zeta}_0$ after a period is obtained by $F\boldsymbol{\zeta}_0$ where F is a deformation tensor at $\boldsymbol{\zeta}_0$ (see section 2.4). Similarly the displacement of the point after n periods is obtained via

$$F^n\boldsymbol{\zeta}_0 = c_2\lambda_2^n\boldsymbol{e}_2 + c_3\lambda_3^n\boldsymbol{e}_3. \tag{5.2}$$

Equation (5.2) holds true only in a linearised neighbourhood of periodic point. Because $\lambda_2 > \lambda_3 > 1$, as n increases the displacement vector rapidly converges in the $\boldsymbol{e}_2$ direction leaving the vector $\boldsymbol{e}_3$ irrelevant. The particle trajectories in the neighbourhood of a such hyperbolic-node period-1 point are shown in figure 5.1. Similarly, in another case where $\lambda_1 > 1$ and $\lambda_2 < \lambda_3 < 1$, the effective eigenvector directions are $\boldsymbol{e}_1$ and $\boldsymbol{e}_2$. Of all the three real eigenvalues of an hyperbolic node period-1 point, an eigenvector of an eigenvalue whose absolute value is closest to one loses its relevance as n increases.

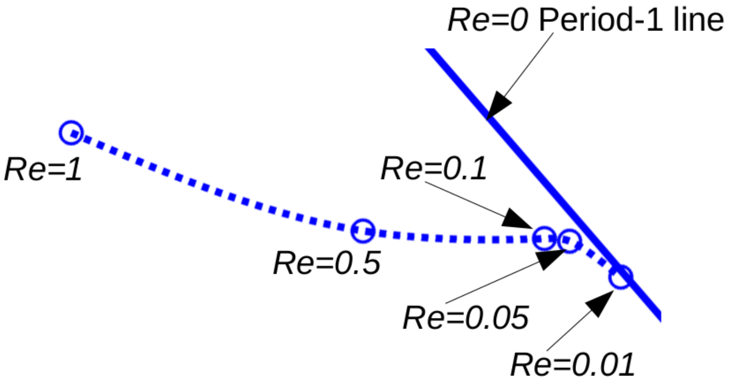

(a) a hyperbolic-focus period-1 point approaches a point on an elliptic period-1 line segment of the Stokes flow

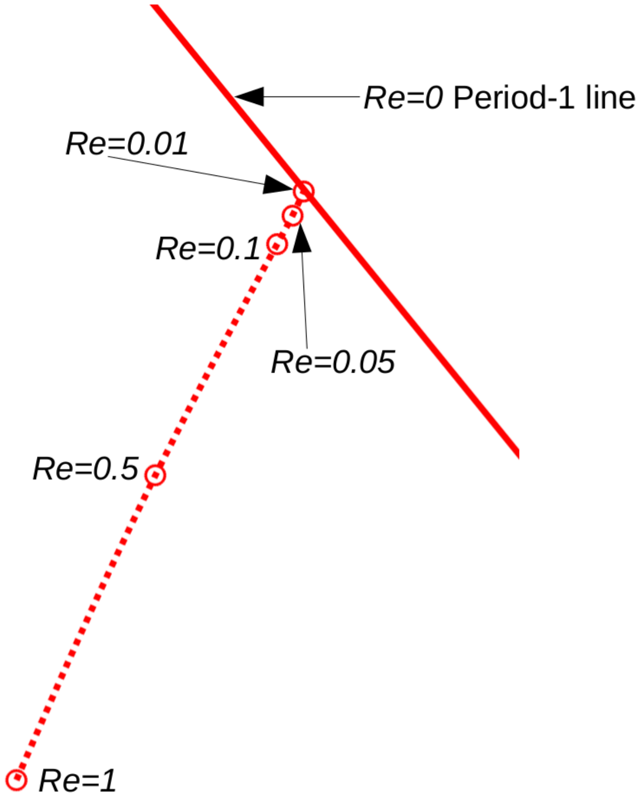

(b) A hyperbolic-node period-1 point approaches a point on a hyperbolic period-1 line segment of the Stokes flow

Figure 5.2: In the limit $Re \to 0$, isolated period-1 points approach points on the Stokes period-1 line.

5.1.3 Some features of the isolated period-1 points

Isolated period-1 points are calculated using the method discussed in section 3.7 for various system parameter values (Θ and β) in the inertial regime with $Re \in (10^{-2}, 1)$. From these calculations, some of the observed features of the isolated period-1 points are listed below, and the actual results are discussed later in this chapter.

1. In the limit $Re \to 0$; an isolated period-1 point approaches a point on the Stokes period-1 line as shown in figure 5.2. In this figure, a hyperbolic-focus period-1 point moves toward an elliptic point of the Stokes period-1 line and hyperbolic-node period-1 point moves toward a hyperbolic point of the Stokes period-1 line.
2. The isolated period-1 points of the inertial flow are located very close to the Stokes period-1 line (separation $\lessapprox 10^{-3}$ for $Re = 1$).
3. As β increases, the length of the period-1 line increases in the Stokes flow, whereas in the inertial flow the number of isolated period-1 points increases.
4. The period-1 line of the Stokes flow manifests into 1D manifolds of the inertial flow as shown in figure 5.5(a).
5. A heteroclinic connection always appears between two hyperbolic-focus period-1 points as shown in the figure 5.5(b).

5.1.4 General conventions regarding figures

Some general conventions regarding figures followed in this chapter are listed below.

Viewing isolated period-1 points: Since period-1 points are found very close to the Stokes period-1 line which is on the symmetry plane, a thin slice (width $\approx 10^{-2}$ of hemisphere radius) of the hemisphere centred at the symmetry plane is considered such that the slice contains the isolated period-1 points. Then the slice of the hemisphere containing the Stokes period-1 line and isolated period-1 points of the inertial flow is viewed perpendicular to the symmetry plane (see example figure 5.5(a)). Hyperbolic-focus type period-1 points are shown as solid blue circles, and hyperbolic-node type period-1 points are shown as solid red circles. An elliptic period-1 line segment is shown as a blue coloured line, and the hyperbolic period-1 line segment is shown as a red line.

Viewing action and arc length values of the isolated period-1 points: To see the origin of an isolated period-1 point from the period-1 line, action vs arc length plot of the isolated period-1 points is helpful because in the limit $Re \to 0$ an isolated period-1 point $\to$ some point on the period-1 line. Although arc length values cannot be ascribed to the isolated period-1 points in the inertial regime, because the isolated period-1 points are located very close to the Stokes period-1 line, arc length and action values of isolated period-1 points are taken from their nearest Stokes period-1 points correspondingly. The purpose of finding the nearest point on the Stokes period-1 line is to see quickly where an isolated period-1 point is coming from the period-1 line. Then, action and arc length values of the isolated period-1 points and the Stokes period-1 line are plotted together (see example figure 5.5(b)). Hyperbolic-focus type period-1 points are shown as solid blue circles, and hyperbolic-node type period-1 points are shown as solid red circles. An elliptic period-1 line segment is shown as a blue coloured line, and the hyperbolic period-1 line segment is shown as a red line.

Viewing Poincaré sections: To understand fluid advection, particle orbits can be plotted in 3D space, and Poincaré section of the orbits can be made. But, plotting the particle orbits in 3D hemisphere space is cumbersome, and it is not possible to get a Poincaré section where particle piercing positions are recorded on the plane. To understand particle orbits, their periodic locations are plotted as dots with separate colours for each particle and only viewed on a thin slice containing Stokes period-1 line (see figure 5.7(c)).

5.2 A preview of main results for finite *Re*

To examine the effect of inertia on various possible Lagrangian structures of the Stokes flow that are due to the different parameter values (Lid displacement and Reorientation angle) of the PRHF, the structures are chosen for perturbation one by one in the order of increasing complexity identified in chapter 4. Due to the complexity of the system, only the structures up to the perturbed 1:1 resonance (see chapter 4) will be included in this thesis. Before the actual computational results are shown, the main findings of the perturbed flow are presented. A schematic of the Stokes Lagrangian structures and the corresponding perturbed Lagrangian structures are shown in figure 5.3. The left column of this figure presents a case structure on the Stokes symmetry plane of the hemisphere (that has been stretched onto a sphere). It shows the Stokes period-1 line (continuous line) and the invariant shells (dotted circles) of the Stokes PRHF. The right column of this figure presents the isolated period-1 points (blue and red circles represent hyperbolic-focus and hyperbolic-node period-1 points respectively) and the manifolds associated with them. Although, $Re = 1$ is considered in this schematic, other values $Re \in (0, 1)$ also produce qualitatively similar perturbed structures that will be shown later in section 5.3.1. The parameter β plays a significant role, with qualitative Lagrangian features changes as β

increases. The main features are described below.

Very low β value (see figure 5.3(a)): Generally, for very low β values, all period-1 points of the period-1 line are elliptic in the Stokes regime and each shell is pierced twice. After inertial perturbation, nested spheroids turn into nested tori. Two hyperbolic-focus points are associated with the nested tori, and a heteroclinic connection that connects the two hyperbolic-focus period-1 points occurs at the centre of the nested tori. Some examples of this type of Lagrangian structure are discussed in sections 5.3.1 and 5.3.2

Moderate β value (see figure 5.3(b)): As β increases, the length of the period-1 line increases in the Stokes regime, and the number of isolated period-1 points increase in the inertial regime. Because the period-1 line manifests subtly into 1D manifolds of the inertial flow, a chain of heteroclinic connections is formed connecting the isolated-focus period-1 points. An example of this kind of Lagrangian structure is discussed in section 5.3.3.

1:1 resonance (see figure 5.3(c)): As β increases further, the period-1 line becomes tangent to the invariant shells at two places on the period-1 line (see left of figure 5.3(c)), and the points at which the period-1 line is tangent to the invariant shell are called 1:1 resonance points. 1:1 resonance points always develop as pairs with increasing β. A period-1 line segment consisting of a pair of 1:1 resonance points are called a wiggle, and the part of the period-1 line segment between the two 1:1 resonance points is hyperbolic. It is observed, always, a hyperbolic-node period-1 point emerges from a point on the hyperbolic period-1 line segment which connects two 1:1 resonance points (from a wiggle). When the Stokes flow 1:1 resonance structure is perturbed by inertia, a 3D chaotic transport structure featuring non-heteroclinic connections of tubular transition regions is formed. This type of structure has not been observed before. The dotted circle in the figure represents a fuzzy shell (mixing zone) where chaotic mixing occurs. The heart of the matter is the advection of fluid particles proceeds in the following way: tubes → mixing zone → return to several isolated period-1 points → tubes. Numerical calculations of 1:1 resonance examples are discussed in section 5.4.

In the Stokes PRHF, for any fixed reorientation angle Θ, as β increases the complexity of the Lagrangian structures increases (see figure 5.4). The effect of the perturbation on these Stokes structures is discussed one by one in the following sections.

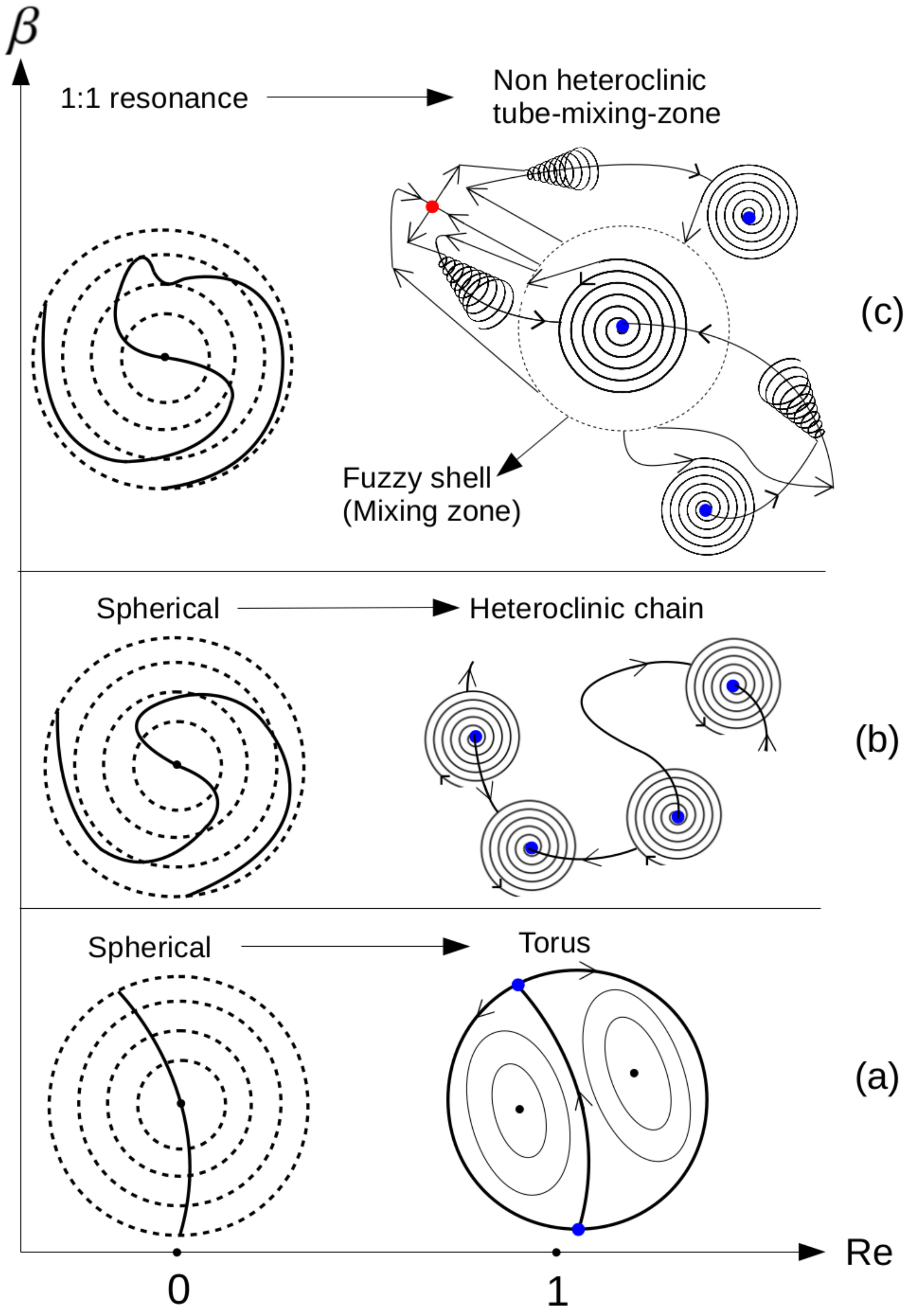
β
1:1 resonance
Non heteroclinic
tube-mixing-zone
Fuzzy shell
(Mixing zone)
(c)
Spherical
Heteroclinic chain
(b)
Spherical
Torus
(a)
Re
0
1

Figure 5.3: Schematic of the main results for the inertial PRHF

Stokes period-1 line structures		Period-1 line piercings on shells	Constant Θ
Simple ↓ Complex	Entire period-1 line is elliptic	2	β ↓
	Period-1 line contains elliptic line segments and hyperbolic line segments	2	
	Period-1 line contains one wiggle as well as elliptic line segments and hyperbolic line segments.	2 to 4	
	Period-1 line contains two wiggles as well as elliptic line segments and hyperbolic line segments.	2 to 6	

Figure 5.4: Stokes flow period-1 structures in the increasing order of complexity

5.3 Two period-1 piercings on shells

5.3.1 Very low β value

To examine the effect of inertia, the PRHF with the parameters $\Theta = \pi/8$ and $\beta = 0.1$ is considered since it has a pure elliptic period-1 line. The effect of the perturbation on this flow is first presented with $Re = 1$, and then the effect of varying Re on the Lagrangian transport structures is discussed later in this section. A numerical search for period-1 points in the $Re = 1$ flow found three hyperbolic-focus period-1 points. The isolated period-1 points and 1D manifolds of isolated period-1 points, and the Stokes period-1 line are shown in figure 5.5(a), and the corresponding action - arc length values are shown in figure 5.5(b). The period-1 line is also shown in this figure as a wide transparent blue line. This figure shows 1D manifolds of the inertial flow are close to the Stokes period-1 line.

To understand fluid particle orbits, a single particle is initialized at an arbitrary location and tracked for 4.85×10^4 periods. In figure 5.6, the position of the particle after every period is shown as dots in mint colour, and blue circles on the period-1 line are hyperbolic-focus period-1 points, and the solid black line is a 1D manifold with arrows showing the direction of the manifold. It is observed from figure 5.6 that the fluid particle moves on a toroidal surface. For low β, particle trajectories change from spheroids to toroids after the perturbation. In the Stokes flow, fluid particles move on a closed curve due to the elliptic nature of the period-1 line, and it can be considered as a two action flow locally. Adding inertia to the fluid, in this case, generated a secondary motion along the Stokes period-1 line that makes the particles move on a tube (particles spiral and move along the Stokes period-1 line) and it can be considered as a one action flow locally. After adding inertia, fluid particles in most of the flow (except some part of the domain at the bottom) spiral upwards around a 1D manifold (which is very close to the Stokes period-1 line) towards the lid, and spiral downwards, and join as shown in figure 5.6.

To find the effect of the magnitude of *Re* on fluid transport, three fluid particles positioned distantly from each other are considered and tracked until their orbits cover a full torus for Reynolds number values $\{0.01, 0.05, 0.1, 0.5, 1\}$. The particle orbits on a thin slice centered at the symmetry plane are shown in figure 5.7 for $Re = 0$ in (a), $Re = 0.01$ in (b), and $Re = 1$ in (c); black colour for particle 1, magenta for particle 2, and mint for particle 3. In figure 5.7 (a), the blue line represents the Stokes period-1 line, and because the particles move on a closed curve around an elliptic period-1 line in the Stokes flow, only dots are seen on the thin slice. In figure 5.7(b) and (c), blue solid circles represent isolated period-1 points. Isolated period-1 points are not exactly on the symmetry plane, but because they are very close to the symmetry plane, we can see them on the plot because they stay inside the slice. Black, magenta and mint lines on the plot are particle trajectories that move on toroidal surfaces. The particle orbits for $Re = 0.05$ and 0.5 are not shown in the figure 5.7 as they are qualitatively similar to the $Re = 0.01$ and 0.1 cases. From figure 5.7, it is observed, for low β values, fluid particle orbits remain on a torus. A torus is a product of two circles, and it has two periods (or two frequencies). The number of periods N required for a particle to complete advecting a full torus is equal to the largest period of the two periods of the torus. N is calculated for the same three particles with different *Re* values is shown in figure 5.7. As Reynolds number increases, a fluid particle requires fewer periods to complete a full torus. The magnitude of inertia effects the speed of transport: higher the inertia faster will be fluid transport. Although increasing inertia increases the speed with which Lagrangian structures form, it does not qualitatively change the Lagrangian structures of the flow when $Re \in (0, 1)$. This is true for higher values of β as well. Figure 5.8 shows the relationship between the speed of evolution of Lagrangian structures with Reynolds number. Because increasing inertia speeds up the process of computing Lagrangian structures without qualitatively changing them, the effect of inertia on Lagrangian transport structure is studied exclusively with $Re = 1$.

5.3.2 Low β values

In the Stokes flow, as β increases, the length of the period-1 line increases (see chapter 4). In the inertial flow, as β increases, the number of isolated period-1 points increases. For $\theta = \pi/8$ and $\beta = 1, 2, 3$ and 4, isolated period-1 points are calculated numerically and are shown in figure 5.9 (left) , and the corresponding action-arc length values are shown in figure 5.9 (right).

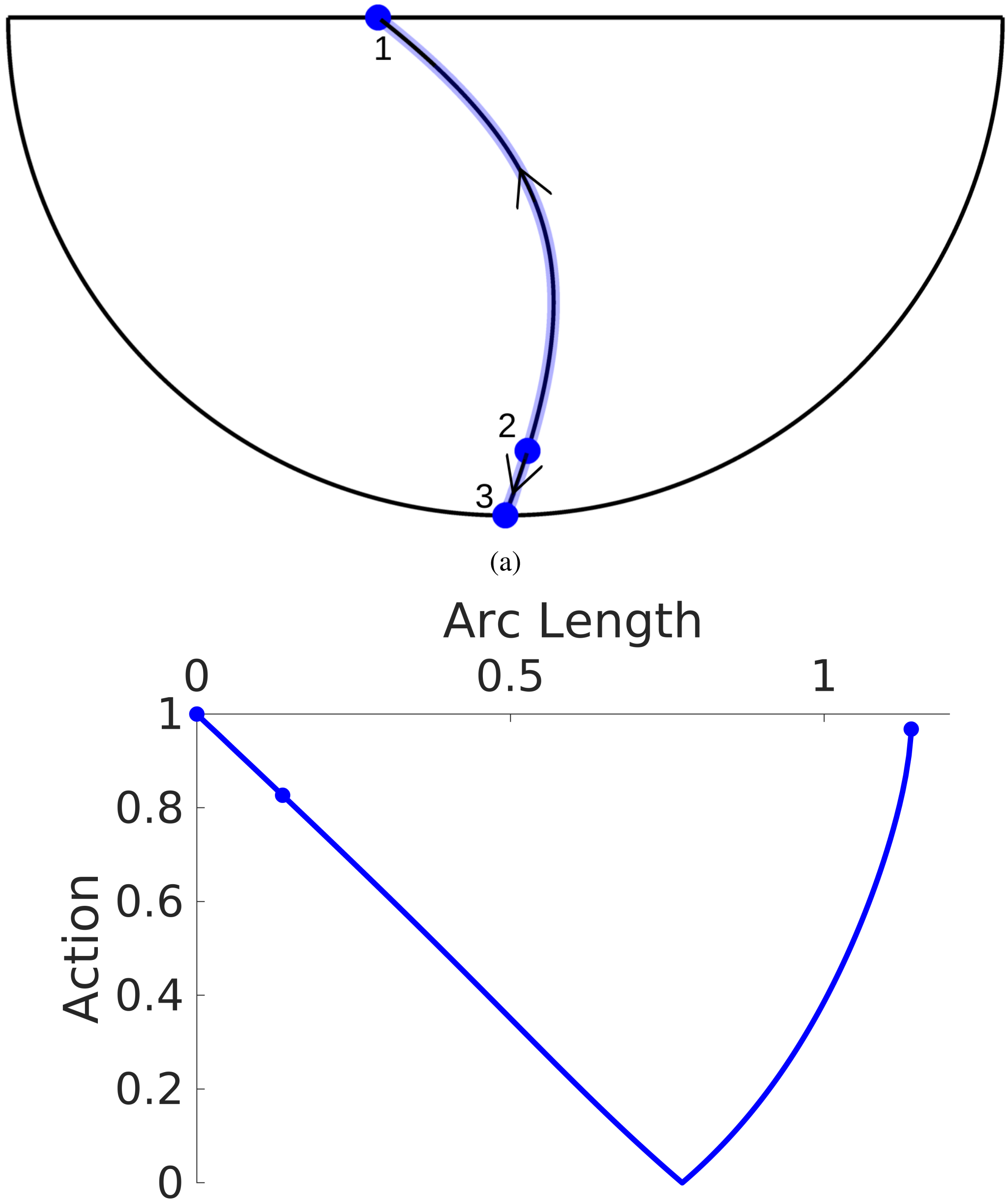

(a)

(b)

Figure 5.5: For $\Theta = \pi/8$ and $\beta = 0.1$: (a) For $\Theta = \pi/8$ and $\beta = 0.1$: a thin slice of the hemisphere centred at the symmetry plane containing isolated period-1 points which are shown as solid circles for $Re = 1$, 1D manifolds of isolated period-1 points (black continuous line), and the Stokes period-1 line (wide transparent blue line); (b) the same period-1 line and the isolated period-1 points paramaterized by action and arc length along the line. Arc length is in units of radius.

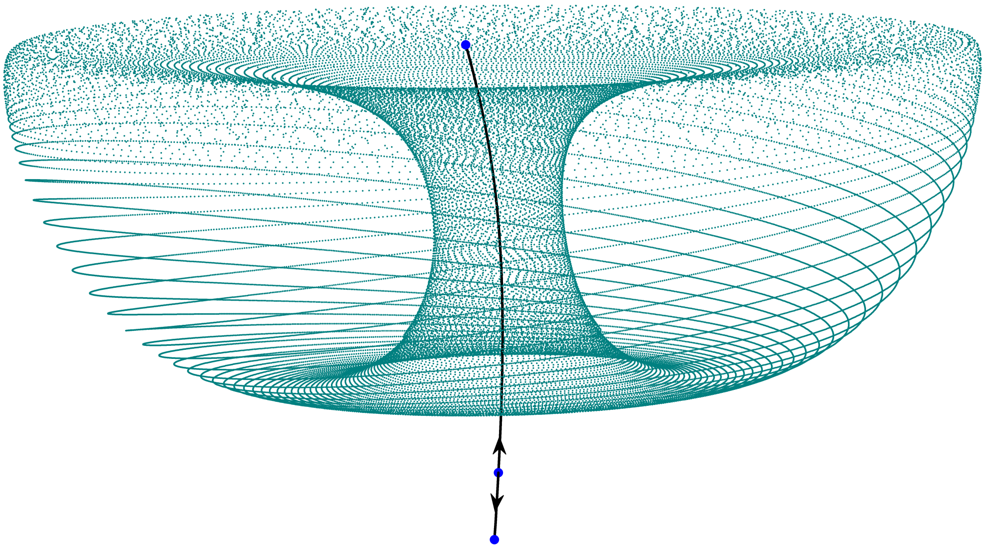

Figure 5.6: A fluid particle orbit (mint colour) for 4.85×10^4 periods with parameters $\Theta = \pi/8, \beta = 0.1$; Isolated period-1 points (in solid circles) and their 1D manifolds(black continuous lines with arrows showing the direction of the manifolds) are also seen.

In order to understand fluid transport, a few particles are chosen arbitrarily for each β and tracked to obtain their orbits for $\Theta = \pi/8$ and $\beta = 1, 3, 4$. $\beta = 0.5$ and 2 are omitted as they has similar period-1 structures to $\beta = 0.1$ and 1 correspondingly. The particle orbits are shown on a thin slice centred at the symmetry plane with separate colours for each orbit (see figure 5.10 (left)). The isolated period-1 points and the Stokes period-1 line are also shown in figure 5.10 (left). The trace1 (τ) and the trace2 (σ) values of the corresponding isolated period-1 points (bigger dots) and the Stokes period-1 line (small dots) are shown in figure 5.10 (right). It is difficult to detect where the isolated period-1 points that are close to the $y = x$ line on the trace1 vs trace2 plot fall, above or below the line without zooming in. Small arrows are added in the trace1 vs trace2 plots to such type of isolated period-1 points to show their location and hence their stability. For instance $\beta = 0.5$ in the figure 5.10 (right), point 1 has 1D stable/2D unstable manifolds and point 2 has 1D unstable/2D stable manifolds. A group of hyperbolic-focus period-1 points near the hemisphere bottom can be seen for all different β cases in figure 5.9. As β increases, the group of hyperbolic-focus period-1 points moves close to the hemisphere boundary, and hence their effect on the fluid transport becomes smaller except the period-1 point which is furthest from the hemisphere boundary in the group. The rest of the group of points have a minor effect. The hyperbolic-focus period-1 points in the group are connected with their neighbouring points by heteroclinic connections, and the hyperbolic-focus period-1 points have consecutively with alternative 1D stable/2D unstable and 1D unstable/2d stable manifolds. The low β behaviour of toroids persists until $2 < \beta < 3$

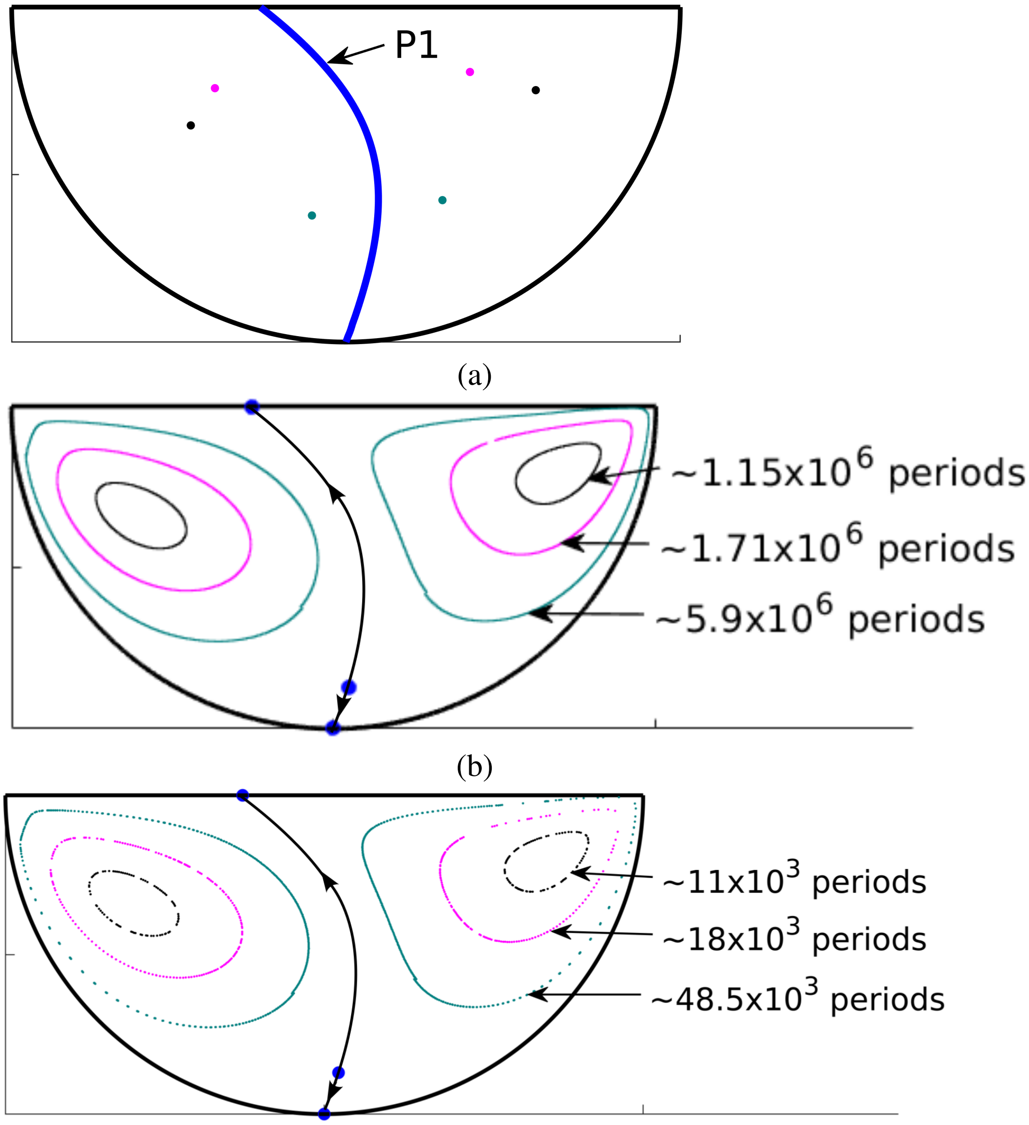
P1
~1.15x10^6 periods
~1.71x10^6 periods
~5.9x10^6 periods
~11x10^3 periods
~18x10^3 periods
~48.5x10^3 periods

(a)

(b)

(c)

Figure 5.7: A thin slice of the hemisphere with the width about 10^{-2} centered at the symmetry plane viewed perpendicular to the symmetry plane; Three particle orbits for $\beta = 0.1$ and $\Theta = pi/8$ are shown in black, magenta, and mint colours for $Re = 0$ in (a), $Re = 0.01$ in (b) and $Re = 1$ in (c). In (a), solid blue colour line represents Stokes period-1 line. In (b) and (c), solid circles represent isolated period-1 points of hyperbolic focus nature and black continuous line represents 1d manifolds.

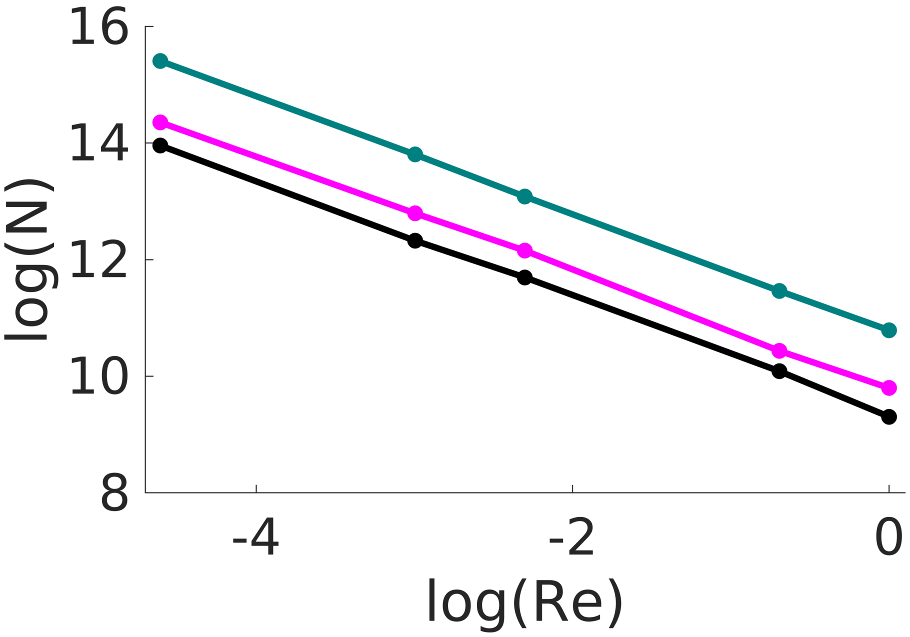

Figure 5.8: Logarithm of no of periods required for a particle orbit to form one torus for $\beta = 0.1$ and $\Theta = \pi/8$ versus logarithm of Reynolds numbers; 5 solid circles on lines correspond to 5 different Reynolds number values. i.e. Re ={ 0.01, 0.05, 0.1, 0.5, 1}

after which other isolated period-1 points emerge, and the particle orbits start becoming complex as seen in figure 5.10 for $\beta = 3$ and 4.

5.3.3 A chain of heteroclinic connections

The PRHF with the parameters $\Theta = \pi/4$ and $\beta = 8$ is considered because $\beta = 9$ has a 1:1 resonance structure in the Stokes regime, and in the order of the complexity of the Stokes Lagrangian structures $\beta = 8$ structures precede 1:1 resonance structures. The Stokes period-1 line and the isolated period-1 points are shown in figure 5.11(a). The isolated period-1 points numbered 1 and ≥ 6 are very close to the hemisphere boundary, and hence their influence on fluid transport is small. The isolated period-1 points numbered from 2 to 5 in figure 5.11(a) are important in forming the Lagrangian structures as they are away from the hemisphere boundary. The period-1 points 2-5 are shown in the trace1 vs trace2 plot in figure 5.11(b) from which their stability can be deduced. Points 2 and 4 have 1D unstable and 2D stable manifolds since they fall below the $y = x$ line, and points 3 and 5 have 1D stable and 2D unstable manifolds since they fall above $y = x$ line. The Stokes period-1 line and the inertial flow isolated period-1 points are parameterized by action, and arc length along the Stokes period-1 line are shown in figure 5.11(c).

The manifolds of the period-1 points 2-5 are calculated numerically as described in section 5.1.2 and are shown in figure 5.12 which is a thin slice of the hemisphere centred at the symmetry plane viewed perpendicular to the symmetry plane. In figure 5.12, the

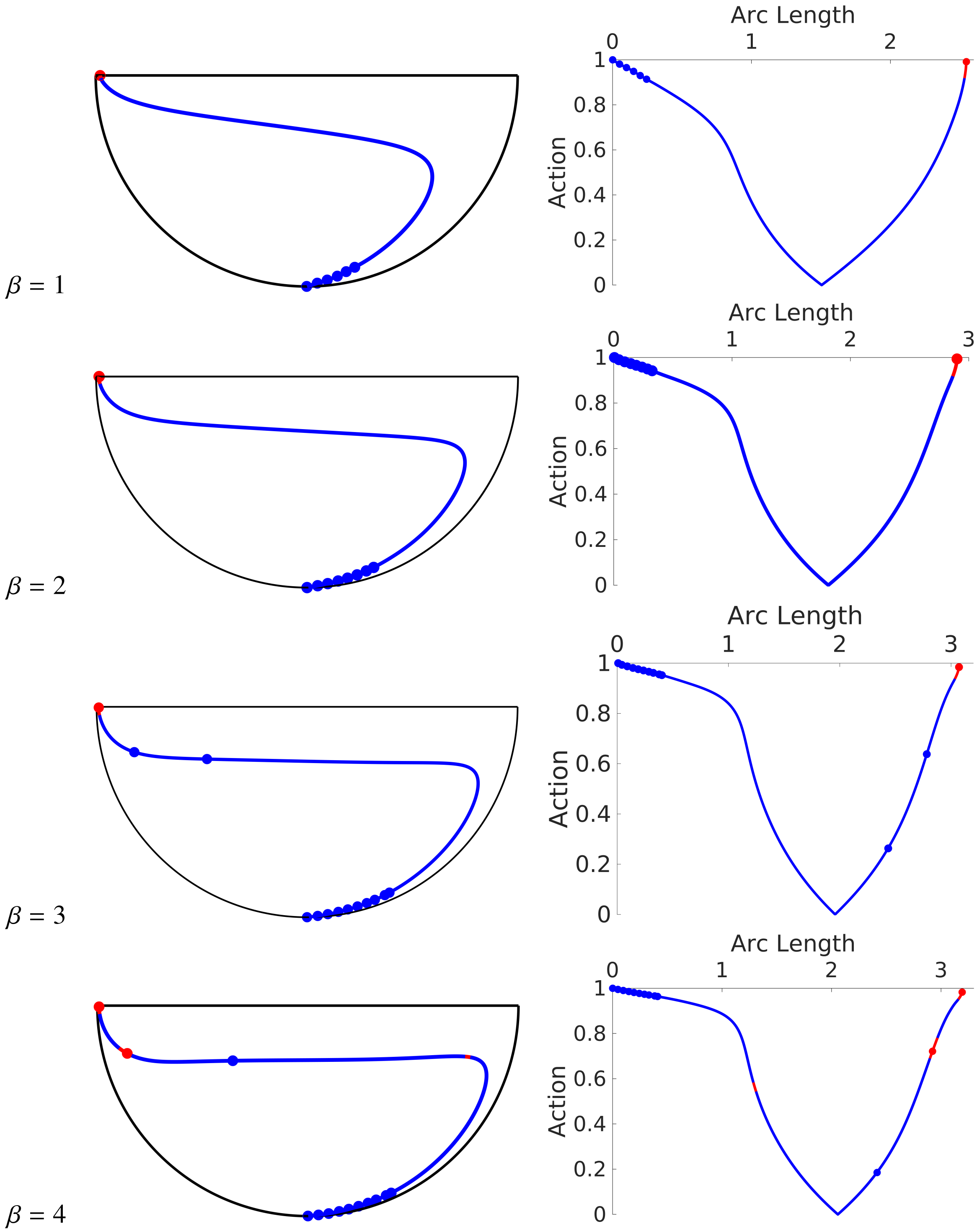

Figure 5.9: For $\Theta = \pi/8$ and indicated values of β: (left) a thin slice of the hemisphere centred at the symmetry plane containing the Stokes period-1 line which is shown as a continuous line and isolated period-1 points which are shown as solid circles for $Re = 1$ is viewed perpendicular to the symmetry plane; (right) the same period-1 line and the isolated period-1 points paramaterized by action and arc length along the line.

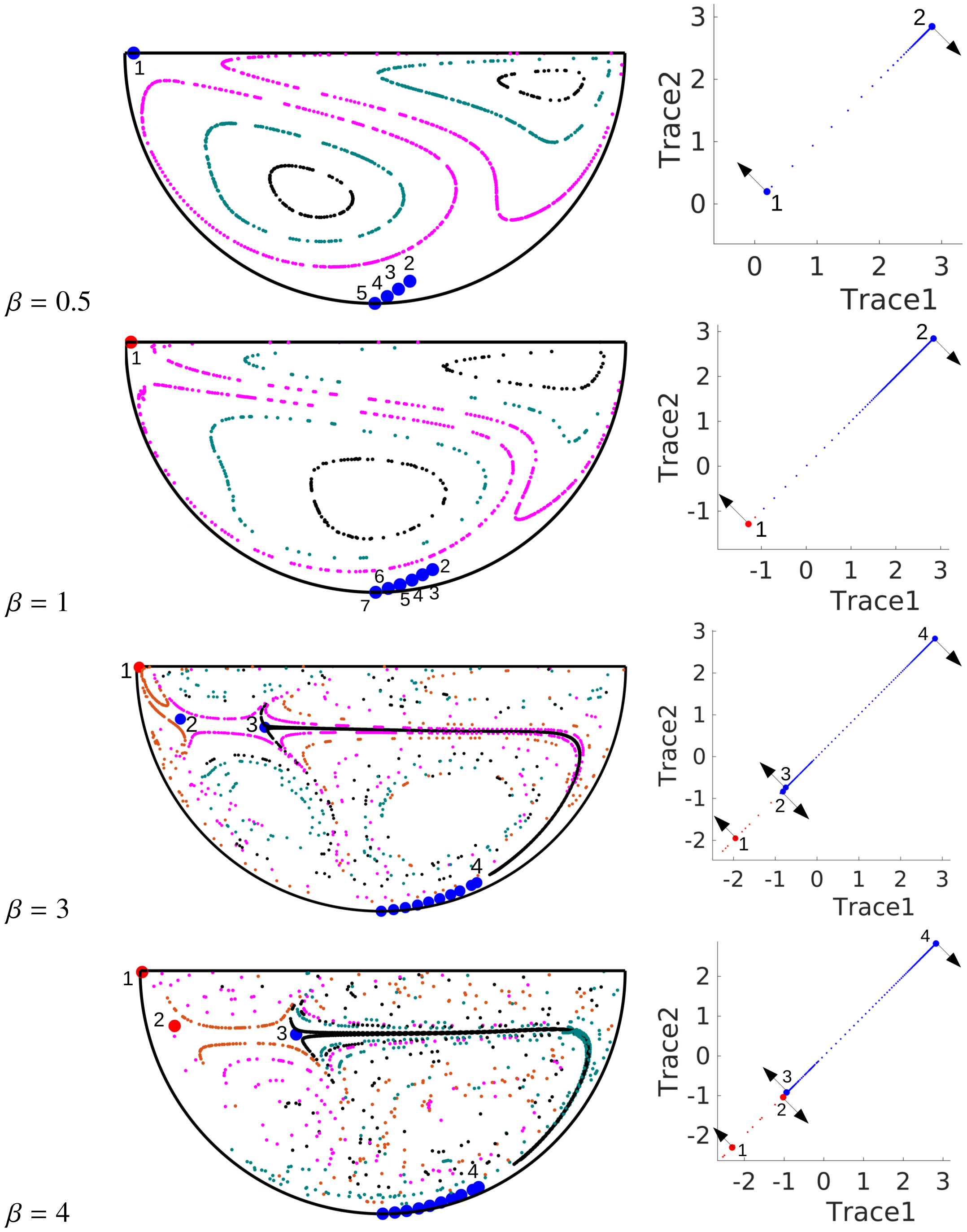

Figure 5.10: For $\Theta = \pi/8$ and indicated values of β: (left) a thin slice of the hemisphere with width about 10^{-2} centred at the symmetry plane containing particles orbits which are shown as dots with separate colours for different orbits for $Re = 1$ and the isolated period-1 points which are shown as solid circles; (right) Trace 1 vs Trace2 of the period-1 points of both stokes flow and Re=1 flow; small dots represent stokes period-1 points; bigger dots represent $Re = 1$ flow period-1 points.

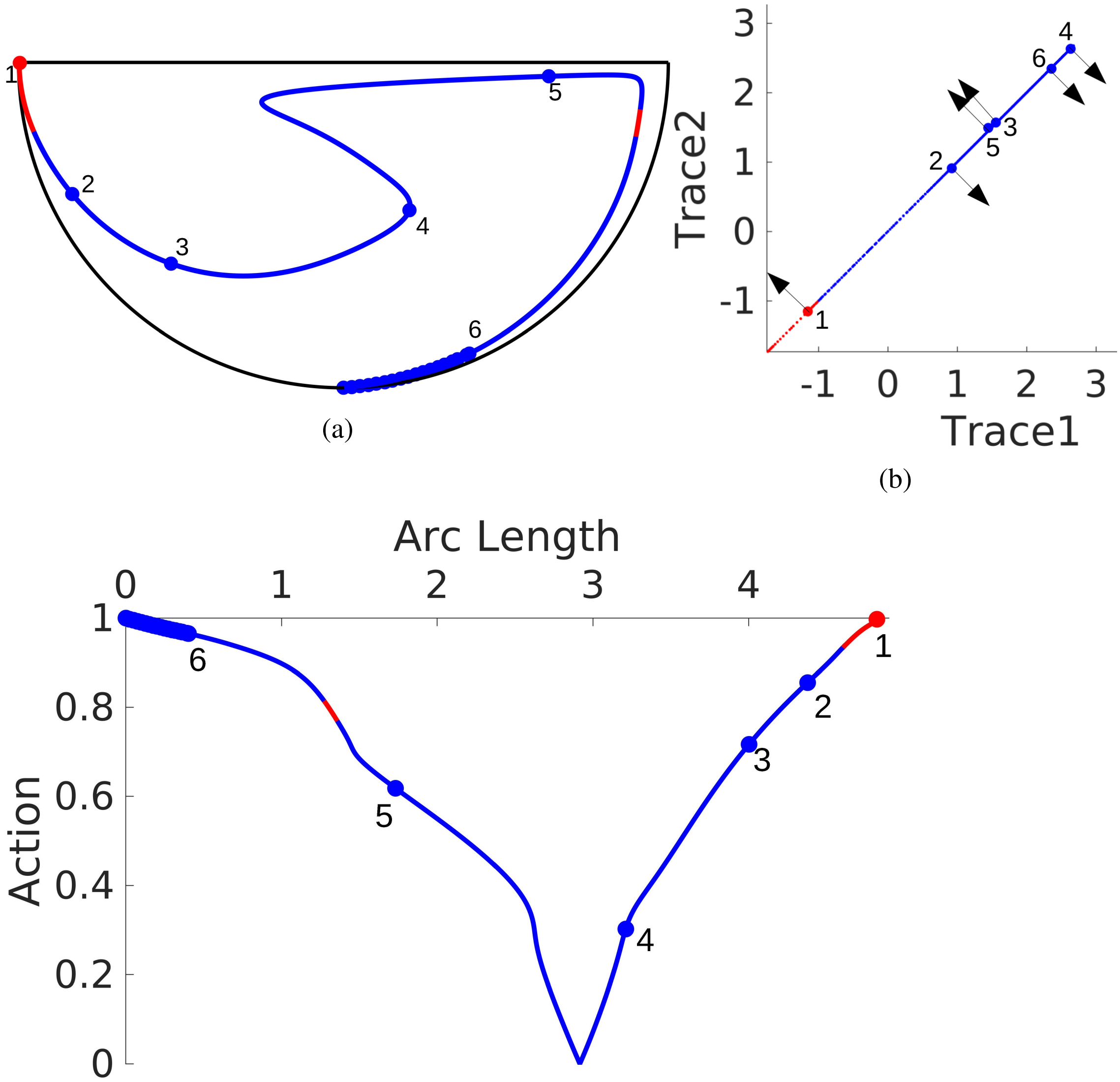

(a)

(b)

(c)

Figure 5.11: For $\Theta = \pi/4$ and $\beta = 8$: (a) Stokes Period-1 line and the isolated period-1 points of $R = 1$ flow; (b) Trace 1 vs Trace2 of the period-1 points of both the Stokes flow and Re=1 flow (small dots represent stokes period-1 points and bigger dots represent $Re = 1$ flow); (c) The Stokes period-1 line and the isolated period-1 points of $Re = 1$ flow are parameterized by action and arc length.

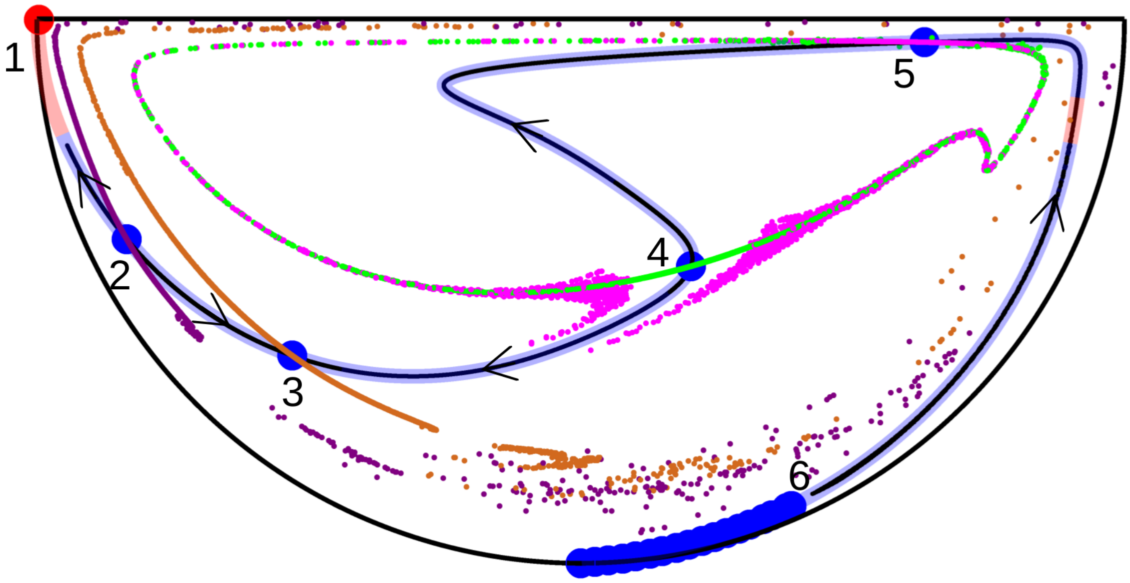

Figure 5.12: For $\Theta = \pi/4$ and $\beta = 8$ (a thin slice of the hemisphere centered at the symmetry plane viewed perpendicular the symmetry plane): Isolated period-1 points are shown as solid circles; Thick transparent line represents the Stokes period-1 line; Continuous black line represents 1D manifolds of the isolated period-1 points; Small dots represent 2D manifolds of the isolated period-1 points (2D unstable manifold of point 5 in magenta, 2D stable manifold of point 4 in green, 2D unstable manifold of point 3 in chocolate and 2D stable manifold of point 2 in violet)

large solid circles represent the isolated period-1 points, the transparent continuous line represents the Stokes period-1 line, continuous black lines represent the 1D manifolds, and small dots represent 2D manifolds. The 1D manifolds of the isolated period-1 points follow the Stokes period-1 line seen in figure 5.12. Heteroclinic connections between point 2 and 3, and between 3 and 4, and between 4 and 5 can be seen in the figure, and there is a chain of heteroclinic connections from point 2 to point 5. The 2D unstable manifold of point 5 merges with the 2D stable manifold of point 4 and forms a fuzzy shell. Fluid particles inside this fuzzy shell spiral around the 1D manifold and move along the direction of the 1D expanding manifold. Similarly, the 2D stable manifold of point 2 merges with the 2D unstable manifold of point 3 and forms another fuzzy shell. In the Stokes regime, in the neighbourhood of an elliptic period-1 line segment, fluid particles move on a closed curve, making it a two action flow locally. After the inertial perturbation, the elliptic period-1 line segments turn into 1D manifolds of isolated period-1 points, and the fluid particles move along the 1D manifold while spiralling around it. Mixing occurs in the space of fuzzy shell regions where 2D manifolds of different isolated period-1 points merge. The fuzzy shells appear to act as barriers to mixing.

5.4 One wiggle

As β increases further, a wiggle appears in the Stokes period-1 line that has two 1:1 resonance points at the local extrema of the wiggle. Across the wiggle, the period-1 line stability goes from elliptic to hyperbolic to elliptic, and the period-1 line segment between the two extrema is hyperbolic. Although most shells have two piercings in the Stokes flow, a subset has four piercings. When perturbed this, the wiggle results in a 3D chaotic transport structure featuring non-heteroclinic connections of tubular transition regions.

5.4.1 $\Theta = \pi/5$ and $\beta = 10$

The PRHF with the parameter values $\Theta = \pi/5$ and $\beta = 10$ is considered as an example of a period-1 line with a wiggle. The Stokes flow period-1 line and the isolated period-1 points are shown in figure 5.13(a). The Stokes period-1 line and the inertial period-1 points are parameterized by action and arc length along the Stokes period-1 line are shown in figure 5.13(c). The period-1 points from 2 to 7 are away from the hemisphere boundary, and their influence on fluid transport is large compared to the remaining period-1 points. The trace1 vs trace2 values of the period-1 points are shown in figure 5.13(b) which allows us to determine the nature of the stability of the period-1 points.

The stable and unstable manifolds of the period-1 points from 2-7 are calculated numerically as described in section 5.1.2 and are shown on a thin slice of the hemisphere centred at the symmetry plane in figure 5.14. Figure 5.14 shows: the isolated period-1 points as solid large circles, the Stokes period-1 line as a transparent thick line, 1D manifolds as continuous black lines and 2D manifolds as small dots (2D unstable of point 7 in green, 2D unstable of point 5 in magenta, 2D stable of point 4 in sky blue, 2D unstable of point 3 in chocolate and 2D stable of point 2 in violet). The manifolds of point 6 are not shown in figure 5.14 as they do not appear because they are nearly perpendicular to the thin slice plane.

The 2D stable manifold of point 4 and the 2D unstable manifold point 7 merges and form a fuzzy shell (called $S1$). The 2D unstable of point 5 also joins the fuzzy shell $S1$. The 2D unstable manifold of point 3 and 2D stable manifold of point 2 also merge. The manifolds of the period-1 points from 2 to 7 and their manifold connections are described one by one below.

- The manifolds of point 7 are shown in figure 5.15a: The right side of the yellow 1D stable manifold of point 7 comes from the bottom of the hemisphere and spirals around the Stokes period-1 line. The reason for the straight edges of the yellow 1D

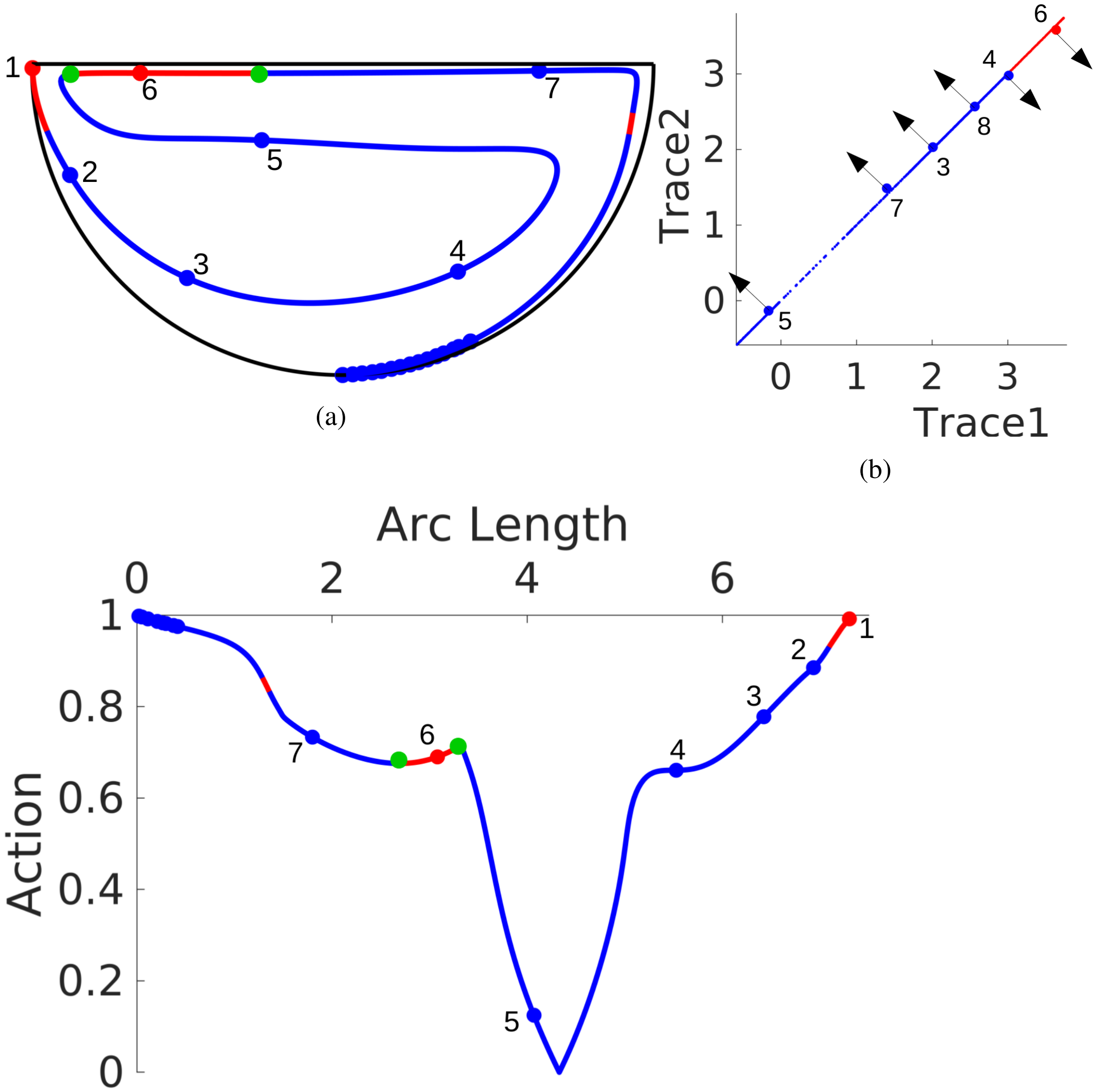

(a)

(b)

(c)

Figure 5.13: For $\Theta = \pi/5$ and $\beta = 10$: (a) Stokes Period-1 line and the isolated period-1 points of $R = 1$ flow; (b) Trace 1 vs Trace2 of the period-1 points of both the Stokes flow and Re=1 flow (small dots represent stokes period-1 points and bigger dots represent $Re = 1$ flow); (c) The Stokes period-1 line and the isolated period-1 points of $Re = 1$ flow are parameterized by action and arc length.

manifold at the bottom of this figure is explained in the following. Because fluid particles move discretely on the 1D manifold, I made the discrete 1D manifold line continuous by joining the points on the manifold. There are few points on the 1D manifold, and hence straight edges appear. The left side of the yellow 1D stable manifold of point 7 comes from the fuzzy shell $S1$, and the green 2D unstable manifold of point 7 forms the fuzzy shell $S1$.

- The orange unstable manifold of point 6 spirals about the yellow 1D stable manifold of point 7 and merges with the green 2D unstable manifold of point 7 (see figure 5.15b). The stable and unstable manifolds of point 6 are shown in figure 5.15c. The cyan stable manifolds of point 6 come from the fuzzy shell $S1$.

- The orange unstable manifold of point 6 spirals about the white 1D stable manifold of point 5 and joins the magenta 2D unstable of point 5 (see figure 5.15d). The stable and unstable manifolds of point 5 are shown in figure 5.15e.

- The salmon colour unstable manifold of point 4 spirals about the white 1D stable manifold of point 5 and joins the magenta 2D unstable of point 5 (see figure 5.15f). The stable and unstable manifolds of point 4 are shown in figure 5.15g.

- The salmon colour unstable manifold of point 4 spirals about the green-yellow clour 1D stable manifold of point 3 and joins the chocolate colour 2D unstable manifold of point 3 (see figure 5.15h). The stable and unstable manifolds of point 3 are shown in figure 5.15i.

- Point 2 and point 3 are connected via a heteroclinic connection (see figure 5.15i).

All the manifolds from point 5 to point 7 are shown together in the top image of figure 5.16, and all the manifolds from the point 2-5 are shown together in the bottom image of the figure 5.16. Importance of these observations is summarised after providing another example.

5.4.2 $\Theta = \pi/4$ and $\beta = 9$

Another example for one wiggle case with the parameter values $\Theta = \pi/4$ and $\beta = 9$ is briefly considered to compare it with the case $\Theta = \pi/5$ and $\beta = 10$. The Stokes flow period-1 line and the $Re = 1$ flow period-1 points are shown in figure 5.17(a). The Stokes period-1 line and the inertial period-1 points are shown in figure 5.17(c). The period-1 points from 2 to 7 are away from the hemisphere boundary, and their influence on fluid transport is large compared to the remaining period-1 points. The trace1 and trace2 values

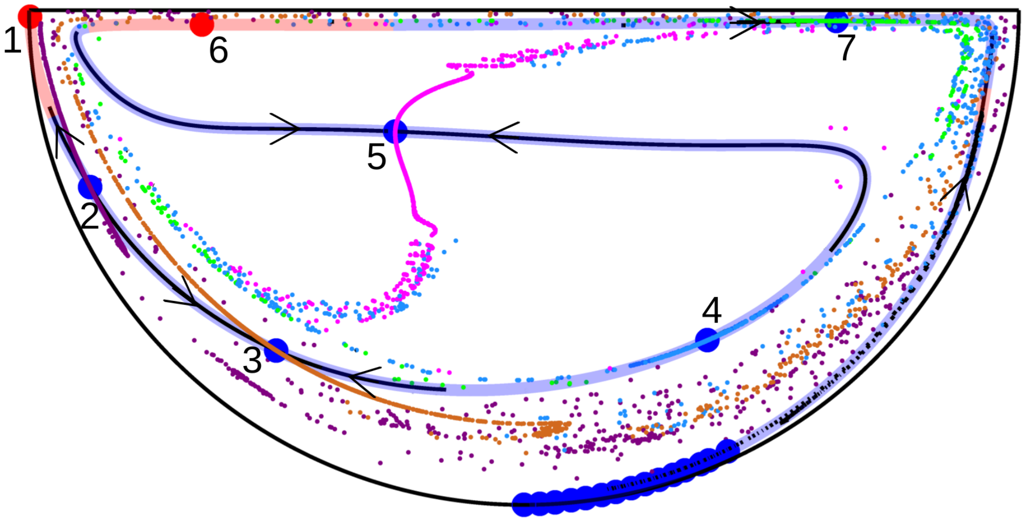

Figure 5.14: For $\Theta = \pi/5$ and $\beta = 10$ (a thin slice of the hemisphere centered at the symmetry plane viewed perpendicular the symmetry plane): Isolated period-1 points are shown as solid circles; Thick transparent line represents the Stokes period-1 line; Continuous black line represents 1D manifolds of the isolated period-1 points; Small dots represent 2D manifolds of the isolated period-1 points (2D unstable manifold of point 7 in green, 2D unstable manifold of point 5 in magenta, 2D stable manifold of point 4 in sky blue, 2D unstable manifold of point 3 in chocolate and 2D stable manifold of point 2 in violet)

of the period-1 points are shown in figure 5.17(b) which allows us to determine the nature of the stability of the period-1 points.

The stable and unstable manifolds of the period-1 points are calculated numerically for points 2-7 as described in the section 5.1.2 and they are shown on a thin slice of the hemisphere centred at the symmetry plane in figure 5.18. Figure 5.18 shows: the isolated period-1 points as solid large circles, the Stokes period-1 line as a transparent thick line, 1D manifolds as continuous black lines and 2D manifolds as small dots (2D unstable manifold of point 7 in green, 2D unstable manifold of point 5 in magenta, 2D stable manifold of point 4 in sky blue, 2D unstable manifold of point 3 in chocolate and 2D stable manifold of point 2 in violet). The manifolds of point 6 are not shown in the figure 5.18 as they do not appear because they are perpendicular (not exactly perpendicular but slant) to the thin slice. The 2D stable manifold of point 4 and the 2D unstable manifold point 7 merge and form a fuzzy shell, the 2D unstable manifold of point 5 also joins with the fuzzy shell. The 2D unstable manifold of point 3 and 2D stable manifold of point 2 also merges.

All the manifolds from points 5 to 7 are shown together in the top image of figure 5.16, and all the manifolds from points 2-5 are shown together in the bottom image of the figure 5.16.

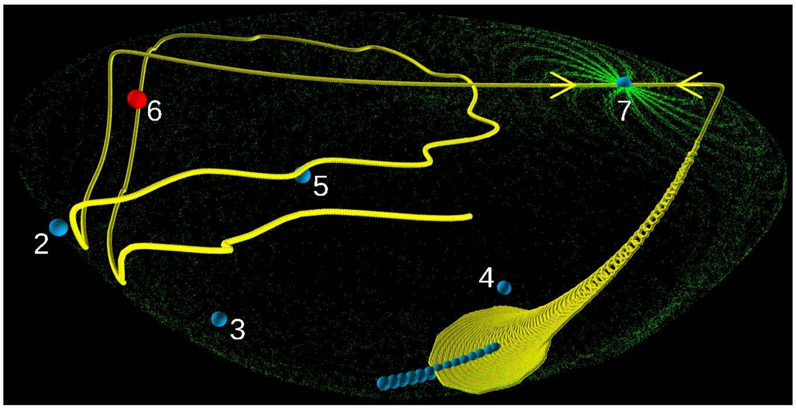

(a) Point 7 manifolds: 2D unstable manifold in green and 1D stable manifold in yellow

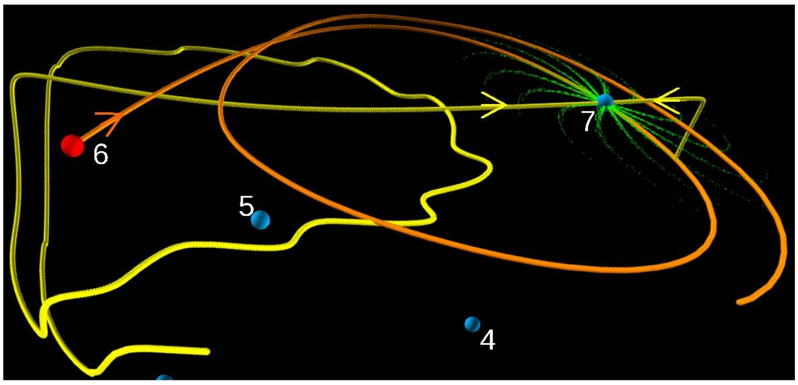

(b) Orange 1D unstable manifold of point 6 spirals around yellow 1D stable of point 7.

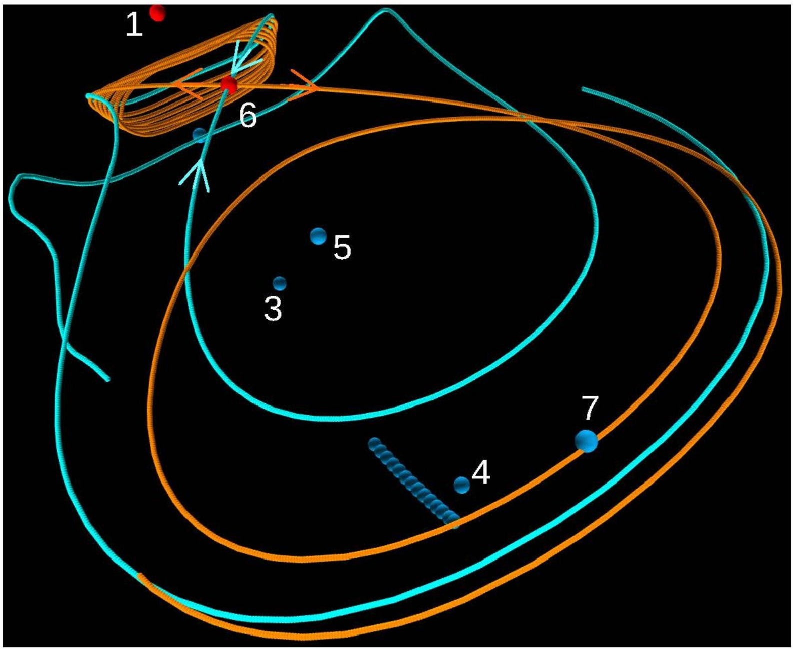

(c) Point 6 manifolds: 1D unstable manifold in orange and 1D stable manifold in cyan

Figure 5.15: A 3D view of the manifolds and their interactions of the period-1 points 6 and 7 for $\Theta = \pi/5$ and $\beta = 10$

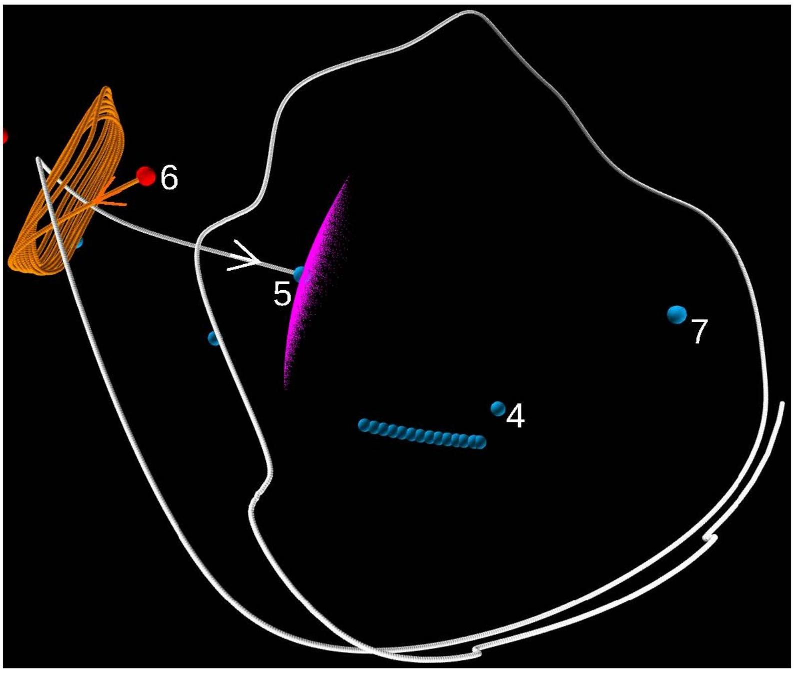

(d) Orange 1D unstable manifold of point 6 spirals around white 1D stable of point 5.

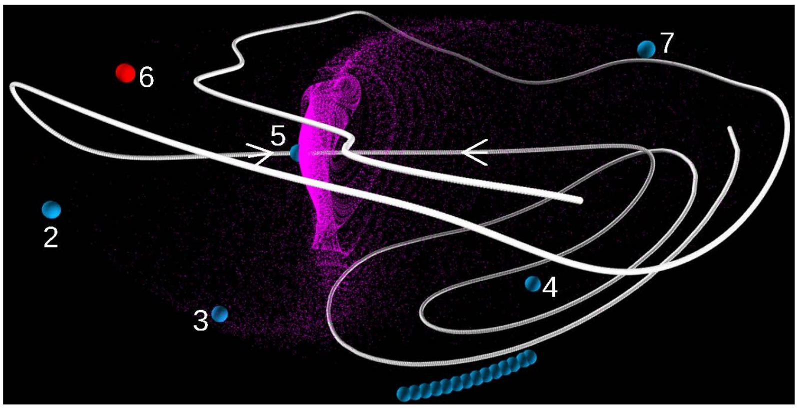

(e) Point 5 manifolds: 2D unstable manifold in magenta and 1D stable manifold in white.

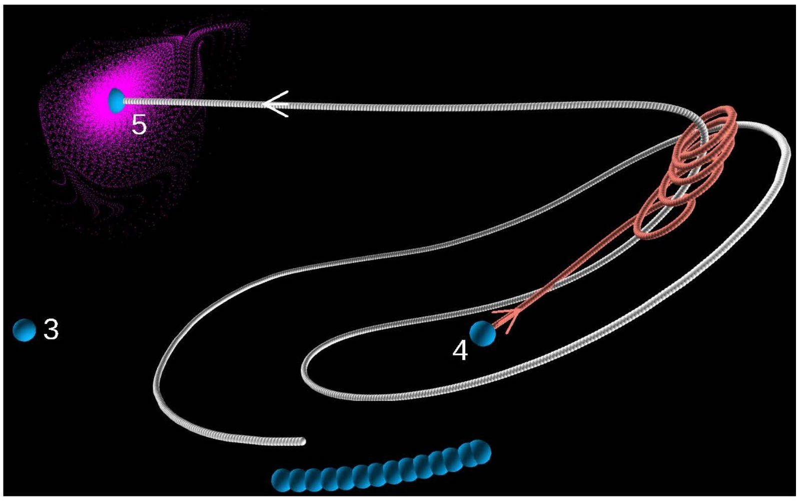

(f) Salmon colour 1D unstable manifold of point 4 spirals around yellow 1D stable manifold of point 5.

Figure 5.15: A 3D view of the interaction of the manifolds of the period-1 points 4,5 and 6 for $\Theta = \pi/5$ and $\beta = 10$

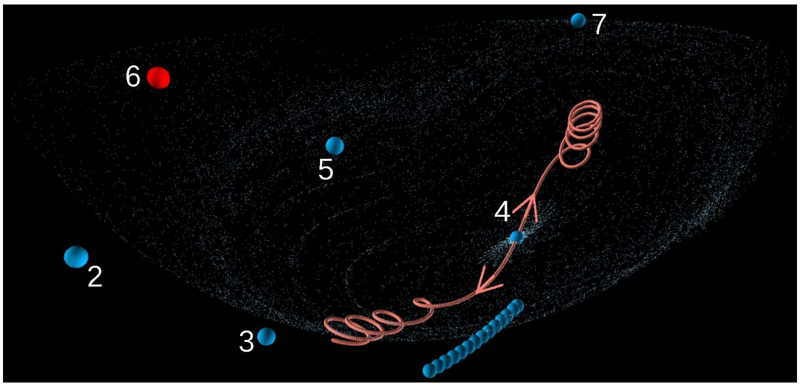

(g) Point 4 manifolds: 2D stable manifold in sky blue and 1D unstable manifold in salmon colour

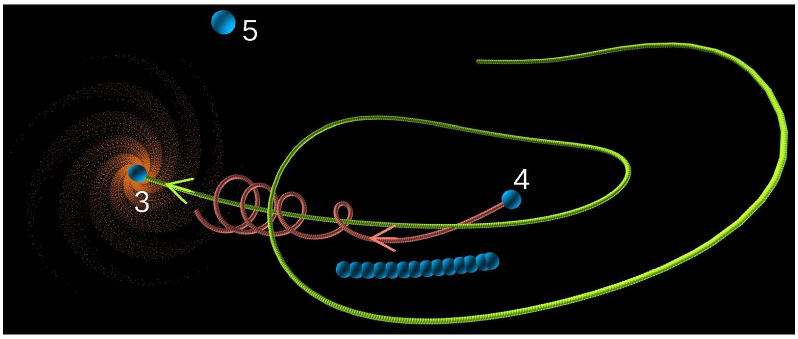

(h) salmon colour 1D unstable manifold of point 4 spirals around yellow 1D stable manifold of point 3.

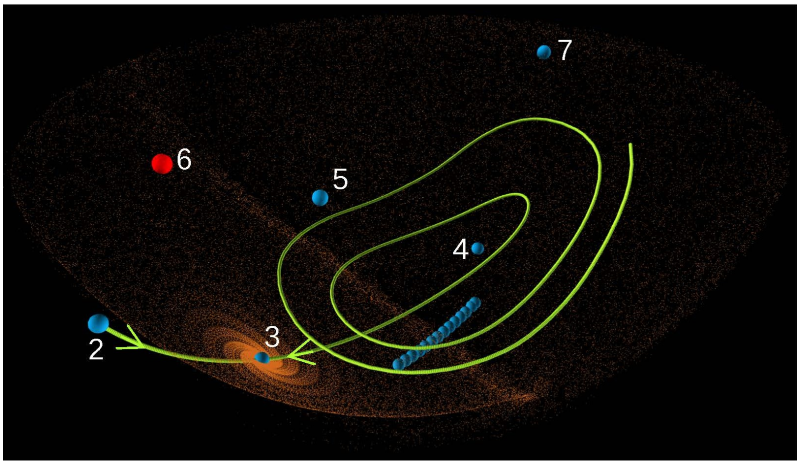

(i) Period-1 point 3 manifolds: 2D unstable manifold in chocolate colour and 1D stable manifold in green-yellow colour

Figure 5.15: A 3D view of the interaction of the manifolds of the period-1 points 3 and 4 for $\Theta = \pi/5$ and $\beta = 10$

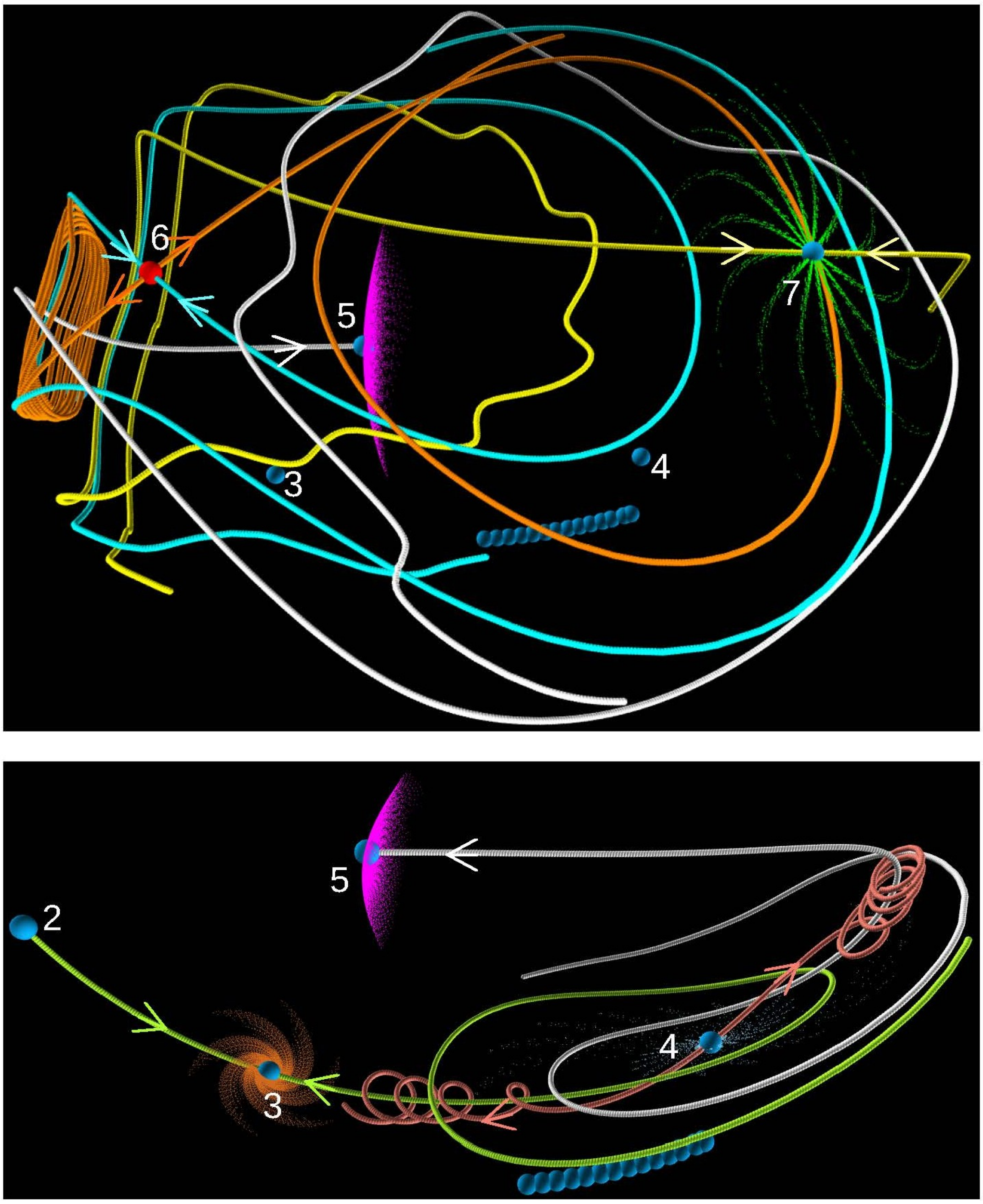

Figure 5.16: A 3D view of the isolated period-1 points and their manifolds for $\Theta = \pi/5$ and $\beta = 10$: (top) 1D stable manifold in yellow and 2D unstable manifold in green for point 7, 1D unstable manifold in orange and 1d stable manifold in cyan for point 6, and 1d stable manifold in white and 2D unstable manifold in magenta for point 5; (bottom) 1D stable manifold in white and 2D unstable manifold in magenta for point 5, 1D unstable manifold in salmon colour and 2D stable manifold in sky blue for point 4, and 1D stable manifold in green-yellow and 2D unstable manifold in chocolate colour for point 3.

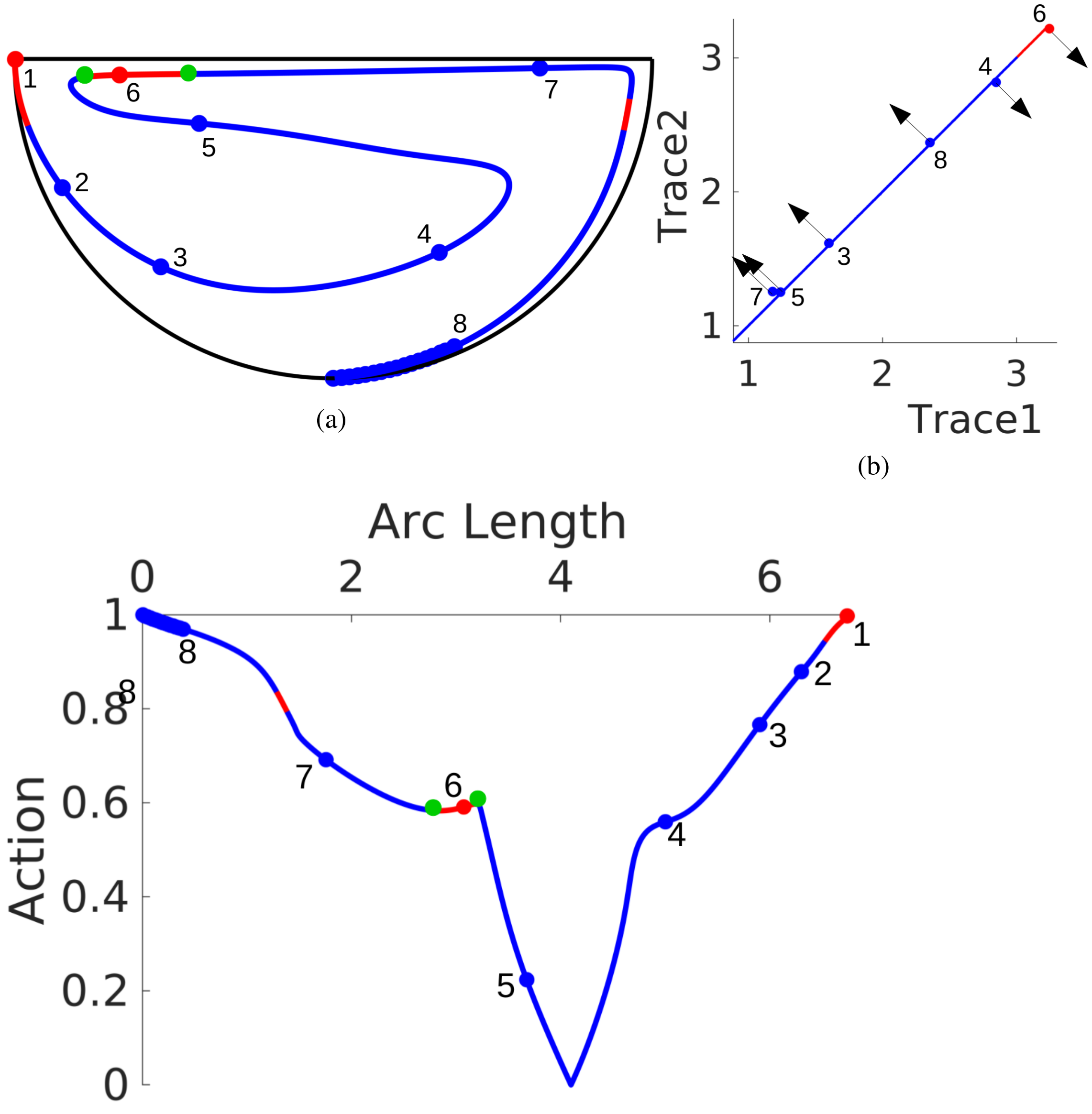

(a)

(b)

(c)

Figure 5.17: For $\Theta = \pi/4$ and $\beta = 9$: (a) Stokes period-1 line and the isolated period-1 points of $R = 1$ flow; (b) Trace 1 vs Trace2 of the period-1 points of both the Stokes flow and Re=1 flow (small dots represent stokes period-1 points and bigger dots represent $Re = 1$ flow); (c) The Stokes period-1 line and the isolated period-1 points of $Re = 1$ flow are parameterized by action and arc length.

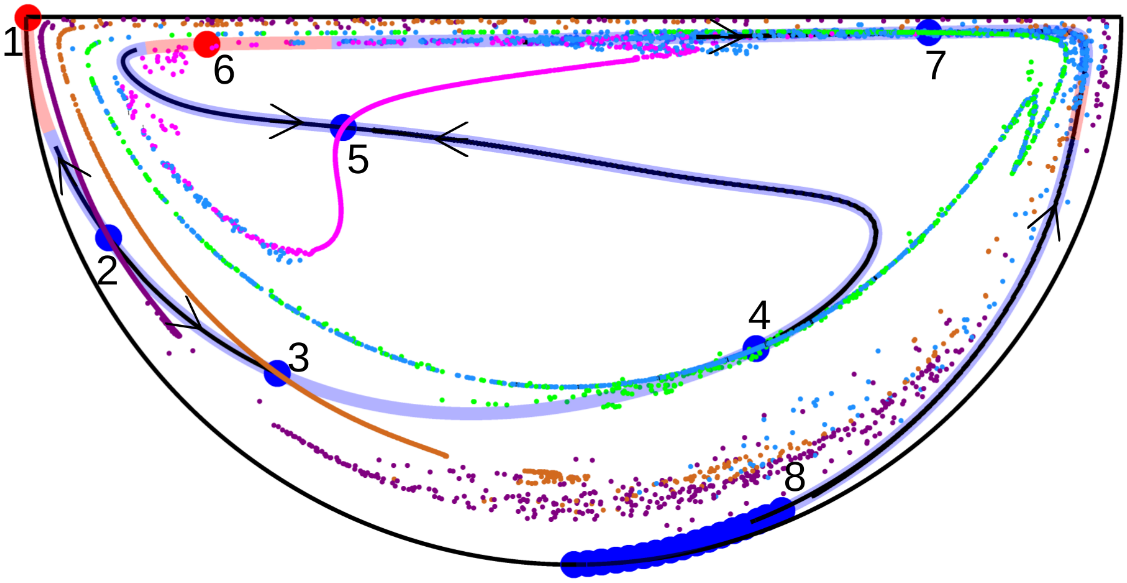

Figure 5.18: For $\Theta = \pi/4$ and $\beta = 9$ (a thin slice of the hemisphere centered at the symmetry plane viewed perpendicular the symmetry plane): Isolated period-1 points are shown as solid circles; Thick transparent line represents the Stokes period-1 line; Continuous black line represents 1D manifolds of the isolated period-1 points; Small dots represent 2D manifolds of the isolated period-1 points (2D unstable manifold of point 7 in green, 2D unstable manifold of point 5 in magenta, 2D stable manifold of point 4 in sky blue, 2D unstable manifold of point 3 in chocolate colour and 2D stable manifold of point 2 in violet)

The figures (5.14, 5.18) and (5.16, 5.19) show that both the cases ($\Theta = \pi/5, \beta = 10$) and ($\Theta = \pi/4$, $\beta = 9$) have similar Lagrangian transport structures (similar manifolds connections between the isolated period-1 points) in the inertial regime. The effect of perturbation via inertia on the similar Stokes Lagrangian structures is also similar irrespective of the parameter values.

In the two examples of one wiggle case (a pair of 1:1 resonance points), a fluid transport pattern is seen that fluid particles from the fuzzy shell region (chaotic mixing zone) → several isolated period-1 points → tubular regions → the fuzzy shell. This pattern is shown in the the schematic figure 5.3(c). This is one of the mechanisms by which chaotic transport occurs, and it has never been observed before. Interestingly, this kind of tubular transition regions are generally observed in Hamiltonian systems of higher dimensions (Ross *et al.*, 2018), and for the first time, they are observed in incompressible fluids. This kind of transport structure emerges whenever a pair of 1:1 resonance points are perturbed by inertia. Hence, it is conjectured to be a generic behaviour.

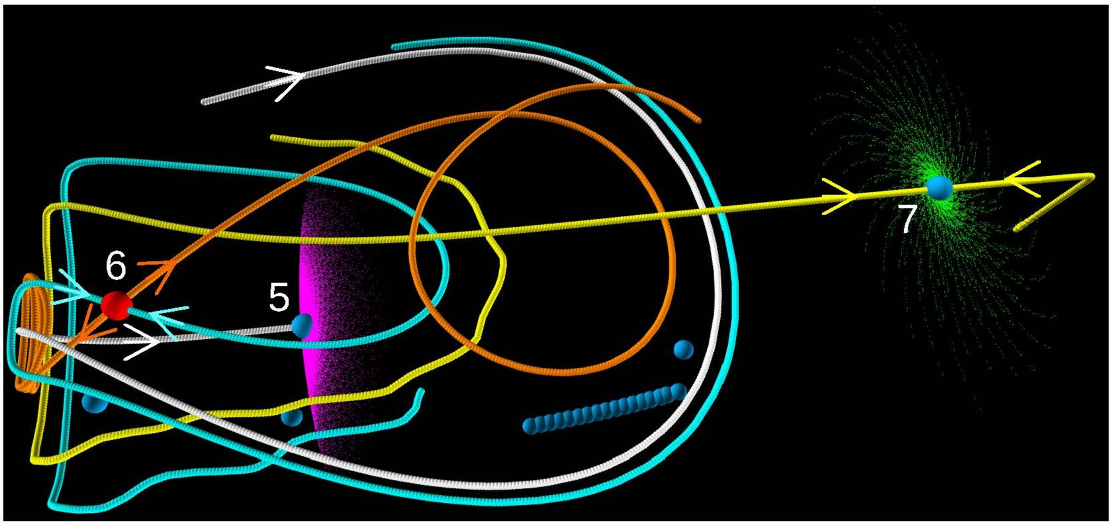

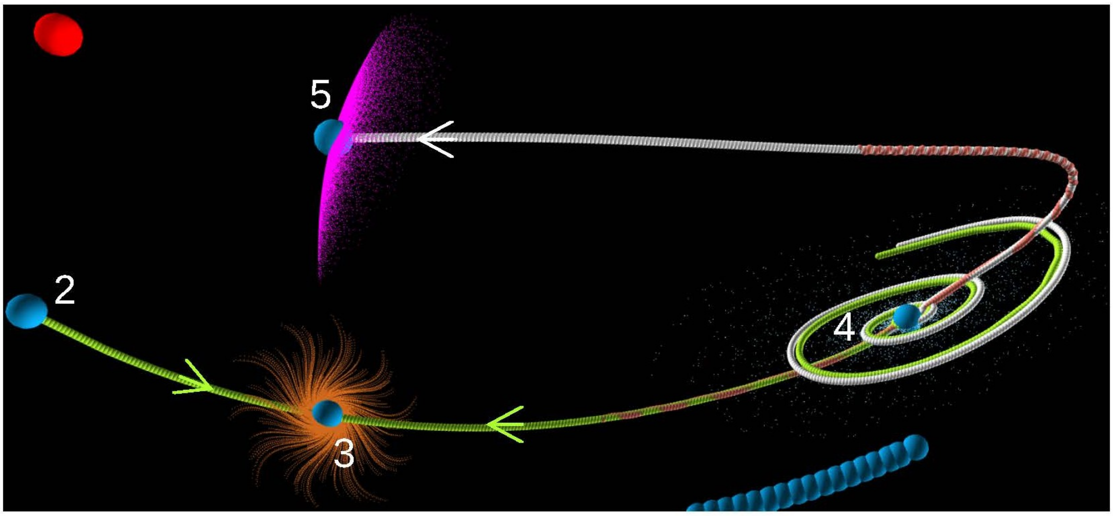

Figure 5.19: A 3D view of the isolated period-1 points and their manifolds for $\Theta = \pi/4$ and $\beta = 9$: (top) 1D stable manifold in yellow and 2D unstable manifold in green for point 7, 1D unstable manifold in orange and 1d stable manifold in cyan for point 6, and 1d stable manifold in white and 2D unstable manifold in magenta for point 5; (bottom) 1D stable manifold in white and 2D unstable manifold in magenta for point 5, 1D unstable manifold in salmon colour and 2D stable manifold in sky blue for point 4, and 1D stable manifold in green-yellow colour and 2D unstable manifold in chocolate colour for point 3.

5.5 Two wiggles

5.5.1 $\Theta = \pi/8$ and $\beta = 8$

The PRHF with the parameters $\Theta = \pi/8$ and $\beta = 8$ is considered to analyse inertial effects on the Stokes two wiggle period-1 line structures. Figures 5.20 and 5.21 are plotted in the same way to figures 5.17 and 5.18 respectively.

The figure 5.21 shows: the isolated period-1 points as solid large circles, the Stokes period-1 line as a transparent thick line, 1D manifolds as continuous black lines and 2D manifolds as small dots (2D unstable manifold of point 7 in green, 2D unstable manifold of point 5 in magenta, 2D stable manifold of point 4 in sky blue, 2D unstable manifold of point 3 in chocolate colour and 2D stable manifold of point 2 in violet). The manifolds of points 4 and 6 are not shown in figure 5.21 as they do not appear because they are perpendicular to the thin slice.

The Lagrangian structures for the two wiggle case is similar to the Lagrangian structures for one wiggle case (compare figure 5.21 to figure 5.14 and figure 5.23 to figure 5.16) except for the stability of the period-1 point 4. The period-1 point 4 is a hyperbolic-focus point in a one wiggle case, whereas in the two wiggle case, it is a hyperbolic-node point. The stable and unstable manifolds of point 4 (two wiggle case) are shown in figure 5.22 and the stable and unstable manifolds of point 4 (one wiggle case) are shown in figure 5.15g. In both cases, unstable manifolds are similar, and stable manifolds are different. Unstable manifolds in both the cases join the fuzzy shell $S1$.

5.5.2 $\Theta = \pi/4$ and $\beta = 16$

Another example of two wiggles case is considered with the parameters $\Theta = \pi/4$ and $\beta = 16$. The figures 5.24, 5.25 and 5.26 are obtained in the same way similar to figures 5.20, 5.21 and 5.23 respectively. The Lagrangian structures of both cases ($\Theta = \pi/4, \beta = 16$) and ($\Theta = \pi/8, \beta = 8$) shouble be compared in these figures. In both case the effect of inertia is similar.

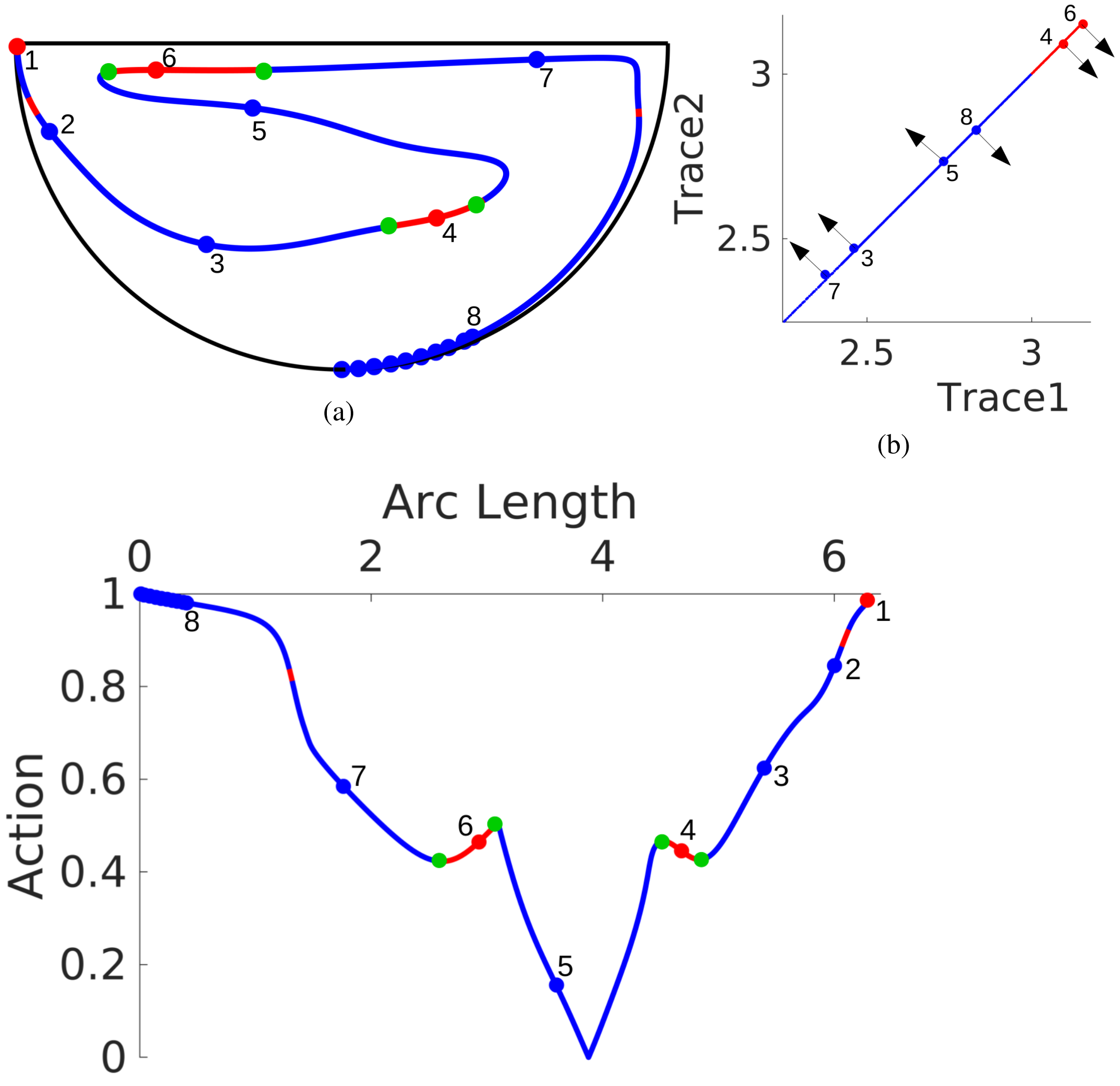

(a)

(b)

(c)

Figure 5.20: For $\Theta = \pi/8$ and $\beta = 8$: (a) Stokes Period-1 line and the isolated period-1 points of $R = 1$ flow; (b) Trace 1 vs Trace2 of the period-1 points of both the Stokes flow and Re=1 flow (small dots represent stokes period-1 points and bigger dots represent $Re = 1$ flow); (c) The Stokes period-1 line and the isolated period-1 points of $Re = 1$ flow are parameterized by action and arc length.

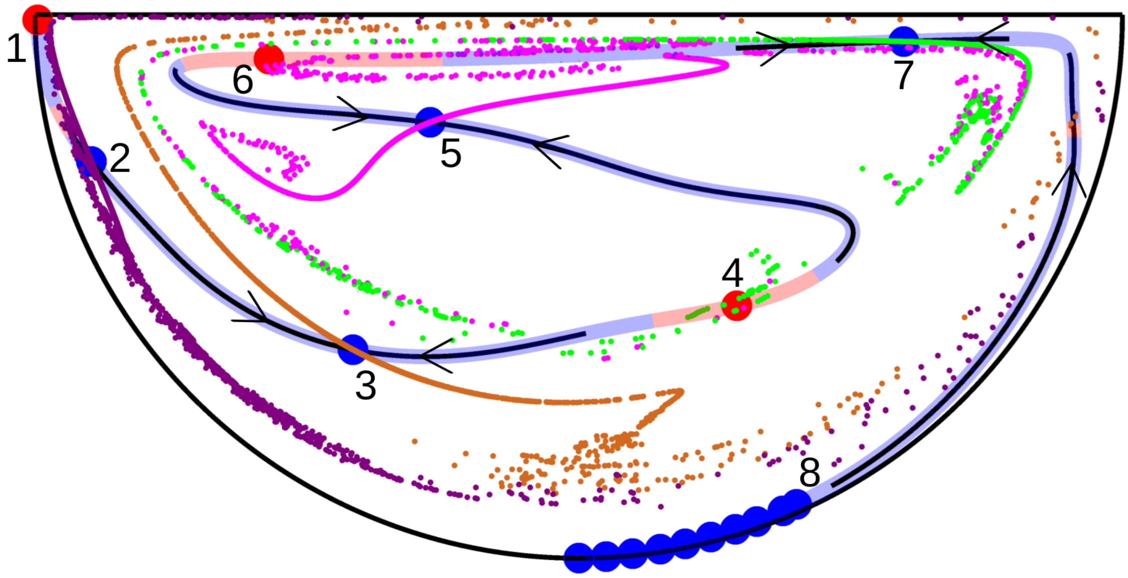

Figure 5.21: For $\Theta = \pi/8$ and $\beta = 8$ (a thin slice of the hemisphere centered at the symmetry plane viewed perpendicular the symmetry plane): Isolated period-1 points are shown as solid circles; Thick transparent line represents the Stokes period-1 line; Continuous black line represents 1D manifolds of the isolated period-1 points; Small dots represent 2D manifolds of the isolated period-1 points (2D unstable manifold of point 7 in green, 2D unstable manifold of point 5 in magenta, 2D unstable manifold of point 3 in chocolate colour and 2D stable manifold of point 2 in violet)

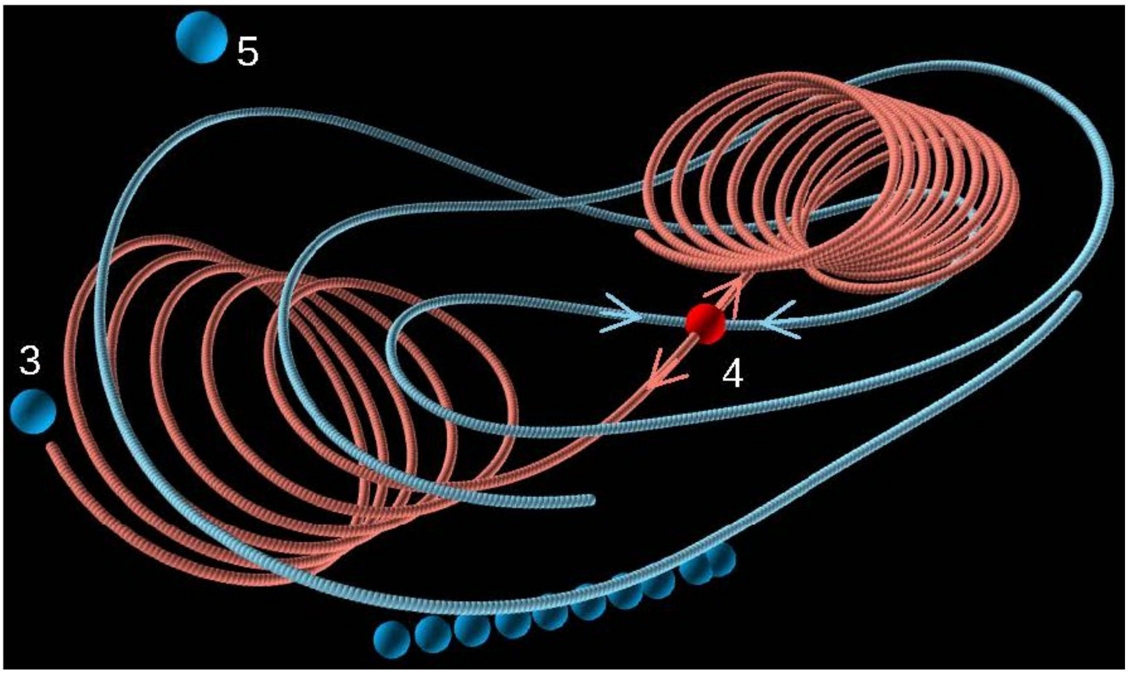

Figure 5.22: A 3D view of the manifolds of the hyperbolic-node period-1 point 4 for $\Theta = \pi/8$ and $\beta = 8$: 1D unstable manifold in salmon colour and 2D stable manifold in sky blue colour.

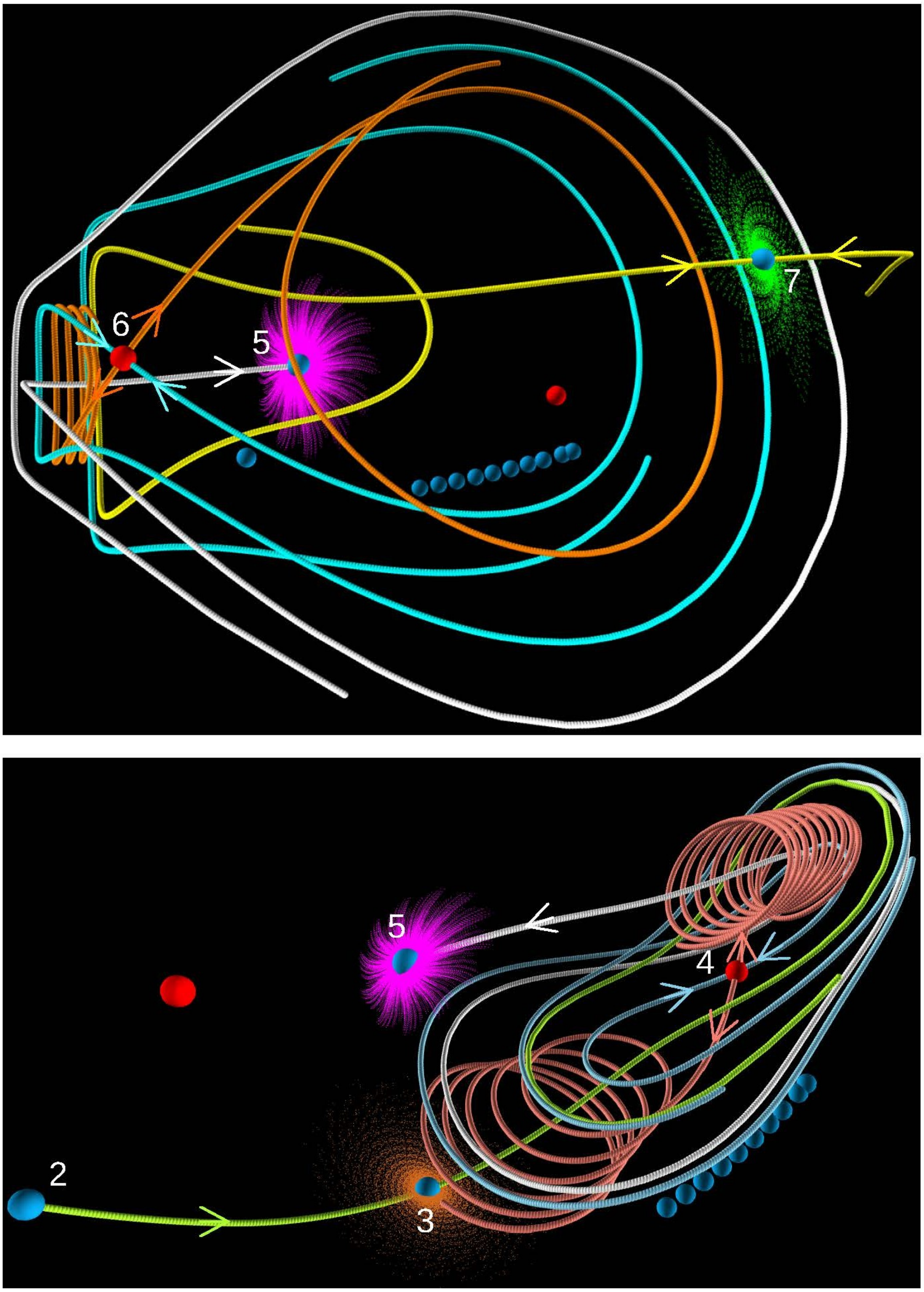

Figure 5.23: A 3D view of the isolated period-1 points and their manifolds for $\Theta = \pi/8$ and $\beta = 8$: (top) 1D stable manifold in yellow and 2D unstable manifold in green for point 7, 1D unstable manifold in orange and 1d stable manifold in cyan for point 6, and 1d stable manifold in white and 2D unstable manifold in magenta for point 5; (bottom) 1D stable manifold in white and 2D unstable manifold in magenta for point 5, 1D unstable manifold in salmon colour and 2D stable manifold in sky blue for point 4, and 1D stable manifold in green yellow and 2D unstable manifold in chocolate colour for point 3.

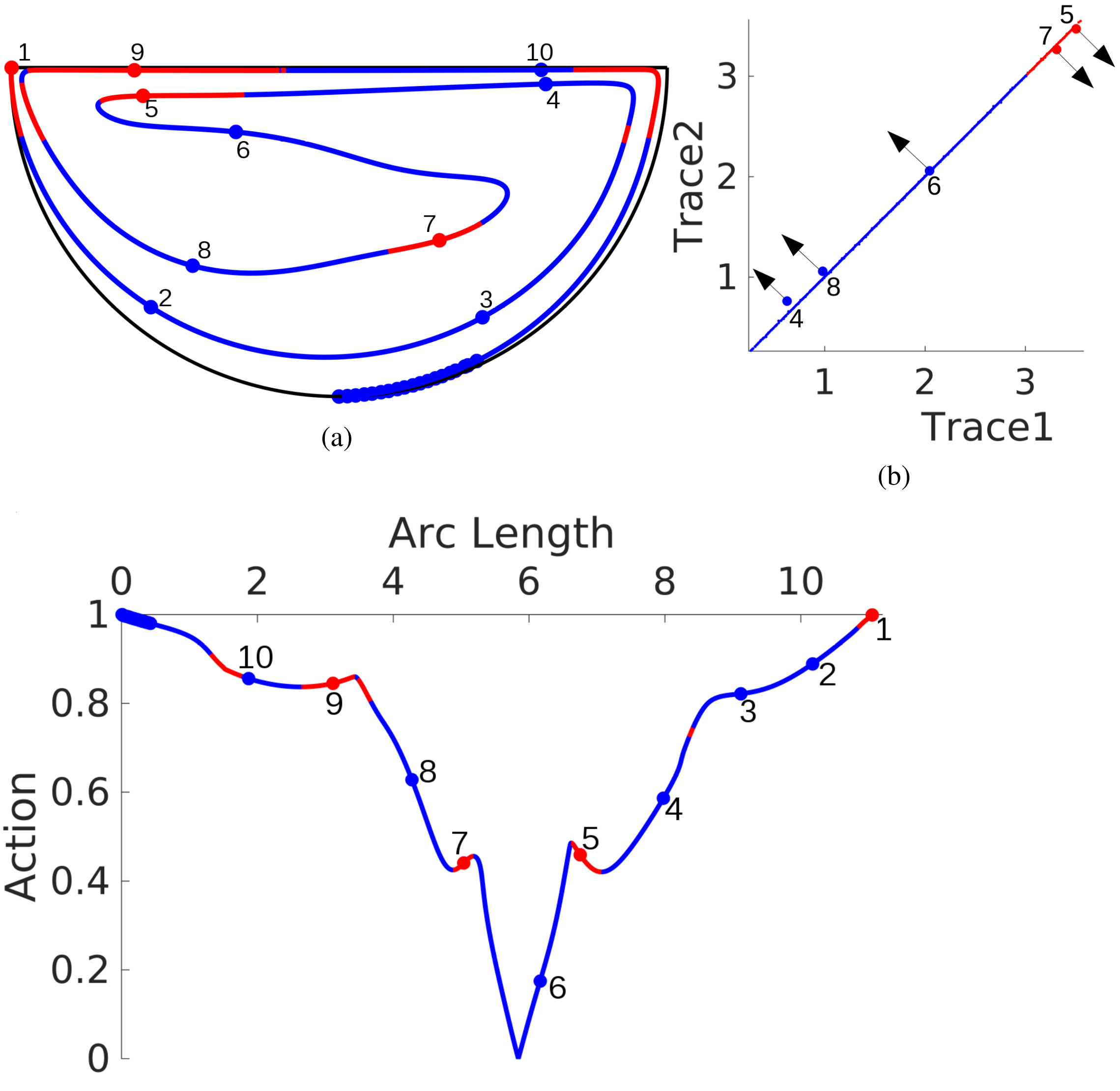

(a)

(b)

(c)

Figure 5.24: For $\Theta = \pi/4$ and $\beta = 16$: (a) Stokes Period-1 line and the isolated period-1 points of $R = 1$ flow; (b) Trace 1 vs Trace2 of the period-1 points of both the Stokes flow and Re=1 flow (small dots represent stokes period-1 points and bigger dots represent $Re = 1$ flow); (c) The Stokes period-1 line and the isolated period-1 points of $Re = 1$ flow are parameterized by action and arc length.

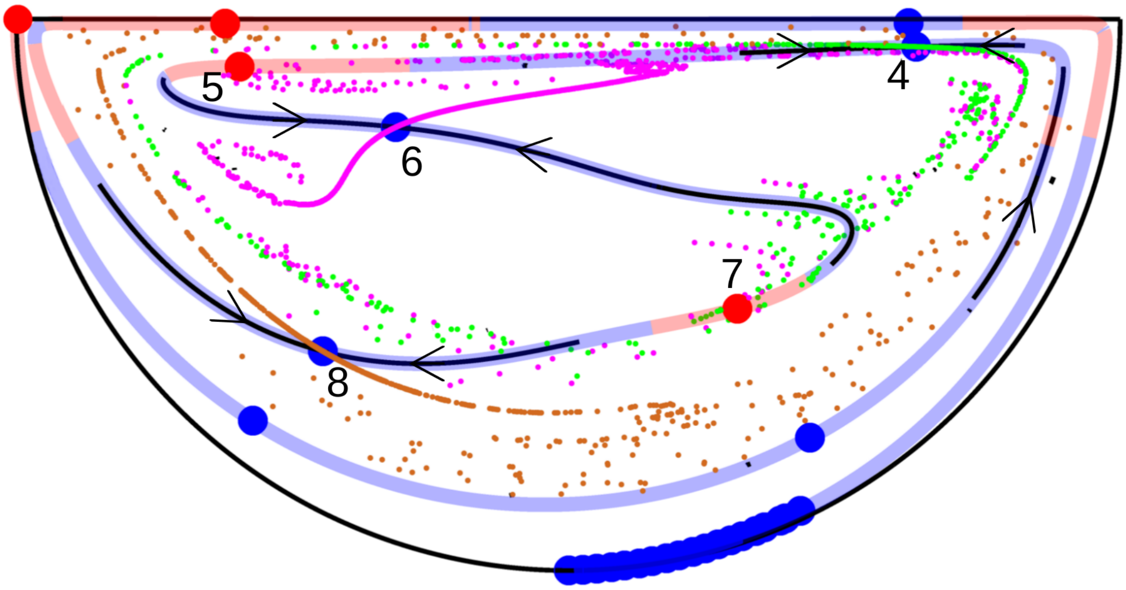

Figure 5.25: For $\Theta = \pi/4$ and $\beta = 16$ (a thin slice of the hemisphere centered at the symmetry plane viewed perpendicular the symmetry plane): Isolated period-1 points are shown as solid circles; Thick transparent line represents the Stokes period-1 line; Continuous black line represents 1D manifolds of the isolated period-1 points; Small dots represent 2D manifolds of the isolated period-1 points (2D unstable manifold of point 4 in green, 2D unstable manifold of point 6 in magenta and 2D unstable manifold of point 8 in chocolate colour).

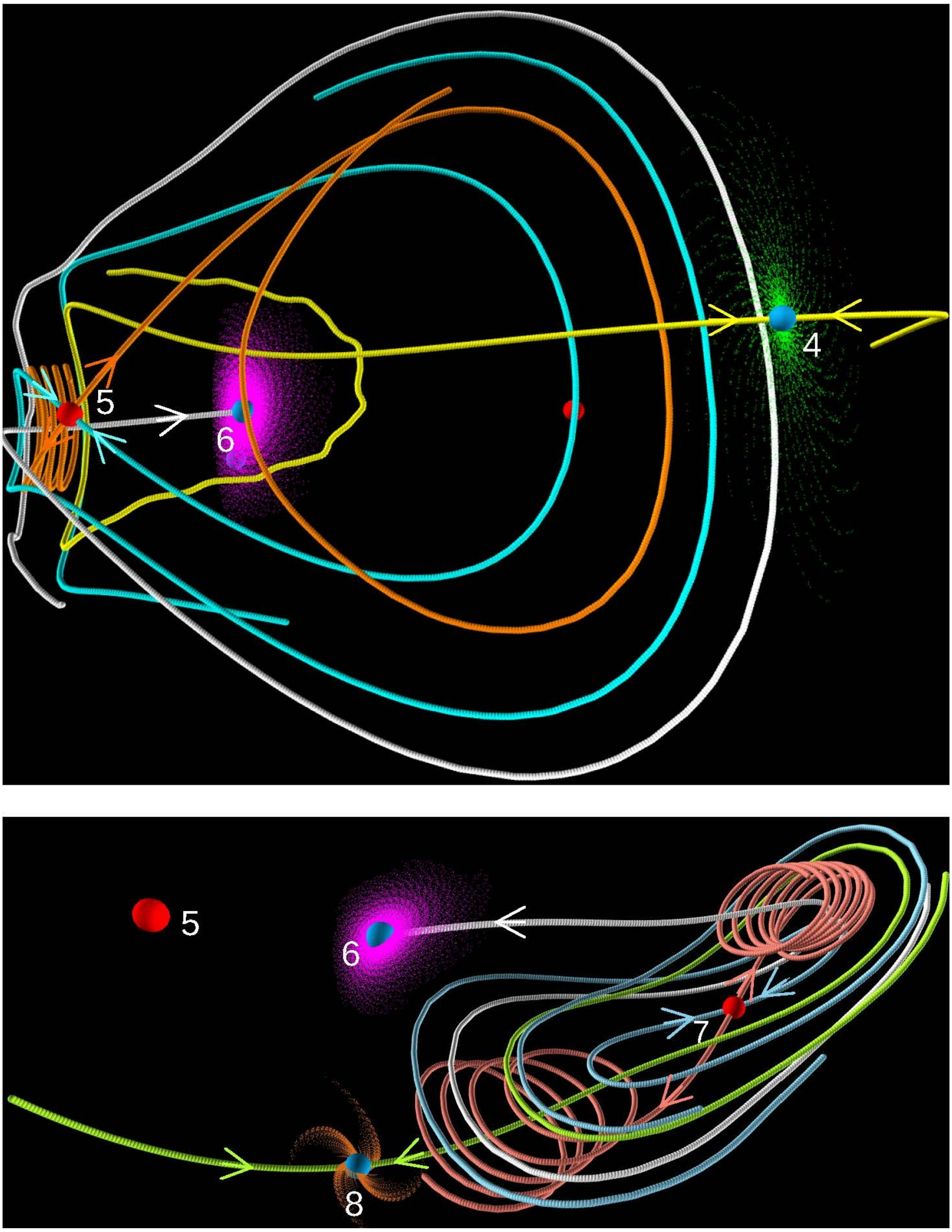

Figure 5.26: A 3D view of the isolated period-1 points and their manifolds for $\Theta = \pi/4$ and $\beta = 16$: (top) 1D stable manifold in yellow and 2D unstable manifold in green for point 4, 1D unstable manifold in orange and 1d stable manifold in cyan for point 5, and 1d stable manifold in white and 2D unstable manifold in magenta for point 6; (bottom) 1D stable manifold in white and 2D unstable manifold in magenta for point 6, 1D unstable manifold in salmon colour and 2D stable manifold in sky blue colour for point 7, and 1D stable manifold in green-yellow and 2D unstable manifold in chocolate colour for point 8.

5.6 Summary

To generate 3D transport in the PRHF, the symmetry of the PRHF is broken by adding inertia to the flow, and the inertial PRHF has zero-invariants. The inertia destroys periodic lines which existed in the Stokes flow. Isolated period-1 points which are not part of any period-1 line are found in the inertial regime, and their positions in the hemisphere domain are found very close to the Stokes period-1 line. In the limit $Re \to 0$, an isolated period-1 point moves to a point on the Stokes period-1 line. As β increases while keeping Θ constant, the length of a period-1 line increase in the Stokes regime, and the number of isolated period-1 points increases in the inertial regime. Isolated period-1 points are of two types: hyperbolic-focus and hyperbolic-node. The hyperbolic-focus period-1 point has a 2D manifold that spirals in or out and a 1D manifold. The hyperbolic-node period-1 point observed here has effectively two 1D manifolds, and the third 1D manifold direction rapidly converges with the dominant 1D manifold direction. Isolated periodic points and their manifolds determine the 3D Lagrangian transport structures. Isolated period-1 points which are close to the central stagnation point have a larger influence on transport structures than the period-1 points which are close to the hemisphere boundary. It is found that the Lagrangian structures do not change qualitatively with varying inertia at least in the range $Re = 10^{-5}$ to 1, but the speed with which a point traverses on the Lagrangian structures in a numerical computation depends on the magnitude of the Reynolds number. In the range $Re \in (0, 1)$, $Re = 1$ flow takes lesser time (less number of periods) to calculate a Lagrangian structure than a $Re < 1$ flow and hence the perturbation effect of inertia on the stokes Lagrangian structures is carried out with $Re = 1$ to speed up the computation time.

In one invariant flows, in the neighbourhood of an elliptic period-1 line segment, fluid particles move on a closed curve that is like a two action flow locally. After the inertial perturbation, the two action flow turns into a one action flow locally. The consequence of it is that fluid particles move on a tube locally in the inertial regime. We observe that the elliptic period-1 line segments turn into 1D manifolds of the isolated period-1 points and the fluid particles are moving in along the 1D manifold while spiralling around it. The effect of the inertial perturbation on a pure elliptic period-1 line of the Stokes flow is that the fluid particles move on nested tori. As β increases, a chain of heteroclinic connections is observed. Fluid particles spiral around heteroclinic connection and move along it. Some heteroclinic connections become the centre of nested toroids as shown in figure 5.7.

As β increases further, a wiggle which has a hyperbolic segment between two local extrema (1:1 resonance points) is formed on a period-1 line in the Stokes regime. After the perturbation, a hyperbolic-node period-1 point emerges from the hyperbolic period-1 line segment. Stable and unstable manifolds of several isolated period-1 points form the fuzzy shell (or mixing zone) as shown in figure 5.3. Fluid particles enter the fuzzy shell travelling along the tubular regions, then depart towards several isolated period-1 points, and again enter the fuzzy shell travelling along the tubular regions.

When qualitatively similar Lagrangian structures of the PRHF in Stoke regime are perturbed by inertia, the resulting perturbed Lagrangian structures are found to be qualitatively similar. The parameter β plays an important role that varying β produces fundamentally different Lagrangian transport structures. As β increases in the inertial flow, Lagrangian structures change from nested tori to a chain of heteroclinic connections to a 3D chaotic transport structure featuring non-heteroclinic connections of tubular transition regions. Whenever a 1:1 resonance exists in the Stokes flow, this kind of transport mechanism (non-heteroclinic and tubular transition) is observed upon inertial perturbation. The other 3D transport mechanisms that are reported so far have small regions of space where fast 3D transport happens upon perturbation away from one-invariant or two-invariant flows. The 3D transport mechanism presented here has large regions of space where 3D transport occurs that can result in the improvement of mixing quality. One of the major findings is that these tubular transition regions are generally observed in Hamiltonian systems of higher dimensions, for the first time they are observed in a 3D incompressible fluid.

Chapter 6

Conclusions

Understanding Lagrangian trajectories and controlling them is essential in designing efficient mixing devices for highly viscous fluids and microfluidic devices. Such devices often have spatial symmetry and/or time periodicity. Symmetries in a flow manifest as invariants of the flow, and destroying these invariants is a necessary, but not sufficient, condition for obtaining good mixing. In this thesis, the steady incompressible flow in a lid-driven hemisphere was considered. When the hemisphere lid moves uniformly in one direction, in the Stokes limit, a steady base flow is obtained which has left-right and fore-aft symmetries as shown in section 2.1.1. These two symmetries manifest as two invariants of the base flow, and fluid particles are constrained to move on closed invariant curves. These two invariants can be destroyed one after the other to generate one invariant and zero invariant flows. The first invariant is destroyed here by periodically reorienting the base flow (called PRHF - periodically reoriented hemisphere flow), which resulted in a time-reversal-reflection symmetry (see section 2.3.1), giving a one-invariant flow. In this one-invariant flow, fluid particles are constrained to move on closed invariant surfaces, which are topologically spheres. The advection of fluid particles on these invariant surfaces is Hamiltonian everywhere except at stagnation points. The last invariant is destroyed by adding small inertia to the PRHF, giving a zero invariant flow.

Numerical computation of Lagrangian structures is essential in understanding fluid transport. An analytic solution for the velocity field of the base flow does not exist, so velocity is obtained numerically. While the numerics provides velocity on a mesh grid to calculate a fluid particle trajectory, velocity between the grid points is needed. Hence an interpolation method is needed, but typical interpolation schemes do not preserve volume conservation, which is an essential requirement for studies of Lagrangian transport. A divergence-free interpolation method is critical to computing Lagrangian structures accurately, especially when the flow has invariants which must be obeyed by particle trajectories. A new divergence-free interpolation method was developed (see section 3.2). This numerical method is used in all of the computations of this thesis.

This method constructs spline functions for a vector potential $\boldsymbol{A}$ from the grid-based velocity data. The spline functions are calculated using standard B-splines, which are C^2 continuous and have compact support. Once the spline coefficients of the vector potential $\boldsymbol{A}$ are determined, the velocity field is determined simply through taking analytical derivatives of A. This method guarantees that any grid-based velocity data that samples a continuous divergence-free velocity field can be approximated with an analytic spline-based representation that is analytically divergence-free and matches all components of the velocity on the grid almost exactly. Apart from the solenoidal description, the benefits of this approach are that the subsequent interpolation is local (i.e. the relevant spline coefficients are defined only in a small sub-domain) and is therefore computationally cheap to use once the spline is determined. In particular, it is two to four orders of magnitude more accurate, dependent on the measure of accuracy, than the current best practice algorithm.

Although the new divergence-free interpolation scheme was developed with a primary motivation of accurately computing Lagrangian coherent structures, it is worth briefly mentioning two other areas in which obtaining an accurate vector potential is of interest. First, in Bajer's nearly everywhere Hamiltonian formulation of 3D flow (Bajer, 1994), components of the vector potential in a particular gauge occupy the roles of the Hamiltonian and the canonical momentum. Direct extraction, then, of the vector potential from data would aid in uncovering underlying 3D mathematical structures of fluid transport. Secondly, 3D velocimetry data is still almost always measured as two velocity components in a plane with a set of planes measured. The third velocity component (Say v_z) is estimated by integrating the divergence (i.e. $\int \frac{dv_z}{dz}dz = \int -(\frac{dv_x}{dx} + \frac{dv_y}{dy})dz$) along the third direction (Wereley and Meinhart, 2010). However, as this requires numerical derivatives in-plane and integrations transverse to the planes, there is scope for error to be introduced. On the other hand, a vector potential fit to only the in-plane data has the advantage that, once the spline coefficients are calculated, estimating the third velocity component requires only analytic derivatives and no integrations, meaning that estimating the velocity component via determination of the vector potential is much less prone to error.

In 3D flows with time-reversal reflection symmetry, period-1 points (and by extension the period-1 line) must lie on the symmetry plane as shown in section 2.3.2. In one invariant flows, isolated periodic points cannot exist (see section 2.3.4); closed periodic lines or periodic lines with ends attached to the boundary are possible. Hence, periodic lines and their manifolds constitute all of the Lagrangian structures in one invariant flows.

These periodic lines, in turn, control transport in the flow. In this one invariant flow, fluid motion is confined to shells (or invariant surfaces) and the nature of the periodic points determines the mixing on the shell. Wherever a periodic line pierces a shell, it imparts its character onto that shell in the neighbourhood of the piercing site. The Lagrangian topology on a shell depends on the number of piercings of periodic lines and the local stability at the piercings. It is difficult to identify how many periodic piercings a particular invariant surface has just by looking at periodic lines plots drawn in 3D space. Enumeration of the action variable along a periodic line is shown to be a useful way of understanding the Lagrangian topology on an invariant surface of a one invariant flow. Plotting action vs arc length along periodic lines allows us to determine the number of periodic line piercings and their stability on any shell by drawing a horizontal line at the shell (action) value. From action vs arc length plots of periodic lines, the local topology on any invariant surface can be quickly inferred. Because lower-order periodic lines exert more impact on fluid transport than higher-order periodic lines, period-1 lines become a skeleton for the Lagrangian structures. When searching for period-1 lines on the symmetry plane of PRHF, a single period-1 line is always found irrespective of the parameter values. The period-1 line starts at the bottom of the hemisphere and goes through the central stagnation point, and attaches at the rim of the hemisphere lid. The period-1 line comprises of elliptic and hyperbolic line segments, with segments of opposite type joining at degenerate points. For low lid displacement values (β), the period-1 line pierces each invariant surface twice. As the lid displacement increases, the length of the period-1 line increases, which results in an increase in the number of period-1 piercings on some shells.

A type of bifurcation point is found in the one invariant flow, that, in the shell normal direction at degenerate points, the local topology changes (see section 4.3). This behaviour can be viewed in terms of classical planar bifurcation theory by considering a 3D one invariant flow to be analogous to a 2D dynamical system with one parameter. In 3D one-invariant flows (action-angle-angle flows), since the flow occurs on 2D surfaces, angle variables are treated as phase space variables of a 2D system, and the action variable is treated as a parameter of the 2D system. The degenerate points on a periodic line are analogous to the resonance points in classical planar bifurcation theory. At an n^{th} order degenerate point on a period-1 line (termed a 1:n resonance point), n period-n lines intersect the period-1 line except for $n = 1$ and 2. At a 1:1 resonance point, the period-1 line is tangent to an invariant surface. At a 1:2 resonance point, a period-2 line intersects with the period-1 line. A period-m line of map $\mathbf{\Psi}$ can be considered as a period-1 line of map the $\mathbf{\Psi}^m$. This way, resonance points on the period-m line are treated as resonance points on a period -1 line but with the map $\mathbf{\Psi}^m$. In general, an m:p resonance point can exist on a period-m line, where $p > m$ and $p = m \times n$, where n is a positive integer. n ($= p/m$) period-p lines intersect at the m:p resonance point on the period-m line. Resonances like 2:3 cannot exist because a period-2 line can never intersect with a period-3 line. The eigenvalues of the deformation tensor at a 1:n resonance point are $1, e^{\pm i\frac{2\pi}{n}}$ which then makes the trace value to be $1 + 2\cos(\frac{2\pi}{n})$ at that point. The resonance points on periodic lines are identified by their trace values, and the corresponding higher-order periodic lines are obtained using the method discussed in section 3.6. The 1:1, 1:2, 1:3 and 1:4 resonances are called strong resonances (Gelfreich, 2002). These resonance bifurcations are local bifurcations because they can be found in the neighbourhood of degenerate points on periodic lines. A higher-order periodic line extending from a resonance point may attach to the boundary or join with another periodic line of the same order extending from another resonance point to form a closed higher-order periodic line. An example was shown in section 4.4 where the Lagrangian structures emanating from different resonance bifurcation points may connect and form truly global Lagrangian transport structures.

These degenerate points coordinate lower order and higher periodic lines and act as nodes in a Lagrangian network of periodic lines. The significance of these resonances points is that one invariant flows can be fully understood by finding the resonance points on the period-1 lines first, and then calculating the corresponding higher-order periodic lines, and then calculating period-2 lines and the corresponding higher-order periodic lines, and so on. This process is continued recursively until enough Lagrangian transport structures are revealed for any given purpose. This way of building extended structures from lower to higher order periodic lines allows the global Lagrangian transport structures to be uncovered for any 3D incompressible flow with one invariant.

In the one invariant PRHF, fluid transport is restricted to 2D spherical surfaces. To generate 3D chaotic transport, the symmetry of the one invariant flow must be broken. This could be done in different ways; here, inertia is used.

With the elimination of the last invariant, period-1 lines which existed in the one-invariant flow are lost; instead, isolated period-1 points are found in the zero-invariant flow. In the zero-invariant flow, when $Re \in (0, 1)$, the isolated period-1 points of the zero-invariant flow are spatially very close ($\approx 10^{-3}$ of hemisphere radius) to the period-1 line of the one-invariant flow. In the limit $Re \to 0$, an isolated period-1 point in the inertial flow approaches a point on the period-1 line of the one-invariant Stokes flow. The period-1 line (particularly elliptic segments of the period-1 line) of the one-invariant flow manifest as 1D manifolds of the zero-invariant flow. As β increases, the number of isolated period-1 points increases. Isolated period-1 points in this flow are of two types: hyperbolic-focus and hyperbolic-node. Isolated periodic points and their manifolds determine transport in the zero-invariant flow. It was found that the Lagrangian structures in the zero-invariant flow do not change qualitatively with varying inertia at least in the range $Re = 10^{-5}$ to 1, but the magnitude of the Reynolds number affects the speed with which a point traverses the Lagrangian structures in numerical computation. High Re flow takes fewer periods to calculate a Lagrangian structure than low Re flow.

For very low β values, when the Stokes period-1 line is pure elliptic, on perturbation, the flow changes from nested spheroids to a nested tori (see section 5.3.1). A heteroclinic connection between two isolated hyperbolic-focus period-1 points becomes the centre of a perturbed nested tori structure. Fluid particles spiral around heteroclinic connection and move along it. As β increases, a chain of heteroclinic connections between hyperbolic-focus period-1 points is observed (see section 5.3.3). A new result of this thesis is that topologically similar Lagrangian structures of the one-invariant flow, when perturbed, always produce topologically similar Lagrangian structures in the zero-invariant flow. This happens regardless of the specific flow parameters.

In this thesis, a detailed resolution of this transition from the 1:1 resonance transport structure is given. Upon inertial perturbation of 1:1 resonance points which always emerge as pairs on a period-1 line of the one-invariant flow, a hyperbolic-node period-1 point is always observed to emerge from the hyperbolic period-1 line segment which is between the 1:1 resonance points. This leads to a new mechanism of 3D chaotic transport featuring non-heteroclinic connections of tubular transition regions observed in section 5.4. The important thing is that fluid particle advection proceeds in the following way: chaotic zone → several isolated period-1 points → tubes → chaotic zone (see figure 5.3(c)). This transport mechanism is always observed here, upon inertial perturbation of any pair of 1:1 resonance points in the one-invariant flow. Hence it is conjectured to be a generic behaviour. Qualitatively similar tubular transition zones have been observed in Hamiltonian systems of higher dimensions, and for the first time, they are observed in a 3D incompressible flow.

6.1 Future work

Although the symmetry of the one-invariant flow is destroyed by the inertial perturbation, it's remnant seems to manifest in a more subtle way in the inertial flow. The reasons to speculate about the role of the symmetry plane in the inertial flow are: the isolated period-1 points are spatially located very close to the Stokes period-1 line which is on the symmetry plane, and the elliptic period-1 line segments of the Stokes flow are transforming into 1D manifolds of isolated period-1 points in the inertial flow. This aspect of the symmetry breaking can be investigated. Similarly, n^{th} order periodic lines of the one-invariant flow may transform into 1D manifolds of n^{th} order isolated periodic points of the zero-invariant flow upon perturbation, that can be examined. Also, the interaction between manifolds of lower-order and higher-order isolated periodic points can be explored.

Inertial perturbation of a pair of 1:1 resonance points in the one-invariant flow leads to a generic behaviour in the zero invariant flow, producing a new 3D chaotic transport mechanism. The new 3D chaotic transport mechanism with non-heteroclinic connections and tubular transition regions observed here in fluids for the first time and generally in Hamiltonian systems (Ross *et al.*, 2018) is not understood. Further study is needed to understand how such a transport structure is created, works, and evolves. The effect of the inertial perturbation on other resonance points (1:2, 1:3, etc.) of the one-invariant flow may lead to other generic behaviours that are yet to be investigated.

The Lagrangian structures of the PRHF in the inertial regime remain qualitatively same in the range $Re \in (0, 1)$ (see section 5.3.1). But this is unlikely to be the case when $Re \gtrapprox 10$. How the Lagrangian structures of the PRHF evolve in the inertial regime as $Re >> 1$ may open up entirely different avenues for transition to 3D chaos. The PRHF may yet prove to contain the seeds of additional, undiscovered global transport mechanisms in 3D flows.

Appendix A

Interpolation Conditions

A.1 Modified ABC flow

Table A1: Interpolation conditions for f - modified ABC flow.

Spline Direction	New Method
y	$f(y_0, z) = 0$ $\frac{\partial^2 f}{\partial y^2}(y_0, z) = \frac{\partial^2 f}{\partial y^2}(y_{n_y}, z)$
z	$\frac{\partial f}{\partial z}(y, z_0) = \frac{\partial A_y}{\partial z}(y, z_{n_z})$ $\frac{\partial^2 f}{\partial z^2}(y, z_0) = \frac{\partial^2 f}{\partial z^2}(y, z_{n_z})$

Table A2: Interpolation conditions for A_y - modified ABC flow.

Spline Direction	FC Method	New Method
x	$\frac{\partial A_y}{\partial x}(x_0, y, z) = v_z(x_0, y, z)$ $\frac{\partial A_y}{\partial x}(x_{n_x}, y_q, z_r) = v_z(x_{n_x}, y, z)$	$A_y(x_0, y, z) = 0$ $\frac{\partial^2 A_y}{\partial x^2}(x_0, y, z) = \frac{\partial^2 A_y}{\partial x^2}(x_{n_x}, y, z)$
y	$\frac{\partial A_y}{\partial y}(x, y_0, z) = \frac{\partial A_y}{\partial y}(x, y_{n_y}, z)$ $\frac{\partial^2 A_y}{\partial y^2}(x, y_0, z) = \frac{\partial^2 A_y}{\partial y^2}(x, y_{n_y}, z)$	$\frac{\partial A_y}{\partial y}(x, y_0, z) = \frac{\partial A_y}{\partial y}(x, y_{n_y}, z)$ $\frac{\partial^2 A_y}{\partial y^2}(x, y_0, z) = \frac{\partial^2 A_y}{\partial y^2}(x, y_{n_y}, z)$
z	$\frac{\partial A_y}{\partial z}(x, y, z_0) = \frac{\partial A_y}{\partial z}(x, y, z_{n_z})$ $\frac{\partial^2 A_y}{\partial z^2}(x, y, z_0) = \frac{\partial^2 A_y}{\partial z^2}(x, y, z_{n_z})$	$\frac{\partial A_y}{\partial z}(x, y, z_0) = \frac{\partial A_y}{\partial z}(x, y, z_{n_z})$ $\frac{\partial^2 A_y}{\partial z^2}(x, y, z_0) = \frac{\partial^2 A_y}{\partial z^2}(x, y, z_{n_z})$

Table A3: Interpolation conditions for A_z - modified ABC flow.

Spline Direction	FC Method	New Method
x	$\frac{\partial A_z}{\partial x}(x_0, y, z) = -v_y(x_0, y, z)$ $\frac{\partial A_z}{\partial x}(x_{n_x}, y, z) = -v_y(x_{n_x}, y, z)$	$A_z(x_0, y, z) = 0$ $\frac{\partial^2 A_z}{\partial x^2}(x_0, y, z) = \frac{\partial^2 A_z}{\partial x^2}(x_{n_x}, y, z)$
y	$\frac{\partial A_z}{\partial y}(x, y_0, z) = \frac{\partial A_z}{\partial y}(x, y_{n_y}, z)$ $\frac{\partial^2 A_z}{\partial y^2}(x, y_0, z) = \frac{\partial^2 A_z}{\partial y^2}(x, y_{n_y}, z)$	$\frac{\partial A_z}{\partial y}(x, y_0, z) = \frac{\partial A_z}{\partial y}(x, y_{n_y}, z)$ $\frac{\partial^2 A_z}{\partial y^2}(x, y_0, z) = \frac{\partial^2 A_y}{\partial y^2}(x, y_{n_y}, z)$
z	$\frac{\partial A_z}{\partial z}(x, y, z_0) = \frac{\partial A_z}{\partial z}(x, y, z_{n_z})$ $\frac{\partial^2 A_z}{\partial z^2}(x, y, z_0) = \frac{\partial^2 A_z}{\partial z^2}(x, y, z_{n_z})$	$\frac{\partial A_z}{\partial z}(x, y, z_0) = \frac{\partial A_z}{\partial z}(x, y, z_{n_z})$ $\frac{\partial^2 A_z}{\partial z^2}(x, y, z_0) = \frac{\partial^2 A_z}{\partial z^2}(x, y, z_{n_z})$

Bibliography

Alexandroff, P., 1961, *Elementary Concepts of Topology* (Dover Publications).

Aref, H., 1983, “Integrable, chaotic, and turbulent vortex motion in two-dimensional flows,” *Annual Review of Fluid Mechanics* **15**, 345–389.

Aref, H., 1984, “Stirring by chaotic advection,” *Journal of Fluid Mechanics* **143**, 1–21.

Aref, H., 2002, “The development of chaotic advection,” *Physics of Fluids* **14**, 1315–1325.

Aref, H., Blake, J. R., Budišić, M., Cartwright, J. H. E., Clercx, H. J. H., Feudel, U., Golestanian, R., Gouillart, E., Guer, Y. L., van Heijst, G. F., Krasnopolskaya, T. S., MacKay, R. S., Meleshko, V. V., Metcalfe, G., Mezić, I., de Moura, A. P. S., Omari, K. E., Piro, O., Speetjens, M. F. M., Sturman, R., Thiffeault, J.-L., and Tuval, I., 2017, “Frontiers of chaotic advection,” *Reviews of Modern Physics* **89**, 025007 (66 pages).

Arnold, V. I., 1978, *Mathematical Methods of Classical Mechanics* (Springer-Verlag New York).

Bajer, K., 1994, “Hamiltonian formulation of the equations of streamlines in three-dimensional steady flows,” *Chaos, Solitons and Fractals* **4**, 895–911.

Blackburn, H., and Sherwin, S., 2004, “Formulation of a Galerkin spectral element Fourier method for three-dimensional incompressible flows in cylindrical geometries,” *Journal of Computational Physics* **197**, 759 – 778.

Bott, R., 1982 09, “Lectures on morse theory, old and new,” *Bull. Amer. Math. Soc. (N.S.)* **7**, 331–358.

Boyland, P. L., Aref, H., and Stremler, M. A., 2000, “Topological fluid mechanics of stirring,” *Journal of Fluid Mechanics* **403**, 277 – 304.

Cartwright, J. H. E., Feingold, M., and Piro, O., 1995 Nov, “Global diffusion in a realistic three-dimensional time-dependent nonturbulent fluid flow,” *Phys. Rev. Lett.* **75**, 3669–3672.

Cartwright, J. H. E., Feingold, M., and Piro, O., 1996, “Chaotic advection in three-dimensional unsteady incompressible laminar flow,” *Journal of Fluid Mechanics* **316**, 259–284.

Cartwright, J. H. E., Feingold, M., and Piro, O., 1999, “An introduction to chaotic advection,” in *Mixing: Chaos and Turbulence*, edited by Chaté, H., Villermaux, E., and Chomaz, J.-M. (Springer US, Boston, MA). ISBN 978-1-4615-4697-9, pp. 307–342.

Cartwright, J. H., Feingold, M., and Piro, O., 1994, “Passive scalars and three-dimensional liouvillian maps,” *Physica D: Nonlinear Phenomena* **76**, 22 – 33.

Chaiken, J., Chu, C. K., Tabor, M., and Tan, Q. M., 1987, “Lagrangian turbulence and spatial complexity in a Stokes flow,” *The Physics of Fluids* **30**, 687–694.

Cheng, C. Q., and Sun, Y. S., 1989 Sep, “Existence of invariant tori in three-dimensional measure-preserving mappings,” *Celestial Mechanics and Dynamical Astronomy* **47**, 275–292.

Coltice, N., Gérault, M., and Ulvrová, M., 2017, “A mantle convection perspective on global tectonics,” *Earth-Science Reviews* **165**, 120 – 150.

Dimotakis, P. E., 2005, “Turbulent mixing,” *Annual Review of Fluid Mechanics* **37**, 329–356.

Dullin, H. R., Meiss, J. D., and Sterling, D., 1999 dec, “Generic twistless bifurcations,” *Nonlinearity* **13**, 203–224.

Dullin, H., and Meiss, J., 2008, “Nilpotent normal form for divergence-free vector fields and volume-preserving maps,” *Physica D: Nonlinear Phenomena* **237**, 156 – 166.

Erwin, L., 2011, *Encyclopedia of Polymer Science and Technology* (American Cancer Society). ISBN 9780471440260

Finn, J. M., and Chacón, L., 2005 May, “Volume preserving integrators for solenoidal fields on a grid,” *Physics of Plasmas* **12**, 1–4.

Fountain, G. O., Khakhar, D. V., Mezić, I., and Ottino, J. M., 2000, “Chaotic mixing in a bounded three-dimensional flow,” *Journal of Fluid Mechanics* **417**, 265–301.

Fountain, G. O., Khakhar, D. V., and Ottino, J. M., 1998, "Visualization of three-dimensional chaos," *Science* **281**, 683–686.

Franjione, J., Leong, C., and Ottino, J., 1989, "Symmetries within chaos: A route to effective mixing," *Physics of Fluids A: Fluid Dynamics* **1**

Gelfreich, V., 2002, "Near strongly resonant periodic orbits in a hamiltonian system," *Proceedings of the National Academy of Sciences* **99**, 13975–13979.

Gómez, A., and Meiss, J. D., 2002, "Volume-preserving maps with an invariant," *Chaos* **12**, 289–299.

Grebogi, C., Hammel, S. M., Yorke, J. A., and Sauer, T., 1990, "Shadowing of physical trajectories in chaotic dynamics: Containment and refinement," *Physical Review Letters* **65**, 1527–1530.

Habermann, C., and Kindermann, F., 2007 July, "Multidimensional spline interpolation: Theory and applications," *Computational Economics* **30**, 153–169.

Haller, G., and Mezić, I., 1998, "Reduction of Three-Dimensional Volume-Preserving Flows with Symmetry," *Nonlinearity* **11**, 319–339.

Haller, G., 2015, "Lagrangian coherent structures," *Annual Review of Fluid Mechanics* **47**, 137–162.

Hammel, S. M., Yorke, J. A., and Grebogi, C., 1987, "Do numerical orbits of chaotic dynamical processes represent true orbits?." *Journal of Complexity* **3**, 136–145.

Handscomb, D., 1993 February, "Local recovery of a solenoidal vector field by an extension of the thin-plate spline technique," *Numerical Algorithms* **5**, 121–129.

Hilborn, R. C., 2000, *Chaos and Nonlinear Dynamics: An Introduction for Scientists and Engineers*, 2nd ed. (Oxford University Press). ISBN 9780198507239

Jordan, T. F., 2004, "Steppingstones in hamiltonian dynamics," *American Journal of Physics* **72**, 1095–1099.

Katok, A., and Hasselblatt, B., 1995, *Introduction to the Modern Theory of Dynamical Systems*, Encyclopedia of Mathematics and its Applications (Cambridge University Press).

Kuznetsov, Y., 1998, *Elements of Applied Bifurcation Theory*, Applied Mathematical Sciences (Springer New York). ISBN 9780387983820

Lester, D. R., Metcalfe, G., Trefry, M. G., Ord, A., Hobbs, B., and Rudman, M., 2009 Sep, "Lagrangian topology of a periodically reoriented potential flow: Symmetry, optimization, and mixing," *Phys. Rev. E* **80**, 036208.

Lester, D. R., Rudman, M., Metcalfe, G., Trefry, M. G., Ord, A., and Hobbs, B., 2010 Apr, "Scalar dispersion in a periodically reoriented potential flow: Acceleration via lagrangian chaos," *Phys. Rev. E* **81**, 046319.

Lowitzsch, S., 2005 December, "Error estimates for matrix-valued radial basis function interpolation," *Journal of Approximation Theory* **137**, 238–249.

Malyuga, V., Melesko, V., Speetjens, M., Clercx, H., and van Heijst, G., 2002, "Mixing in the Stokes flow in a cylindrical container," *Proceedings of the Royal Society* **A458**, 1867–1885.

Meiss, J., 2012, "The destruction of tori in volume-preserving maps," *Communications in Nonlinear Science and Numerical Simulation* **17**, 2108 – 2121.

Mezić, I., and Wiggins, S., 1994, "On the integrability and perturbation of three-dimensional fluid flows with symmetry," *Journal of Nonlinear Science* **4**, 157–194.

Moharana, N. R., Speetjens, M. F. M., Trieling, R. R., and Clercx, H. J. H., 2013, "Three-dimensional lagrangian transport phenomena in unsteady laminar flows driven by a rotating sphere," *Physics of Fluids* **25**, 093602.

Morrison, P. J., 1998 Apr, "Hamiltonian description of the ideal fluid," *Rev. Mod. Phys.* **70**, 467–521.

Mullowney, P., Julien, K., and Meiss, J., 2005, "Blinking rolls: Chaotic advection in a three-dimensional flow with an invariant," *SIAM Journal on Applied Dynamical Systems* **4**, 159–186.

Narcowich, F. J., and Ward, J. D., 1994 October, "Generalized Hermite interpolation via matrix-valued conditionally positive definite functions," *Math. Comp.* **63**, 661–687.

Nguyen, N.-T., and Wu, Z., 2004 dec, "Micromixers—a review," *Journal of Micromechanics and Microengineering* **15**, R1–R16.

Ott, E., 2002, *Chaos in Dynamical Systems*, 2nd ed. (Cambridge University Press).

Ottino, J. M., 1989, *The kinematics of mixing : stretching, chaos, and transport*, Cambridge texts in applied mathematics [3] (Cambridge University Press, Cambridge ; New York). ISBN 0521363357

Ottino, J. M., 1990, "Mixing, chaotic advection, and turbulence," *Annual Review of Fluid Mechanics* **22**, 207–254.

Ottino, J. M., Muzzio, F. J., Tjahjadi, M., Franjione, J. G., Jana, S. C., and Kusch, H. A., 1992, "Chaos, symmetry, and self-similarity: Exploiting order and disorder in mixing processes," *Science* **257**, 754–760.

Ottino, J., Souvaliotis, A., and Metcalfe, G., 1995, "Chaotic mixing processes: New problems and computational issues," *Chaos, Solitons and Fractals* **6**, 425 – 438.

Pouransari, Z., Speetjens, M., and Clercx, H., 2010, "Formation of coherent structures by fluid inertia in three-dimensional laminar flows," *Journal of Fluid Mechanics* **654**, 5–34.

Priye, A., Hassan, Y. A., and Ugaz, V. M., 2013, "Microscale chaotic advection enables robust convective dna replication," *Analytical Chemistry* **85**, 10536–10541.

Ravu, B., Rudman, M., Metcalfe, G., Lester, D. R., and Khakhar, D. V., 2016, "Creating analytically divergence-free velocity fields from grid-based data," *Journal of Computational Physics* **323**, 75 – 94.

Ross, S. D., BozorgMagham, A. E., Naik, S., and Virgin, L. N., 2018 Nov, "Experimental validation of phase space conduits of transition between potential wells," *Phys. Rev. E* **98**, 052214.

Salmon, R., 1988, "Hamiltonian fluid mechanics," *Annual Review of Fluid Mechanics* **20**, 225–256.

Samelson, R., 2013, "Lagrangian motion, coherent structures, and lines of persistent material strain," *Annual Review of Marine Science* **5**, 137–163.

Shankar, P., and Deshpande, M., 2000, "Fluid mechanics in the driven cavity," *Annual Review of Fluid Mechanics* **32**, 93–136.

Smith, L. D., Rudman, M., Lester, D. R., and Metcalfe, G., 2016, "Bifurcations and degenerate periodic points in a three dimensional chaotic fluid flow," *Chaos: An Interdisciplinary Journal of Nonlinear Science* **26**, 053106.

Smith, L. D., Rudman, M., Lester, D. R., and Metcalfe, G., 2017, "Localized shear generates three-dimensional transport," *Chaos: An Interdisciplinary Journal of Nonlinear Science* **27**, 043102.

Speetjens, M., Clercx, H., and van Heijst, G., 2004, “A numerical and experimental study on advection in three-dimensional Stokes flows,” *Journal of Fluid Mechanics* **514**, 77–105.

Speetjens, M., Clercx, H., and van Heijst, G., 2006a, “Inertia-induced coherent structures in a time-periodic viscous mixing flow,” *Physics of Fluids* **18**, 083603.

Speetjens, M., Clercx, H., and van Heijst, G., 2006b, “Merger of coherent structures in time-periodic viscous flows,” *Chaos* **16**, 043104.

Squires, T. M., and Quake, S. R., 2005 Oct, “Microfluidics: Fluid physics at the nanoliter scale,” *Rev. Mod. Phys.* **77**, 977–1026.

Strogatz, S. H., 2001, *Nonlinear Dynamics And Chaos: With Applications To Physics, Biology, Chemistry, And Engineering*, 1st ed., Studies in Nonlinearity (Westview Press). ISBN 9780738204536

Suh, Y. K., and Kang, S., 2010, “A review on mixing in microfluidics,” *Micromachines* **1**, 82–111.

Thakur, R., Vial, C., Nigam, K., Nauman, E., and Djelveh, G., 2003, “Static mixers in the process industries—a review,” *Chemical Engineering Research and Design* **81**, 787 – 826.

Todd, D. B., 2004, *Mixing of Highly Viscous Fluids, Polymers, and Pastes* (John Wiley Sons, Ltd). ISBN 9780471451457, Chap. 16

Vainchtein, D. L., and Abudu, A., 2012, “Resonance phenomena and long-term chaotic advection in volume-preserving systems,” *Chaos: An Interdisciplinary Journal of Nonlinear Science* **22**, 013103.

Vainchtein, D. L., Widloski, J., and Grigoriev, R. O., 2007 Aug, “Resonant chaotic mixing in a cellular flow,” *Phys. Rev. Lett.* **99**, 094501.

Vainchtein, D. L., Widloski, J., and Grigoriev, R. O., 2008 Aug, “Resonant mixing in perturbed action-action-angle flow,” *Phys. Rev. E* **78**, 026302.

Ward, K., and Fan, Z. H., 2015 aug, “Mixing in microfluidic devices and enhancement methods,” *Journal of Micromechanics and Microengineering* **25**, 094001.

Wereley, S., and Meinhart, C., 2010, “Recent advances in micro-particle image velocimetry,” *Annual Review of Fluid Mechanics* **42**, 557–576.

Wiggins, S., 2003, *Introduction to Applied Nonlinear Dynamical Systems and Chaos* (Springer-Verlag New York).

Wiggins, S., 2005, “The dynamical systems approach to lagrangian transport in oceanic flows,” *Annual Review of Fluid Mechanics* **37**, 295–328.

Wiggins, S., 2010, “Coherent structures and chaotic advection in three dimensions,” *Journal of Fluid Mechanics* **654**, 1–4.

Wiggins, S., and Ottino, J. M., 2004, “Foundations of chaotic mixing,” *Philosophical Transactions of the Royal Society of London A: Mathematical, Physical and Engineering Sciences* **362**, 937–970.

List of Publications

- Ravu, B., Rudman, M., Metcalfe, G., Lester, D. R., and Khakhar, D. V., 2016, "Creating analytically divergence-free velocity fields from grid-based data," Journal of Computational Physics, 323, 75 - 94.

Submitted:

- Ravu, B., Metcalfe, G., Rudman, M., Lester, D. R., and Khakhar, D. V., "Global Organization of Three-Dimensional, Volume-Preserving Flows: Constraints, Degenerate Points, and Lagrangian Structure" Chaos (under review), full paper is available at: https://arxiv.org/abs/1911.04607.